Graphene Chemiresistors for Sensing Applications

A thesis submitted for the partial fulfilment of the requirement for the degree of

Doctor of Philosophy

In the faculty of Science of Durham University

By Selene Munoz-Vargas

Durham University

Department of Chemistry

University Science Laboratories

South Road

Durham

2024

Copyright

Declaration

This work was conducted in the Department of Chemistry at Durham University between October 2020 and December 2023. The work has not been submitted for a degree in this, or any other university. It is my own work, unless otherwise indicated.

XPS data collection was performed at the EPSRC National Facility for XPS (‘HarwellXPS’), operated by Cardiff University and UCL, under contract No. PR16195.

Acknowledgements

First, thanks to my supervisors, Professors Karl Coleman and Robert Pal. Thank you, Professor Karl for give me the opportunity to work in your group, for your advice during the experimental work and the enjoyable talks that we had. Thank you Professor Robert Pal, for all you help in the final stage of my PhD studies, especially with the revisions, I really enjoyed all the food that you cooked.

Thanks to all the staff at Durham University, Helene Rusby, Tony Humphries, Tony Baxter, Annette Passmoor, Jean Eccleston, Emily Chester, Meghan Smith, and all those who help me during my PhD studies. I would like to express my deepest gratitude to the glassblowing (Aaron Brown and Malcolm Richardson), mechanical (Neil Holmes, Paul White and Tony Newman), and electrical (Kelvin Appleby and Bryan Denton) workshops. Thank you for your help in making the set-ups and for your invaluable advice on this project. Thanks also to Leon Bowen and Diana Alvarez-Ruiz for the trainings in electron microscopy.

Thank you, Marcos, for letting me be a part of your life, for all the love and good times we have had together. Thanks for all the laughs in the lab, for all the (crazy) ideas, for your engineer advice, for all the academic discussions, and specially for the support and encouragement during my PhD studies.

I want to thank you to all my family and friends for always be there for me and for your loving words. "*Gracias mamá por todo tu amor, apoyo y palabras de aliento durante mi vida, te amo mamá. Gracias a mi hermano, sobrino y cuñada por sus palabras de aliento, y por estar ahí cuando más les he necesitado. Los quiero mucho.*"

Thanks to the National Council of Humanities, Sciences and Technologies (Conahcyt, Mexico) for giving me the opportunity to study at Durham University with the scholarship grant reference 2020-000000-01EXTF-00159.

Dedication

With love to my father Jorge Francisco Muñoz Solís (1951-2021).

"Por creer en mí y apoyarme siempre. Te seguiré contando por las noches como va todo y lo mucho que sigo extrañándote, te amo papá."

Abbreviations

AFM	Atomic force microscopy
APCVD	Atmospheric pressure chemical vapour deposition
CNTs	Carbon nanotubes
Cu	Copper
CuAAC	Copper(I)-catalysed alkyne–azide cycloaddition
CVD	Chemical vapour deposition
DI	Deionized
DOS	Density of states
EE	Electrochemical exfoliation
EEG	Electrochemically exfoliated graphene
EEG-N_3	Azidated electrochemically exfoliated graphene
EEG-TU	Electrochemically exfoliated graphene functionalised with TU
FET	Field effect transistors
FWHM	Full width at half maximum
Gr	Graphene
GIC	Graphene intercalated compound
GNP	Graphene nanoplatelets
GNSs	Defect-free graphene nanosheets
GO	Graphene oxide
HOPG	Highly oriented pyrolytic graphite
HRTEM	High-resolution TEM
I_{2D}	Intensity of 2D peak
I_G	Intensity of G peak
LPCVD	Low pressure chemical vapour deposition
PC	Polycarbonate
PMMA	Polymethyl methacrylate
Pos2D	2D peak position
Pos2G	G peak position
SAED	Selected area electron diffraction

SEM	Scanning electron microscopy
SOP	Standard operation procedure
SWCNTs	Single-walled carbon nanotubes
rGO	Reduced graphene oxide
TEM	Transmission electron microscopy
TGA	Thermogravimetric analysis
TRT	Thermal release tape
TU	1-(3,5-bis(trifluoromethyl)phenyl)-3-(prop-2-yn-1-yl)thiourea
UV	Ultraviolet
VOCs	Volatile organic compounds
XPS	X-ray photoelectron microscopy
XRD	X-ray diffraction

Abstract

Graphene has attracted significant attention since its discovery in 2004, as a result of its good mechanical, optical and electrical properties, that renders suitable for numerous applications. The most common method to produce high-quality monolayer graphene is chemical vapour deposition (CVD). However, the cold wall commercial equipment to synthesise it is too expensive, and even the cost of a small piece of graphene on copper could pose as a bottleneck for laboratories to study graphene. An alternative graphene production is the electrochemical exfoliation of graphite foil in inorganic salts; however, its quality is inherently compromised.

On the other hand, gas sensors capable of detecting vapours markers in real-time are desirable. Graphene materials have attracted scientific interest for the fabrication of gas sensors because of their single atom thick two-dimensional structures, high conductivity, and large specific surface area. In addition to this, graphene can be functionalised, opening the door to make highly selective graphene-based gas sensors.

In this work, two different approaches for graphene synthesis were used: low-pressure chemical vapour deposition (LPCVD) and simultaneous electrochemical exfoliation and functionalisation. Graphene films were grown on copper foil using methane as a carbon source. Herein a custom designed set up and an accompanying standard operation procedure is reported as well as the expected batch to batch variations and variation introduced by the position in the reactor. The synthesis of graphene films, comparable in quality and uniformity to those produced by commercial brands, has been achieved through the use of a cost-effective LPCVD setup and easily accessible copper foil without any pre-treatment. Despite the slight variations observed in the reported metrics, any residual strain and unintentional doping can partially explain these. Furthermore, the average spectrum of each sample exhibits a weak D peak signal, suggesting few defects comparable to those found in commercial samples.

Electrochemical exfoliated graphene functionalised with azide groups was synthesised by simultaneous electrochemical exfoliation and functionalisation from graphite foil in sodium sulphate/sodium azide electrolyte. This method can be an alternative to easily produce azidated graphene in a larger scale. The azidated graphene flakes range from monolayer to few-layer and the electrical conductivity was preserved. Here, we used the azide groups on the surface of graphene to covalently attach a sensing

molecule to the surface of graphene, demonstrating its convenient application in the development of graphene chemical resistors.

Both materials, graphene produced by CVD and electrochemical exfoliation, were functionalized with a sensing molecule, that has shown selectivity to cyclohexanone, and tested as chemiresistor under cyclohexanone, acetone, hexane, and ethanol. CVD graphene and electrochemical exfoliated graphene-based sensors show a better sensitivity with functionalization than without functionalization when they are exposed to different concentrations of cyclohexanone vapour; however, the latter shown better performance in terms of response, and sensitivity, having a limit of detection of 4.55 ppm. Figure 1 describes the whole process of the work done.

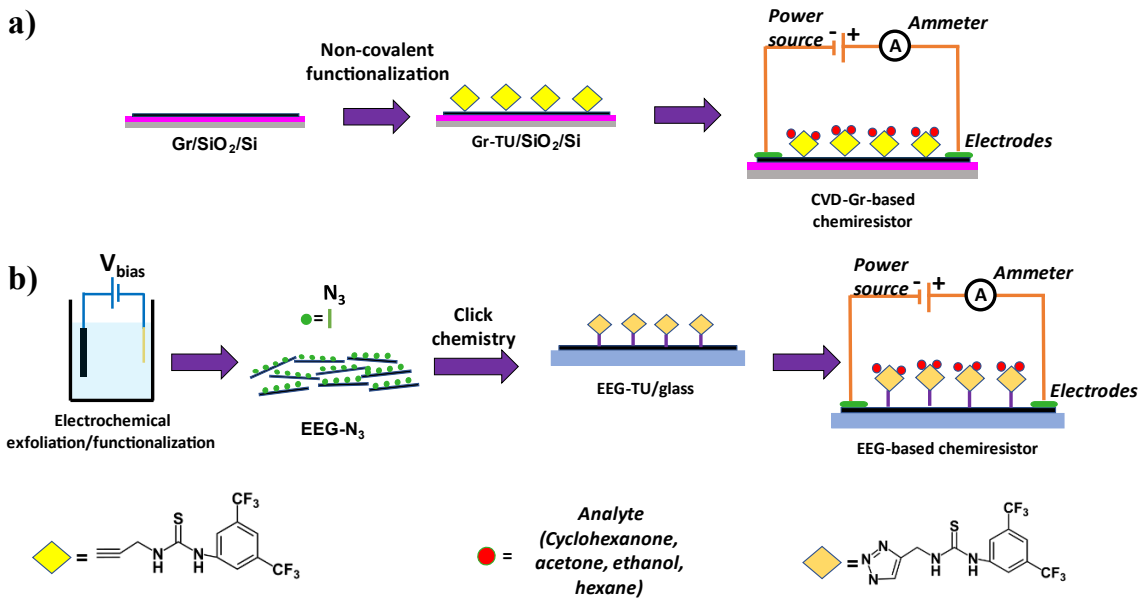

Figure 1. a) CVD graphene on copper was transferred to SiO_2/Si, then the selector was drop casted on it and it was tested under analyte vapour exposure as a chemiresistor. b) Simultaneous electrochemical exfoliation and functionalization of graphite to produce azidated graphene, after click chemistry the selector was introduced, the flakes were deposited on a glass substrate by drop casting, and it was tested under analyte vapour exposure as a chemiresistor.

Contents

1 Introduction.

In this brief introduction a systematic literature review will be provided to understand the structure of graphene and its properties. This will be complemented by a review of the production methods of graphene, focusing on chemical vapour deposition (CVD) and electrochemical exfoliation, the two most common and relevant to this thesis. Functionalisation approaches, non-covalent and covalent, and click chemistry as a tool to make graphene selective in gas sensor applications and current applications will also be discussed.

1.1 Graphene structure and properties.

Carbon can form three different types of hybridization, namely sp, sp^2 and sp^3, because of its four electrons in the valance shell. These can form different allotropes of carbon such as diamond (sp^3 hybridized bonds), graphite and fullerenes (sp^2 hybridized bonds).[1] Graphite has a lamellar structure formed by layers that have its carbon atoms arranged in a hexagonal structure. Two kinds of stacking can be observed in graphite: hexagonal or rhombohedral, despite both having very similar physical properties, with the hexagonal being the most stable. The hexagonal lattice is formed by sharing three sp^2 electrons with three neighbouring carbon atoms, the carbon-carbon bond length is approximately 0.142 nm, and the fourth electron of carbon is delocalised over the whole plane of graphite. The sp^2 carbon has very strong in-plane bonding (covalent bond) but weak out-of-plane bonding. The weak interplanar van der Waals interactions allows graphite sheets to slide over each other to form graphene,[1,2] which is the basic structural building block of other allotropes like graphite, carbon nanotubes and fullerenes (Figure 1.1).[3] However its discovery took 60 years since its prediction until it was obtained from graphite using micromechanical cleavage.[1]

The electronic structure of a single graphite layer was studied by Philip Wallace in 1947,[4] but the term graphene layer was defined as a single carbon layer in 1985 by Boehm *et al.*[5] At first graphene was considered as a hypothetical unit structure of graphite, far from a real nanomaterial.[1,6] In 1999, Ruoff´s group suggested that rubbing highly oriented pyrolytic graphite (HOPG) on silicon wafer could be a way to get multiple or even single layers of graphene, but further examination of the thickness of the outcome materials was neglected.[7] It was not until 2004 when Andre Geim and Konstantin Novoselov published the first method to afford single layer graphene, by mechanical exfoliation, and tested the

electronic field effect properties of graphene.[8] This discovery resulted in them receiving the Nobel Prize in Physics in 2010. Since then, graphene has received a lot of attention in a bid to make the synthetic processes scalable, and currently graphene growth by chemical vapour deposition (CVD) on copper foil[9] is one of the most promising methods to scale up graphene film production. This is attributed to the low solubility of carbon in copper, which enables the growth of large single layer graphene films.

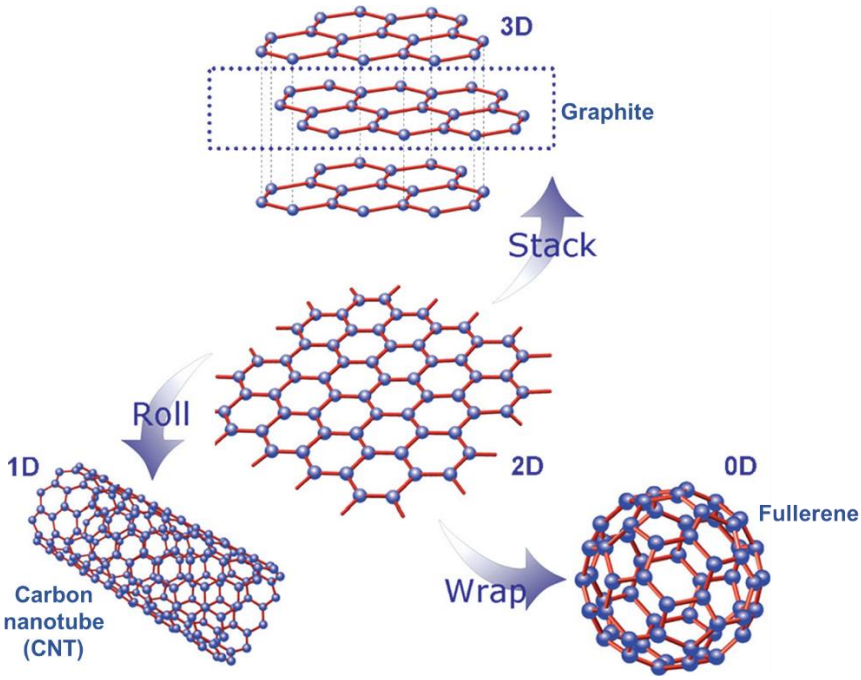

Figure 1.1 Graphene is the basic building block of other important allotropes of carbon: wrapping it to form fullerene, rolling it to form carbon nanotube (CNT) and stacking it to get graphite. Adapted from reference 3.

Graphene possesses remarkable properties in terms of optical transparency, electric conductivity, mechanical strength, and thermal conductivity. Graphene is one atom thick and only absorbs 2.3 % of the incident white light, so it has a high transparency of 97.7% which decreases with the number of graphene layers.[10,11] Figure 1.2a, b and c show the UV-vis spectra of graphene films and the optical transparency decreasing with the number of layers.

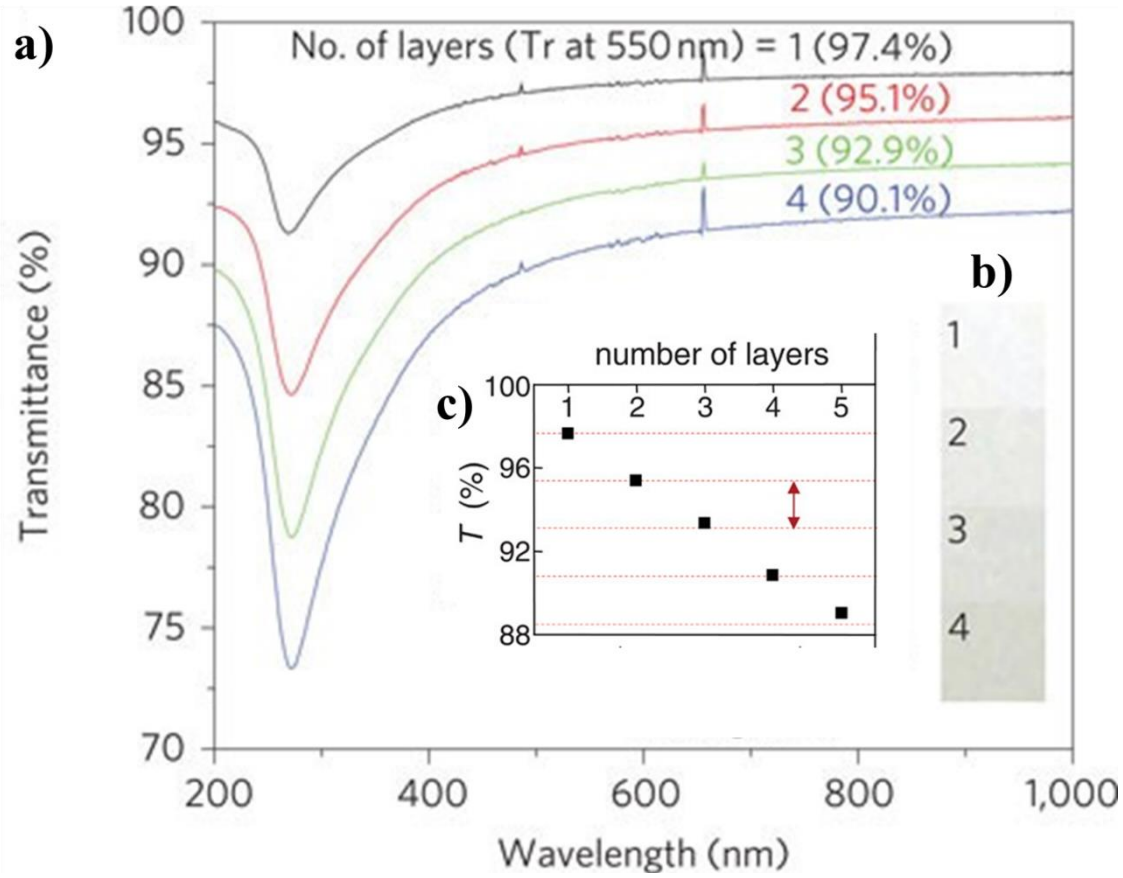

Figure 1.2 a) and b) UV–vis spectra and optical images corresponding to different number of graphene layers (1 - 4) on quartz substrates. Adapted from reference 11. c) Transmittance of white light as a function of the number of graphene layers (squares). Adapted from reference 10.

Because of the refraction and interference of the light, optical image contrast of graphene on SiO_2/Si substrates can be used to distinguish the layers of it, as it is showed in Figure 1.3, where the contrast increase with the number of layers.[12]

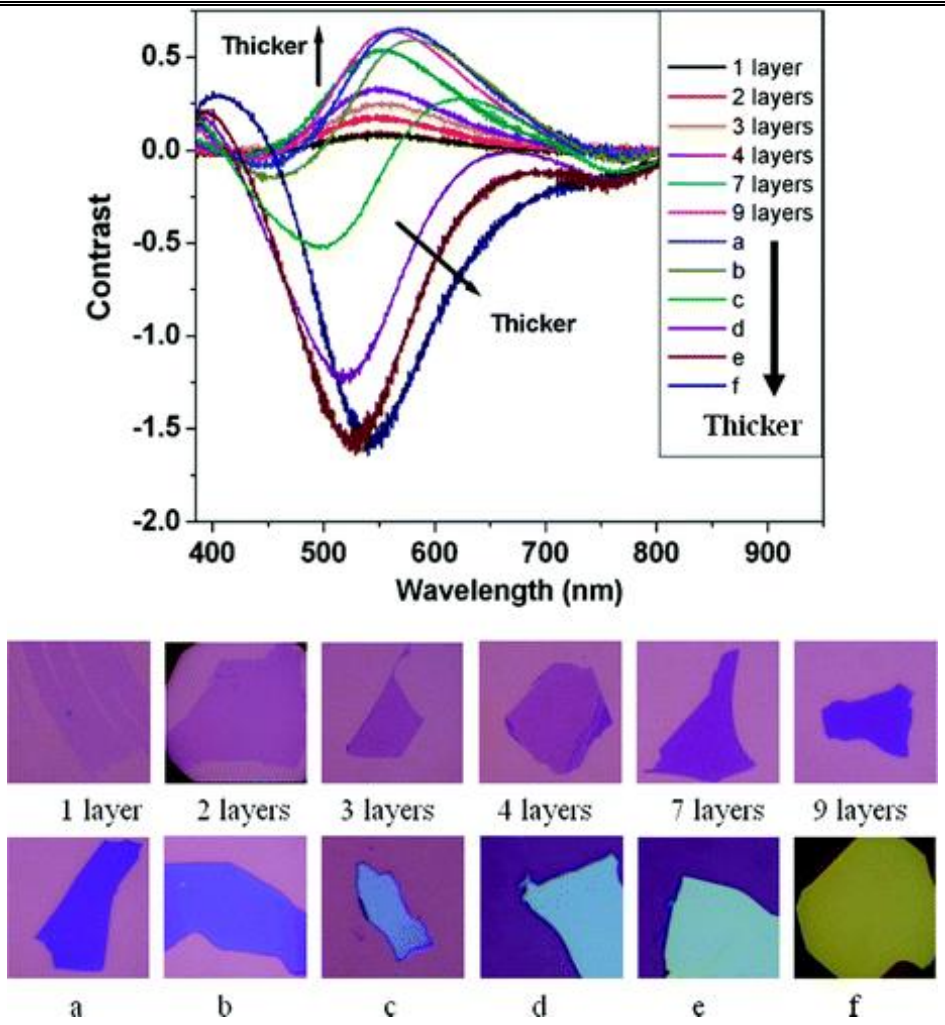

Figure 1.3 The contrast spectra and optical images of graphene sheets with different thickness, from 1 to 9 layers and more than 10 layers (a - f). Reprinted from reference 12.

Graphene is a highly conductive material at room temperature, with a conductivity up to $1.46 \pm 0.82 \times 10^6$ S/m [13] that varies according to the synthesis method used to produce it. As seen in Figure 1.4a, CVD graphene is a conductive and optically transparent material, however this is not enough to satisfy the conditions to replace indium thin oxide (ITO) membranes, that have a sheet resistance ~100 Ω/□ (ohms per square) and transmittance ~ 90%.[14]

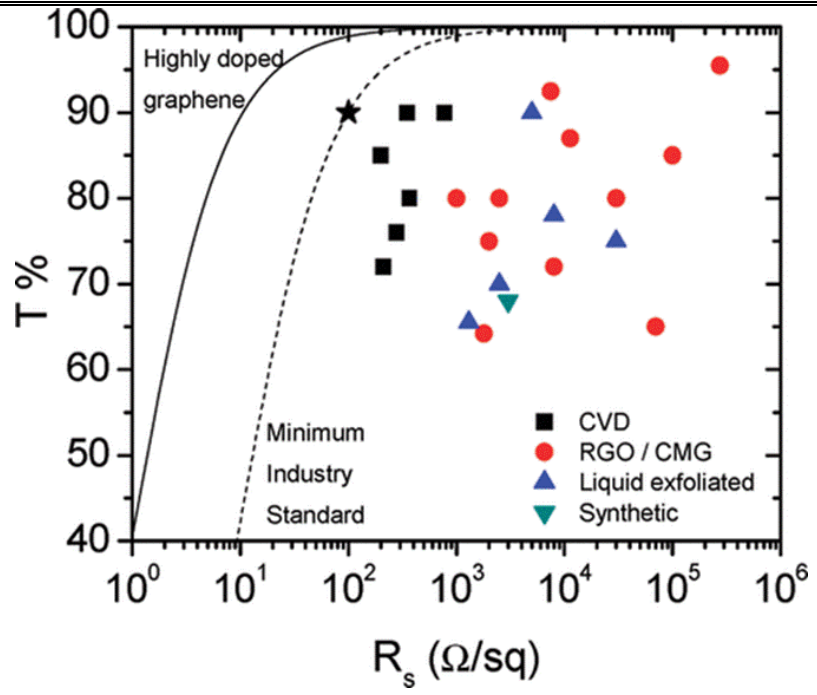

Figure 1.4 a) Transmittance and sheet resistance data for papers appearing in the literature for films prepared by CVD, reduced graphene oxide or chemically modified graphene, pristine exfoliated graphene, or chemically synthesised graphene. The star (★) represents the minimum industry standard for transparent electrodes. Adapted from reference 14.

Graphene has ambipolar behaviour, so charge carriers can be continuously tuned between electrons and holes in concentrations as high as 10^{13} cm^{-2},[6,8] also it shows a high electron mobility around 2×10^5 cm^2 V^{-1} s^{-1}.[15] As shown in Figure 1.5a graphene bonds are hybridised in sp^2 configuration, there are three in-plane σ bonds/atom and one *p* orbital develops into delocalized π and π* states that form the highest occupied valence band and the lowest unoccupied conduction band.[16,17] The formed valence and conduction bands touch 6 points (the Dirac cones) at the boundary of the first Brillouin zone (Figure 1.5b).[17] In monolayer graphene, there is an overlap in a single point between the conduction and the valence band, Figure 1.5c, so the electrons at the top of the valence band could flow into the bottom of the conduction band with lower energy without any heat stimulation.[1]

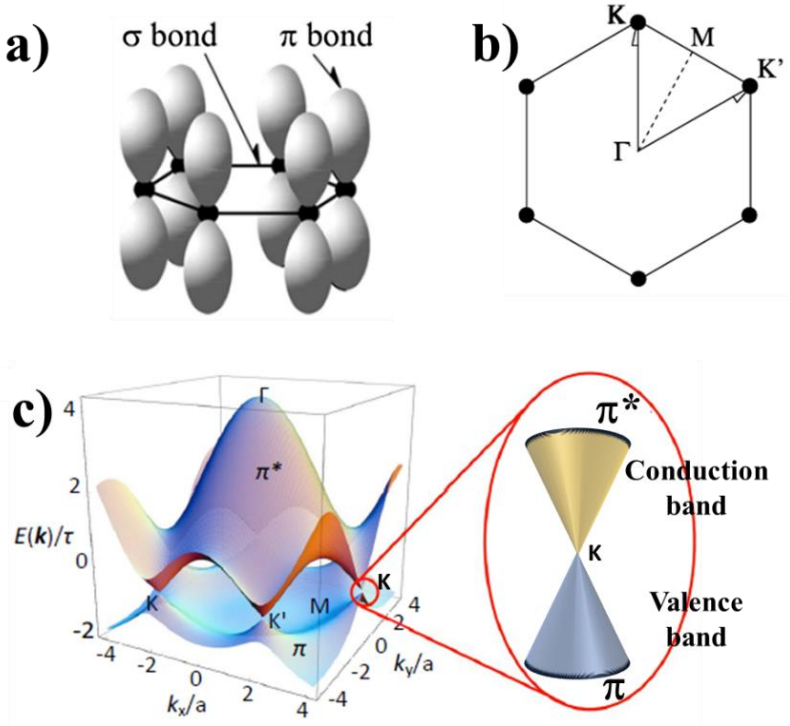

Figure 1.5 a) Schematic of the in-plane σ bonds and the π orbitals perpendicular to the plane of the graphene sheets, and b) the Brillouin zone. The Dirac cones are located at the K and K' points. Reproduced from reference 16*. c) Electronic dispersion in the honeycomb lattice, the six Dirac cones are showed. Adapted from reference* 18*.*

Since the density of states (DOS) for prefect graphene is zero at the Dirac points, electronic conductivity is quite low. Defect or doping can change the Fermi level (E_F) creating free electrons or holes that modify the electronic properties of graphene, Figure 1.6a. A notable feature on graphene transistors is its ability to continuously vary the resistivity (ρ) by controlling the back gate voltage (V_g), Figure 1.6b.[6]

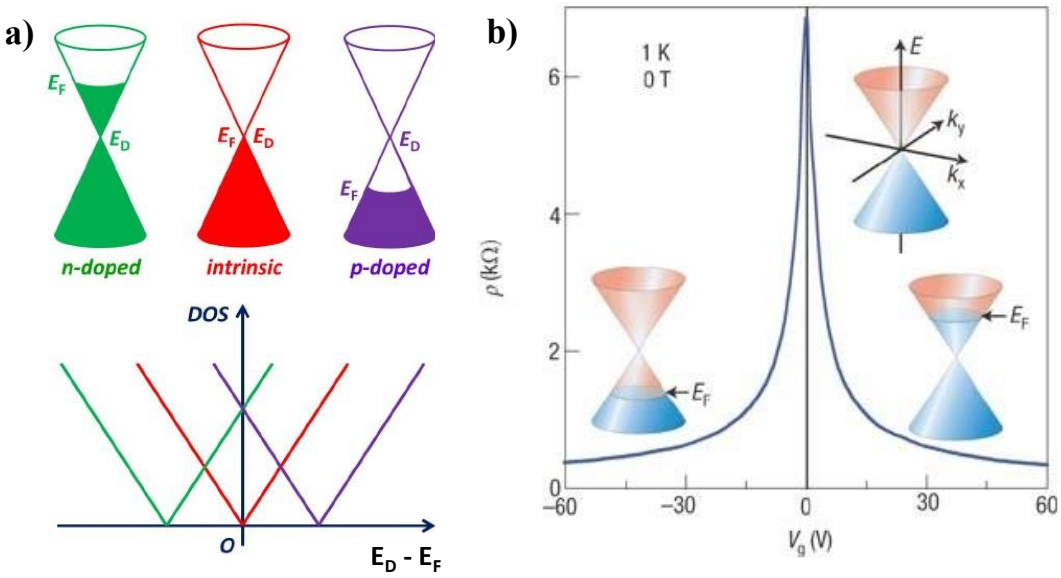

Figure 1.6 a) Representation of the density of states (DOS) of n-doped graphene (green), intrinsic graphene (red), and p−doped graphene (purple), Fermi level (E_F) and Dirac point (E_D). Reproduced from reference 19. *Ambipolar electric field effect in single-layer graphene, indicating changes in the position of the Fermi level, E_F, with changing gate voltage V_g. Positive (negative) V_g induce electrons (holes). Reproduced from reference* 6.

Graphene mechanical strength and thermal conductivity are also outstanding. These mechanical properties were measured by placing a graphene flake on silicon with circular holes and tapping an AFM tip in the centre of them, the tensile strength and elastic modulus were 130 GPa and 1.1 TPa, respectively, while the strength limit reached 42 N/m which is 100 times stronger than the strongest steel.[20] The high tensile strength is attributed to the C-C bond strength of sp^2-hybridised carbon. Even though the theoretical density is 0.77 mg/m^2, it is 200 times stronger than structural steel.[2] The strength and elastic modulus for bilayer and trilayer graphene are 126 GPa and 1.04 TPa, and 101 GPa and 0.98 TPa, respectively.[21] This is the reason for incorporating graphene as a reinforcing element in polymer composites, graphene fibres, and graphene reinforced cement composites. The thermal conductivity for monolayer graphene at room temperature is between ~ 4.84×10^3 to 5.3×10^3 W m^{-1} K^{-1}. This property makes graphene suitable for electronic applications and as a material for thermal management in optoelectronics, photonics, and bioengineering.[22] Another important property is its specific surface area of up to 2630 m^2 g^{-1},[23] which is important for microdetectors for gas molecules, by monitoring the change in

resistance because of adsorption and desorption of gas molecules,[24] as it will be discussed in Chapter 6. Graphene applications are widespread due to its outstanding properties, and some of the most interesting ones for this work will be discussed in Section 1.4.

1.2 Graphene synthesis.

With the emergence of many graphene-based materials and their applications, there is a need to synthesise high-quality graphene on a large scale. Currently, various approaches of graphene production have been proposed and they can be divided into two sections: top-down and bottom-up. Top-down methods produce graphene flakes that comes from graphite exfoliation, the graphene flakes can be divided in graphene nanoplatelets (GNP), graphene oxide (GO), and reduced graphene oxide (rGO). On the other hand, chemical vapour deposition (CVD) graphene films are produced from a bottom-up method that involves the high-temperature dehydrogenation of carbon precursor and subsequent formation of large-area continuous graphene films on metal substrates.[25] The most popular methods for each category will be discussed briefly; however, the electrochemical exfoliation of graphite (top-down) and chemical vapour deposition (bottom-up) will be discussed in depth as they are the ones used in this work to produce graphene flakes and CVD graphene films, respectively.

1.2.1 Top-down production of graphene.

This approach involves detachment of the graphene layer from a layered precursor like graphite or highly oriented pyrolytic graphite (HOPG). Micro-mechanical cleavage, liquid phase exfoliation, chemical exfoliation, electrochemical exfoliation, thermal exfoliation, and reduction are in this category. The primary concept of these methods is overcoming the van der Waals forces between the graphene layers to produce few-layer or monolayer flakes.[2,26,27]

1.2.1.1 Micromechanical cleavage.

The method was introduced by Novoselov and Geim in 2004,[8] it is also known as Scotch tape® method because it uses the tape for the exfoliation. As illustrated in Figure 1.7, a small piece of highly oriented pyrolytic graphite (HOPG) is peeled off multiple times until getting single layer graphene. Then, the adhesive tape is pressed against a SiO_2/Si substrate to deposit the flakes on it utilising the favourable van der Waals attraction

between them; and finally, residual glue is removed using a solvent, such as acetone. The image in Figure 1.7 shows an optical image of a graphene flake with regions with different layers. Raman spectroscopy and optical contrast can be used to determine the number of layers. This method is useful for preparing high-quality and micron-size area graphene flakes, however it is limited to laboratory research because it is not scalable for industrial production.[28–30] Additionally, alternative scalable techniques have been suggested, including liquid-phase exfoliation, ball milling, sonication, and chemical exfoliation, all of which utilize graphite as the initial material.

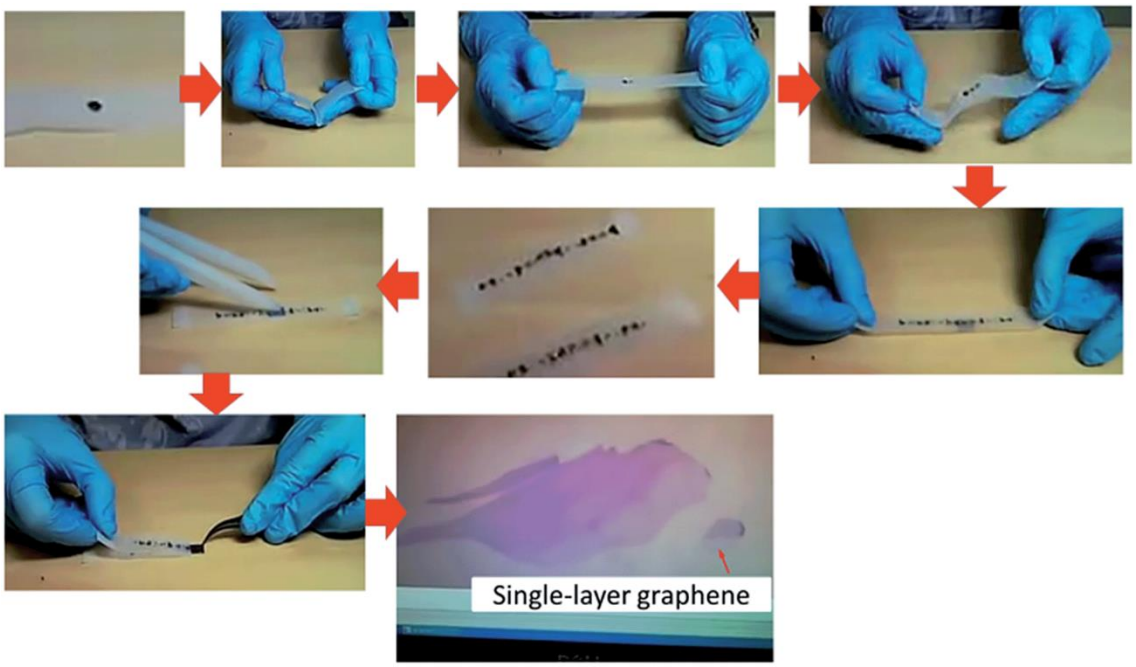

Figure 1.7 Mechanical cleavage of HOPG method where a piece of bulk graphite is placed on the Scotch tape®, then it is peeled off multiple times and finally pressed against the substrate. In the last figure an optical image of a single layer of graphene can be observed. Adapted from reference 28.

1.2.1.2 Ball milling.

It is a common method in the powder production industry known for its high production capacity and high shear force, which is very well suited for the exfoliation of graphite to produce graphene flakes.[31] Graphite is placed in a rotating vessel along with the balls. The exfoliation mechanism is illustrated in Figure 1.8. The balls collide with the graphite flakes when the vessel is rotating, which results in graphite exfoliation and fragmentation.[27] The shear force is highly desired for achieving large-sized flakes, and

vertical impacts should be minimised to avoid fragmentation of large flakes and damage to the crystalline structure.[28]

Ball milling can be done in a dry or wet environment. Wet ball milling requires a surfactant with similar surface energy to that of adjacent graphene flakes, such as N,N-Dimethylformamide (DMF) or N-methyl-2-pyrrilidone (NMP). In dry ball milling, a mixture of chemically inert water-soluble inorganic salts such as sodium sulphate (Na_2SO_4) and graphite are milled, then washed and sonicated.[28,32] This method has the advantage of producing a high-quality graphene and is scalable, however the high concentration of defects due to the collisions and the use of toxic solvents in the wet method are still a disadvantage.

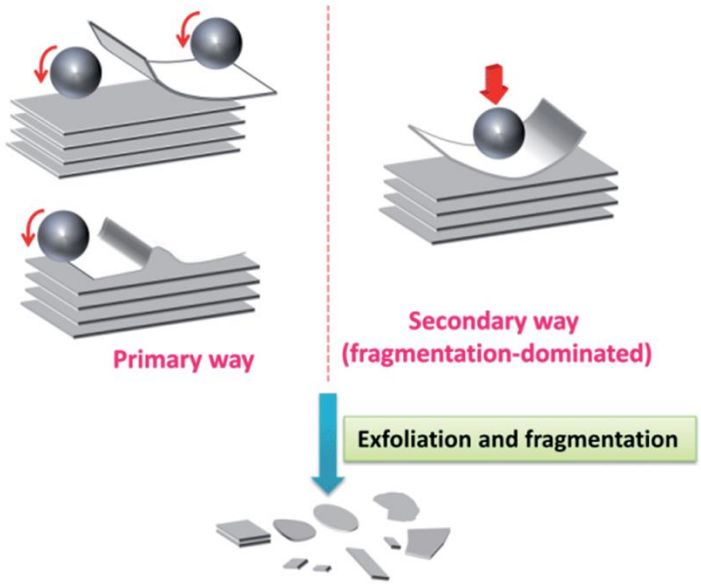

Figure 1.8 Ball milling exfoliation mechanism. Adapted from reference 28.

1.2.1.3 Sonication.

Sonication can be used to extract nanomaterials from the bulk starting material (graphite) and to suppress the aggregation of carbon nanomaterials.[31] In this method, ultrasound energy is used to produce cavitation by agitating the liquid solution to form cavitation bubbles around the graphite flakes. As illustrated in Figure 1.9, the bubbles collapse, micro-jets and shock waves will induce compressive stress waves across all the graphite flakes. Then, a tensile stress wave can be reflected back through the graphite body. As a result, the explosion of several micro-bubbles results in excessive tensile stress in the graphite, resulting in the separation of graphene layers from graphite. In addition, a secondary process is possible where the unbalanced lateral compressive stress can also

separate two adjacent layers by a shear effect. Also, the micro-jets may split the graphite flakes just as a wedge is driven into the interlayer. But, it is the tensile stress that effectively exfoliates graphite into graphene flakes, resulting in a normal force dominated way.[28] The exfoliation of graphite by sonication can be done using a bath sonicator or a tip sonicator; the first being the simplest and cheapest, however the results can be difficult to reproduce, as it depends on the water level, volume of dispersion, vessel shape, power output and position of the sample. Also, the yield is low even for long processing times, which also compromises the quality of the graphene.[31]

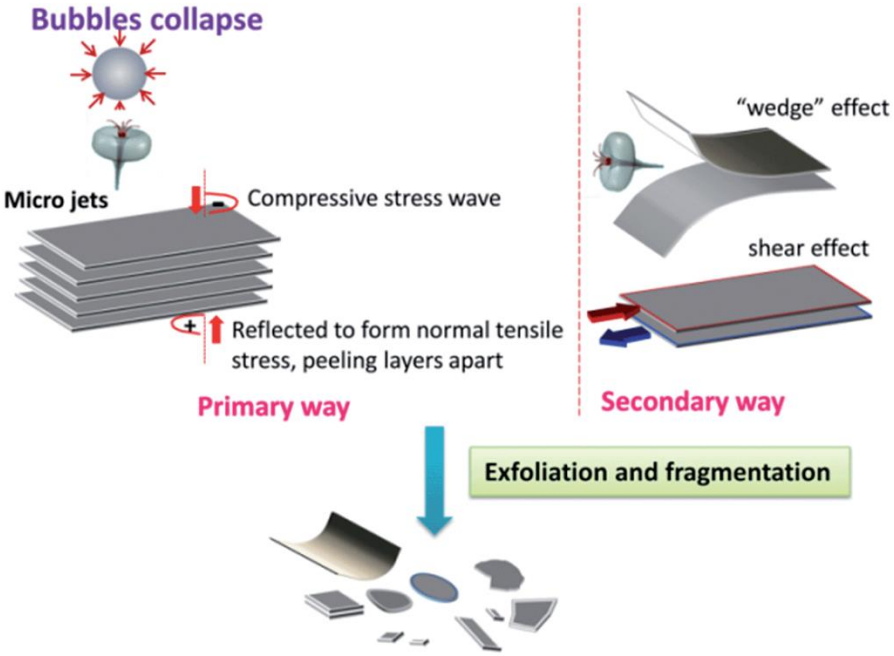

Figure 1.9 Exfoliation mechanism using sonication. Adapted from reference 28.

1.2.1.4 Shear exfoliation in liquid media.

Sonication as a method has the limitation of scalability as it operates in small volumes, however shear exfoliation can increase the yield of relatively defect-free graphene nanosheets (GNSs) using rotor-stator mixers (Figure 1.10a), which are available in a wide range of configurations (Figure 1.10b). The robustness of the method allows for the use of blenders with rotating blades. Figure 1.10c1 shows a sectional drawing of the elements of a high shear mixer that is composed of a rotator and a stator with drain holes. Three energy dissipation regions are shown in Figure 1.10c2, the rotor swept region, jet region, and a hole region, which are responsible for the shear force, jet cavitation, and edge or random collision, respectively (Figure 1.10c3-c6).[33,34]

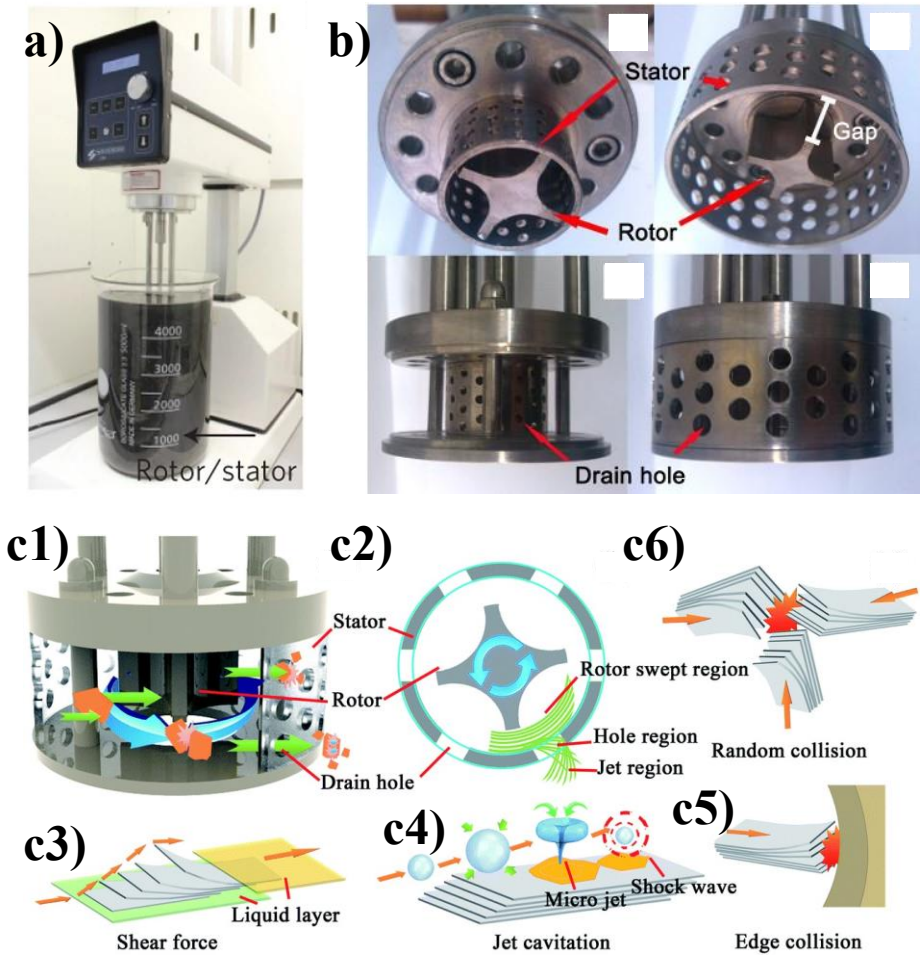

Figure 1.10 a) Commercial high-shear mixer (Silverson model L5M) while in operation. Adapted from reference 33. *b) different stators, c1) sectional draw of a high shear generator which comprises the stator and the rotor, c2) main energy dissipation regions: the rotor swept region, jet region and hole region, corresponding to c3) shear force, c4) jet cavitation, and c5) edge collision or c6) random collision, respectively. Adapted from reference* 34.

In this method, a rotor-stator or rotating blade is used to move the solution with graphite at high speed within the gap between the stator and the rotor to create shear stress which peels off the graphene layers.[27] Also, when high-speed fluid jets out from drain holes of the stator, jet cavitation can be induced by the high pressure difference and the abrupt velocity and geometrical changes, and as in sonication, the tensile stress generated from the shock waves and micro jets can exfoliate the graphite. However, as the drain holes are too large to generate enough high-pressure difference for cavities growth and

bubble implosion, the jet cavitation has a minor role in GNSs production. Because the graphite particles are subjected to tremendous collisions when the dispersion periodically and rapidly impact on the hole edges, collision effects have a significant effect. The frequent and random collisions between graphite particles can also occur by the extremely large inertial force in the turbulence region. Overall, this method can produce a minority of single layer graphene and predominantly produce few-layer graphene flakes with lateral dimensions in the submicron scale.[34] Moreover, the exfoliation efficiency is much higher than in standard sonication or ball milling exfoliation methods, so industrial rotating blade stirred tank reactors could be used for large-scale graphene production.[28]

1.2.1.5 Chemical method – graphene oxide.

This is a two-step process: oxidation and exfoliation. First, graphite is oxidised by the Hummer's method,[35] using oxidising agents such as sulfuric acid, sodium nitrate, and potassium permanganate, to introduce oxygen groups, increasing the interlayer spacing of graphene and reducing the interlayer van der Waals forces, to produce graphite oxide a graphite intercalated compound (GIC). Then the GICs are exfoliated by any of the methods mentioned above to get single or few-layer graphene oxide. However, their electrical conductivity is low, and reduction is necessary to restore the graphene lattice and thus conductivity. The new material is named reduced graphene oxide (rGO). Thermal annealing, hydrothermal reduction and chemical reduction are known process to afford rGO.[27,36] The process steps are illustrated in Figure 1.11, showing some modifications to the Hummer's method that have been proposed, but the main strategy is unchanged, and these methods are commonly known as modified Hummers methods.[37]

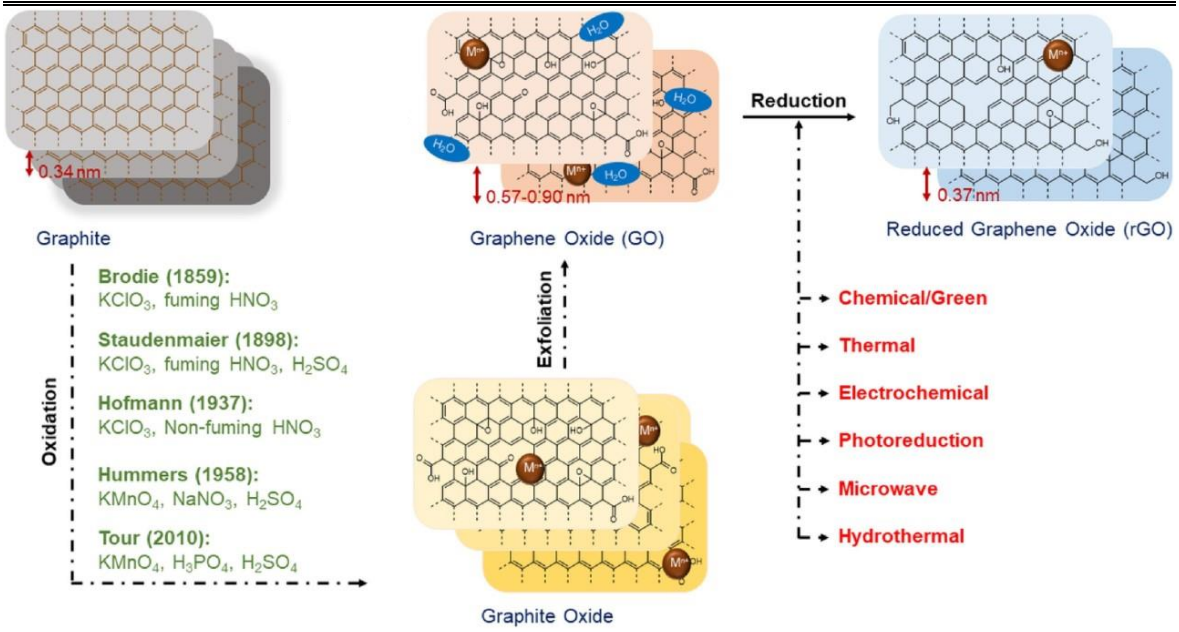

Figure 1.11 Chemical exfoliation involves the transformation from graphite to graphite oxide, to facilitate exfoliation into graphene oxide, and the subsequent reduction to recover the graphitic lattice. Adapted from reference 37.

In our group, a modified Hummers'[38] method has been used to produce GICs using potassium permanganate, and a mixture of sulfuric acid and phosphoric acid, followed by removal of residual metal ions by crossflow filtration, the results showed that at this point most of the flakes were monolayer graphene oxide with lateral size over 10 µm. Tip sonication was used to reduce the lateral size, showing no further reduction in thickness (~ 1.1 nm). Thermal reduction under argon atmosphere was used to synthesized rGO as it was required for applications in polymer composites, showing an improvement in the electrical properties of the composites.[39]

1.2.1.6 Electrochemical exfoliation

Electrochemical exfoliation of graphite to produce graphene sheets is based on the production of GICs by intercalation of ions driven by an electric potential.[40–42] It has become an effective top-down technique, offering many advantages over other strategies such as short synthesis duration, a facile production process, low instrumental cost, high yields for mass production, and the possibility of production and modification of good-quality graphene.[32,42]

The graphene exfoliation involves two consecutive steps: intercalation and expansion. The electrochemical exfoliation process requires the immersion of electrodes in an electrolyte solution (aqueous or non-aqueous) with the application of voltage between the electrodes.[43] The set up has a working electrode (graphene source), a counter electrode, a reference electrode (with three cell configurations), the electrolyte and a power supply. Highly orientated pyrolytic graphite (HOPG), graphite powders, graphite rods, graphite foil, or graphite flakes have been used as working electrodes; and Platinum (wire, mesh, plate), or rods of graphite as counter electrodes. Depending on the voltage applied to the graphite working electrode, the process can be classified as cathodic (negative voltages, attracting positive charged ions) or anodic (positive voltage, attracting negative charged ions) exfoliation, as it is shown in Figure 1.12.[42] One of the drawbacks of the anodic exfoliation is the introduction of significant amount of oxygen functionalities into the produced graphene material. Although cathodic exfoliation can produce high-quality graphene and non-oxidized exfoliated materials, it is less efficient and slower as compared to anodic exfoliation; because most of these approaches requires the formation of oxygen-containing functional groups to weaken the van der Waals forces between the graphene sheets that permit the exfoliation.[44–46]

Electrochemical exfoliation of graphite had been performed using two types of electrolytes: ionic liquids[47,48] and aqueous acids.[49] The first gives a low yield of graphene, small lateral size flakes (<5 μm), and often graphene is functionalised, disrupting the electronic properties of graphene. When graphite is exfoliated in acidic electrolytes, graphene with a better quality and larger lateral size is obtained, but also a significant amount of oxygen-containing functional groups on its surface are present because of the over oxidation of graphite.[49,50]

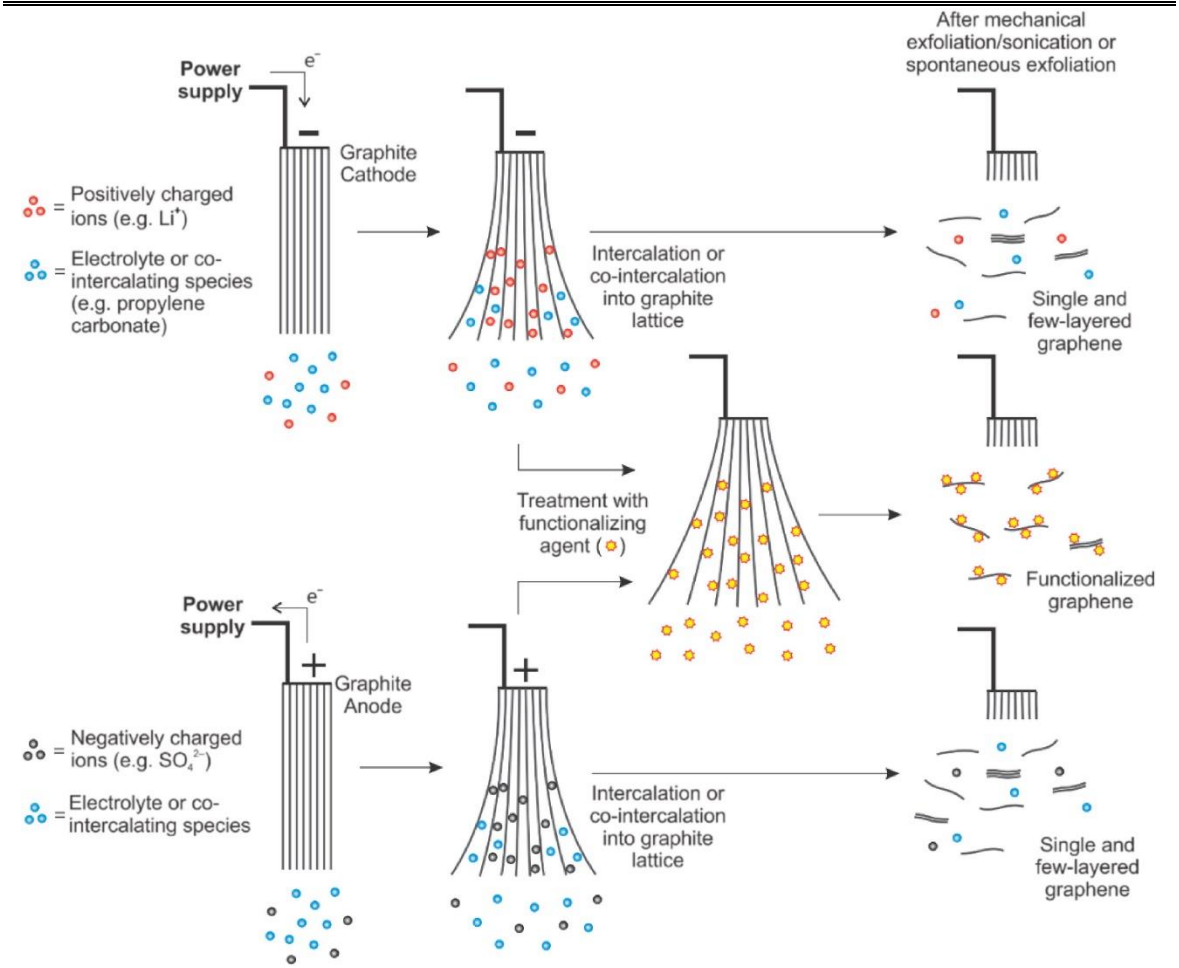

Figure 1.12 Cathodic and anodic electrochemical exfoliation mechanisms. Due to the positive or negative voltage applied at the graphite electrode, oppositely charged ions are attracted and intercalated; also, co-intercalating molecules could be present. Adding functionalising molecules during or after the exfoliation can functionalise graphene. Reproduce from reference 42.

In 2014 Parvez *et al.* proposed graphite exfoliation in inorganic salts to balance high-quality and large-quantity synthesis of exfoliated graphene, as they showed the lowest oxidation level when comparing to that reported for graphene exfoliation in acidic solutions and solution processed rGO. They found that the electrolytes containing sulphate (SO_4^{2-}) anions exhibit better exfoliation efficiency compared to others such as Cl^-, NO_3^- and ClO_4^-. Also, few-layer graphene flakes were rapidly obtained in less than 5 min. The SO_4^{2-} anions are expected to be more favourable, having a low reduction potential of 0.20 V, and generating gaseous species like SO_2, which are responsible for the rapid exfoliation.[51] Since the anodic electrochemical exfoliation process has shown better results

in terms of efficiency and quality for graphene flakes, it was chosen for this work as the synthesis process and only this mechanism will be discussed.

The exfoliation mechanism proposed by Parvez *et al*. as illustrated Figure 1.13a and b. First a nucleophilic attack to sp^2 carbon by OH^- ions (product of water reduction at the cathode due to the voltage applied) occurs at the edge sites and grain boundaries of graphite, introducing C-OH groups, followed by the formation of two vicinal OH groups (b1) which can interact with each other to form epoxide groups (b2). Alternatively, they can dissociate to form two carbonyl groups through additional oxidation (b3). This leads to depolarisation and expansion of the graphite layers and facilitates the SO_4^{2-} intercalation between the graphite layers. Other reactions, including evolution of CO_2 (b4), O_2 (b5) and the reduction of sulphate ions, produce gaseous species that can exert large forces on the graphite layers, which are enough to separate weakly bonded graphite layers from one another.[42,51,52]

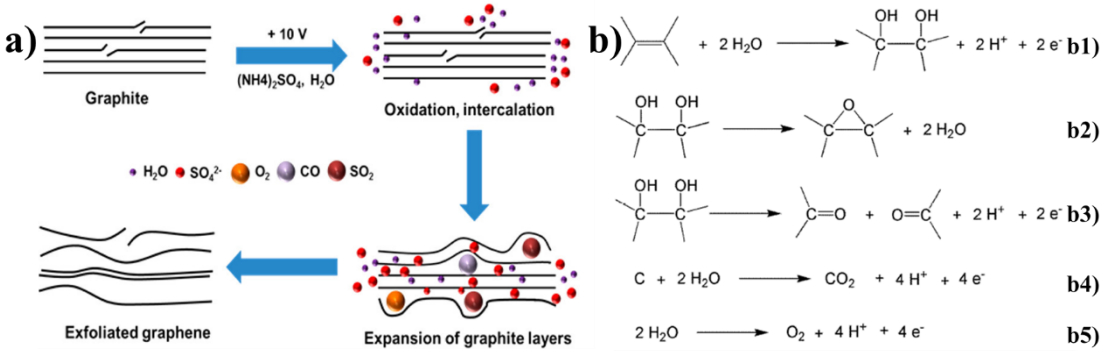

Figure 1.13 a) Mechanism of the anodic electrochemical exfoliation, b) electrochemical oxidation process of the graphite electrode. Adapted from reference 51.

Apart from producing high-quality and a high yield of graphene flakes in few minutes, this method has been adapted to produce functionalised graphene. It follows the same anodic or cathodic exfoliation mechanism, but functionalising agents are added either during or after exfoliation. Functionalisation includes covalent or non-covalent bonding of functional groups to the graphene surface. This approach can lead to better dispersibility of graphene, better exfoliation of graphene from graphite, and provide advantage for certain applications.[42] The introduction of fluorine, nitrogen, phosphorus and sulphur atoms into electrochemically exfoliated graphene has been reported. However, the doping content is low, as it only occurs at the defective sites and edges of graphene during the

electrochemical exfoliation. N-doping of electrochemical exfoliated graphene can be achieved by adding urea, ammonia, azide, and glycine in electrolytes during the exfoliation process, the nitrogen content is summarized in Table 1-1.[53]

Table 1-1 N-doping results in different electrolyte systems.

Functionalizing agent	Electrolyte	Nitrogen content (atomic %)	Reference
Urea	H_2SO_4	0.43	54
Ammonia	NaOH	0.71	55
Sodium azide	Sodium azide	0.60	56
Glycine/ammonia	Glycine/ammonia	6.05	57
Sodium azide	Na_2SO_4	4.00	58

Using the anodic exfoliation in sodium sulphate (Na_2SO_4) electrolyte, Li *et al.* proposed a combination of simultaneous exfoliation and functionalization of graphene with azide groups in a sodium sulphate/sodium azide (Na_2SO_4/NaN_3) electrolyte. They observed that the oxygen/carbon (O/C) ratio was higher in the graphene sample exfoliated in a solution of (Na_2SO_4/NaN_3) rather than that exfoliated in just Na_2SO_4, 20 and 12 respectively. This could be related to the higher voltage required to exfoliate the first one, which points to competitions between the SO_4^{2-} intercalation and N_3^- azidation process.[58]

By utilizing the anodic exfoliation of graphite foil, it becomes possible to produce monolayer and few-layer graphene in a more accessible and scalable manner. Moreover, this method introduces azide groups onto the surface of graphene flakes with a reduced degree of oxidation in comparison with graphene oxide. A single-step procedure is outlined in Chapter 5, enabling the large-scale production of azidated graphene flakes while circumventing the utilization of graphene oxide as a precursor. This strategy effectively reduces the production of hazardous waste and eliminates the need for the reduction step that can convert azide to amino groups, consequently preventing the application of click chemistry. The interest in the use of click chemistry approach on the azidated graphene flakes is because it allows to explore more specific applications, as it can be functionalize with any alkyne termination molecule. The click chemistry approach applied in this work will be discussed in the Section 1.3.2.

1.2.2 Bottom-up synthesis of graphene film.

Here, graphene is produced through the decomposition of carbon-containing precursors (both gaseous and liquid) followed by the formation of a hexagonal structure of graphene layers. Chemical vapour deposition (CVD), thermal pyrolysis, epitaxial growth, laser-assisted synthesis, and organic synthesis can be found in this category. These approaches use high energy to decompose the carbonaceous material and graphitize the carbon produced to form graphene.[27,32,37]

1.2.2.1 Epitaxial growth.

In this method, graphene is grown on a silicon carbide (SiC) crystal by thermal decomposition at temperatures greater than 1000°C under an ultrahigh vacuum. As silicon has a higher vapor pressure than carbon atoms, it vaporises from the substrate during the annealing step while the carbon atoms remain forming graphene layers. The epitaxial graphene growth is high-quality, and no transfer process is required since it grows directly on the substrate, however the difficulty of controlling the number of layers and the high cost of SiC wafers are the drawbacks of this method.[27,32]

Graphene can be grown on Si- terminated (0001) or C-terminated ($000\bar{1}$) faces. As seen from Figure 1.14, the SiC crystal structure is formed by stacking of the SiC bilayer. On the Si-face a buffer layer is present (broken lines) where mono, bi and multilayer layers graphene grow homogeneously. On the other hand, graphene grown on the C-face is multilayer rotationally stacked graphene, has no buffer layer, and is less homogeneous.[59] The epitaxial graphene growth method is a promising process for large-scale production and commercialisation of graphene for applications in electronics.[36]

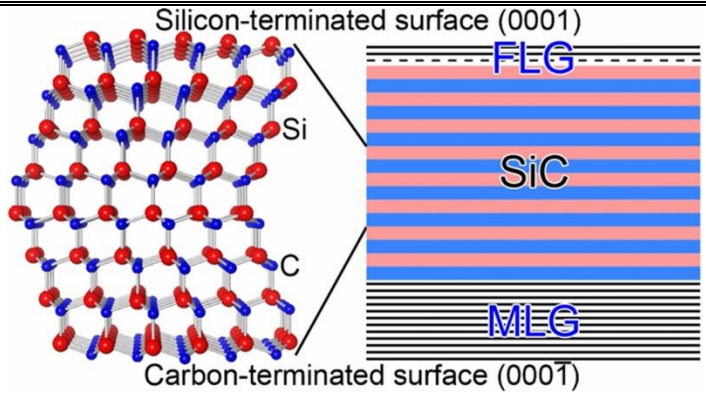

Figure 1.14 Schematic illustration of Si-terminated (0001) and C-terminated (000$\bar{1}$) faces of hexagonal SiC crystal structure, eight stacked SiC bilayers are shown. Red and blue spheres correspond to silicon and carbon atoms, respectively; and the dashed black line represents the buffer layer. FLG for few-layer (2 layers in the image) graphene and MLG for multilayer graphene. Adapted from reference 59.

1.2.2.2 Chemical vapour deposition (CVD).

Chemical vapour deposition is a promising method to grow high-quality, large-area, and uniform graphene films. In this method, a carbon source is thermally decomposed, and the carbon atoms are deposited into a honeycomb structure on top of a metallic catalyst film.[60,61] Many CVD configurations are available and they can be classified based on temperature (low, high, ultra-high), pressure (atmospheric, low, ultrahigh), wall/substrate (cold, hot), nature of precursor (solid, liquid or gas), and process operation (continuous, batch).[62] Cold wall and hot wall CVD are two different methods used for growth graphene onto substrates. In a cold wall CVD set up the specimen is placed directly on a resistively heated stage inside the chamber. On the other hand, in the hot wall CVD configuration the heating elements are placed outside the tube and the irradiated heat enters the quartz tube, heating up the copper foil placed inside.[63]

In 2009, the Ruoff group reported the use of hot wall CVD technique to growth graphene films.[64] An optimisation of the reported process led to the growth of nearly 100 % monolayer graphene coverage.[65] Currently, it is widely used by many laboratories and even for commercial production. Figure 1.15 illustrates the schematic CVD setup, which comprises the following modules: the precursor injection, the reaction site, and the gas ejection. It is operated at high-temperature, low-pressure, in a hot wall chamber (as a

furnace is heating the quartz tube where the reaction occurs), using gas precursor and in a batch operation mode, but also a continuous process has been developed.[66]

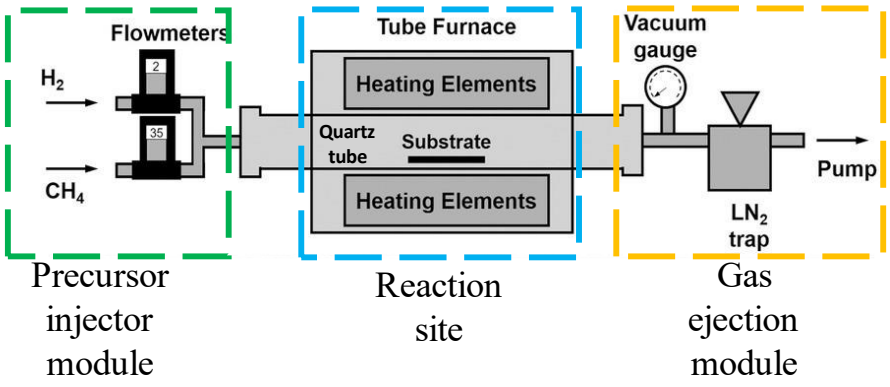

Figure 1.15 A horizontal LPCVD configuration for graphene growth using methane as carbon source. Adapted from reference 67.

As mentioned above, the graphene growth by CVD can be done at atmospheric pressure (APCVD), low-pressure (LPCVD, 0.1 - 1 Torr), and ultrahigh vacuum (UHVCVD, $10^{-4} - 10^{-6}$ Torr).[68] And the growth mechanism not only depends on the partial pressure but also on the transition metal, which acts as a catalyst to lower the energy barrier of the reaction. Table 1-2 summarises the solubility of carbon in various metal substrates and the growth mechanism. In metals having high carbon solubility, the carbon will diffuse/dissolve into the heated substrate and as the substrate cools, the dissolved carbon will segregate to the surface to form graphene sheets. However, in metals with low carbon solubility such as copper, carbon atoms will nucleate and laterally expand around the nucleus to form graphene domains, this process will stop when the metal is fully covered by a graphene layer. It was considered that the process was self-limited, but few-layer graphene can be produced under APCVD, a very slow cooling rate and a high methane concentration.[69] In addition to controlling the growth of adlayers, copper foil can also be reused through the electrochemical transfer method.[70,71]

Table 1-2 Common metals for graphene production by CVD, their carbon solubility, and the growth mechanism. Adapted from reference 69.

Metal	Carbon solubility at 1000 °C (at.%)	Primary growth mechanism
Copper (Cu)	0.04	Surface deposition /penetration
Cobalt (Co)	3.41	Segregation
Platinum (Pt)	1.76	Segregation /surface deposition
Nickel (Ni)	2.03	Segregation /surface deposition
Palladium (Pd)	5.98	Segregation

As many transition metals have been studied for the growth of graphene, so have different precursors. Some of them are summarised in Table 1-3, being methane the most common as it has the lowest dehydrogenation energies 410 kJ mol^{-1} when compared with ethylene and acetylene (443 kJ mol^{-1} and 506 kJ mol^{-1}, respectively).[72]

Table 1-3 Precursors used to grow graphene by CVD classified according to their physical state. Reproduced from reference 61.

Physical state	Precursors
Gas	Methane, acetylene, ethylene, propene, biogas.
Liquid	Ethanol, hexane, benzene, methanol, pyridine, 1-propanol, 2-phenylethanol, palm oil.
Solid	PMMA, hexabenzocoronene, highly oriented pyrolytic graphite, cookie, cockroach leg, grass, camphor.

The graphene steps to growth graphene by LPCVD, are as follows:[73]

1) Copper substrate is loaded in the chamber and evacuated until it reaches the desire pressure.
2) The copper substrate and the hydrogen gas are heated to the pre-process temperature in a controlled atmosphere.
3) High temperature, 1000 °C, is maintained (annealing step) to clean the catalyst surface and to modify its crystalline orientation, roughness (smoothing), and grain size.

4) Introduction of the methane and graphene growth on the copper. The pressure, hydrogen/methane ratio, residence time, temperature, gas flow, among others can be modified.
5) Cooling the reactor under the same growth atmosphere, until the reactor temperature is below 200 °C, to prevent oxidation of copper non covered areas.
6) Backfill with argon gas up to atmospheric pressure and open the reactor chamber.

Here, the growth mechanism for LCPVD on copper foil using methane as a precursor will be discussed, as this is the approach employed in this work. Figure 1.16a shows a steady state gas flow of a mixture of methane, hydrogen, and argon over the copper surface catalyst. Inevitably, a stagnant boundary layer with δ thickness will form; then the carbon species (1) diffuse through the boundary layer and reach the surface, where they (2) get adsorbed on the surface, (3) dehydrogenate totally or partially to form active carbon species, (4) diffuse on the surface of the catalyst or into the catalyst close to the surface, generate nucleation sites and form the graphene islands that grow and merge forming a grain boundary where the mismatch orientation is overcome by the formation of 5, 6, 7, and 8 membered rings (Figure 1.16b), (5) inactive species (such as hydrogen) get desorbed from the surface, form molecular hydrogen, and (6) diffuse away from the surface through the boundary layer and are eventually swept away by the bulk gas flow.[61,68,74,75]

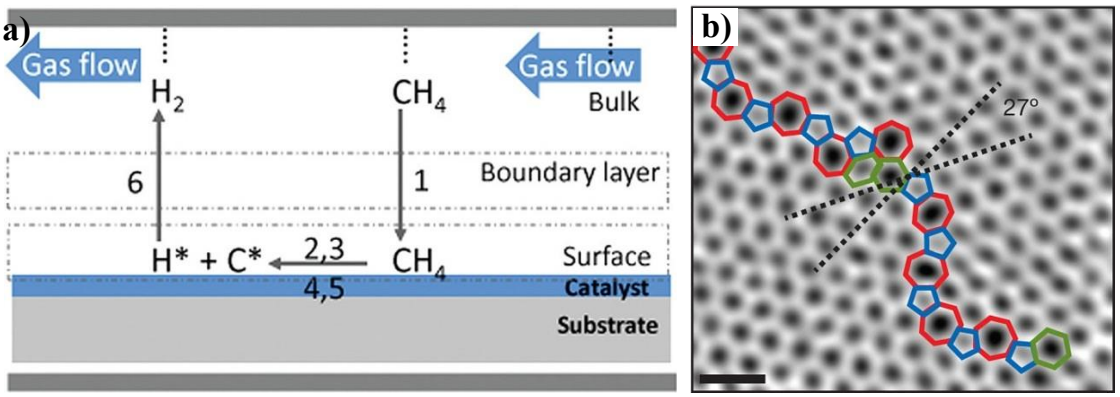

Figure 1.16 a) Steps involved in the graphene synthesis on copper by CVD. Adapted from reference 68. *b) Merging of two graphene grains where the presence of the pentagons (blue), heptagons (red) and distorted hexagons (green) are observed; scale bars, 5 Å. Adapted from reference* 76.

Bhaviripudi *et al.* reported that during APCVD graphene synthesis at higher syntheses temperatures (> 900 °C), diffusion through the boundary layer is usually the rate limiting step and the process is governed by this step. However, at LPCVD the surface reaction regime is rate limiting, and if the temperature is maintained uniform across the length of the copper, the thickness of the graphene is uniform. Few-layer graphene is likely to be synthesised at APCVD conditions and single layer graphene under LPCVD.[68]

Several graphene growth mechanisms have been proposed for each metal catalyst, however there is not a consensus on a single mechanism. It is a complex process and many reaction models have been proposed, including over 900 reactions that involve over 200 species.[77] Figure 1.17 shows a general reaction mechanism proposed by Muñoz *et al.*, the first step to be considered is the competitive dissociative chemisorption of H_2 (facilitated by the empty d-shell of the transition metals that serves as an electron acceptor[78]) and physisorption of CH_4 on surface sites(s) of the metal substrate, according to A1 and B2. Hydrogen recombine and desorb from the surface (B2, A1) this is highly favoured for Ni but in Cu, saturation would be necessary to desorb molecular hydrogen, as it has high solubility in Cu.[73,79]

The next steps are the dehydrogenation of the CH_x (CH_4) species, according to B1. According to density functional theory (DFT), dehydrogenation reactions probably take place up to $x = 2$, with the CH monomer dissociation being the rate-limiting step, and difficult to complete for Cu catalyst. The lower activity of Cu compared to Ni in the catalytic dissociative chemisorption of CH_4 is attributed to the filled 3d orbital ($[Ar]3d^{10}4s^1$), that leaves only one unpaired electron available for the interaction.[73,79]

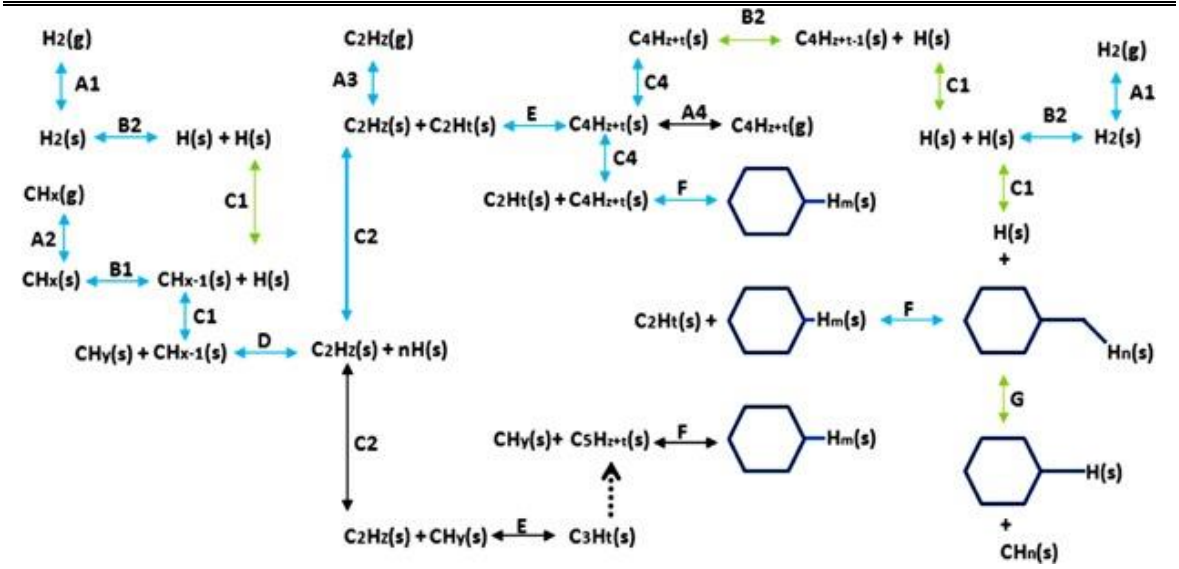

Figure 1.17 Reaction mechanism in CVD graphene growth on transition metal as a catalyst-substrate proposed by Muñoz et al.[73]*. The most likely reaction mechanism showed by blue arrows, where z, t, and m=0; reactions with hydrogen showed by green arrows; and (s) represents a metal surface site. Reaction type: A adsorption-desorption, B dehydrogenation-hydrogenation, C surface diffusion or migration (more favourable for dimers C_2), D dimerisation with or without simultaneous dehydrogenation-cracking decomposition, E polymerisation-cracking decomposition, F aromatisation-decomposition; and G decomposition of aromatics by hydrogen attack.*

On Cu, there is a competitive process between the dissociative chemisorption of H_2 and the physical adsorption and dehydrogenation of CH_4 on metal surface sites(s), according to A1-B2 and A2-B1, respectively. Furthermore, the chemisorbed H(s) (B2, B1) can have an inhibitor role blocking/reducing the number of surface sites available for CH_x dissociative chemisorption and subsequent dehydrogenation. [73,79]

CH monomers on Cu start graphene nucleation, where dimer formation with simultaneous dehydrogenation occur (D), the formed C=C dimers are stable on all sites on a Cu surface, but those containing hydrogen can desorb or decompose on a surface with low adsorption energy. Reaction D with z=0 could be considered as carbon deposition with the formation of C=C bonds with sp^2-hybridisation.[73,79]

Other routes have been suggested by DFT such as carbon dimers, trimers, and tetramers because of carbon atom-by-atom incorporation (E, F in black). Once the nucleated graphene structure is stable at the surface, the growth continues by attachment of carbon species onto graphene edges, the addition of C should occur preferentially (but not

only) as dimers onto the armchair (AC) edges of graphene. After a C_2 dimer diffuses to an AC site and forms a hexagon on the pristine AC edge, the second hexagon then forms at an adjacent AC site by insertion of another C_2 dimer.[73]

Once graphene has grown on Cu foil, it needs to be transferred onto other substrates, most commonly SiO_2/Si. A number of transfer procedures have been reported, and the choice depends on the final application of graphene. Table 1-4 summarised the most common ones.

Table 1-4 Graphene transfer methods their advantage and disadvantages. Reproduced from reference 80.

Transfer method	Advantages	Disadvantages
Wet transfer	Non-destructive, successful up to laboratory scale	High chance of contamination, time consuming, expensive
Electrochemical bubble transfer	Growth substrate repeatability, scalable, minimal use of etching/cleaning chemicals, fast and efficient removal of contaminants, growth substrate self-polishing	Limited to conducting substrates, complicated voltage optimisation
Non-electrochemical bubble transfer	Can be applied to both metallic and non-metallic substrates	Relatively slow
Dry transfer	High-quality, scalable, growth substrate repeatability, short processing time	Appearance of cracks due to interaction with hard surfaces
Roll-to-roll transfer	Application compatible, low cost, short processing time	Limited to flexible substrates, appearance of cracks
Support-free transfer	No organic residue, low cost, short processing time	Growth substrate/etchant residues, high risk of damage

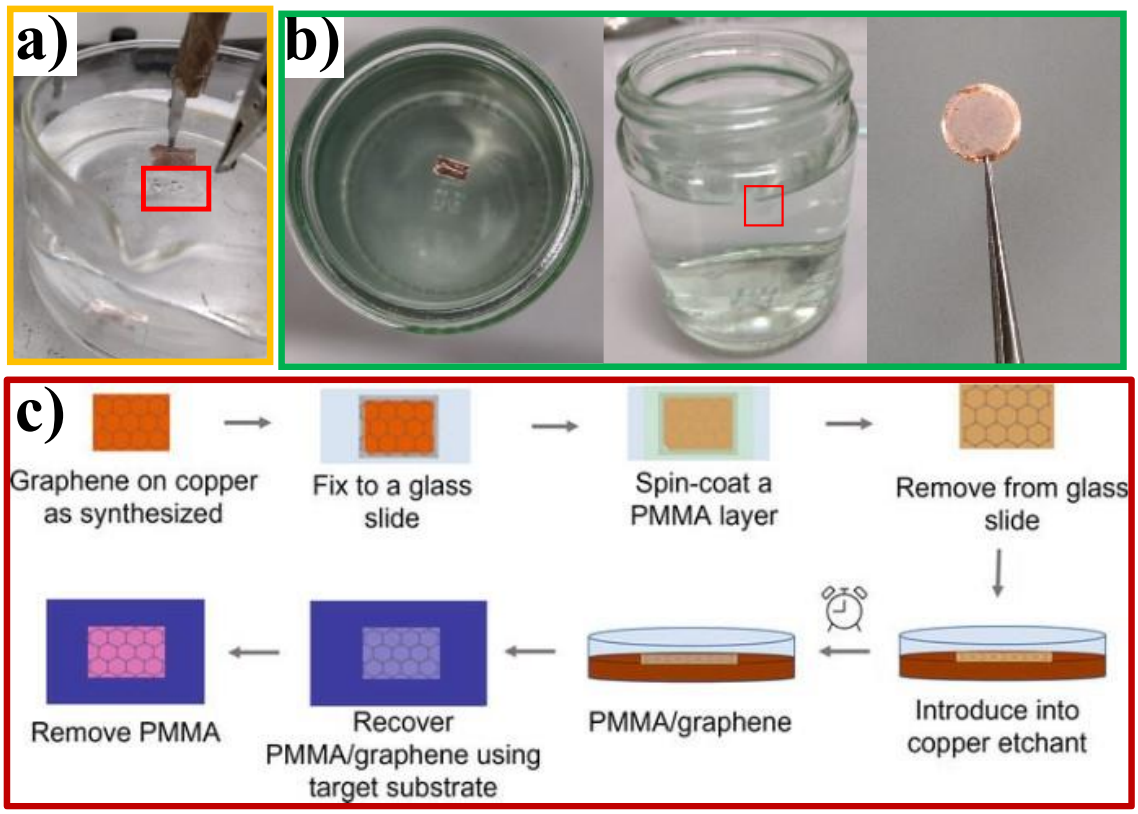

Figure 1.18 a) Electrochemical bubble transfer from this work. Red rectangle is enclosing the PMMA/graphene film. b) Support-free transfer method from this work. Copper is etched in ammonium persulphate solution, red square shows the graphene film at the interface of hexane/ammonium persulfate, and finally graphene on TEM grid. c) Wet transfer method, reproduced from reference 61.

Figure 1.18a shows the electrochemical method graphene (Gr) on Cu is spin coated with polymethyl methacrylate (PMMA) layer, immersed in a 0.5 M sodium chloride (NaCl) solution and a negative voltage applied while platinum (Pt) wire is used as a counter electrode; then the PMMA/Gr film is washed in deionized (DI) water bath three times, placed on a substrate and finally washed in acetone bath.[70,71] This method is suggested if reusing the Cu foil is desired. The polymer/graphene film can be detached from the foil as fast as one minute. With Cu etching in ferric chloride, it can take up to 25 minutes to get the polymer graphene film ready. Continuous process to transfer large area graphene such as the roll-to-roll transfer[11] has been proposed. Dry method[81] can transfer graphene without etching copper foil, however, transfer zero-hole graphene films on substrates is still a challenge. Figure 1.18b shows the polymer-free method which consists

in remove the Gr film from one side of Cu substrate, place the Gr/Cu piece between ammonium persulfate ($(NH_4)_2S_2O_8$) and hexane solution, after the Cu has been dissolved it is fished out on TEM grid and washed on DI water bath.[82] This method avoids the polymer residual on graphene, but if synthesised graphene is not a continuous film, it can disintegrate.

Although many transfer methods exist, the most common involves the use of a protective polymer layer, for example PMMA or polycarbonate (PC).[65] It involves the following basic steps: coating graphene on copper with a polymer layer; removal of the back graphene and copper etch using $FeCl_3$; rinsing the polymer/graphene with deionised (DI) water; removal of the polymer/graphene stack from the solution and transferring it onto the target substrate; drying the polymer/graphene/substrate assembly; removing the polymer with an organic solvent; drying, and annealing of the graphene for further removal of solvents.[67] The whole process is illustrated in Figure 1.18c. In this work, the polymer transfer method, electrochemical delamination, dry transfer method and polymer free method have been used to transfer graphene onto SiO_2/Si, glass, or TEM grid substrates. Also, the transfer conditions have been optimized by using polycarbonate as a supporting layer and tilting the sample around 45° during the dry and acetone bath of graphene on the substrate. The results show a better transfer process in terms of fewer polymer residues and fewer holes along the film.[39] This is very important especially for graphene functionalisation, where clean graphene films on SiO_2/Si are required.

As discussed in this section, CVD has demonstrated to be a good process for synthesising high-quality graphene, especially for electronic applications. A cold wall configuration equipment is very expensive, so a hot-wall set-up seems to be more affordable for many laboratories worldwide. Currently, graphene reproducibility is still an active area of research and variations in terms of quality during the growth process between batches still occurs. For these reasons, in this work a LPCVD set-up (Section 4.1), a standard operation procedure (SOP, Section 4.2) for graphene production; an optimised transfer procedure (Section 4.2.1); and a statistical analysis of Raman spectra to assess the variation of the synthesised graphene along the sample position and batches are reported. This gives an opportunity for more laboratories to produce their own graphene and explore more applications using low-cost methods.

1.3 Graphene functionalisation for specific applications.

Graphene functionalisation expands its applications in different fields, because through the introduction of molecules, graphene can be more selective towards the analytes in the case of sensing field and other properties can also be tailoring by controlling the concentration of the molecules on its surface.[83,84] Since graphene has a zero band gap and inertness to reaction, functionalisation of the basal plane opens the band gap, making it useful in electronic and photonic applications.[85] Graphene functionalisation can be covalent or non-covalent; the former find applications as catalysts, electrocatalysts, electrode materials in energy storage applications and in fuel cells. On the other hand, non-covalent functionalised graphene materials possess high selectivity towards aromatic moieties which will be helpful for immobilisation of biomolecules like nucleic acids, peptides, and antibodies to be used in fabricating aptamer-based biosensor materials.[58,85,86] Both approaches will be discussed in the next section, emphasising on radical addition, as used during the research presented in this work.

1.3.1 Covalent and non-covalent functionalisation of graphene.

1.3.1.1 Covalent functionalisation of graphene.

In covalent functionalisation, re-hybridization from sp^2 to sp^3 bonds of one or more sp^2 carbon atoms of the aromatic structure is induced, causing the loss of electronic conjugation and strain in the plane.[87,88] This approach enhances graphene's properties like opening its band gap, tuning conductivity, increased stability and solubility.[86] Covalent functionalisation can be achieved at the two faces, at the edges and at the defect sites (such as vacancy defects, and grain boundaries).[83,88] It can be classified as free radical addition, atomic radical addition, nucleophilic addition, cycloaddition and electrophilic substitution reactions.[88]

Direct covalent functionalisation of pristine graphene is difficult due to the low reactivity of the graphene basal plane, so it requires highly reactive conditions for its covalent modification.[89] Free radical addition is a major route to graphene basal-plane functionalisation.[58,90] It involves the reaction between moieties with unpaired electrons and the aromatic structure of graphene to form covalent bonds. External energy is required to generate radicals such as plasma, UV, electrochemical, e-beam, gamma radiation, microwave radiation, laser irradiation, or thermal heating.[88,91] In the case of electrochemical methods, the potential applied can shift the Fermi level of graphene,

increasing its reactivity as compared to direct attack of the covalent sp^2 bonds with aggressive chemicals.[89] Electrochemical approaches have been reported as an effective method to functionalize graphene in a controllable way by adjusting the voltage applied, cell configuration, electrolyte concentration, and reaction time.

Aryl radicals are usually produced from aryl diazonium salts through thermal decomposition, but electrochemical decomposition of diazonium salts under mild conditions is also possible.[90] Xia *et al.* reported the electrochemical grafting of 4-docosyloxy-benzenediazonium tetrafluoroborate (DBT) on CVD graphene due to the highly reactive diazonium salt group that allows the covalent attachment of DBT to graphene, disrupting its sp^2 covalent lattice.[89] Electrochemical functionalisation of CVD graphene on SiO_2/Si substrates has been reported is effective method to graft organic molecules such as D-(+)-biotin (Bio), 4-(phenyldiazenyl)-aniline (Dz), and gallic acid (Gall) using cyclic voltammetry. The graphene mobility was not damaged, and their capability for biosensing was demonstrated.[92] Eissa *et al.* demonstrated the functionalisation of CVD monolayer graphene by electrochemical reduction of carboxyphenyl diazonium salt in acidic aqueous media, and can be used as a sensitive and selective platform for protein biosensing.[93]

Following the electrochemistry approach to generate radicals, Li *et al*.[58] developed a strategy to electrochemically generate azidyl radicals at the graphene surface in situ through the oxidation of the simple salt sodium azide (NaN_3) in an aqueous solution (Figure 1.19a). This approach leads to efficient and tunable azidation of the graphene surface, which then allows to expand surface functionality through copper(I)-catalysed alkyne–azide cycloaddition (CuAAC) click chemistry (Figure 1.19b). High electrical conductivity and carrier mobility of graphene after azidation, cycloaddition, and bioconjugation, were maintained, which is ideal for electronics and biosensing applications. Also, in 2021 they reported the successful reaction of CVD graphene with chlorine, bromine, iodine, and a functionalisation with chlorine and azide groups through a two-step approach. First the chlorination and then the azidation, this allows the application of graphene can be extended, as this procedures are done at ambient conditions, with no toxic chemicals or special equipment.[94]

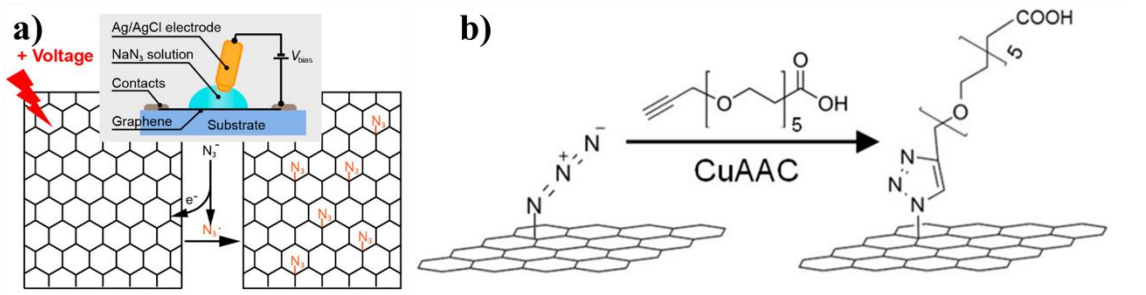

Figure 1.19a) Schematic of the azidation process, the electrochemical oxidation of N_3^- at the graphene surface generates azidyl radicals ($N_3\cdot$), which react in situ with the basal plane. b) Subsequent CuAAC click chemistry of azidated graphene with alkyne-polyethylene glycol (n=5)-acid. Reproduced from reference 58.

Instead of graphene production and subsequent functionalisation, simultaneous electrochemical exfoliation and functionalisation of graphite is possible and has the advantage that monolayer or few-layer graphene can be functionalized and stabilised in situ. Many nanoparticles or heteroatoms have been used to functionalise graphene in a one pot electrochemical exfoliation.[95] For example, Ustavytska *et al.* reported one-step electrochemical preparation of multilayer graphene functionalised with nitrogen via electrochemical exfoliation in sodium azide, results showed a promising pathway for fuel cells and electroanalysis of biomarkers in liquids.[56] Also, Li *et al.* proposed a bulk production of azidated graphene flakes from graphite by combining electrochemical azidation with electrochemical exfoliation, this resulted in graphene flakes with azide groups available for CuAAC click chemistry functionalisation.[58]

1.3.1.2 Non-covalent functionalisation of graphene.

Since the process of covalent functionalization, through electrochemical radical generation, may occasionally result in damage to the CVD graphene film (refer to Section 4.7), so non-covalent functionalization can be a solution. Non-covalent functionalization attaches functional groups to the graphene surface by polymer wrapping, π–π interactions, electron donor–acceptor complexes, hydrogen bonding, or van der Waals forces.[96] Aromatic molecules with planar structures are ideal candidates because they can be easily anchored to the graphene surface through π–π interactions. This method does not alter the conjugated network of graphene, so its intrinsic transport properties are preserved.[87] As graphene oxide (GO) and reduced graphene oxide (rGO) contain defects in the basal plane

through the presence of oxygen containing moieties, such as epoxides, alcohols, ethers, and carboxylates, additional interactions such as hydrogen-bonding and donors and acceptor interactions are possible. But in pristine graphene van der Waals forces or π–π interactions with organic molecules or polymer will occur.[96] Further details on the non-covalent functionalisation on CVD graphene will be discussed in the following paragraphs as it was only used on this kind of material.

Non-covalent functionalisation can be done simply, as demonstrated by Shown and Ganguly, who functionalized CVD graphene with 1,4-benzenedimethanethiol (BDMT) via non-covalent π–π interaction between the aromatic rings, followed by immobilised gold nanoparticles (AuNPs) through thiol functional groups from BDMT. The AuNPs/BDMT/G electrode exhibits highly active electrocatalytic sites for hydrogen peroxide (H_2O_2) detection.[97]

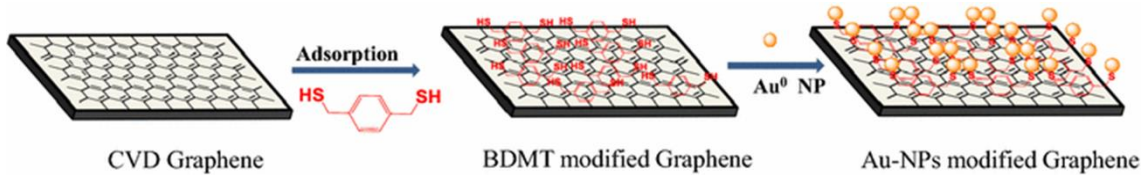

Figure 1.20 Schematic representation of functionalization steps for a CVD-grown graphene by non-covalent process (self-assemble monolayer formation) with Au nanoparticles (AuNPs). Reproduced from reference 97.

Li *et al*. followed a similar procedure, they anchored 5,5′-di(4-biphenylyl)-2,2′-bithiophene (BP2T) molecules through strong π–π interactions of aromatic structures and CVD graphene. The sensor showed 3 times higher sensitivity comparing to that of the pristine graphene.[98] Similar increase in sensitivity towards ammonia was achieved by functionalising CVD graphene with modified cobalt porphyrin. The functionalised sensor response to ammonia increased four times when compared to pristine graphene.[99]

This approach seems to be effective for the development of graphene sensors with special sensing molecules on it, especially those with aromatic rings, as they are preferred for the π–π interactions. This technique is also attractive as no complicated functionalizing procedures are required; and the target molecule could be deposited on graphene just by immersing the graphene/SiO_2/Si electrode in the solution or by drop casting.

The reason for reviewing these two functionalization techniques, namely covalent and non-covalent, is their application in functionalizing graphene flakes and films, respectively. In the case of graphene films, non-covalent functionalization is a viable option; due to the continuity of the film was disrupted after radical azidation although the presence of azide groups was confirmed by XPS analysis. Also, having azide groups attached to the graphene makes copper(I)-catalysed alkyne-azide cycloaddition (CuAAC) click chemistry reaction an option for further functionalisations as it is discussed in the next section.

1.3.2 Copper(I)-catalysed alkyne-azide cycloaddition (CuAAC) click chemistry.

In 2001 Kolb *et al.* introduced the term "click chemistry", more than a set of organic reactions it is a synthetic philosophy inspired by nature in terms of their efficiency, selectivity, and simplicity. A click reaction is simple to perform, versatile in nature, give very high yields, generate only inoffensive by products easily removed by non-chromatographic methods, and stereospecific (but not necessarily enantioselective). Among all the click reactions, copper-catalysed 1,3-dipolar Huisgen cycloaddition (HDC) between a terminal alkyne and an azide is the most valuable.[100,101]

The HDC reaction needs high temperatures, is generally slow and is not regioselective. A copper(I)-catalysed version of the cycloaddition reaction between azides and terminal alkynes has been reported which is 10^7 times faster than the uncatalysed one.[102,103] The copper(I)-Catalysed Azide–Alkyne Cycloaddition (CuAAC) click reaction can be done at room temperature and using in situ generated copper(I), obtained through the reduction of copper sulphate pentahydrated ($CuSO_4 \bullet 5H_2O$) with ascorbic acid in solution. The reaction is selective for the formation of 1,4-substituted [1,2,3]-triazole (Figure 1.21).

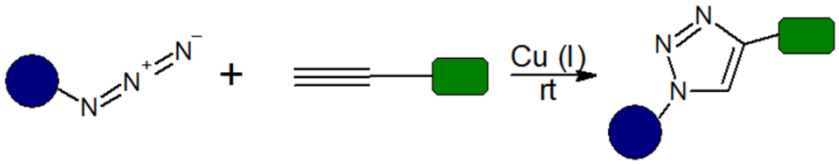

Figure 1.21 Schematic of the CuAAC click reaction with the only regioisomer formed.

The click chemistry synthesis approach is very attractive for surface carbon materials modifications for sensing proposes. Eagler *et al.* reported a procedure for azide functionalisation on the surface of graphene oxide (GO), preserving its functional groups.

This approach opened the door to apply CuAAC click chemistry to generate molecular architectures while the basic structure of GO is preserved.[104] Following this path, Cernat *et al.* reported the further use of CuAAC to attach ethynylferrocene the resulting electrode was used to detect one electroactive molecule.[105] Li *et al.* also reported the successful CuAAC click chemistry approach to functionalise azidated CVD graphene and azidated electrochemical exfoliated graphene just to test the homogeneity of the azide groups on the sample by attaching a fluorescent dye-tagged alkyne.[58] This results in a novel strategy for controlled immobilisation of different (bio)molecules, with application on the development of electrochemical sensors or targeted delivery systems.[106]

Click chemistry can also be done on non-covalent functionalised graphene, as it was reported by Shen *et al.* They used alkyne-functionalized pyrene to adsorb on graphene oxide via π–π interaction, then CuAAC click chemistry was used to attach azide-terminated self-assembled monolayer (SAMs) on gold surfaces. They suggest that such a strategy may facilitate new ways to design graphene-based electrochemical devices.[107] Non-covalent functionalisation and further click chemistry was also done on single-walled carbon nanotubes (SWCNTs) to make selective sensors through cyclohexanone vapours. SWCNTs were wrapped with a copolymer containing 4-vinylpyridine (4VP) groups and azide groups (P(4VP-VBAz)). The P(4VP-VBAz)–SWCNT composite was immobilized on functionalized poly(ethylene terephthalate) (PET); subsequent CuACC click chemistry was performed to incorporate a thiourea selector into the composites, resulting in P(Q4VP-VBTU)–SWCNT, for the detection of cyclohexanone via hydrogen bonding interactions. It showed highly selectivity to cyclohexanone under interfering volatile organic compounds (VOCs).[108]

The click chemistry between azide groups on graphene surface and alkyne terminated molecules seems to be an attractive way to explore graphene gas sensing properties. By integrating the azidation approach for CVD and electrochemical exfoliated graphene proposed by Li *et al.* and the thiourea selector proposed by Yoon *et al.* graphene-based chemiresistor sensors were developed and the performance will be evaluated to see the influence of the defects in the sensing mechanism. The integration of these two separate works, as documented in the literature, yielded the sensors featured in Chapter 6.

1.4 Applications.

Graphene, graphene oxide (GO), reduced graphene oxides (rGO), and its composites have been widely used in a diverse range of applications, including electrochemical energy-storage, electronic, optical, biomedicine, environmental, among others.[32,109] Here some of them will be briefly discussed but more of them can be found elsewhere.[32,45,62,110,111]

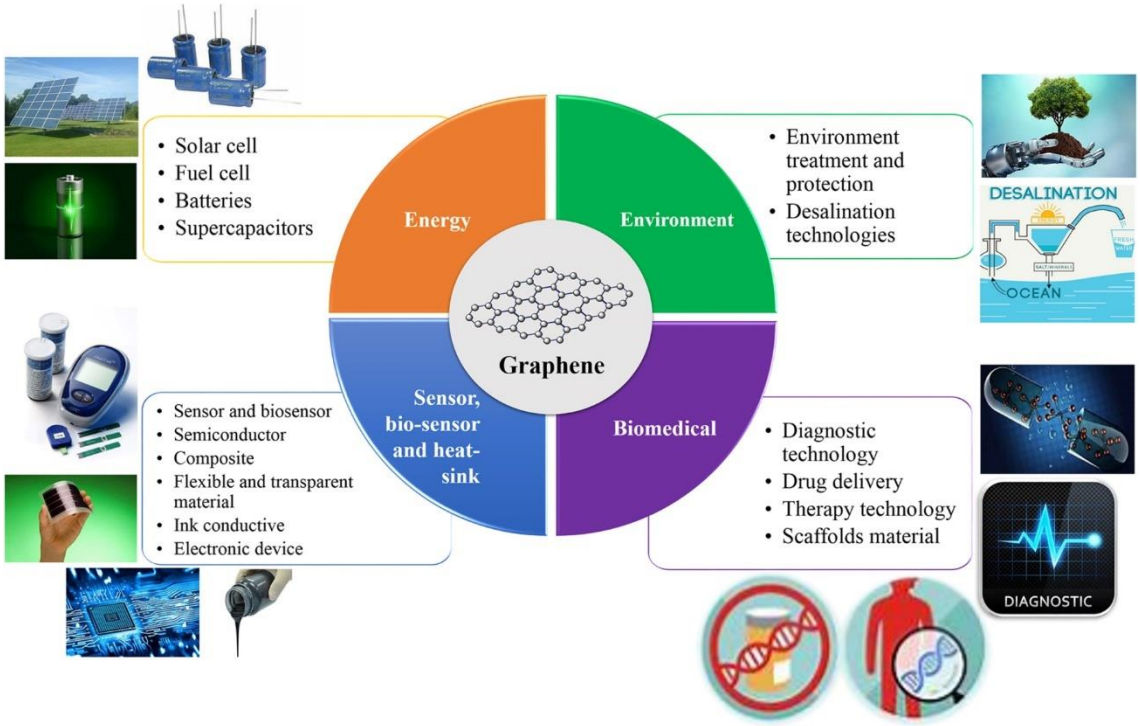

Figure 1.22 Graphene applications in a range of fields. Reproduced from reference 110.

1.4.1 Applications of electrochemical exfoliated graphene flakes and CVD graphene films.

Electrochemically exfoliated graphene (EEG) is used as an electrode material for supercapacitors, batteries or as a conducting film, but also for development of sensors, catalysts, hybrid membranes, anticorrosion coatings, fire hazard suppression materials, or as a component for preparing new composite materials.[43] It can also be included in structural materials for the enhancement of mechanical, electrical and thermal properties. Nano-filtration and adsorption of pollutants are applications in the environmental science. In chemistry research, electrochemical exfoliated graphene and GO are included as carbocatalysts and electrochemical catalysts.[45]

CVD graphene finds application in electronics, energy, biomedicine, and environmental engineering. The applications include energy conversion and storage (for

example solar cells, fuel cells batteries and super-capacitors), biosensors, antimicrobial material, field-effect transistors, sensing, drug delivery, tissue engineering, sorbents, and membranes, among others. Because of its high carrier mobility, CVD graphene has been included in touch panels, logic circuits, bioinspired devices, sensing materials for tactile sensors and semiconducting channels for field-effect transistors. As a graphene surface can be modified chemically and molecularly, it could be used as antibody-functionalised graphene sheets for biodevices.[62] For example, a solution gated CVD graphene-based field effect transistor (FET) was functionalized with glucose oxidase (GOD), it measured hydrogen peroxide and glucose levels continuously in a flexible sensor. So, it could be used as wearable or implantable biosensor.[112] Because monolayer graphene transmits over 97% of light and it is conductive, it has been included in optoelectronic devices like organic light-emitting diodes (OLEDs).[109]

By reviewing the applications of graphene, CVD graphene and EEG has almost the same applications; however, when high quantities are required, as in reinforcement materials, EEG could be preferred. Those applications that require uniform conductive films, CVD graphene would be more relevant. Taking advantage of its large specific surface area of 2630 m^2g^{-1},[23] along with its versatility towards chemical modification, graphene has received attention for gas sensing applications. As the aim is to develop graphene-based chemiresistors the following section highlights key works in the area of gas sensing.

1.4.2 Functionalised graphene-based gas sensors.

Graphene is highly sensitive to changes in its chemical environment because of its high electron mobility, high surface area per volume, and low electrical noise. With these qualities ultrahigh detection of different gases in various environments are possible.[113]

Specific gases can be qualitative or quantitative detected by a gas sensor. Conventional metal oxide-based gas sensors work on the surface adsorbed oxygen ions mechanism; and 2D nanomaterials-type gas sensors on the charge-transfer processes between gas molecules and the surface of sensing materials. As it was discussed previously, the pristine graphene surface is chemically inert, so the adsorption of molecules on it is weak, however due to the functionalisation approaches presented in the Section 1.3 the sensing performance can be improved. There are two main graphene gas sensor devices: chemiresistors and field-effect transistors.[114]

In a graphene-based FET, the conductive channel is formed by placing the graphene layer between two electrodes (source and drain). A gate electrode is covered on one side of the conductive channel through a thin dielectric layer. The conductivity of the channel can be modulated by a voltage applied to the gate electrode. The target gas can be detected by observing the transfer characteristics and the output characteristics of the device.[114] Schedin *et al*. fabricated a graphene-based FET which detected individual events when a gas molecule attaches to or detaches from graphene's surface.[24] Both sensitivity and selectivity of chemiresistors and FET-type graphene-based sensors depend of the synthetic conditions, morphological structures, concentrations of dopants and analytes.[115]

Chemiresistors are characterized by their simple fabrication and operation, high sensitivity, and long-term stability. The sensing layer is placed on an insulating substrate between two interdigitated electrodes. When the gas molecules are adsorbed on the graphene surface its electrical conductivity changes due to the change in the local carrier concentration induced by the surface adsorbates, which act as electron donors or acceptors.[114,116] Gas adsorption can increase the number of holes if it is an acceptor (such as NO_2, H_2O, and I_2) or increase the number of electrons if the gas is a donor (for example CO, ethanol, and NH_3). This change in the carrier concentration is the basic mechanism that governs the operation of all electrical conductivity-based graphene gas sensor devices.[113] CVD graphene based chemiresistors are made by transferring graphene onto SiO_2/Si and contacting them at the end; for EEG-based chemiresistors a solution of EEG is drop casted between to pre-deposited electrodes. Due to the simplicity and affordability of graphene-based chemiresistors configurations, in Chapter 6 we developed selectively cyclohexanone gas sensors by using a selective thiourea-based sensing molecule.

1.5 Aims and objectives.

The aim of the project is to compare the behaviour of graphene, synthesised by two different methods, under cyclohexanone and volatile organic compound vapours exposure when it is used as a sensing material.

As discussed in Chapter 1, graphene produced by chemical vapour deposition (CVD) and electrochemical exfoliation (EE) offer many benefits over other existing production methods. Graphene grown by CVD is a way to produce a high-quality and large area single-layer graphene. However, it has some known difficulties associated to the experimental setup and gas control. On the other hand, EE of graphite is a cheap and relatively easy way to produce few layer graphene flakes that can easily be scaled up. The specific research objectives are:

1. Design a cost-effective set-up and provide a protocol to consistently produce high-quality graphene by chemical vapour deposition and to make it accessible for more research groups around the world.
2. Analyse the variations, between positions in the same batch and from batch-to-batch of the CVD graphene synthesised, based on the statistical analysis of the 2D peak full width at half maximum (FWHM) and the intensity ratio between the 2D peak and G peak (I_{2D}/I_G ratio) using Raman spectroscopy. The monolayer nature will be determined according to the parameters: FWHM of 2D peak ≤ 35 cm^{-1} or $I_{2D}/I_G \geq 2$.
3. Produce azidated graphene flakes by simultaneous electrochemical exfoliation and functionalization as a low cost and scalable method.
4. Functionalization of CVD graphene films and azidated graphene flakes with 1-(3,5-bis(trifluoromethyl)phenyl)-3-(prop-2-yn-1-yl) thiourea (TU) molecule using non-covalent functionalization and CuAAC click chemistry reaction, respectively. The sensing molecule was selected as a similar molecule has shown a selective response to cyclohexanone which is a precursor in explosives* synthesis.[108]
5. Evaluate the response of functionalized and non-functionalized of graphene-based chemiresistors towards cyclohexanone, acetone, ethanol and hexane.

*__Disclaimer:__ *no explosives of any kind have been purchased, bought to Durham University premises for examination or study at any point and part of this study*.

1.6 Structure of the thesis.

Graphene is a promising material for sensing applications, however pristine graphene-based sensors can show low selectivity and to improve it they can be covalently or noncovalently functionalized. Here, bottom-up and top-down approaches will be used to produce graphene.

Chapter 1 presented graphene structure and properties, the advantages and disadvantages of the most common production methods, the covalent and non-covalent functionalization approach focusing on the use of click chemistry as a versatile tool for binding molecules to the surfaces of azidated graphene, and its sensing applications.

In Chapter 2 the main characterisation techniques used in this work will be discussed highlighting its relevance in the graphene field. Raman spectroscopy is discussed more in depth as it is a non-destructive technique to assess the quality of graphene.

Chapter 3 describes the experimental methods in detail, mentioning the possible difficulties other researchers may find if trying to reproduce the results reported in this work.

In Chapter 4 a CVD the design of a customised setup is reported, a standard operation procedure is presented in detail, the synthesised graphene films were characterised, and the variation of the process is reported.

Chapter 5 presents the simultaneous electrochemical exfoliation and functionalization process used to produce azidated graphene (EEG-N_3). Flakes were characterised to examine the quality of the material. Also, the results of the functionalization with the sensing molecule are reported.

In Chapter 6 we presented the results of the performance of the graphene chemiresistors prepared from CVD graphene and azidated flakes. Their performance will be compared in terms of sensor response, sensitivity, selectivity towards cyclohexanone, limit of detection (LOD), response and recovery times.

In the final part of thesis, the overall conclusions and future work are presented (Chapter 7). In the Appendix A the NMR spectrum, mass spectroscopy, and elemental analysis results of the synthesised sensing molecule are depicted. Sampling code used in Chapter 4, as well as the total of Raman Spectrum collected are presented in Appendix B.

2 Characterisation techniques.

Graphene characterisation requires the aid of many microscopic and spectroscopic techniques, that allows us to determine the size, thickness, number of layers, crystal structure, electronic characteristics, among others of graphene. These techniques will be discussed in detail with the focus on how they apply to graphene specifically.

2.1 X-ray diffraction (XRD).

X-ray diffraction (XRD) is a non-destructive method for material characterization. As X-rays wavelengths (between 0.2 and 10 nm) are comparable to the interplanar distances in crystals. This technique is used to study the crystal structure of solids, including lattice constants and geometry, identification of unknown materials, orientation of single crystals, preferred orientation of polycrystals, defects, stresses, crystal size, among others.[2,117] The set up involve a radiation source and a detector for X-rays located at the circumference of the graduated circle, centred on the powder specimen. Divergent slits between the X-ray source and the specimen and between this and the detector, help limiting the scattered radiation, reducing the background noise, and collimating the radiation. The sample holder and detector are coupled to a goniometer, then the rotation of the specimen is in conjunction with that of the detector at a ratio of 2:1 (Figure 2.1a).[118]

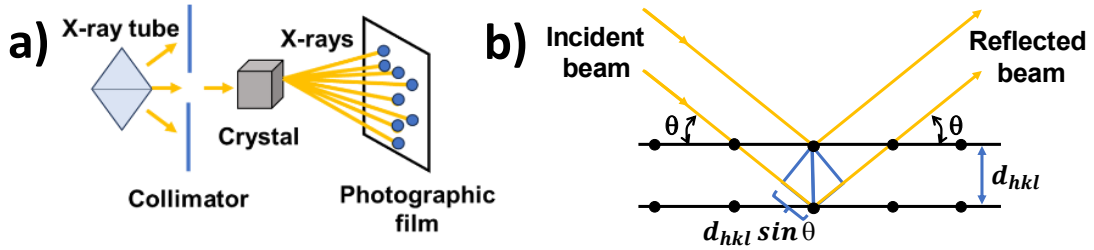

Figure 2.1 a) X-ray diffraction set-up and b) X-ray diffraction; adapted from reference 118.

The material to be characterized is irradiated with X-rays and then the intensity of the X-rays, which are scattered with respect to the scattering angle, is measured.[119] The interatomic space and the crystallite size of the material can be determined by the Brag's law (Eq. 2.1) and the Scherrer equation (Eq. 2.2), respectively.

$$2d_{(hkl)}\ sin\ \theta = n\lambda \qquad \textit{Eq. 2.1}$$

$$L_{hkl} = \frac{K\lambda}{\beta \cos\theta} \qquad \textit{Eq. 2.2}$$

where $d_{(hkl)}$ is the perpendicular distance between pairs of adjacent planes, ***hkl*** are the Miller indexes, θ is the angle of incidence or Bragg angle, ***n*** is the order of the reflection, λ is the wavelength of the X-ray beam, L_{hkl} is the crystallite size, ***K*** is the Scherrer constant (0.91), β is full width at half maximum (FWHM) intensity of the reflection peak.[117]

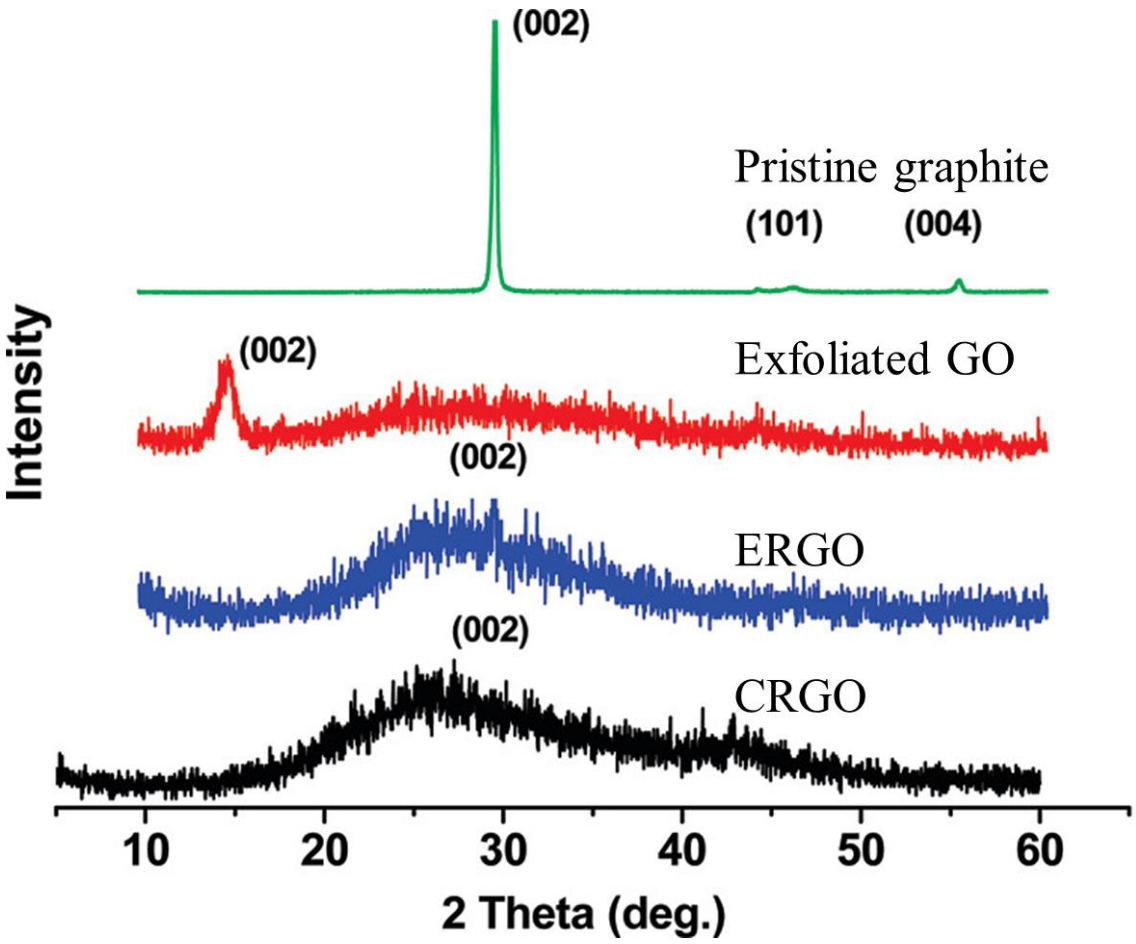

Figure 2.2 XRD spectra of Pristine graphite, exfoliated graphene oxide (GO), electrochemically reduced graphene oxide (ERGO) and chemically reduced graphene oxide (CRGO). Adapted from reference 120.

XRD in graphene materials is used to determine the stacking of graphene and graphene oxide (GO), quantitative estimation of the degree of exfoliation, the intercalation of compounds, etc. The XRD spectra of pristine graphite, using a Cu Kα radiation source (λ=0.154184 nm), show a diffraction peak at the 2θ value of 26.52° (002), corresponding to an interlayer distance of 0.34 nm. But in the XRD spectra of GO this peak is displaced towards lower angles (~10°) because the increase of the interlayer distance due to oxygen functionalities. After GO reduction, the 002 peak is shifted to angles closer to the graphite as the interlayer space is decreased because of the removal of functionalities on the surface of GO, this is used to confirm the formation of reduced graphene oxide (rGO).[119] Figure 2.2 shows the different XRD spectra in which the characteristics peaks described above are observed. The increase in the interlayer spacing in the exfoliated GO (0.849 nm) respect to the pristine graphite is due to the intercalated water molecules between layers.[120]

The Miller indexes are used to describe the planes in the graphite lattice which corresponds to a hexagonal closed packed (HCP) structure. These are convenient for cubic crystals due to their symmetry, however for HCP structures is better to use the four-index Miller–Bravais system, where all the three basal axes are 120° from each other and the fourth axis is orthogonal to all three basal plane axes.

2.2 Scanning electron microscopy (SEM).

SEM is used on graphene materials to collect information about the topography, shape, size, and composition of a sample. Unlike an optical microscope, in SEM an electron beam is directed toward the specimen instead of visible light. Figure 2.3 shows a schematic of a SEM instrument. The primary components of the SEM are the electron column, a specimen chamber, and a computer control system. The electron column holds an electron gun, two or more electron lenses, scan coils, and condenser and objective apertures within its body. The SEM instrumentation typically include secondary electron (SE) and backscattered electron (BSE) detectors, an energy-dispersive x-ray spectrometer (EDS), and an electron backscattered diffraction (EBSD) detector.[121]

The electron column contains the scanning coils through which the electron beam is passed to the final lens. The beam is deflected in vertical and horizontal directions, so scanning can be done over a rectangular area. With the help of electronic devices signals are detected and amplified and the image is displayed as a distribution map of the intensity emitted from the scanned area.[118] When the electron beam hits the sample, backscattered

electrons, secondary electrons, Auger electrons, and X-rays are emitted. Backscattering electrons show contrast based on the composition of multiphase samples, secondary electrons are most valuable for showing morphology/topography, Auger electrons are used for surface analytical techniques, and X-rays are used for the chemical analysis of the sample.[117,122]

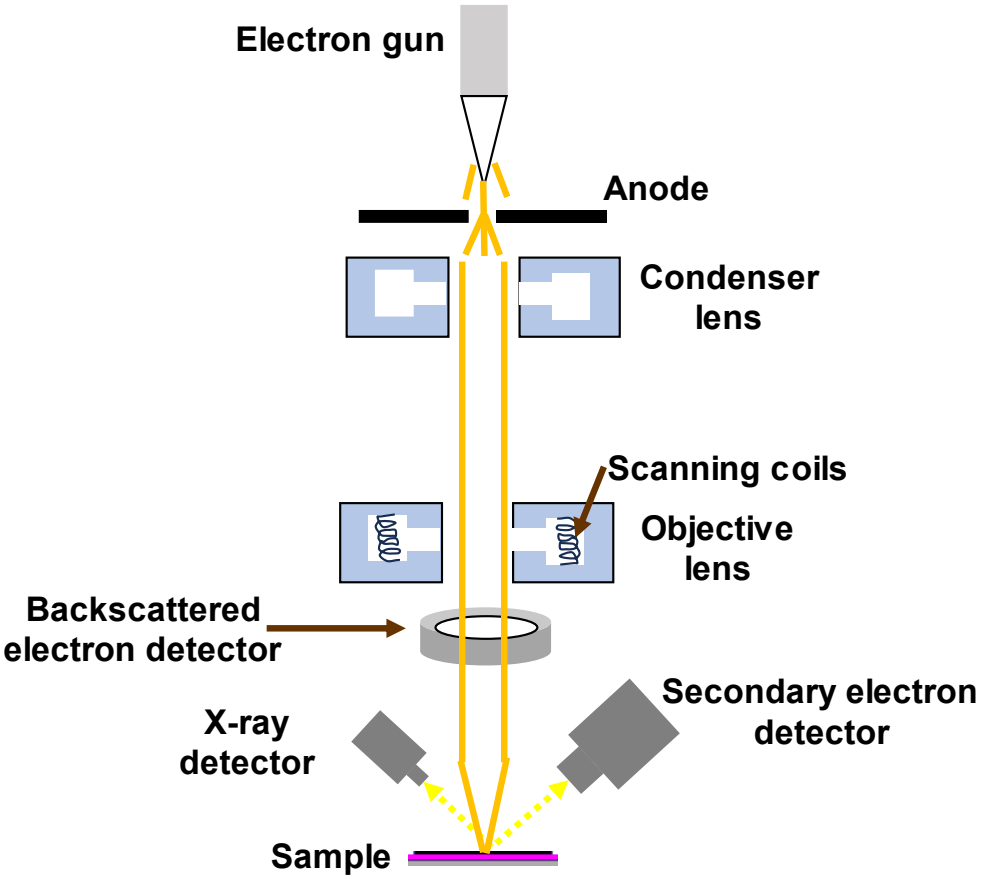

Figure 2.3 SEM elements. Adapted from reference 123.

In this work, SEM will be used to visually examine if expansion of the graphite foil is occurring during the electrochemical exfoliation (Figure 2.4a), Parvez *et al.* suggested that after applying a constant voltage the edge of graphite foil will be expanded and the flakes will be disperse in the electrolyte solution.[51] Figure 2.4a shows the graphite foil expansion of our material after the electrochemical exfoliation and Figure 2.4b shows a large exfoliated graphene flake around 18.7 µm in dimension. Also the contrast difference can help us to relatively compare the thickness of the graphene, so a brighter flake means a more exfoliated graphene and a darker one can suggest the presence of few-layer graphene or graphitic material.[124] Although X-ray diffraction technique is needed to confirm the

intercalation through the increase in the interlayer distance and thickness needs to be confirmed using Atomic Force Microscopy and Transmission Electron Microscopy, SEM offers a simple and easy way for a first approach to assess the exfoliation.

In Chapter 4 SEM will be used to determine the graphene grain size, and investigate other features such as the boundaries and adlayer, which are observed in Figure 2.4c. Once the graphene has been transferred onto SiO_2/Si substrates (Figure 2.4c), polymer residues, copper grain boundaries, adlayers, wrinkles and cracks can also be observed by SEM.[9,125]

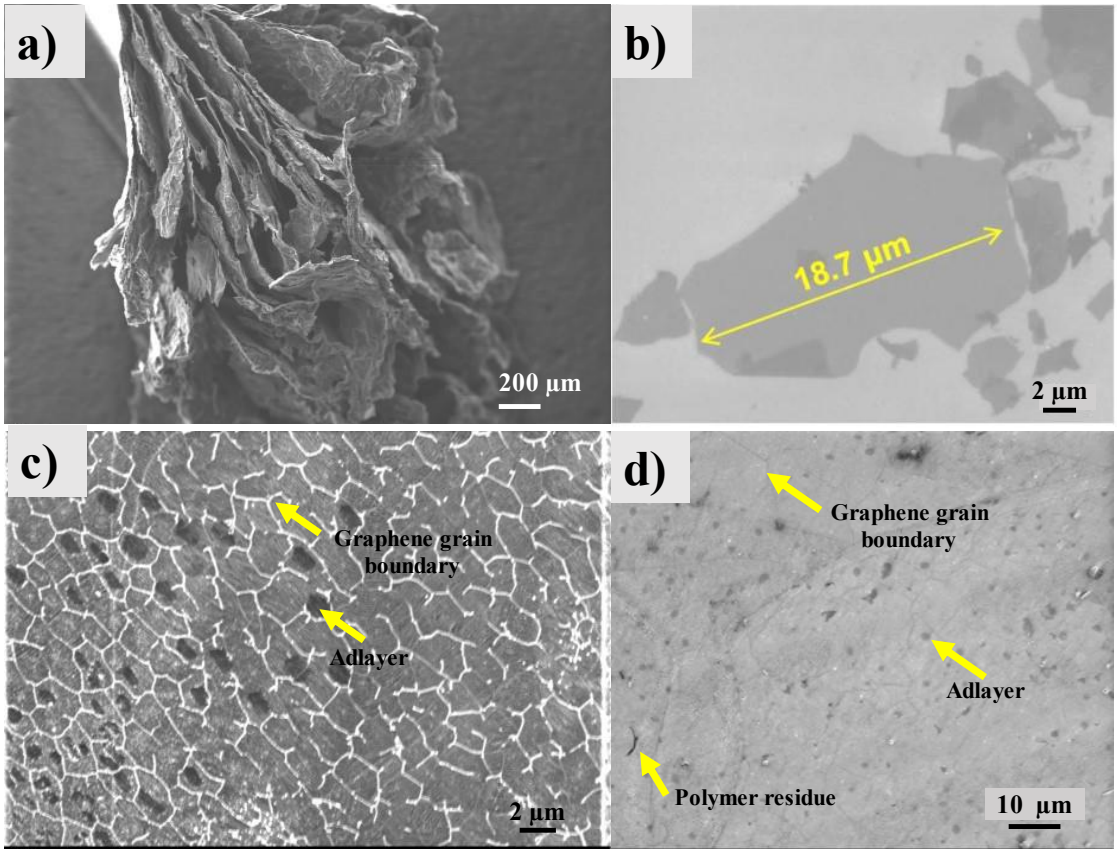

Figure 2.4 Typical SEM images of: graphite foil after electrochemical exfoliaiton where the expansion of the layers can be observed, b) graphene flake produced by electrochemical exfoliation where different indicates different thickness of the flakes,[51] c) graphene grown by LPCVD on copper foil after oxidation on a hot plate to reveal the boundary of the graphene grain; and d) graphene transferred onto SiO_2/Si substrates using a polymer layer.

2.3 Transmission electron microscopy (TEM).

Transmission electron microscopy (TEM) is a powerful tool in graphene characterization. Information, such as, the number of layers, lateral size, crystal structure and grain boundaries, can be determined with this technique. Although the components of a TEM (Figure 2.5) are like those of a standard SEM, the biggest differences are the accelerating voltage, the sample specimen, its position, and the way that the data are collected from the sample. As the electrons have a very small wavelength, the resolution obtained in TEM is very high which is useful in the nanomaterial characterization, allowing us to resolve structures at the atomic level.[117,119,122]

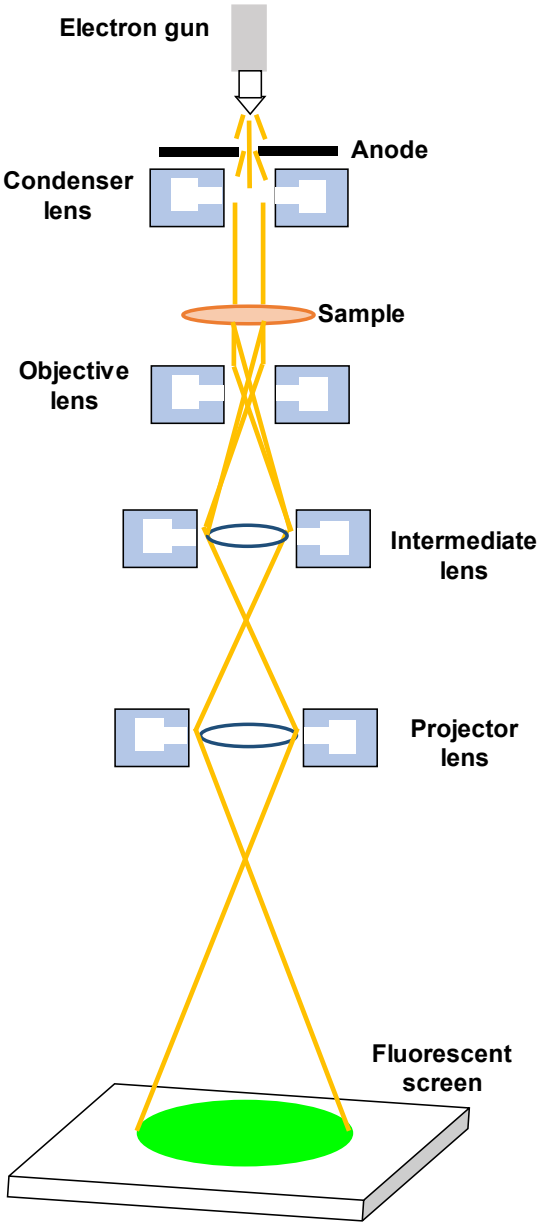

Figure 2.5 Components of a TEM. Adapted from reference 123.

In TEM, an incident high-energy electron beam is transmitted through an ultra-thin specimen (less than 100 nm thickness). As the electron beam enters the thin specimen, electron-electron interactions between the beam and the sample transform the incident electrons into transmitted electrons, elastically scattered and inelastically scattered electrons. The transmitted electrons are focused on a series of electromagnetic lenses and then projected on a screen to generate electron diffraction, amplitude-contrast image, a phase-contrast image, or a shadow image of variable darkness based on the density of transmitted electrons.[2,122] The sample should be less than 1 μm thickness, so when we are working with few layer graphene flakes these are dispersed and drop casted onto a TEM copper grid; in the case of graphene growth by LPCVD this is transferred onto the TEM copper grid using the wet transfer method.[122]

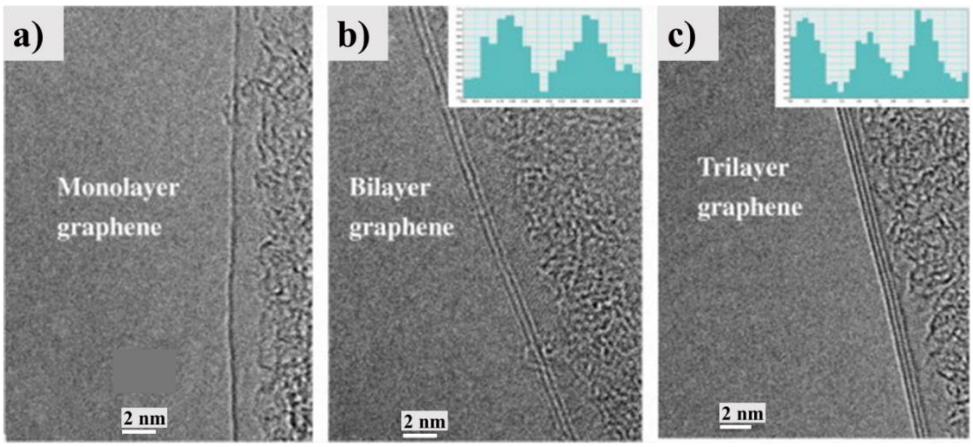

Figure 2.6 HR-TEM image of a) monolayer, b) bilayer and c) trilayer graphene film, the inset in b) and c) are the intensity profiles from which the two and three broad peaks, are indicative of their bilayer and trilayer nature, respectively. Adapted from reference 126.

High-resolution TEM (HR-TEM) is an imaging mode of TEM that allows the direct imaging of the crystallographic structure of a sample at the atomic level. It can be employed to study crystal nanoparticles and their arrangement in the specimen, nanocrystalline features in amorphous films, nanofibers, and their alignment and porous materials.[122] In graphene, this TEM mode is very useful to count the number of layers because the edges of the suspended film always fold back, so a cross-sectional view of the film is observed. The observation of these edges provides an accurate way to measure the number of layers. This has been reported by Kalita *et al.*,[126] where a monolayer, bilayer and trilayer graphene sheets synthetized using a CVD process where distinguished (Figure

2.6). In our work we were able to get atomic resolution as it will be shown in Section 5.5, where the atomic columns of the typical hexagonal pattern of graphene can be observed.

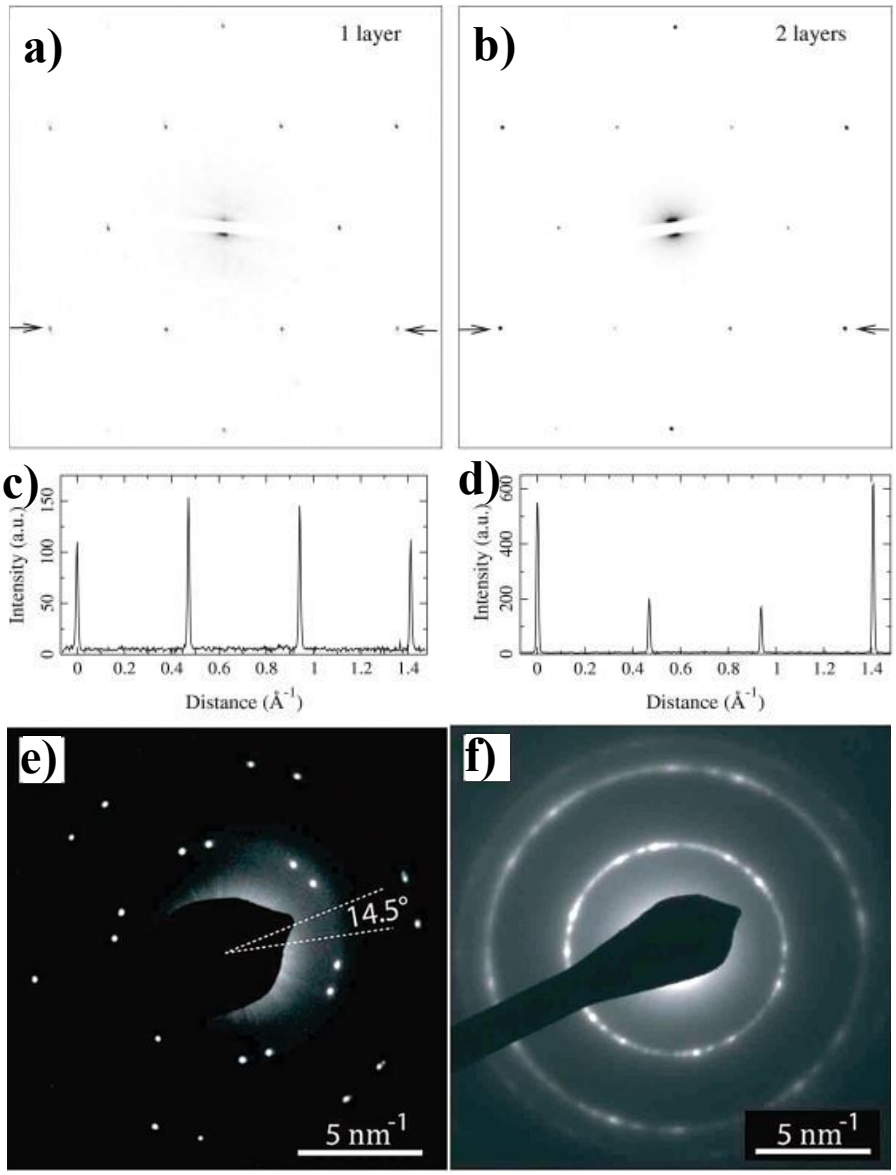

Figure 2.7 Typical selected area electron diffraction (SAED) pattern for a), c) single layer and b), d) bilayer graphene with their respective intensity profiles along the line. Adapted from reference 127. *e) and f) SAED pattern from a double sheet region and from a 15−20 layers thick of graphene oxide (GO), respectively. Adapted from reference* 128.

Selected area electron diffraction TEM mode allows to record the crystal structure in nanomaterials. In this mode, monolayer graphene can be distinguished from bilayer graphene or multilayer graphene by comparing the intensity profiles. Meyer *et al.*, used the

Miller–Bravais indices (*hkil*) for graphite to label the innermost hexagon and the next one as the correspond indices $(0\bar{1}10)$ (2.13 Å spacing) and $(1\bar{2}10)$ (1.23 Å spacing), respectively. In monolayer graphene, Figure 2.7a and c, the inner points are more intense than the outer ones; whereas the opposite means graphene sheets with two or more layers as illustrated in Figure 2.7b and d for the bilayer case.[127,129,130] Figure 2.7e illustrates the SAED pattern of two overlapped and displaced by 14.5° of graphene oxide sheets. SAED pattern of multilayer graphene sheet (15-20 layers) is illustrated in Figure 2.7f.[128]

2.4 Atomic force microscopy (AFM).

Atomic force microscopy (AFM) in graphene characterization is used to study the surface morphology, thickness, layer uniformity and domain growth of graphene. It takes measurements in three dimensions providing a 3D image of the sample. The resolution ranges from 0.1 to 1 nm in the *xy* plane and is 0.01 nm (atomic resolution) in the *z* direction.[122,131]

Figure 2.8 shows the basic components of the AFM instrument. At the end of the cantilever there is a sharp mechanical tip (probe), usually fabricated from silicon or silicon nitride with a radius of curvature on the nanometre scale, which is scanned line by line over the sample. This tip interacts with the force fields associated with the surface producing a deflection of the cantilever according to Hook's law:

$$F = -k\Delta z \qquad \textit{Eq. 2.3}$$

with $\boldsymbol{F}$ being the force, $\boldsymbol{k}$ the spring constat of the cantilever and $\boldsymbol{\Delta z}$ the bending distance of the cantilever. The cantilever deflection is monitored by the photodiode and is influenced by the features on the sample surface. A constant laser position is maintained by controlling the tip height above the surface, reason for which this technique produces an accurate topographic map of the surface features.[122]

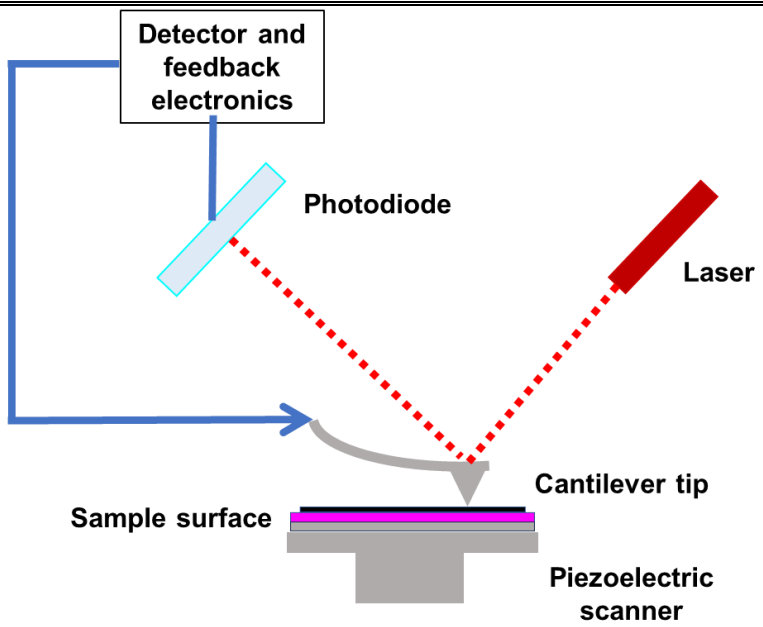

Figure 2.8 AFM components. Adapted from reference 118.

Two scanning modes are possible: non-contact or contact modes. In contact mode the tip is in close contact with the surface sample. The image is produced according to the deflection evaluation. In non-contact mode the images are constructed by tapping the silicon cantilever which oscillates at its resonant frequency. The oscillation reduces as the cantilever starts to occasionally hits the surface and this reduction is used to scan the topography of the sample.[118]

As the contact mode can damage the surface of the graphene sample, non-contact modes are preferred. The number of layers can be determined from the measured height, for monolayer graphene a thickness around 0.34 nm is expected. However, due to impurities adsorbed to the surface, such as water trapped between the graphene and substrate or organic residues, it can be in the range of 0.4 – 1.81 nm.[132,133] Eq. 2.4 can be used to estimate the number of layers as a function of the graphene thickness, where ***N*** is the number of layers; ***P*** is the measured thickness (nm); ***X*** is the measured thickness of monolayer graphene by AFM (nm).[125]

$$N = \frac{P - X}{0.34} + 1 \qquad \textit{Eq. 2.4}$$

Figure 2.9a and b show an AFM image of electrochemically exfoliated few-layer graphene and the height profile across of one flake. In Figure 2.9c graphene oxide (GO) flakes, prepared using the improved Hummers method,[38] are shown. AFM image of a single layer graphene transferred on SiO_2/Si is illustrated in Figure 2.9d, where the boundaries of graphene grains are pointed out by the blue arrows; some particles up to 30 nm height coming from the PMMA, used as a supporting layer during the transfer process. As expected, electrochemically exfoliated graphene and GO, although are chemically different, appear similar in AFM which is more useful for morphology sample determination. Also, other techniques like TEM and Raman should be used to prove the number of layers in graphene samples. In this work, non-contact mode was used to determine the thickness of the flakes and according to Eq. 2.4 the number of layers.

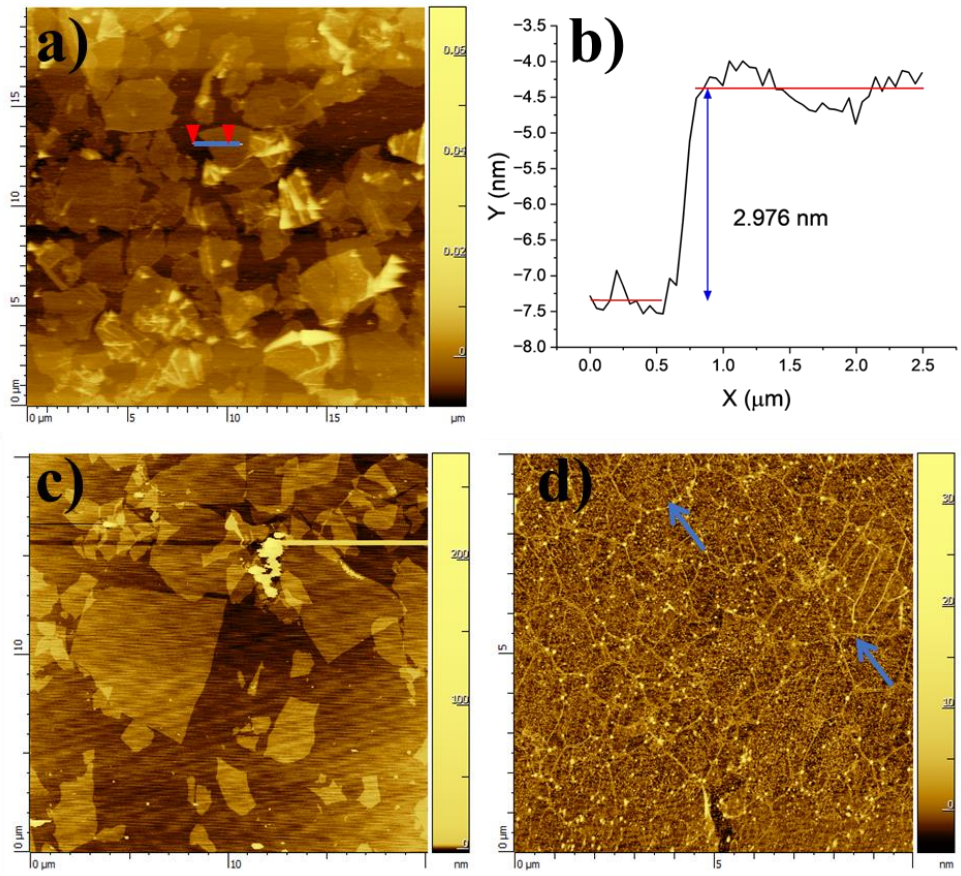

Figure 2.9 Typical AFM height image a) electrochemical exfoliated few layer graphene flakes, b) height profile measured between the red arrows over the blue line in a), c) graphene oxide flakes synthetised using a modified Hummers method,[38] and d) LPCVD-grown graphene film transferred to SiO_2/Si substrates where blue arrows point out graphene grain boundaries.

2.5 Raman spectroscopy.

Raman spectroscopy is a non-destructive technique that can provide information about chemical structure and physical forms. In this technique an incident light strikes a sample, scattering part of this light with the same wavelength as the incident (Rayleigh scattering) or with a different wavelength (Raman scattering, this can be Stokes or anti-Stokes), these are shown in Figure 2.10a. The Stokes scattering process occurs when the molecule is promoted from the ground vibrational state, m, to a higher energy excited vibrational state, n, due to absorption of energy by the molecule. Scattering from an excited state such as n to a ground state m is called anti-Stokes scattering and involves transfer of energy to the scattered photon. The energy difference between the incident light and the Raman scattered light is called Raman shift; and it is equal to the energy required to vibrate or rotate the molecule. Due to the filtering requirements that eliminate photons with the same incident energy and higher, usually Stokes scattering is used in Raman measurements. The Raman spectrum contains peaks, showing the intensity and wavelength position of the Raman scattered light. It is a chemical fingerprint for a molecule or materials, as each peak corresponds to a specific molecular bond vibration and groups of bonds.[134,135]

Figure 2.10b shows the primary components of a Raman spectrometer; a laser (excitation source), an optical microscope (sampling apparatus) and a spectrometer (detector). The excitation laser beam is focused through the microscope to reduce the diameter of the laser spot in the order of micrometres. The instrument is equipped with a video monitor to help focus the spot in a desired area. The Raman signal coming from the sample is collected from a similar area, passes back through the microscope and is isolated from the laser scattered light by the applied optical notch filter. Then, it is passed to the spectrometer where it is dispersed using a diffraction grating and the Raman spectra is collected via a charge coupled device (CCD) to digitize the spectrum. The motorized stage is useful for Raman mapping acquisition; where an image is generated from spectra recorded at defined points of the sample, any fitted parameter can be shown as a function of the position in the sample.[2,136,137]

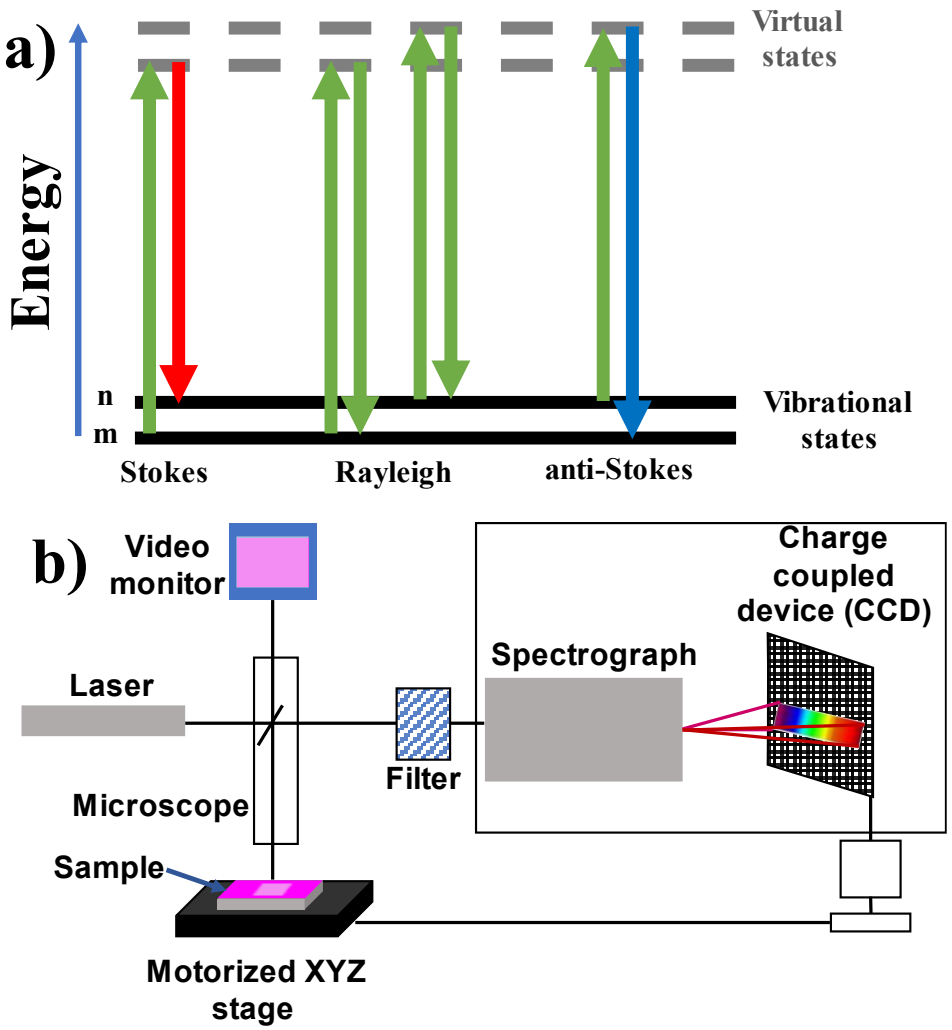

Figure 2.10 a) Diagram of the Rayleigh and Raman (stokes and anti-stokes) scattering, adapted from reference [135]*. b) Schematic diagram of a conventional micro-Raman spectrometer with a charge coupled device (CCD). Adapted from reference* 136.

Monolayer graphene has a hexagonal structure in both real and reciprocal space, Figure 2.11, where a_1 and a_2 are the lattice vectors, Γ marks the Brillouin Zone centre, the high symmetry points at the corner are labelled as K and K' (Dirac points).[138,139]

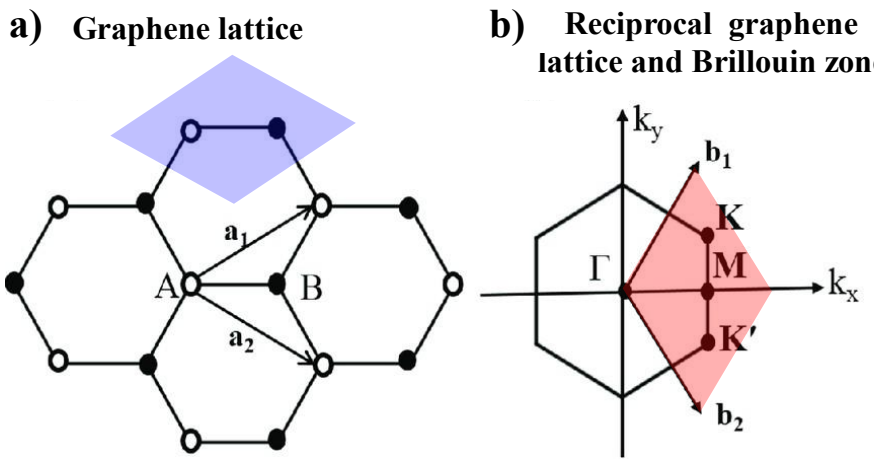

Figure 2.11 a) Honeycomb lattice structure of graphene. The unit cell (blue rhomboid) consists of carbon atoms represented by A and B, a_1 and a_2 are the lattice vectors. b) Corresponding Brillouin zone (black hexagon), showing the high-symmetry points. Adapted from reference 138.

The phonon dispersions of single-layer graphene (SLG) comprise three acoustic (A) and three optical (O) modes. Two of them are longitudinal (L) in the plane (iLA and iLO), two are transversal (T) in the plane (iTA and iTO) and two are transversal out of plane (oTA and oTO).[18] Since monolayer graphene consists of two atoms per unit cell (blue rhomboid in Figure 2.11a), it shows six vibration modes at Γ with irreducible representation: $A_{2u} + B_{2g} + E_{1u} + E_{2g}$ (Figure 2.12).[140,141] There is one degenerate in-plane optical mode (E_{2g}) which is Raman active, and one out-of-plane optical mode (B_{2g}) which is neither Raman nor infrared (IR) active. Figure 2.12 shows the relationship between the vibrational modes of the monolayer graphene and the graphite structure. All the optical modes become Davydov-doublets as the E_{2g} phonon generates an IR active E_{1u} phonon and a Raman active E_{2g} phonon, the B_{2g} phonon goes to an IR active A_{2u} phonon and an inactive B_{2g} phonon.[140,141]

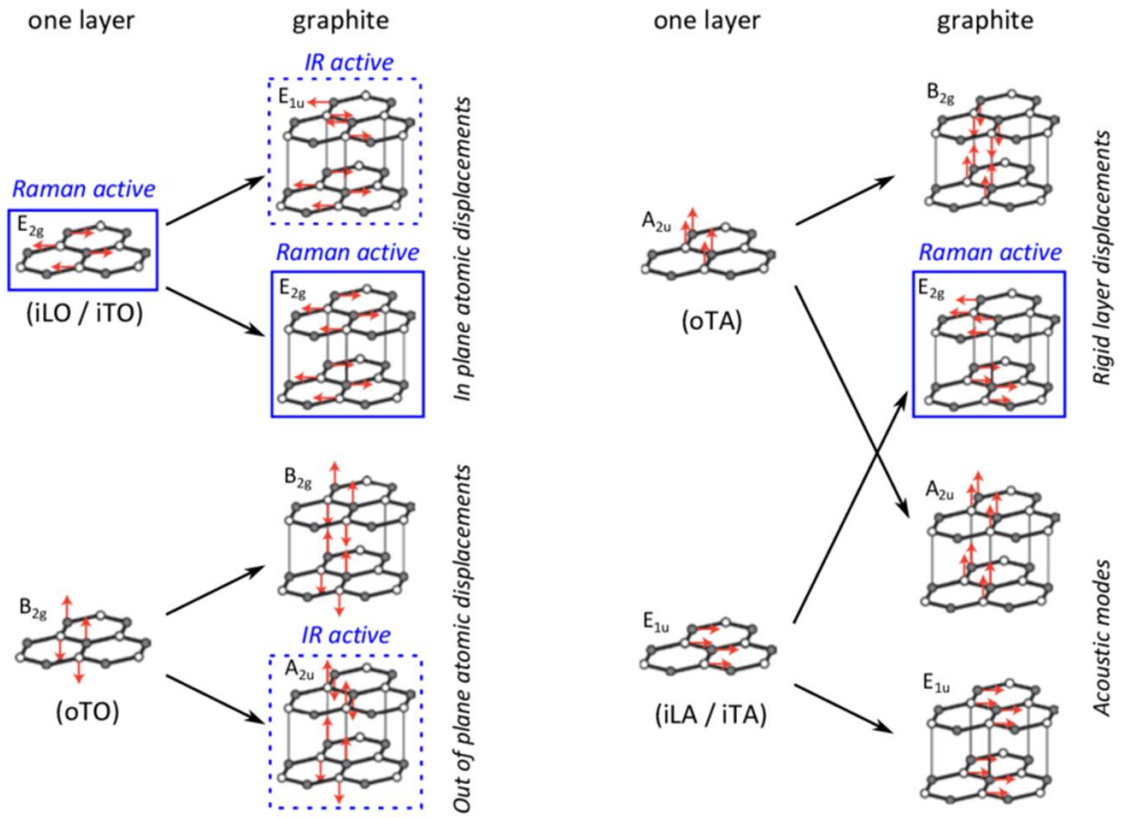

Figure 2.12 Correlation of the zone centre vibrational modes of graphite for a single layer and the 3-dimensional crystal structure. The Raman and IR active modes are marked with straight- and dashed-line blue rectangle, respectively. The red arrows show the atom displacements. The black arrows show how each phonon mode in graphene monolayer gives rise to two phonon modes in graphite. Reproduced from reference 18.

Raman spectroscopy has emerged as a tool to get information about doping, strain, defect density, and number of layers of graphene.[142] This technique can detect sp^2 and sp^3 hybridization of any type of carbon atom allotrope, such as graphite, CNT's, or graphene. Raman spectra can help to distinguish between graphite and graphene materials, even the number of layers in a graphene sample. Also, it gives quick feedback about the carbon material type. Typically, graphite and graphene can show the following peaks: D (1350 cm^{-1}), G (1580 cm^{-1}), D' (1620 cm^{-1}), 2D (2690 cm^{-1}), D+D' (2947cm^{-1}), and 2D' (~3200 cm^{-1}) being D, G and 2D the most important ones, see Figure 2.13a.[143] For these bands the scattering process are showed in Figure 2.13b-d.[144]

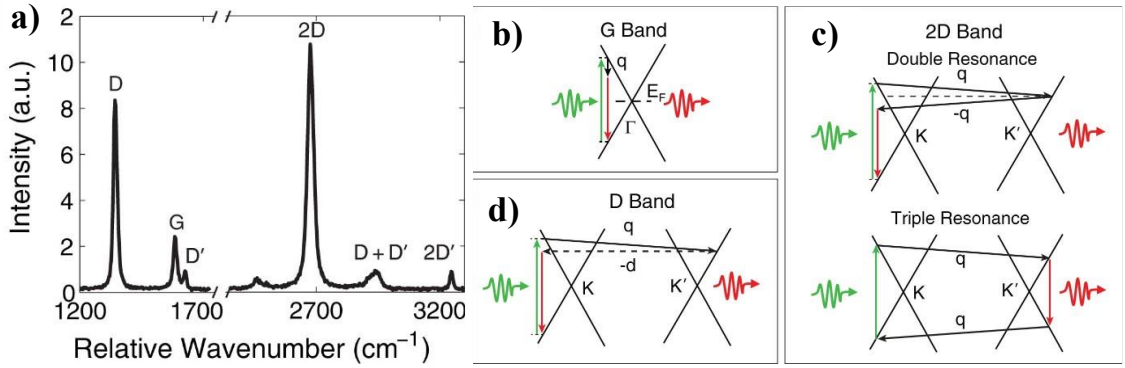

Figure 2.13 Raman Spectra of a damaged flake, which shows the D and D' bands, as well as their combination D+D'. Raman processes in graphene for b) G band, c) 2D band generated through a second-order process that is either double resonant (top) or triple resonant (bottom), and d) D band double resonant process involving a scattering from a defect (horizontal dotted line). Photon absorption (green arrows) and emission (red arrows), q phonon momentum. Adapted from reference 144.

The G band is related to the bond stretching of all pairs of sp^2 atoms in carbon systems and corresponds to the high-frequency E_{2g} phonon at Γ. It is sensitive to doping, and both the frequency and the line width of this peak can be used to get information about it. Both electron donors and electron acceptors broaden the G band increasing its full width at half maximum (FWHM). With the increase of the number of layers, the G peak position shifts to lower frequencies and there is no significant change in its spectral shape.[143]

The D peak is due to the breathing modes of six-atom rings and requires a defect for its activation. It comes from iTO phonons around the Brillouin zone corner K, it is active by double resonance and is strongly dispersive with excitation energy, due to a Kohn anomaly at K. D band appears when the symmetry is broken by the edges or in samples with high density of defects. Defects can occur as chemical adsorbates, edges or structural defects, such as vacancies. Perfect zig-zag edges in graphene cannot produce a D peak. Therefore, the intensity ratio I_D/I_G is used to characterizing the defect concentration in graphitic materials. This ratio increases after the introduction of a dopant into the graphene structure, as it can be observed in Figure 2.15a.[139,143,145,146] Double resonance can also happen as an intravalley process (connecting two points belonging to the same cone around K or K'), giving rise another defect-activated peak, the D' peak. In defective graphene also the combination mode D + D' appears.[139,140]

The 2D and 2D' peaks are the second order modes of the D and D' peak, where the momentum conservation is fulfilled by scattering of two phonons with opposite wave vectors, they do not require defects for their activation and are always present in the Raman spectrum of graphene.[139] The intensities, frequencies, and FWHM of 2D peak in graphene-based materials are influenced by the number of layers, stress, external/intentional or unintentional doping, and laser excitation energy.[143] A single sharp peak is observed for single layer graphene, whereas for graphite two peaks appears in this band. A blue shifted and broader 2D peak is observed as the number of layers increase (Figure 2.14).[147] The I_{2D}/I_G ratio is used to calculate the layers, but also this ratio is sensitive to the kind of doping.[143] It has been reported that N-doped graphene shifted the 2D peak to lower frequencies even when the ratio is higher than 2 for both pristine graphene and N-doped graphene, assuming high crystallinity and quality of both samples.[148]

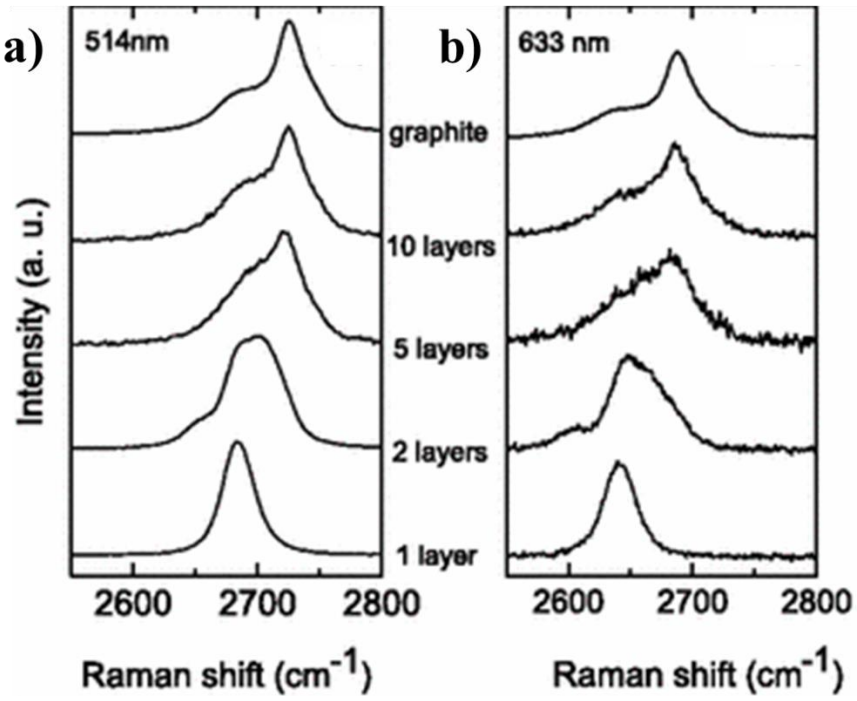

Figure 2.14 a) and b) Evolution of the 2D peak when increasing the number of graphene layers measured at 514 nm and 633 nm, respectively. Reproduced from reference 147.

The comparison is shown in Figure 2.15a, where the blue line shows the Raman spectrum for monolayer graphene synthesised by chemical vapour deposition (CVD) and transferred onto SiO_2/Si substrates. The I_{2D}/I_G ratio around 3 is considered as an indicative

of monolayer graphene nature. After treatment with nitrogen plasma the D peak intensity increase, a slight upshifts for G and 2D bands is observed, and two weak peaks (D' and D+D') appear. The increasing D peak and the reduction in the G and 2D peaks suggested that nitrogen dopped the surface and introduce disorder.[149] Hence, Raman spectroscopy is useful to support XPS analysis about functionalization.

For electrochemical exfoliated graphene sheets this technique is useful for the evaluation and comparison of the quality of graphene dispersions in terms of the amount of defects and sample uniformity; as it can be observed in Figure 2.15b the resulting 2D peak is broader and lower than the G peak, so even when monolayer graphene was observed the Raman spectrum is very different when compared to that of CVD graphene.[49] Hence the FWHM of 2D peak and the I_{2D}/I_G ration cannot be used to quantify the number of layers, and thickness quantification using AFM and TEM is recommended.[150]

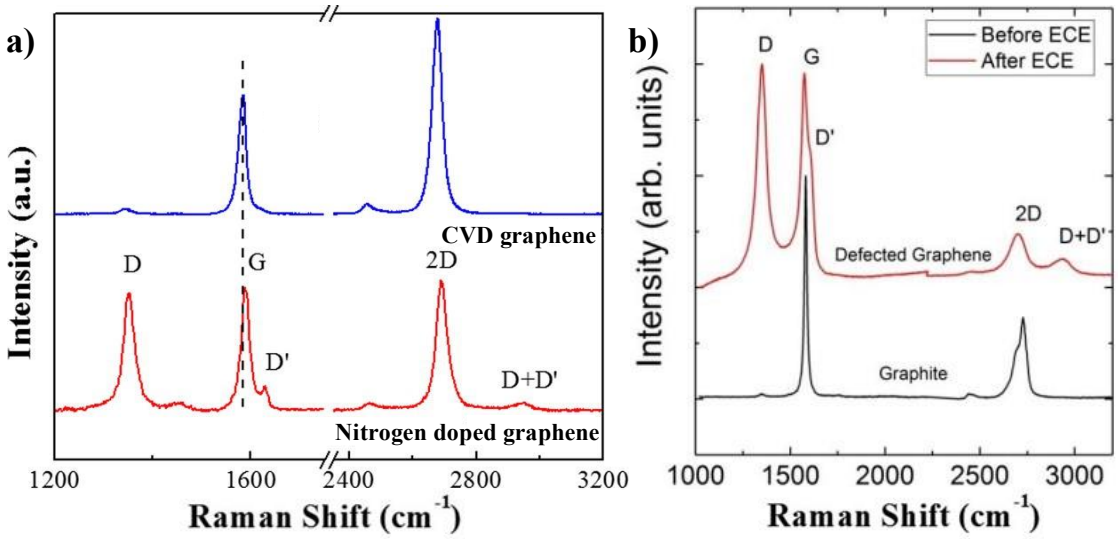

Figure 2.15 a) Raman Spectra from a) CVD graphene on SiO_2/Si (blue curve) and nitrogen doped CVD graphene by micro-plasma jet at atmospheric pressure (red curve). Raman spectra were recorded with 532.0 nm laser wavelength. Adapted from reference 149. *b) Raman spectra, recorded with 514.5 nm laser wavelength of the graphite foil (black curve) and the electrochemically exfoliated graphene (red curve). Adapted from reference* 150.

In this work, Raman spectroscopy will be used to evaluate the homogeneity of graphene synthesised by LPCVD from batch to batch and along the position in each batch and to know the number of layers, however TEM and AFM measurements will be taken to support the monolayer nature. For electrochemical exfoliated graphene Raman spectra

before and after exfoliation will be recorded to see the effect of exfoliation process on the disorder band; to corroborate the number of layers TEM and AFM measurements will be used and XPS is used to get information of the chemical composition of functionalized flakes.

2.6 Thermogravimetric analysis (TGA).

Thermogravimetric analysis (TGA) is a technique for the quantitative analysis of the thermal stability of materials. Also, it is used to understand phenomena like absorption, adsorption, desorption, vaporization, sublimation, decomposition, oxidation, and reduction; and for the evaluation of volatile or gaseous products lost during chemical reactions. Figure 2.16a shows a schematic representation of a TGA instrument, which consist of a highly sensitive scale to measure the weight changes and a programmable furnace. The balance is thermally isolated and located above the furnace from which a high precision hang-down wire is suspended holding a sample pan.[134,151]

As the main principle of the TGA is the change in the mass sample under controlled temperature conditions; this change can be traced as a function of time (isothermal mode) or temperature (scanning mode). Figure 2.16b shows a typical thermogravimetric (TG) curve where a single stage of weight loss or decomposition is occurred. T_i is the temperature at which the decomposition is initiated, and T_f the temperature at which the decomposition reaction is completed. These values depend on the thermal stability of the sample being analysed.[151]

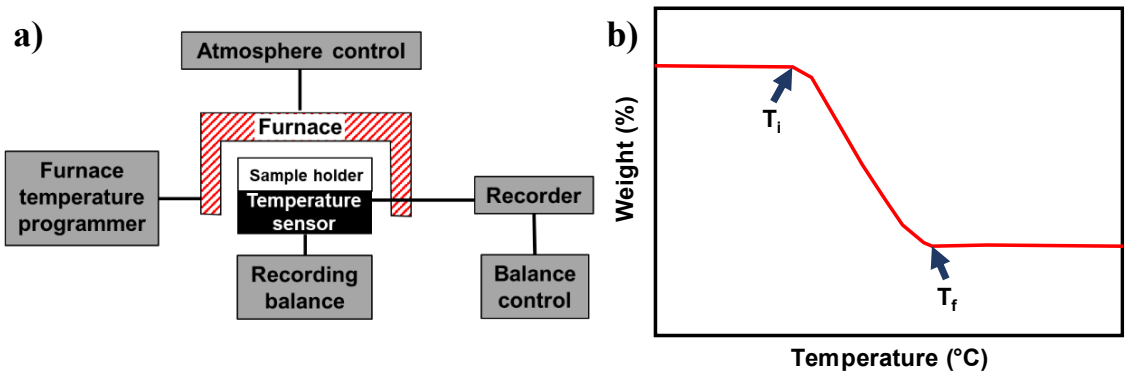

Figure 2.16 a) Diagram representation of a thermobalance, and b) a typical thermogravimetric curve. Adapted from reference 151.

In the graphene field, TGA can provide information about the ability of the reducing agent to restore the crystal structure of the graphene sheets, that is altered during the oxidation process; and even to analyse the presence of functional groups.

As shown in Figure 2.17a, graphite is a thermally stable compound with no decomposition over the tested temperature, however the initial decomposition temperature for the graphene oxide is around 100 °C attributed to the evaporation of water molecules, followed for a rapid weight loss up to 200 °C attributes to the pyrolysis of the reactive oxygen containing functional groups. As in reduced graphene oxide the oxygen is removed from the surface of GO and its graphitic structure is restored then the decomposition temperature is increases. The increase is dependent on the reducing agent, for example for thermally reduced graphene its onset temperature is ~ 600 °C. The higher onset temperature (~500 °C) in graphene functionalized with carboxylic groups, (Figure 2.17a), when compare with GO could be due to the presence of more stable oxygen containing functional groups.[152]

Eigler *et al.*[104] used mass spectrometer (MS) coupled to the TGA to determine that azide groups were successfully attached to graphene oxide sheets; to differentiate the N_2 signal from the CO signal in the sample they used ^{15}N labelled sodium azide and found this signal formed between 150 and 200°C, as it is shown in Figure 2.17b.

In this work, the TGA will be used in Section 5.7 to determine if oxygen and azide groups were attached to electrochemically exfoliated graphene flakes when the TGA spectra are compared respective to the graphite foil. As this is not a definitive prove that the groups were linked to the graphene surface, XPS will be used to provide more evidence about this.

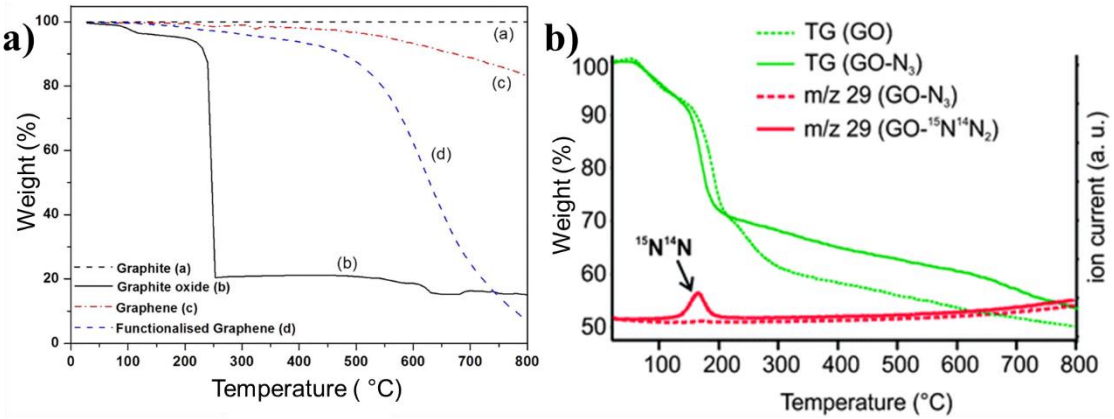

Figure 2.17 a) TGA (a) graphite, (b) thermally reduced graphene and (c) functionalised graphene; and b) TGA curve of GO and GO-$^{15}N^{14}N_2$, m/z 29 of GO-N_3 and GO-$^{15}N^{14}N_2$. Adapted from reference a) 152 *and b)* 104*, respectively.*

2.7 X-Ray photoelectron spectroscopy (XPS).

XPS is a quantitative technique to determine the elemental composition, chemical, and electronic state of the atoms at the surface of the sample. It gives information for all the elements except Hydrogen and Helium with an atomic sensitivity of 0.1% – 1%. In graphene research field it is a powerful tool to study the heteroatoms doping or decorating a graphene surface.[118,122,143]

The sample is penetrated by X-rays, reaching a depth of only a few micrometres. Figure 2.18a shows the kind of electrons generated when they reached the sample. The electrons generated deeply in the sample will encounter many inelastic collisions that involve the loss of energy and eventually will lose all their energy before escaping from the sample (C). Electrons generated nearer to the surface (B) may have only one or two inelastic collisions before escaping from the sample and reaching the detector, leaving the sample with less kinetic energy because they have lost some random amount of energy on their way to the detector; they contribute to the vertical step in the background signal that accompanies any large photoelectron or Auger electron peak showed in a XPS spectrum. The characteristic photoelectron peaks used in XPS analysis are contributed by the electrons that escape the surface without any inelastic collisions. The surface sensitivity of XPS is determined by how deep an electron can be generated and still escape without inelastically scattering.[153]

The intensity of the electron emitted from a sample at depths deeper than ***d***, is given by Eq. 2.5, where $\boldsymbol{I_0}$ represents the total number of electrons generated from the sample,

and λ is the attenuation length of the electron and is similar to the inelastic mean free path (IMFP). The IMFP is the average distance that an electron with certain kinetic energy can travel before inelastically scattering, and it depends on the on the energy of the electron and the material through which it is traveling. For electrons analysed with XPS (KE >100 eV), the IMFP increases as the kinetic energy of the electron increases (Figure 2.18b); so higher energy X-ray sources that generates electrons with higher kinetic energies are required to allow electrons escape form deeper within the sample.[153]

$$I = I_0 e^{-\frac{d}{\lambda}} \qquad \textit{Eq. 2.5}$$

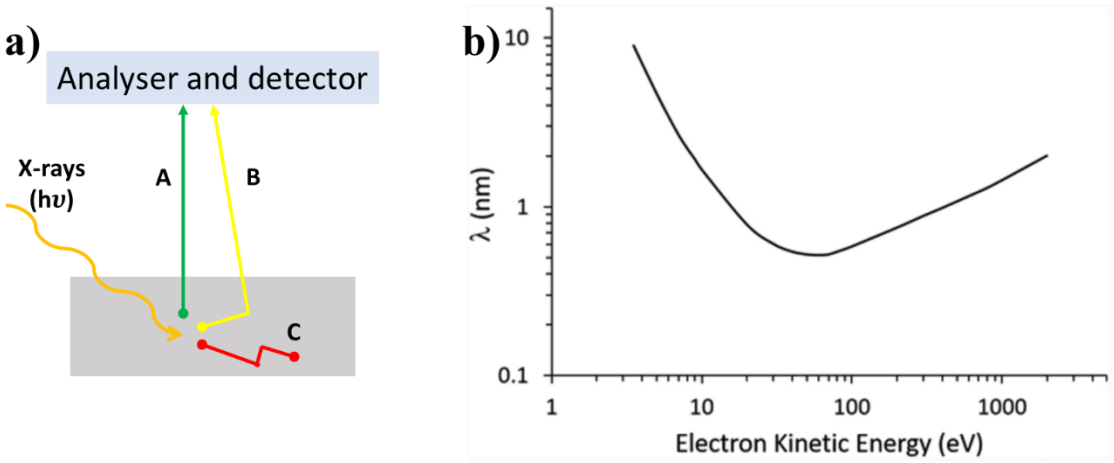

Figure 2.18 a) A Electrons emitted without interaction produce XPS photoelectron and Auger peaks, B electrons which undergo at least one inelastic collision contribute to the background, and C electrons that undergo multiple collisions and do not escape the sample.[153] *b) Inelastic mean free path (IMFP or λ) as a function of electron kinetic energy, reproduced from reference* 154.

Figure 2.19 illustrates the basic components of an X-ray photoelectron spectrometer. An X-ray source, usually AlKα or MgKα, under ultra-high vacuum excites the electrons of the sample (1-10 nm depth) resulting in the emission of a core level electron, that are collected by an electron energy analyser. Between the sample and the analyser are a set of extraction lenses, which define the acceptance angle for collecting electrons emitted from the sample.[153] The electrons travel through the selected area aperture plane which controls the area of the sample from which the electrons are collected. Next, the image of the electrons is projected to the analyser's entrance aperture plane, which is a narrow slit for

high resolution spectroscopy to minimize the angular dispersion of the electrons as they enter the hemispherical energy filter. For energy filtering of the electrons, a potential V_1 is applied to the inner hemisphere, and another potential V_2 to the outer hemisphere, then the difference ΔV is determined by the pass energy. The potentials V_1 and V_2 fluctuate as a function of the potential applied to the lens at the analyser's entrance aperture. Finally, an image of the electrons is projected through the energy filter to the detection plane. Where the number of electrons arriving with a particular kinetic energy are counted.[122,155]

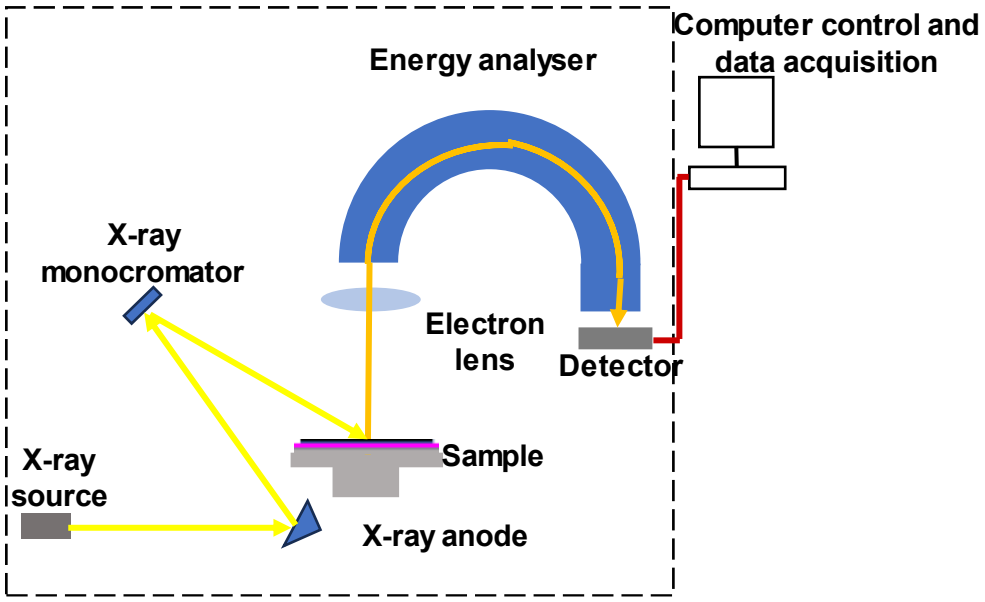

Figure 2.19 Diagram of an X-ray photoelectron spectrometer. Adapted from reference 155.

The XPS spectra is provided by the kinetic energy measurements and the number of electrons that escaped from the sample surface. The binding energy reflects the oxidation state of the surface elements; it can be calculated according to Eq. 2.6 because the energy of the X-ray used to excite the electron from a core orbital is a known quantity.

$$E_{binding} = E_{photon} - E_{kinetic} - \Phi \qquad \textit{Eq. 2.6}$$

where $\boldsymbol{E_{binding}}$ is the energy of the emitted electron, $\boldsymbol{E_{photon}}$ is the X-ray photon energy used, $\boldsymbol{E_{kinetic}}$ is the kinetic energy of the emitted electron; and $\boldsymbol{\Phi}$ is the spectrometer work function. The proportion of the elements is reflected by the number of electrons that

escaped from the surface sample.[118] Therefore, the area under the peak for each bond represents the percentage of that bond that is present.

Analysing the binding energy values, the nature of the binding between carbon atoms, the doped atom configuration, and the carbon bonds with other elements in bulk materials can be confirmed; so, the sample cleanliness and handling are crucial to obtain useful results since the electrons analysed come from the first nanometres of depth. Figure 2.20a shows a typical XPS spectra of single layer graphene on a SiO_2/Si substrate, where the peaks located at 103, 284., and 532 eV are assigned to the characteristic peaks of Si2p, C1s, and O1s, respectively. A high-resolution C1s spectra for single layer graphene is showed in Figure 2.20b and was fitted with three peaks. The sp^2 carbon (284.4 eV) is the predominant peak in the spectra, coming from the conjugated aromatic lattice, while C–H (285.1 eV), and C–O (286 eV) may occur in the H-terminated edges and adsorbed CO_x groups from ambient air and moisture.[156]

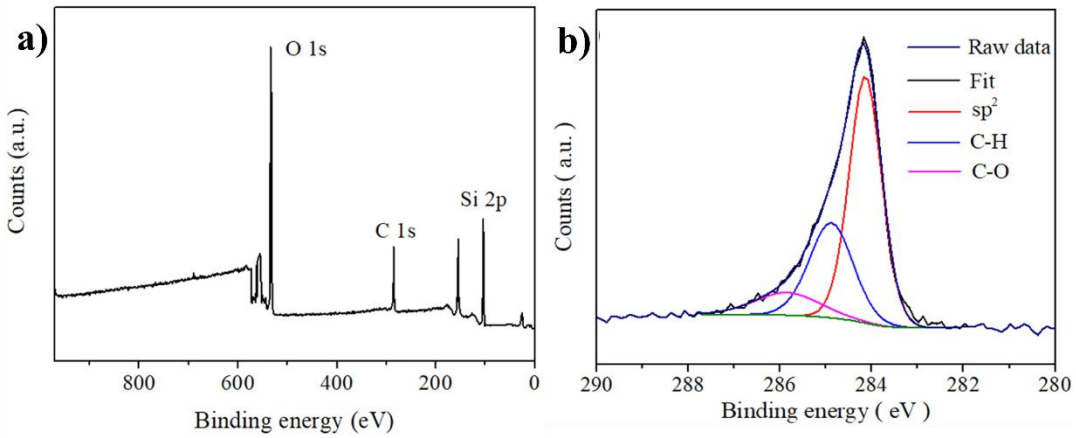

Figure 2.20 a) Survey-mode XPS and b) High-resolution XPS for the carbon 1s region of single layer graphene on SiO_2/Si substrate. Adapted from reference 156.

In this work, XPS will be used to provide evidence that the azide groups were attached to the graphene surface and then that the sensing molecule was also attached to these azide groups. This will be done in both graphene synthetised by LPCVD and electrochemical exfoliated graphene.

2.8 Electrical measurements: the Van der Pauw method.

The determination of a material's resistivity is reliant upon factors such as material type, resistance magnitude, shape, and thickness. Surface measurements are the only viable option for bidimensional materials, thus making the Van der Pauw method the preferred choice. This method was introduced in 1958 to measure the resistivity and Hall coefficient of arbitrary shape semiconductors. The sample should be flat, free of holes, and four small contacts will locate at arbitrary places on the periphery (Figure 2.21). A constant current I_{21} is applied between contacts 2 and 1, and the potential difference between contacts 4 and 3 is measured. Then, the resistance is calculated from Eq. 2.7[157]

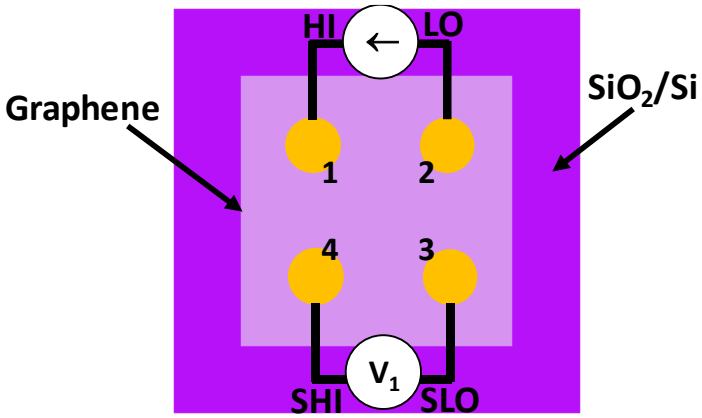

Figure 2.21 Van der Pauw configuration for a sample of graphene on SiO_2/Si.

$$R_1 = \frac{V_4 - V_3}{I_{21}} \qquad \textit{Eq. 2.7}$$

By rotating the sample by 90°, three more resistance values can be calculated (two horizontals and two verticals):

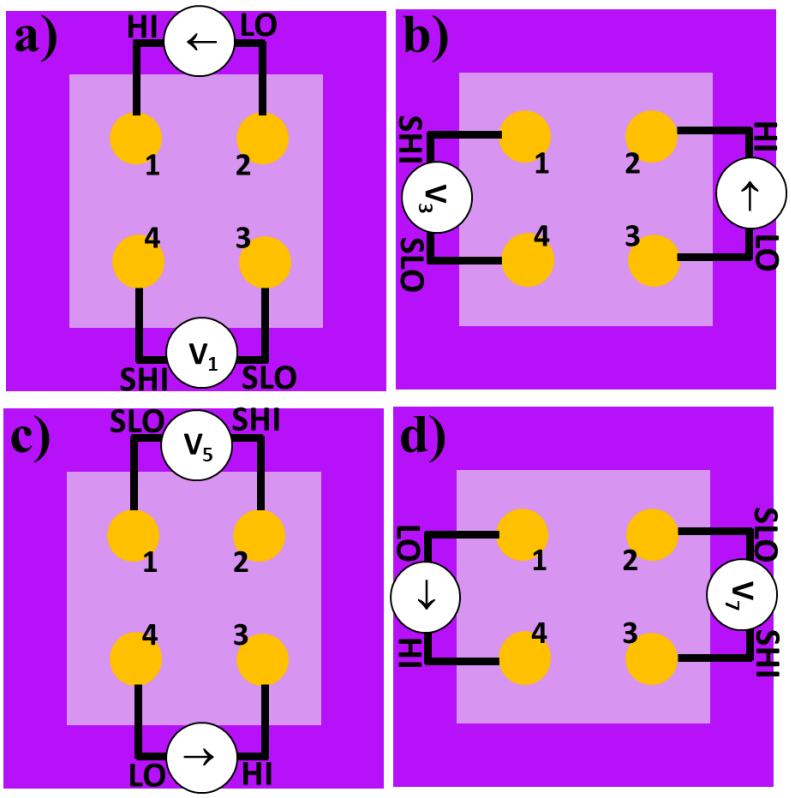

Figure 2.22 Van der Pauw of the four configurations used for the sheet resistance measurements in this work.

The average vertical and horizontal resistances can be calculated with Eq. 2.8 and Eq. 2.9, respectively.

$$R_V = \frac{R_3 + R_7}{2} \qquad \textit{Eq. 2.8}$$

$$R_H = \frac{R_1 + R_5}{2} \qquad \textit{Eq. 2.9}$$

Then, the sheet resistance of the sample is numerically calculated by solving Eq. 2.10.

$$e^{-\frac{\pi R_V}{R_S}} + e^{-\frac{\pi R_H}{R_S}} = 1 \qquad \textit{Eq. 2.10}$$

The Van der Pauw method will be used to determine the sheet resistance for LPCVD synthetised graphene and electrochemically exfoliated graphene.

3 Experimental methods.

3.1 Chemical vapour deposition of graphene (CVD).

Materials: Copper foil 25 μm thickness (Alfa Aesar, 46986.RF), methane (BOC, CP grade, 291372-L, 99.5% purity), hydrogen (BOC, high purity hydrogen, 54-K, 99.99% purity), and argon (BOC, Pure shield Argon Cylinder Industrial Grade, 11-W, 99.998% purity).

3.1.1 Atmospheric-pressure chemical vapour deposition (APCVD).

To test the setup, the conditions provided by Bhaviripudi *et al*.[68] were used. A strip of copper foil (4 cm × 1.5 cm) was placed in a quartz tube furnace and was heated to 1000 °C in the presence of a mixture of 450 : 50 sccm of argon : hydrogen gas flow. After the temperature stabilized the annealing was performed for 30 min. Then, methane gas (1 sccm) was introduced in the furnace and the synthesis was performed for 20 min. The sample was finally cooled to room temperature under hydrogen, methane, and argon flowing.

3.1.2 Low-Pressure chemical vapour deposition (LPCVD).

A 4.5 cm × 6 cm copper foil strip was placed in a quartz tube; the tube was pumped down to 43 mTorr using a vacuum pump. Then, 10 sccm hydrogen gas flow was introduced into the system, and the Cu foil was heated to 1000 °C. The foil was annealed for 30 min to initiate Cu grain growth, remove residual copper oxide, and to smoothen the surface. Subsequently, the hydrogen flow was changed to 15 sccm and 7 sccm methane gas was introduced in the chamber and the synthesis was performed for 10 min. The sample was rapidly cooled under the same hydrogen and methane flow to enhance the growth of large graphene domains. This reduced the time for methane decomposition and nucleation, and minimised the time for hydrogen-induced graphene etching.[158] The process was described in detail in Section 4.2, and the optimized conditions were reported. For SEM and AFM characterisations a small square of graphene on copper foil was mounted on SEM specimen stub or AFM specimen holder with a carbon adhesive disc.

Challenge: The challenges during the growth process are documented in Section 4.1. **Critical step:** It is essential to purge the lines before running any experiment, otherwise you will get incomplete graphene growth as the copper will oxidize.

3.2 Transfer graphene process.

Materials: LPCVD graphene on copper (as prepared in Section 3.1.2), thermal release tape (Nitto Denko, SEC P/N 3195MS, TRT), polymethylmethacrylate (Sigma Aldrich, 182230 M_w ~ 120 000, PMMA), anisole (Fisher Scientific, 15661120), hydrochloric acid (Fischer Scientific, 37%, 10316380), hydrogen peroxide (Fischer Scientific, 30%, 10687022), deionized water, iron (III) chloride (Alfa Aesar, A17015), silicon wafer (πPI-KEM, WAFER-SILI-0034), acetone (Fisher Scientific, A/0600/27), isopropanol (Fisher Scientific, P/7490/17), and nitrogen (Boc, Oxygen free 99.998%, 44-W).

Graphene was transferred on SiO_2/Si substrates using a wet transfer method.[159] A 2 × 2 cm^2 square of graphene/copper foil was cut and attached to the TRT, spin-coated with 200 µl of PMMA (8 % w/w in anisole) at 2000 rpm by 1 min, and cured at 115 °C by 30 sec to release the TRT. The sample was placed for 2 min on the top of a oxidizing solution (2:2:21 v/v HCl (37 %):H_2O_2(30% w/v):H_2O), and washed on deionized water bath for 13 min. It was dried with a Kimwipe and cut into 2 × 0.5 cm^2 strips. The samples were placed in 1 M $FeCl_3$ for 15 min at 55 °C, followed by 3 subsequent deionized water baths, 10 min for each one, and lifted out on SiO_2/Si substrates. Then, they were placed on hot plate at 40 °C for 30 min, after this, they were placed in an oven (GENLAB MINO/100/DIG) at 130 °C for 30 min with ~45° inclination. Finally, they were placed in acetone bath at 55 °C for 2 h, rinsed in fresh acetone, followed by rinsing in isopropanol, and dried under flowing nitrogen gas. The graphene deposited on SiO_2/Si was used for SEM, AFM, TEM, XPS, and Raman characterizations, also for their use for further functionalization and sensors. **Note:** For TEM, the graphene/PMMA was lifted out on a holey carbon TEM grid and PMMA was removed in an acetone bath.

The following suggestions have emerged because of the challenges encountered during the research experiment.

Challenge: The PMMA layer used for support proved problematic due to its rigidity, either being too low or too high for effective dissolution in the acetone bath. **Critical step:** If a different PMMA molecular weight is used the concentration should be less or more is it is heavier or lighter PMMA.

Challenge: Damage of the film during the transfer process. **Critical step:** Make sure that when graphene/copper/graphene is attached to the thermal release tape it is completely flat as it can damage the film during the transfer process.

Challenge: Incomplete PMMA removal during the acetone bath step. **Critical step:** The time for cure step at 115 °C should not exceed 1 minute.

Challenge: Presence of holes in the copper substrates that can damage the graphene film because the contact with oxidizing solution. **Critical step:** Make sure the PMMA/graphene/copper/graphene is placed on the top of the oxidizing solution for 2 minutes to remove the graphene on the back of copper.

Challenge: The film sticks to the silicon wafer used during the washing steps or gets some impurities present on the surface of the wafer. **Critical step:** To transfer the PMMA/graphene films after the copper etching and DI water baths, the film should be fished out on a SiO2/Si wafer. Prior to each use, this wafer must be rinsed and dried to prevent film adhesion or contamination from surface impurities.

Challenge: Poor adhesion between graphene film, visible holes or not continuous film was observed. **Critical step:** PMMA/graphene film should be tilted 45° by placing it on 75 mm ×25 mm glass slide in 100 ml beaker in the oven, as this improves the adhesion between graphene and the substrate.

3.3 Electrochemical azidation of graphene synthetized by LPCVD.

Materials: LPCVD graphene (as prepared in Section 3.2), Ag/AgCl (3 M NaCl) reference electrode (Basi, MF-2052), sodium azide (Sigma Aldrich, 71289), 0.2 M sodium phosphate buffer pH = 7 (Fisher Scientific, 15435709), and deionized water.

Both the graphene strip on SiO_2/Si, contacted at one end with silver paint and attached to an alligator clip (working electrode), and the Ag/AgCl counter/reference electrode were immersed in 25 ml of 0.2 M solution of sodium azide in 0.1 M sodium phosphate buffer. A Keithley 2602 Source Meter was programmed to apply 1.3 V between the graphene and the Ag/AgCl electrodes and the current was recorded as a function of time. After the reaction, the sample was rinsed with deionized water and dried in air. It is called in the text as Gr-N_3. The sample was ready for XPS characterization and click chemistry, see Section 4.7.

Challenge: Graphene film comes off during the electrochemical azidation. **Critical step:** Make sure you carefully followed the transfer procedure in Section 3.2 and controlled the potential applied to be 1.3 V.

3.4 Electrochemical exfoliation and functionalisation of graphene.

Materials: Graphite foil (Alfa Aesar, 43078.RF), platinum wire (Good Fellow, PT005130), sodium sulphate (Sigma Aldrich, 238597), sodium azide (Sigma Aldrich, 71289), 0.1 M sodium phosphate buffer pH=7 (Fisher Scientific, 15435709), deionized water, silicon wafers (πPI-KEM, WAFER-SILI-0034).

Graphite foil was used as working electrode (carbon source) and platinum wire as counter electrode. Electrolyte solution of 40 ml of 0.2 M NaN_3 (in water or buffer solution pH=7) and 40 ml of 0.4 M Na_2SO_4 (in water or buffer solution pH=7) were placed in a 100 ml beaker. A constant voltage was applied to the graphite foil (+5, +7 or +10 V) until the exfoliation was completed, this was determined when the graphite electrode was detached from the alligator clip. The electrochemical exfoliated graphene with sodium azide groups on its surface (EEG-N_3) was then collected on a nylon filter membrane filter (pore size 0.2 µm) and washed repeatedly with deionized water by vacuum filtration. The resultant EEG was dispersed in water using a bath sonicator (Ultrasonic cleaner, 010S) for 15 min. The dispersion was kept for 24 h to allow for the precipitation of un-exfoliated graphite flakes and/or particles. The top part of the dispersion was used for further characterization and reactions.

For electrochemical exfoliated graphene without azide groups on its surface (EEG), 0.4 M Na_2SO_4 in water and +7 V were used, and the process was followed as stated above. The top part of the dispersion was used for further characterization.

The lateral size and thickness of azidated graphene flakes were measured using atomic force microscopy (AFM). 2 ml of the EEG-N_3 dispersion (0.01 mg/ml in 1:6 water:methanol v/v) was added dropwise onto the water surface in the Langmuir Blodgett trough (611D Nima) using a 1 ml disposable syringe. After spreading, film at the air–water interface was left 20 min to evaporate the solvent. Then the film was compressed at a target pressure of 5 mN/m with a compression rate of 20 cm^2/min. EEG sheets were uniformly deposited on mica by vertically dip coating the substrate with a pull-up rate of 2 mm/min. The samples were left to dry for future Raman and AFM characterizations. For XPS and TEM the sample was prepared by drop cast the dispersion on a SiO_2/Si substrate and holey carbon TEM grid, respectively; they were left to dry overnight. Sheet resistance measurements were conducted on thin films prepared by vacuum filtration on a nylon membrane of aqueous solutions of electrochemical exfoliated graphene flakes, without functionalization (EEG) and with azide groups on its surface (EEG-N_3).

Challenge: Difficulties to stabilize the isotherm before drop cast the graphene solution. **Critical step:** Make sure you are using clean ultrahigh purity water during the Langmuir-Blodgett deposition.

3.5 Sensing molecule synthesis.

Materials: Dry Tetrahydrofuran (THF), 3,5-bis(trifluoromethyl)phenyl isothiocyanate (Sima Aldrich, 468517), propargylamine (Fluorochem, 307008), hexane (Fisher Scientific, H/0406/17).

285 µl of propargylamine were added to a solution of 3,5-bis(trifluoromethyl)phenyl isothiocyanate (675 µl) in 10 ml of dry THF, and the mixture was stirred for 5 h. The solvent was removed under reduced pressure. The purification was done by crystallization and vacuum filtration washing the product with hexane. The sensing molecule: 1-(3,5-bis(trifluoromethyl)phenyl)-3-(prop-2-yn-1-yl) thiourea was obtained as a pale yellow powder, it was referred in the text as TU. ^{1}H NMR (599 MHz, DMSO-d_6) δ 10.15 (s, 1H), 8.51 (s, 1H), 8.22 (d, *J* = 1.6 Hz, 2H), 7.73 (s, 1H), 4.31 (s, 2H), 3.19 (t, *J* = 2.5 Hz, 1H). ^{13}C NMR (151 MHz, DMSO-d_6) δ 180.76, 141.71, 130.48, 130.27, 130.05, 129.83, 125.93, 124.12, 122.40, 122.31, 120.50, 116.51, 80.15, 73.87, 40.06, 39.94, 39.80, 39.66, 39.52, 39.38, 39.24, 39.10, 33.30. ^{19}F NMR (376 MHz, DMSO-d_6) δ -61.59. HRMS (ESI) m/z calculated for C12H8N2S1F6 [M+H]+: 327.26, found 327.148 (see Appendix A).

3.6 Click chemistry protocol.

Materials: Azidated monolayer graphene (prepared as stated in Section 3.3, Gr-N_3), and electrochemical exfoliated azidated graphene (prepared as stated in Section 3.4, EEG-N_3), 1-(3,5-bis(trifluoromethyl)phenyl)-3-(prop-2-yn-1-yl) thiourea (synthetized as stated in Section 3.5, TU), methanol (Fisher Scientific, M/4000/17), copper sulphate pentahydrate (Fluorochem, 044725), ascorbic acid (Fluorochem, 093967), and deionized water.

For both samples, Gr-N_3 and EEG-N_3, a copper(I)-catalysed alkyne–azide cycloaddition (CuAAC) click chemistry was used to introduce sensing molecule, TU, to them, see Figure 1.21.

For the G-N_3 sample, 468 µl of 1 mM TU in methanol were placed in a 7 ml vial, then an aqueous solution of 5 mM $CuSO_4 \cdot 5H_2O$ (7.5 µl) and 10 mM ascorbic acid (25 µl) were added. This reaction solution was dropped onto the entire sample of Gr-N_3 and cover with aluminium foil to allow it reacted by 1 hour. Finally, the sample was rinsed with a

mix 1:1 methanol:water three times and dry in air. The sample is ready to use in sensors and characterization (Raman, XPS).

EEG-N_3 were functionalized with the selector as follows: first 47 ml of 1 mM TU solution in methanol was placed in a flask, then 1.3 ml of an aqueous solution of 5 mM $CuSO_4 \cdot 5H_2O$ and 4.4 ml of an aqueous solution of 10 mM ascorbic acid were added to it. This reaction solution was added to a solution of azidated graphene flakes (EEG-N_3) prepared as stated in Section 3.4 in 35 ml (1:1) water:methanol. The sample was left for reaction to react for one hour.

The washing process involved centrifugation at 10000 rpm for 10 minutes, resulting in the recovery of graphene at the bottom and subsequent removal of the supernatant. The sample was dispersed again in a water:methanol (1:1) solution, and this procedure was repeated twice more. The sample was dispersed in 40 ml water:methanol 1:1 (it is referred as EEG-TU) for further use in sensors and characterizations. For XPS the sample was prepared by drop cast the dispersion on a SiO_2/Si substrate. Sheet resistance measurements were conducted on thin films prepares by vacuum filtration on nylon membranes of EEG-TU solution.

Challenge: Ascorbic acid oxidizes quickly. **Critical step:** Ascorbic acid solution should be freshly prepared.

3.7 Graphene-based sensors devices preparation.

Graphene grown by CVD was cut in strips of 2 cm × 0.5 cm and they were transferred onto SiO_2/Si using the PMMA method, Section 3.2. Non-covalent functionalisation was done by drop cast the selector on the graphene surface, then they were washed and dried. Then the graphene strips were contacted at both ends using conductive silver paint, see Figure 6.1a.

To prepare EEG-based sensors, glass slides were cleaned by ultra-sonication in acetone for 15 min and dried. Using a home-made tape mask, with 1 mm gap between the metal electrodes, a layer of gold/palladium of 100 nm thickness was deposited onto the glass slides using a sputter coater (Figure 6.1b). The electrodes were placed on a hot plate at 77 °C, then EEG solution was dropping cast between the electrodes until 15-20 kΩ resistance is achieved. They were left on the hot plate at 77 °C for 30 min before any sensing measurements. It was repeated but using EEG-TU.

3.8 XRD measurements.

Non functionalized and functionalized graphene sheets, produced as stated in Section 3.4, in 0.4 M Na_2SO_4 (control experiment) and 0.2 M Na_2SO_4/0.1 M NaN_3 aqueous solution at 7 V were freeze dried and lightly pressed against a PMMA sample holder. X-ray powder diffractograms were obtained using a Bruker D8 Venture diffractometer Cu Kα1 source (λ = 1.5406 Å) operated in Braggs Beta mode.

3.9 SEM imaging.

SEM images were taking using Zeiss Sigma 360 VP microscope at 5.0 kV and an in-lens detector. SEM was used to characterize the morphology of graphite foil electrodes after exfoliation, and the surface morphology of graphene on copper and after the transfer process on SiO_2/Si substrate.

3.10 TEM imaging.

TEM images were taken using a JEOL 2100F FEG microscope operating at 200 kV. Samples were prepared as it is stated in each Section.

3.11 AFM measurements.

The thickness of the electrochemical exfoliated graphene flakes and graphene films produced by LPCVD were measured with a Scanning Probe Microscope (SPM) SmartSPM-1000 in non-contact mode / tapping-mode using a silicon tip (PPP-NCHR-20, 10-130 N/m). In the case of graphene flakes the lateral size were measured according to the NPL protocol.[160]

3.12 Raman acquisition.

Raman spectra and maps were collected using Horiba LabRAM HR Evolution confocal Raman microscope with 50× Long-Working-Distance (LWD, LMPLFLN50X, NA = 0.5) objective and a 532 nm laser wavelength. Using ~1.2 mW of power. Raman maps were taken over a 13 μm × 13 μm area, with 1 μm step, giving 169 spectra. After base line correction and cosmic ray removal data were fitted using Lorentzian fitting in Origin 2022b software.[161]

3.13 Thermogravimetric analysis (TGA).

TGA was carried out using a Perkin Elmer Pyris I. EEG and EEG-N_3 dry powders, and graphite foil samples (1 - 5 mg) were heated under helium in a ceramic pan from room temperature to 900 °C at a rate of 10 °C per min.

3.14 X-ray photoelectron spectroscopy (XPS).

XPS data collection was performed at the EPSRC National Facility for XPS ('HarwellXPS'), operated by Cardiff University and UCL, under contract No. PR16195. A Kratos Axis Ultra DLD system was used to collect XPS spectra using monochromatic Al Kα X-ray source operating at 144 W (12 mA × 12 kV). Data was collected with pass energies of 80 eV for survey spectra, and 20 eV for the high-resolution scans with step sizes of 1 eV and 0.1 eV respectively.

The system was operated in the Hybrid mode, using a combination of magnetic immersion and electrostatic lenses, and acquired over an area approximately 300 × 700 μm^2. A magnetically confined charge compensation system using low energy electrons was used to minimize charging of the sample surface, and all spectra were taken with a 90° take of angle. A pressure of ca. 5×10^{-9} Torr was maintained during collection of the spectra.

All samples were mounted on to a standard Kratos Axis Ultra sample bar using a small piece of double-sided carbon tape before insertion into the spectrometer. All data was analysed using CasaXPS (v2.3.26)[162] after subtraction of a Shirley background and using modified Wagner sensitivity factors as supplied by the instrument manufacturer. Curve fits were performed using an asymmetric Lorentzian form (LA Lineshape in CasaXPS), whereas the lineshape for graphitic, sp^2 carbon, was derived from that measured from a clean HOPG sample.[163] Data was calibrated to this sp^2 carbon after fitting and taken to have a binding energy of 284.5 eV.

For samples coming from LPCVD procedure, bare graphene, graphene azidated and graphene with the TU molecule were prepared as mentioned in Sections 3.1.2, 3.3 and 3.6, respectively. For samples from electrochemical exfoliation and functionalization, EEG, EEG-N_3 and EEG-TU were prepared as stated in Sections 3.4 and 3.6.

3.15 Van der Pauw method.

Keithley 2602 source meter unit (SMU) in four-wire configuration was used to measure the resistances according to the Van der Pauw method, basically a current of 100 μA was applied between two points and the resistance was measured between the two opposite points of the sample. Four measurements were collected by rotating the current source and the positions of the voltage measurements.[164] These four configurations are showed in Figure 4.32d, with a 5 mm separation between adjacent electrodes. The sheet resistance is computed by numerically solving the equation Eq. 2.10 using the GRG non-linear method as implemented in Microsoft Excel.

Graphene/SiO_2/Si sample transferred according to Section 3.2 and graphene flakes samples prepared as in Sections 3.4 and 3.6, were used for this characterization.

4 Graphene synthesis by chemical vapour deposition (CVD) method.

A detailed background discussion can be found in Section 1.2.2.2. However in summary, monolayer graphene films can be routinely synthesised on copper surface by low-pressure CVD (LPCVD) following the process proposed by Li *et al*., where they showed 95% monolayer with less than 1% tri-layer or few-layer (< 10 layers) and ~3-4% bilayer graphene can be produced.[64] Under atmospheric pressure CVD (APCVD**)** reduced monolayer formation was observed.[68] CVD is a direct synthesis method of graphene from carbon sources or precursors. Methane is the most widely used because of its low pyrolysis rate; however, liquid and solid precursors have also been used.[165–169] Graphene grows on a transition metal substrate, and copper (Cu) foil is the best as it produces monolayer graphene due to its low carbon solubility. Other metals such as nickel (Ni), platinum (Pt), cobalt (Co), gold (Au), Cu-Ni alloys, have been widely used as growth substrates.[69,78,170,171]

The graphene growth mechanism is governed by the carbon solubility in the metal catalyst; for Cu foil (< 0.001 atom %), the synthesis of graphene is limited to the surface, but for intermediate to high solubility (> 0.1 atom %) metal catalysts (Ni or Co) graphene synthesis takes place through a combination of diffusion into the metal thin film at the growth temperature, and precipitation of carbon from bulk to the surface of the metal upon cooling after CVD synthesis.[64,67,172] As Cu has negligibly low carbon solubility, once its surface is fully covered with graphene, the Cu surface loses its catalytic activity, suggesting a self-limited process.[64,173] However, Bhaviripudi *et al*., demonstrated the possibility of multilayer graphene at APCVD conditions,[68] which has motivated further research on the mechanism.[174]

LPCVD allows the growth of large area high-quality graphene, from 1 cm^2 up to 30 inch (76.2 cm) diagonal.[11,64,175] Additionally, advancements in technology have allowed hot wall configurations to operate continuously, in contrast to cold wall configurations. The latter are constrained by stage size, limiting the maximum sample size and requiring batch-to-batch operation mode.[176]

As it was stated in Section 1.2.2.2, there are two different methods for growth graphene onto substrates: cold wall and hot wall CVD. The difference between these two chamber designs lies in their respective heating regimes. When employing a hot wall configuration, uniform radiation extends the heating zone beyond the dimensions of the

specimen, ensuring a consistent temperature throughout. In contrast, the cold wall configuration only provides heating to the substrate, resulting in a significant thermal gradient between the hot stage (T > 1000 °C) and the cold walls (T ~ few tens of °C). However, the prohibitive cost of cold wall chambers restricts access for numerous laboratories. Consequently, there is a need to develop more efficient and cost-effective equipment, as well as a reliable standard operating procedure, in order to improve accessibility of CVD graphene for laboratory use.

LPCVD is the most common method to produce large-area high-quality graphene on copper foil; however, the drawbacks associated with CVD graphene are the cost of the equipment to produce it, the pre-treatment of the copper foil, the production time, and the batch-to-batch reproducibility. The expensive cost of commercial cold wall equipment to synthesise graphene limits access to many laboratories; therefore, an alternative is needed. Using tube furnaces that are less expensive and have precise temperature control, which is crucial, is desirable. Even if a tube furnace is customised with mass flow controllers, adapters and a pressure gauge, the cost of the whole equipment is still considerably less than cold wall ones. Ensuring a consistently high temperature along the tube's wall is crucial for producing high-quality graphene. This condition promotes larger grain size and reduces the number of nucleation sites, which are vital for achieving the exceptional properties found in graphene films.

In this work, we describe in detail a simple chemical vapour deposition (CVD) procedure in a hot-wall configuration (tube furnace) to grow graphene with low-cost equipment, using off-the-shelf commercially available, untreated or processed copper foil. In order to achieve reliability, reproducibility, and a rough estimate of costs, we are providing a detailed standard operating procedure, expected batch-to-batch variations and information on the parts of the customised set-up.

The quality of the graphene film after transferred it on SiO_2/Si and TEM grid was studied by scanning electron microscopy (SEM) and transmission electron microscopy (TEM) to confirm the predominantly monolayer nature of graphene. The quality of graphene was analysed through the statistical analysis of Raman mapping, demonstrating its applicability to assess the synthesised graphene quickly and non-invasively. This study shows a consistent procedure to grow high-quality graphene film that is easily transferred to SiO_2/Si wafers, potentially making graphene more readily available to a wider range of laboratories. We also demonstrate that the graphene films can be covalent or non-

covalently functionalised and subsequently used as a chemiresistor for gas sensing, as shown in Section 6.2.

4.1 CVD experimental set-up and preliminary tests.

Graphene was grown using a custom-built set-up, which consists of a mixer gas chamber with two mass flow controllers for CH_4 and H_2 (Brooks 5850 TR) and one rotameter for Ar (Brooks 1355/D2C2D1C00000), a commercial furnace (Carbolite, EST12450B-230SN), pressure gauge (KJL275806), needle valve, cold trap, and a pump (TRIVAC D 2,5 E). A 32 mm diameter and 1 m long quartz tube was used as a reaction chamber (Figure 4.1a and b).

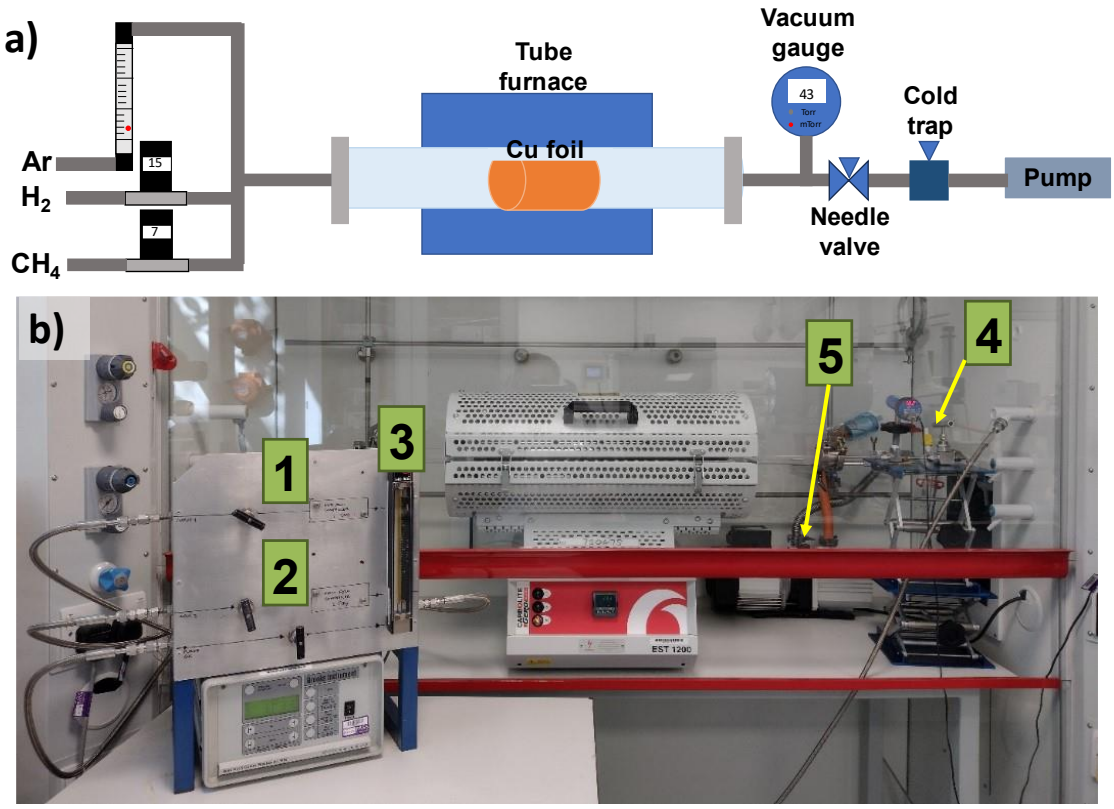

Figure 4.1 a) Schematic diagram and b) operational setup (1, 2, 3, 4, and 5 points out the mass flow controllers for hydrogen, methane, argon, the vent valve, and pump, respectively) for graphene synthesis by LPCVD.

Since in graphene synthesis temperature control is crucial, the temperature distribution along the quartz work tube was recorded. The temperature profile distribution

inside the tube revealed a 10 cm uniform heat zone (5 cm either side of the centre) (Figure 4.2a and b).

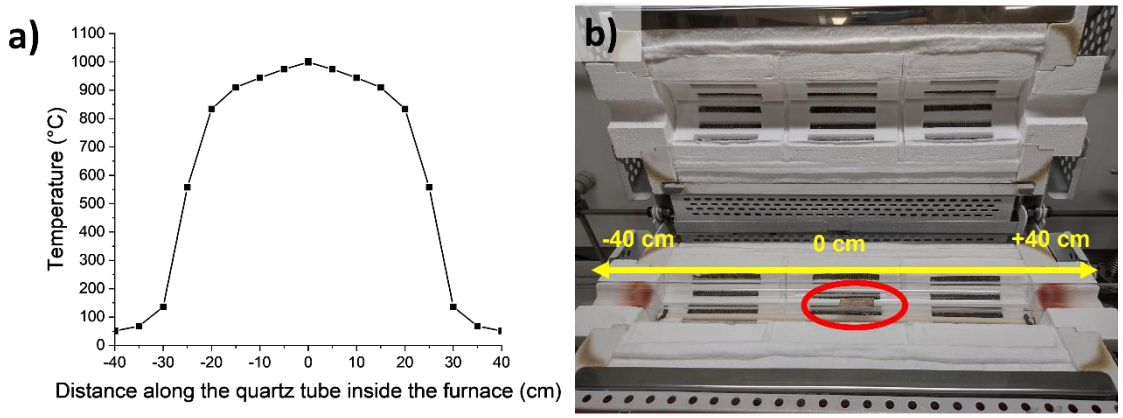

Figure 4.2 a) Temperature profile distribution along the radial axis and b) measurements in the setup the red circle shows the copper position.

To test the set up and found the conditions where monolayer graphene can growth, preliminary experiments were done. As discussed in Section 2.5, intensity ratio of 2D peak to G peak $I_{2D}/I_G>2$ and the D band absence are indicators of free-defect monolayer graphene. The evaluation of graphene quality was conducted through Raman spectroscopy on samples transferred onto SiO_2/Si. These samples were compared to a commercial monolayer graphene sample, Figure 4.3a, which displayed a 2D peak position at 2672.0 cm^{-1} and the absence of a D peak.

Initially a piece of copper (1.5 × 4 cm^2) was used to grow graphene under atmospheric conditions (APCVD). The choice of conditions was determined using a previously established method by Bhaviripudi *et al.*,[68] which involved a growth condition ratio of argon : hydrogen : methane (Ar : H_2 : CH_4) of 450 : 50 : 1 sccm and a duration of 20 minutes (3.1.1). Figure 4.3b show Raman spectra of the sample synthetised under APCVD conditions, where the presence of the D peak (1352.60 cm^{-1}) indicates some defects within the carbon lattice and more than one layer of graphene as the $I_{2D}/I_G = 0.66 < 2$. Despite multiple attempts, using the same conditions, we were unable to reproduce the results of Bhaviripudi *et al.*,[68] who reported monolayer graphene, and predominantly observed multilayer graphene.

After verifying the functionality of the set up in atmospheric conditions to grow carbon, adjustments were made to enable its operation in low pressure conditions

(LPCVD), which is widely acknowledged to favour monolayer graphene formation.[64,68] LPCVD run was done using a hydrogen : methane ratio (H_2 : CH_4) of 7 : 15 sccm and growth time of 20 min as proposed by Bhaviripudi *et al*.[68] Figure 4.3c shows a typical Raman spectrum of graphene, which exhibits the absence of the D peak and I_{2D}/I_G=1.6, indicating a monolayer structure. However, there were some domains in which some adlayers were observed. To decrease the amount of adlayers on the graphene film the growth time was reduced to 10 min and also growth ratios were changed to H_2 : CH_4 of 15 sccm : 7 sccm to keep the pressure constant in both experiments. Moreover, the hydrogen was increased as it has an etching effect, resulting in the decrease the number of layers on the graphene surface.[177] Figure 4.3d shows a typical Raman spectrum, showing no D peak and the ratio I_{2D}/I_G=1.5 indicating monolayer graphene.

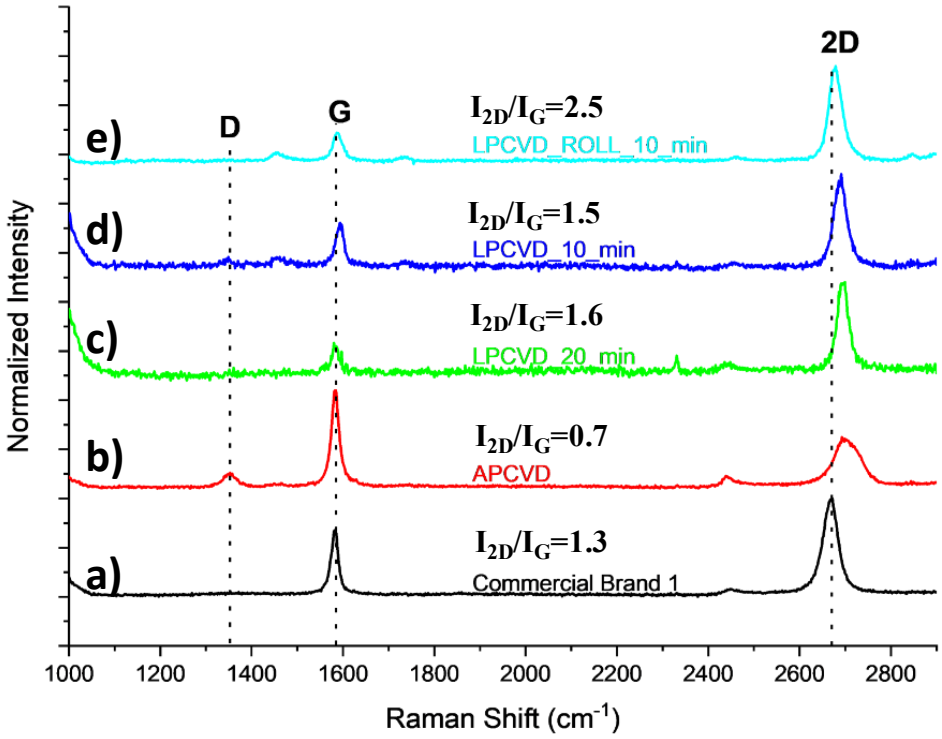

Figure 4.3 Raman Spectra, normalised to the G band, of a) monolayer graphene from a commercial brand 1 on SiO_2/Si. Graphene growth on 1.5 × 4 cm^2 piece of Cu foil using: b) APCVD, 20 min and Ar : H_2 : CH_4=450:50:1 sccm; LPCVD under c) 20 min and H_2 : CH_4=7:15 sccm and d) 10 min and H_2 : CH_4=15:7 sccm. e) Graphene growth on 4.5 × 6 cm^2 piece of Cu foil at LPCVD, 10 min and H_2 : CH_4=15:7 sccm.

All of the runs were tested using a piece of copper foil 1.5 × 4 cm^2. To maximise the growth area, a larger piece of copper foil (6.5 × 4 cm^2) was wrapped against the wall of the quartz tube (Figure 4.4a and b) and the same growth conditions were used (10 min, H_2 : CH_4 of 15 sccm : 7 sccm). Figure 4.3e) shows a typical the Raman spectrum of this sample where no D peak was observed and a higher I_{2D}/I_G=2.5 was obtained, indicating the monolayer nature of graphene.

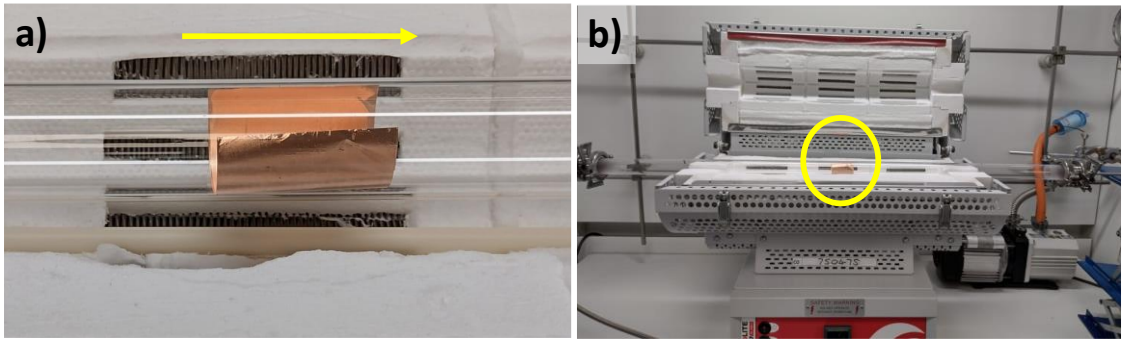

Figure 4.4 a) Actual image of the graphene foil wrapped against wall tube the yellow arrow indicates the flow direction, b) Yellow circle shows copper foil placed at the centre of the furnace.

Another problem we found during the graphene growth process was the formation of copper(I) oxide. We observed that in two consecutive experiments, the first one yielded a heavily oxidized copper that exhibited brittleness upon contact, making transfer unfeasible (Figure 4.5a). On the other hand, the subsequent experiment resulted in the growth on graphene (Figure 4.5b), with a very few oxidised areas. These results suggested a source of oxygen within the lines. Therefore, we decided to purge the lines for 10 minutes before running any experiment. Despite its simplicity, this measure proved to be crucial in achieving the growth of graphene without any oxidized areas (Figure 4.5c and d). It is interesting that in most procedures reported in the literature this step is normally omitted or overlooked and it is not part of the procedure. In this work, we report a procedure that contains as much experimental detail as possible, described in the following section, so it can be adapted in any laboratory, using accessible materials. Moreover, statistical analysis of Raman spectra will be used to assess the variations and uniformity of the synthesized films using this procedure (Section 4.5).

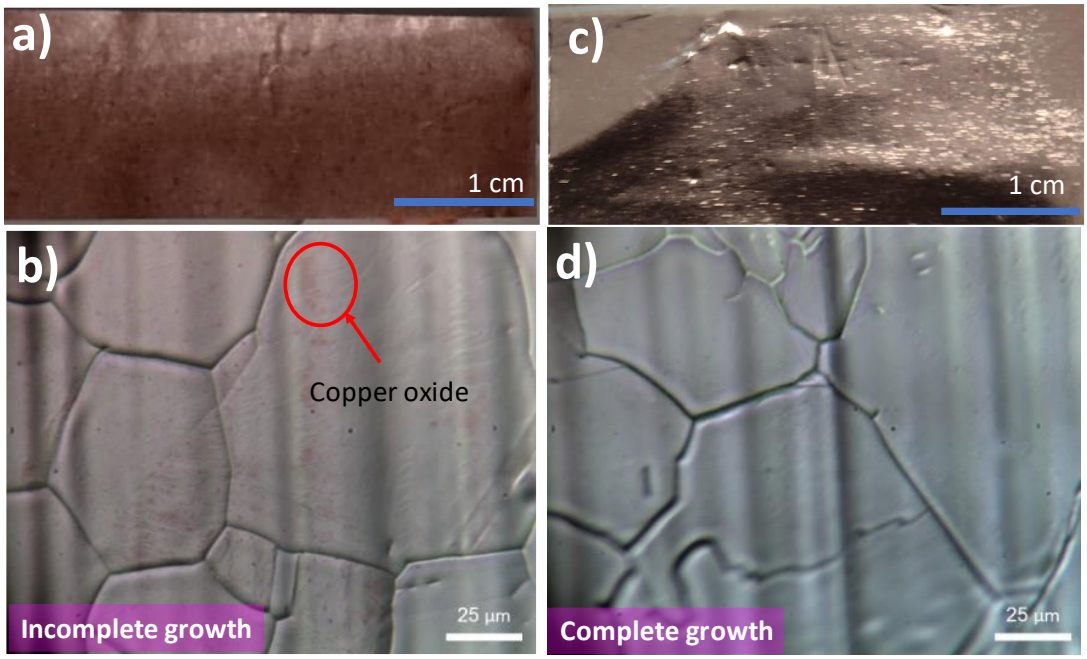

Figure 4.5 a) Photograph of unsuccessful graphene synthesis where copper (I) oxide was obtained when the lines were not purged in advance and b) optical microscope image of incomplete growth (colour stains of copper oxide visible) of graphene because of insufficiently purged lines. c) and d) photograph and optical microscope image of monolayer graphene following successful growth.

4.2 Graphene growth.

To grow graphene, copper foil (Alfa Aesar 46986.RF, 25 µm thickness, 99% purity) were cut to desired size (from 1 cm × 4.0 cm up to 6.5 cm × 4.0 cm), rinsed with acetone followed by isopropyl alcohol rinse and dry with nitrogen gas. Then it was rolled against the quartz tube wall (Figure 4.4a) and placed in the centre of the quartz tube (Figure 4.4b). The lines were purged with 27 lpm : 15 sccm : 15 sccm Ar:CH_4:H_2 for 10 min and another 5 min just under Ar flow. At this point, the vent valve was closed the argon flow was stopped, and the pump was turned on; the system was pumped until 43 mTorr and 10 sccm of hydrogen were introduced to start the heating ramp; the first heating ramp was 43.9 °C/min until 900 °C then it changed to 10 °C/min until reach 1000 °C. The annealing was conducted for 30 min; after this step, hydrogen flow was increased to 15 sccm and 7 sccm methane were introduced in the chamber to start the graphene growth process, which took only 10 min full graphene coverage on copper substrate. The furnace was opened when the temperature was 900 °C, and the cooling process started under hydrogen and methane

flows; at around 180 °C, argon was introduced at 27 lpm flow rate for 5 min, and the hydrogen and methane feeds were closed. Finally, under argon flow, the pump was turned off, the vent valve was opened, the argon flow was stopped, and the quartz tube was opened to take out the graphene on copper foil (Gr/Cu). The fresh graphene was placed in a petri dish and sealed with parafilm for future use. Figure 4.6 illustrates the whole process and the key parameters.

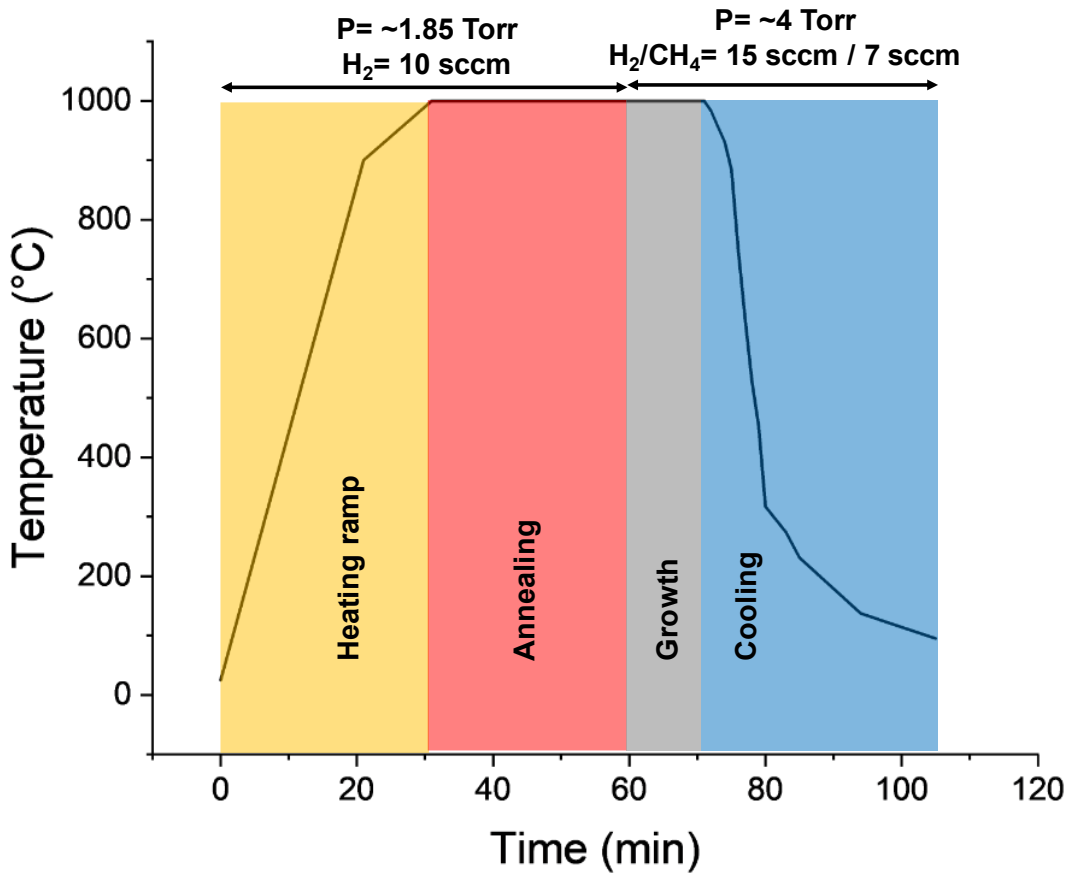

Figure 4.6 Time dependence of experimental parameters: temperature, pressure, and gas composition/flow rate.

4.2.1 Transfer process.

After the graphene has been grown on copper foil, it should be transferred to any desirable substrate for further characterization and applications. For this purpose, many methods have been reported,[80,178] such as wet transfer,[82,179] electrochemical bubble transfer,[70,71] non-electrochemical bubble transfer,[180] dry transfer,[81,181] roll-to-roll transfer[11,182] and support-free transfer.[82,183,184]

Fresh graphene was transferred onto glass and silicon/silicon oxide (SiO_2/Si) using a modified wet transfer method.[39,159] A 1 cm^2 Gr/Cu was cut and attached to thermal release tape (TRT), spin-coated with 50 µl of PMMA (4 % w/w in anisole, M_w ~ 120 000) at 2000 rpm by 1 min, cured at 115 °C by 30 sec and the TRT was released. The PMMA/Gr/Cu was placed for 2 min on an oxidising solution (2:2:21 v/v HCl (37 %):H_2O_2(30% w/v):H_2O), placed in deionised water (DI) bath for 13 min, placed on 1 M $FeCl_3$ for 15 min at 55°C , followed by 3 DI water baths, 10 min each one, and fished them out on glass or SiO_2/Si substrates (PMMA/Gr/SiO_2/Si). The PMMA/Gr/SiO_2/Si was placed on a hot plate at 40 °C for 30 min, then placed in the oven at 130 °C for 30 min with ~45° inclination, which have been demonstrated to improve the adhesion to the substrates.[39] Finally, it was placed in an acetone bath at 55 °C for 2 h and tilted ~45°, rinsed in acetone, another rinse in isopropanol, and dried under nitrogen (N_2); the Gr/SiO_2/Si is ready for further characterisation, functionalisation, and gas sensor devices (see Section 6.2).

4.2.2 Scanning electron microscopy (SEM).

Figure 4.7a,b show an optical image and SEM image of the ‘as-grown’ graphene on copper foil where the copper grain boundary can be easily observed; it confirms the total growth of graphene on copper foil due to the absence of copper oxide areas. In Figure 4.7c, graphene grains and adlayers can be observed. The adlayers crossing the copper grain boundaries indicate the continuous graphene film. The average copper grain size is 167 $\mu m^{2,}$ according to 74 measurements, and the average graphene grain size is 3.38 μm^2, based on 120 measurements. These distribution measurements are shown in Figure 4.8a and b, for copper and graphene grain areas, respectively.

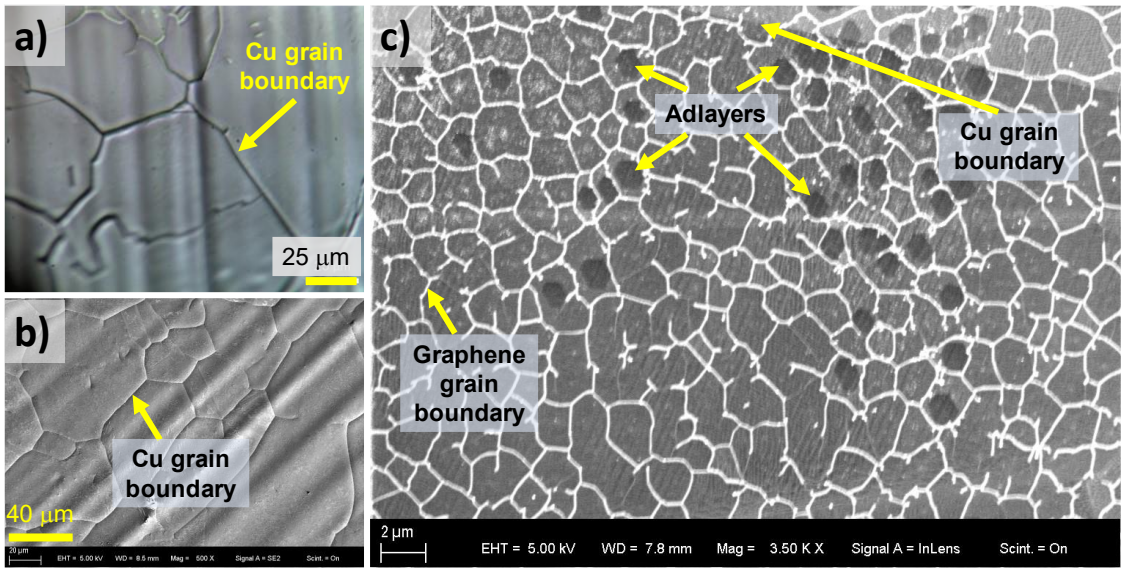

Figure 4.7a) and b) Optical image and SEM image as-grown graphene on copper foil, respectively, copper grain size is clearly shown; and c) graphene grains revealed after graphene on copper foil was oxidised, and adlayers are also shown.

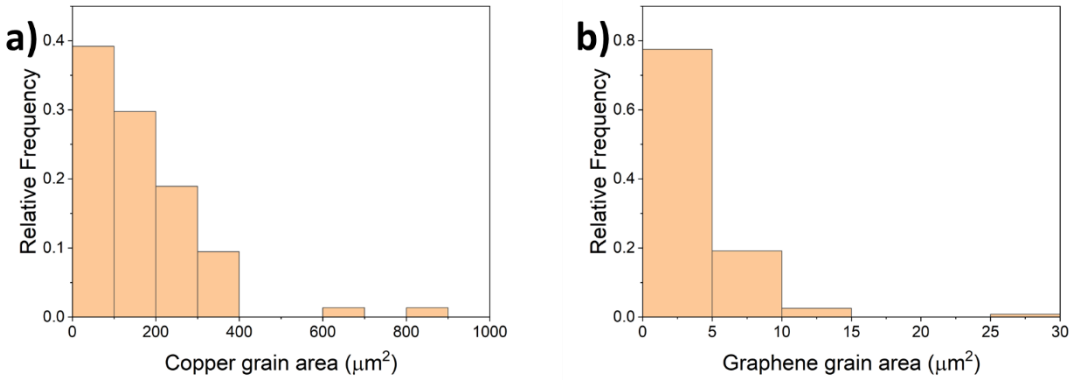

Figure 4.8 a) and b) are histograms of the area distribution for copper grain and graphene grain, respectively.

The graphene transferred onto SiO_2/Si is shown in Figure 4.9a where a continuous film can be observed; some adlayers and polymer residues are also present on the surface of graphene. Figure 4.9b shows a commercial brand graphene sample; adlayers and less polymer residue are found on it. By visualising both samples, they look very similar, and probably the adlayers on commercial brands are uniformly spaced between them; however, in our sample they are more randomly positioned but smaller than the commercial ones.

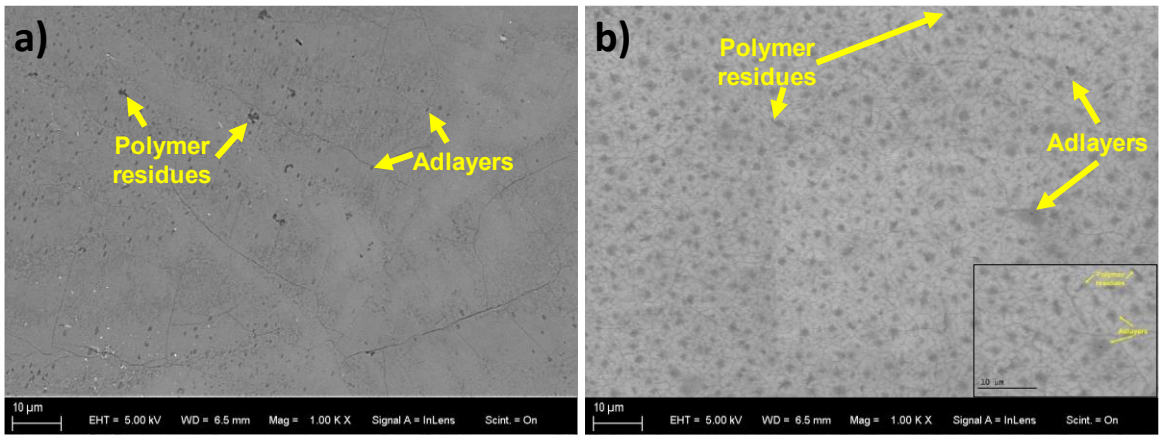

Figure 4.9 SEM image compares a) our synthesised graphene and b) commercial brand graphene onto SiO_2/Si (inside zoom over polymer residues and adlayers).

4.3 Transmission electron microscopy (TEM).

Graphene film was transferred onto a holey carbon TEM grid using PMMA as a supporting layer. The darker spots in Figure 4.10a indicate the presence of polymer residues; continuity of the film over a 4 μm^2 area can be observed. We have intentionally selected this area to distinguish between graphene and holey carbon films. Figure 4.10b shows the selected area electron diffraction (SAED) pattern, which, as expected for monolayer graphene, is the typical hexagonal pattern. The inset figure illustrates the intensity profile through the dashed line, as the inner points are more intense than the outer ones, so the presence of monolayer graphene can be confirmed.[127] The Miller–Bravais indices (*hkil*) for graphite reflections were used to label the peaks so that the innermost hexagon and the next one corresponds to indices (0–110) (2.13 Å spacing) and (1–210) (1.23 Å spacing), respectively.

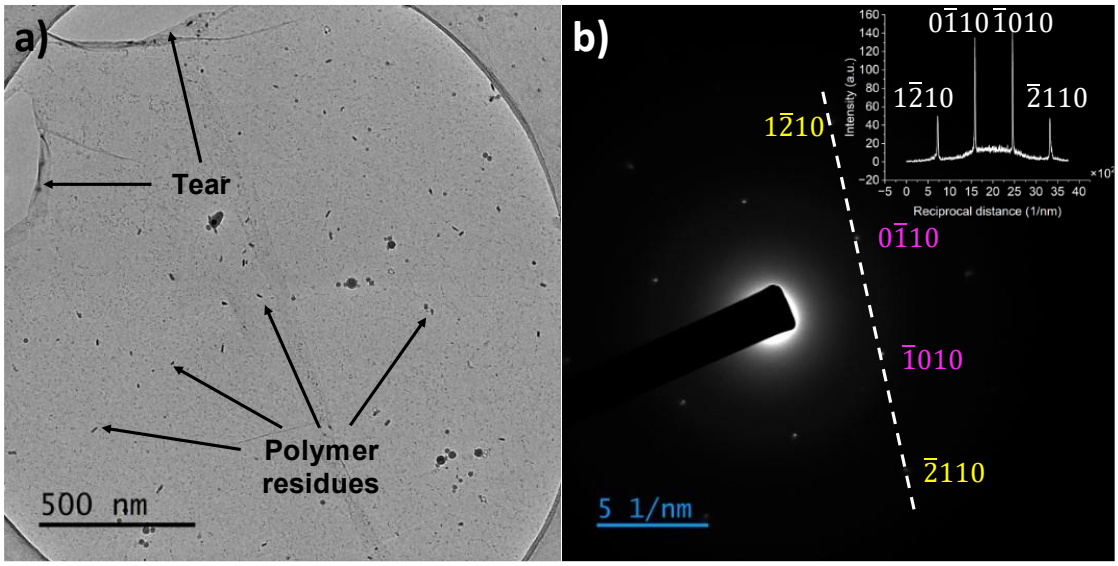

Figure 4.10 a) TEM image of monolayer graphene on TEM grid, b) SAED pattern, inset profile along the dashed line confirm monolayer graphene.

Figure 4.11 shows HRTEM image of graphene area that reveals the honeycomb structure of graphene with the typical interlayer distance of ~0.246 nm.

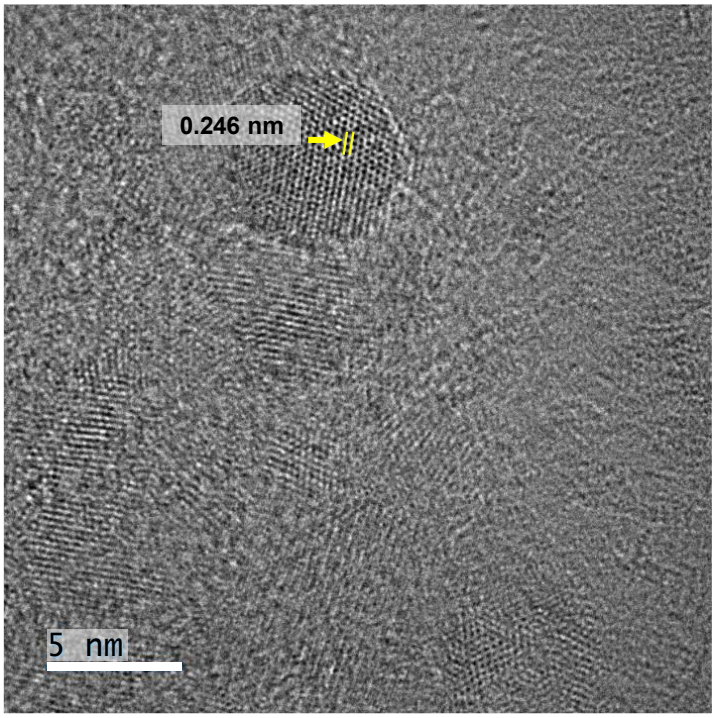

Figure 4.11 High-resolution TEM image of graphene sample. The honeycomb lattice is observed.

4.4 Atomic force microscopy (AFM).

Figure 4.12a shows an AFM image of the graphene film on SiO_2/Si transferred with the PMMA method; the darkest spots are PMMA residues which are up to 56 nm high, and the average graphene grain size is in the range of 0.9 μm, as seen in SEM. The graphene thickness was measured in non-contact mode AFM; it is 1.33 nm, as demonstrated in Figure 4.12b. Although theoretically, the monolayer graphene thickness should be 0.34 nm, the experimental measurements could be in the range of 0.7-1.8 due to variations induced by interactions such as graphene-substrate and graphene-AFM probe.[132,133,185] This was also confirmed by TEM analysis in Figure 4.10b.

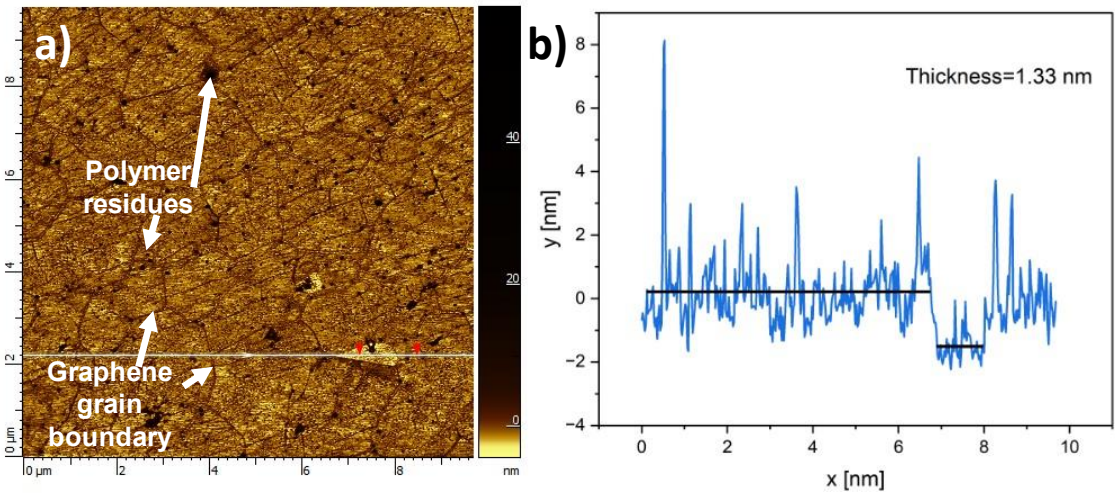

Figure 4.12 a) AFM image and b) thickness measurement between the two red marks across the white line.

4.5 Raman spectroscopy.

Raman spectroscopy is a quick and non-destructive method for analysing graphene. Its spectrum can be used as a unique identifier for analysing graphene grown by CVD. However, its interpretation must be carefully considered as it is sensitive to strain,[186–189] doping[190,191] and chemical functionalisation.[192,193]

Monolayer graphene shows a characteristic spectrum in which three peaks can be identified and used for quality assessment. The D peak at ~1350 cm^{-1} is caused by the breathing mode of the six-atoms ring and is activated by defects such as grain boundaries, imperfect stitching and sp^3 hybridization.[194,195] The G peak at ~1580 cm^{-1} corresponds to the in-plane bond-stretching motion of pairs of sp^2 carbon and does not require the presence of a six-folded ring.[196] The peak at ~2700 cm^{-1} is caused by a second-order

overtone of the D band. Since the 2D band for graphene can be fitted to a single Lorentzian peak, it can be used as a distinctive fingerprint to distinguish between single and multilayer graphene.[147] Figure 4.13a shows a typical monolayer graphene Raman spectrum exhibiting the characteristic bands for graphene: G (~1583 cm^{-1}) and 2D (~2678 cm^{-1}) bands, with no apparent D peak. Figure 4.13b shows the case for minimally defective graphene, exhibiting a small D band (~1340 cm^{-1}).

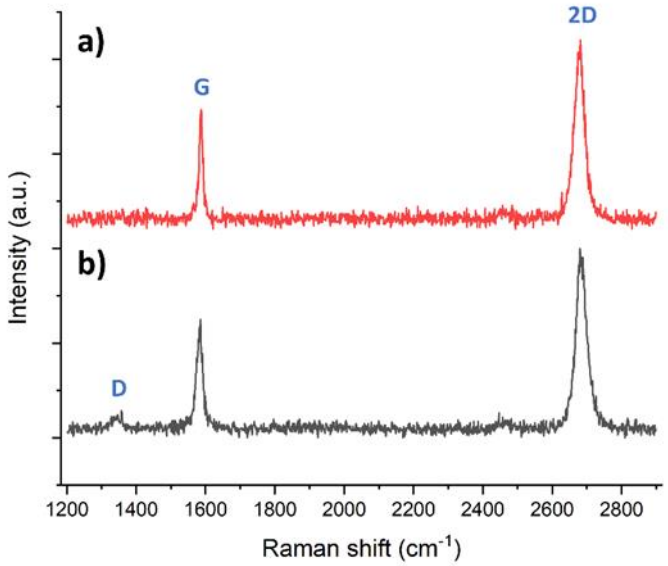

Figure 4.13 Typical point Raman spectra of a) defect-free graphene and b) minimally defective graphene using a 532 nm laser excitation wavelength showing the main peaks of graphene that were fitted.

The UK National Physical Laboratory (NPL), an international leader in graphene standardisation, has proposed the full width at half maximum (FWHM) of the 2D peak as a parameter for identifying monolayer graphene.[160,197] As suggested from the NPL guidelines, a FWHM 2D $\leq$ 35 cm^{-1} is typical for monolayer graphene on SiO_2/Si, based on experimental observations.[64,191,198,199] However, it is worth noting that a turbostratic stacking of graphene layers can also be represented by a single Lorentzian peak, with (FWHM) of 2D $\leq$ 35 cm^{-1}, similar to that of single layer graphene.[200] Nevertheless, our TEM findings indicate that graphene is predominantly monolayer. Also, the I_{2D}/I_G > 2.0 ratio is characteristic of single-layer graphene and an indicator of low level of doping.[201] Consequently, upon verification through TEM observations, these two metrics can be employed for the identification of graphene via Raman spectroscopy.

We examined five specific areas labelled A, B, C, D, and CC, as illustrated in Figure 4.14. This enables us to capture variations caused by changes in gas flow if any. Given that the average grain size is approximately 3.4 μm^2, our objective was to determine the minimum sampling area required to obtain statistically meaningful results from the entire sample. Consequently, we acquired data from a large map consisting of 1024 spectra (32 μm × 32 μm in 1 μm step), so on average we were sampling around 301 graphene grains. Here, we used the methodology described by Turner *et al.*,[197] where the FWHM 2D and the I_{2D}/I_G ratio are the parameters of interest. For calculations D, G, and 2D peaks were fitted in OriginPro 2022b[202] using a Lorentzian function and the fit bounds suggested by Turner *et al.*[197] Cosmic rays on the CCD detector were manually removed and spectra were normalized to 1 with respect to the intensity of the 2D peak.

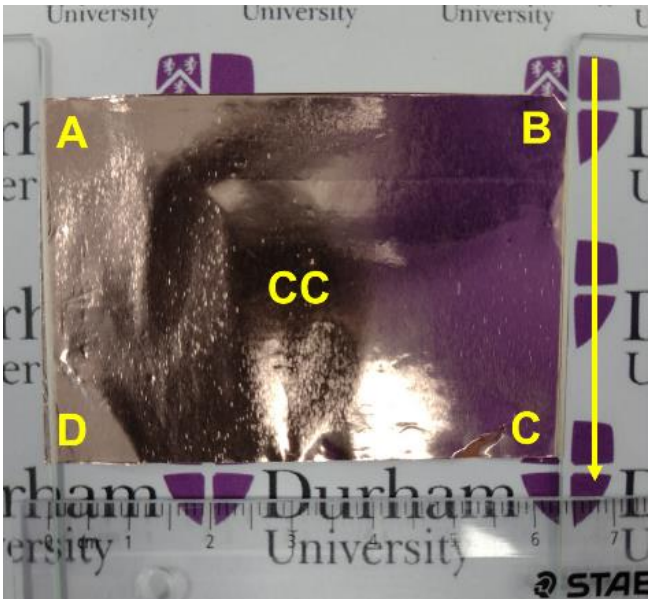

Figure 4.14 Graphene on copper foil showing where the samples were taken. The yellow arrow indicates the flow direction of the carbon source in the growing process.

First, a large map (32 μm x 32 μm in 1 μm steps, Figure 4.15a) was measured and processed. The 1024 spectra from this map were fitted in OriginPro 2023b;[161] in brief, the data were imported in a .txt format and reshaped the Raman map into an XYY (X Raman shift and Y intensity of each spectrum) format. Cosmic rays were manually removed, and all spectra were normalised respect to the 2D peak to further fitting. D, G, and 2D peaks were fitted between the bonds specified in Table 4-1 and using a Lorentzian peak function

within the peak analyser option in OriginPro software.[197] The mean of the 1024 spectra analysed was 26.2 cm^{-1} for 2D FWHM and 2.4 for the I_{2D}/I_G ratio.

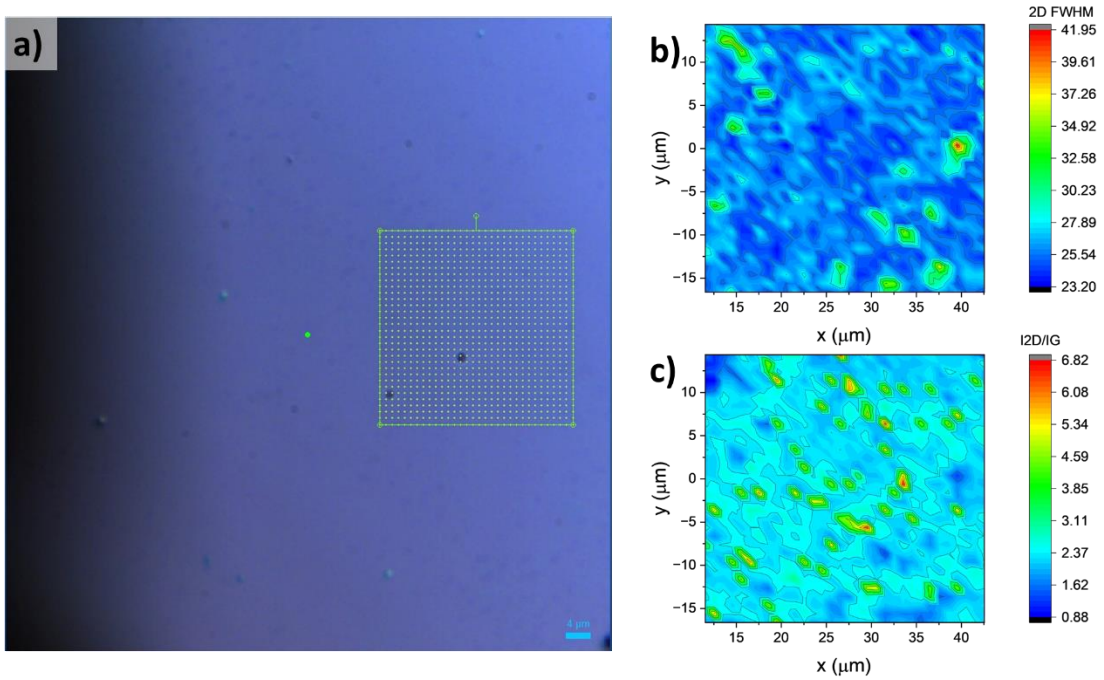

Figure 4.15 a) Optical image of graphene on SiO_2/Si the green square represents the map area, a large area Raman b) 2D FWHM and c) I_{2D}/I_G map.

Table 4-1 The Lorentzian peak fit bounds used to fit all spectra using OriginPro.[197]

Peak	Fit metric	Lower bound (cm^{-1})	Upper bound (cm^{-1})
D	Peak centre	1250	1450
	FWHM	1	100
	Area	1	100
G	Peak centre	1480	1680
	FWHM	1	100
	Area	1	100
2D	Peak centre	2600	2800
	FWHM	1	100
	Area	1	100

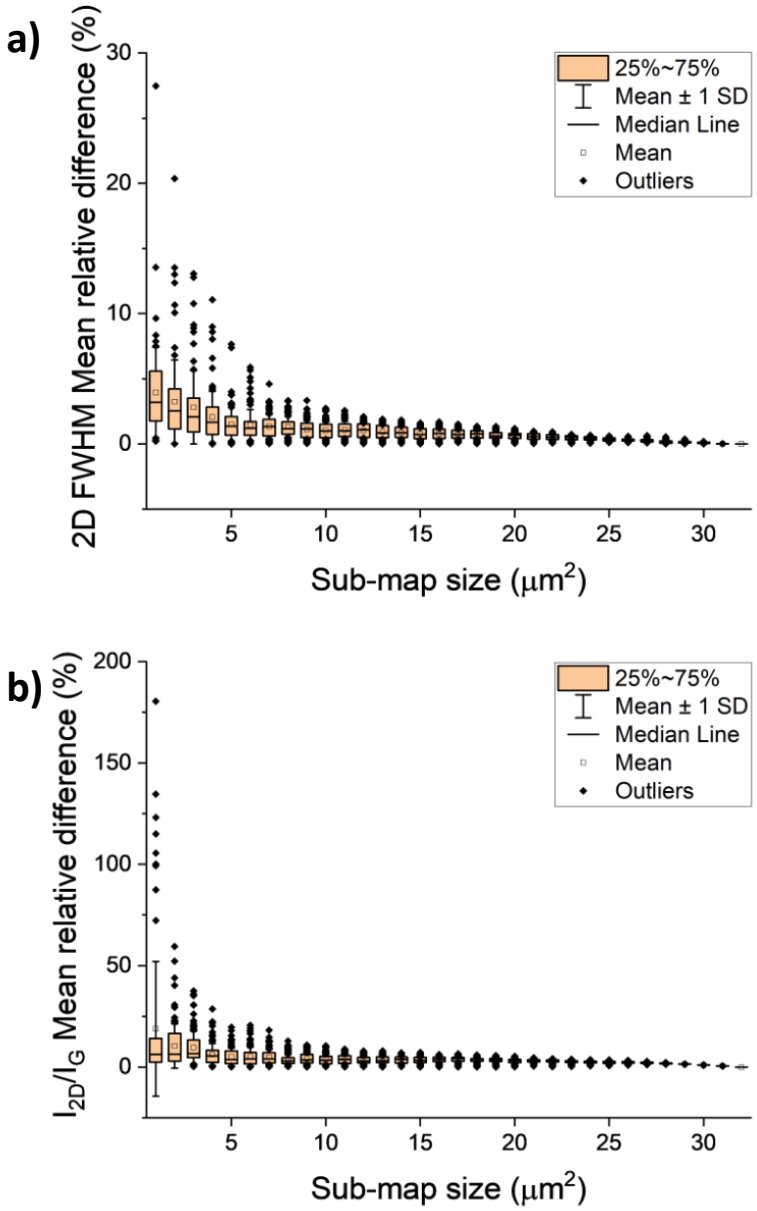

Figure 4.16 The mean relative difference between the mean in each sub-map with respect to the mean in the large area map for a) 2D FWHM and b) I_{2D}/I_G ratio, as a function of sub-map size.

We use the procedure described by Turner *et al.*[197] to determine the optimum size for the Raman map for each sample; the large map was split into smaller sub-maps with sizes ranging from 1 × 1 to 32 × 32 μm^2 and 1 μm steps. A random position was selected for each submap, from which a square of the desired size was traced with that point as the upper left corner. For every sub-map size, 100 sub-maps were created at random positions throughout the large area map using MATLAB[203] code (Appendix B), and the mean values

of the FWHM 2D and I_{2D}/I_G ratio were calculated. Finally, the relative difference between the mean values of each sub-map and the large area map was computed as a function of sub-map size and summarized in Figure 4.16a and b, respectively. It was observed that for maps 13 × 13 μm^2, the relative difference with respect to the large map is 0.9 %, which is an acceptable error given the fewer spectra collected.

Five pieces of graphene of ~1 × 1 cm^2 from different positions A, B, C, D, and CC (Figure 4.14) were transferred to SiO_2/Si substrates by PMMA method. Statistical analysis was conducted on a 13 × 13 μm^2 map recorded for each position in 5 independent batches. Each Raman spectrum was fitted using Lorentzian fitting and were considered monolayer if the 2D FWHM is less than 35 cm^{-1} and the I_{2D}/I_G ratio more than two according to the conditions used by Turner *et al*.[197] The G and 2D peaks are observed for all recorded spectra, and only a minimal number of spectra showed the presence of a small D peak, suggesting a graphene film with very few defects. To perform a comparative analysis, we compared our samples with two commercially available ones obtained from different suppliers under identical mapping conditions. The suppliers claim that these samples consist mainly of single monolayer graphene, as per the information provided.

By measuring the standard deviation from the background, $\sigma_{background}$, in all normalized spectra in a region 1800-2200 cm^{-1} where no signal is shown it is observed that in all batches the D band have a minimal intensity, the same magnitude as the background $\mu+\sigma_{background}$, where μ is the average signal in this range and the $\sigma_{background}$ its standard deviation (See Table B1). Moreover, D intensities from the average spectrum are comparable with those of commercial brands, suggesting that graphene films have a low defect density. Appendix B Figures B1 - B6 show all Raman spectra collected for each sample from each batch and the two commercial brands.

Figure 4.17 to Figure 4.22 show the Raman maps for the spatial distribution of FWHM 2D for each position and batch. According to the FWHM 2D, most of the scanned area can be considered monolayer graphene. The largest FWHM 2D obtained is 45.5 cm^{-1}; it is presented just in small areas in only two samples (CC position batches 2 and 3), while the lowest value is 21.8 cm^{-1}. The varied values observed may be attributed to the p-doping effects caused by ferric chloride during the copper etching process.[204] From Figure 4.23 to Figure 4.28, samples show higher I_{2D}/I_G ratios than the commercial product; the 2D peak intensity is almost twice the intensity of the G peak, and the highest ratio is 6.4 and the lowest 0.62.

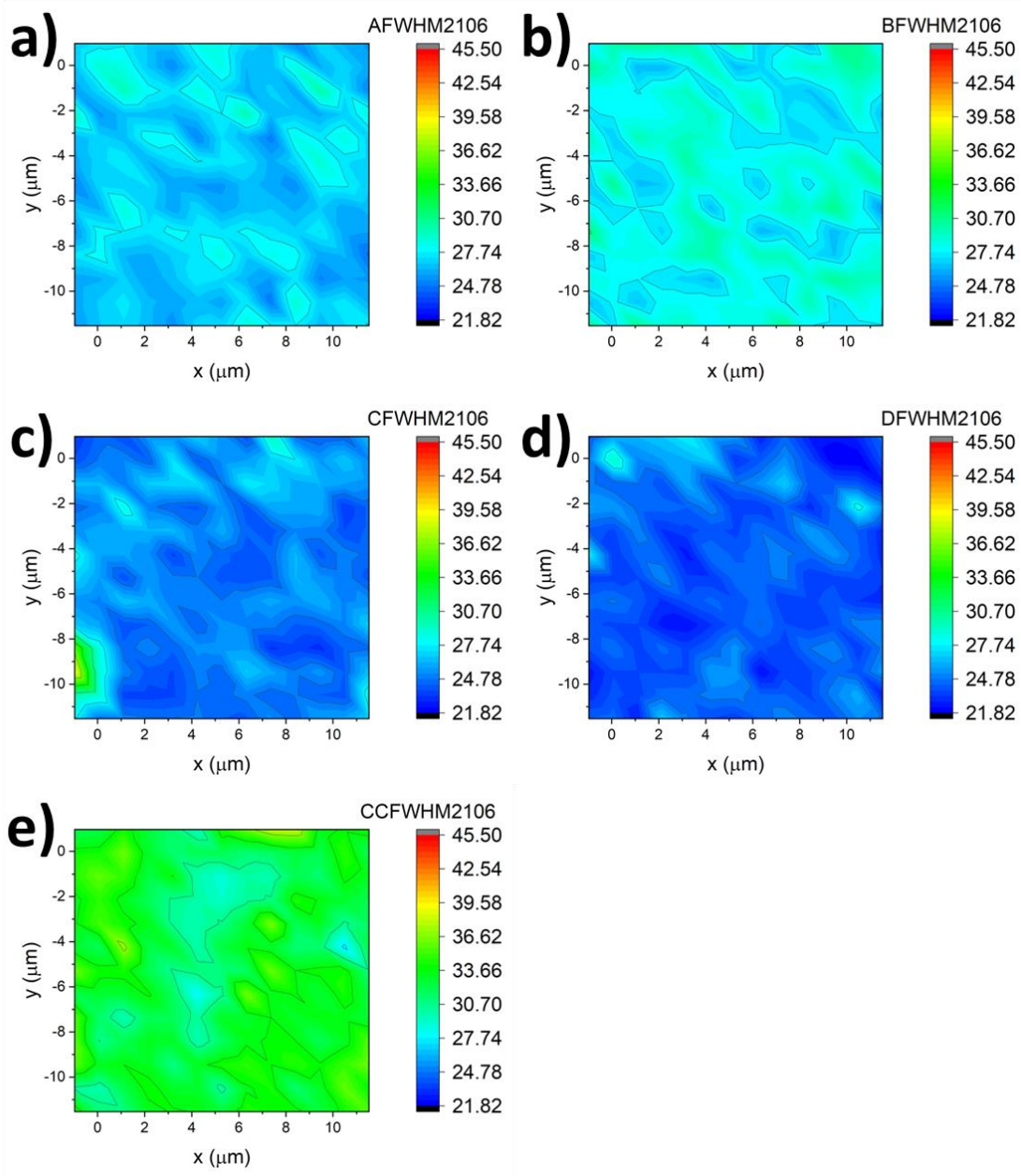

Figure 4.17 Raman maps of 2D peak FWHM for each position of batch one. Mapping areas of samples are 13 × 13 μm² with one μm step.

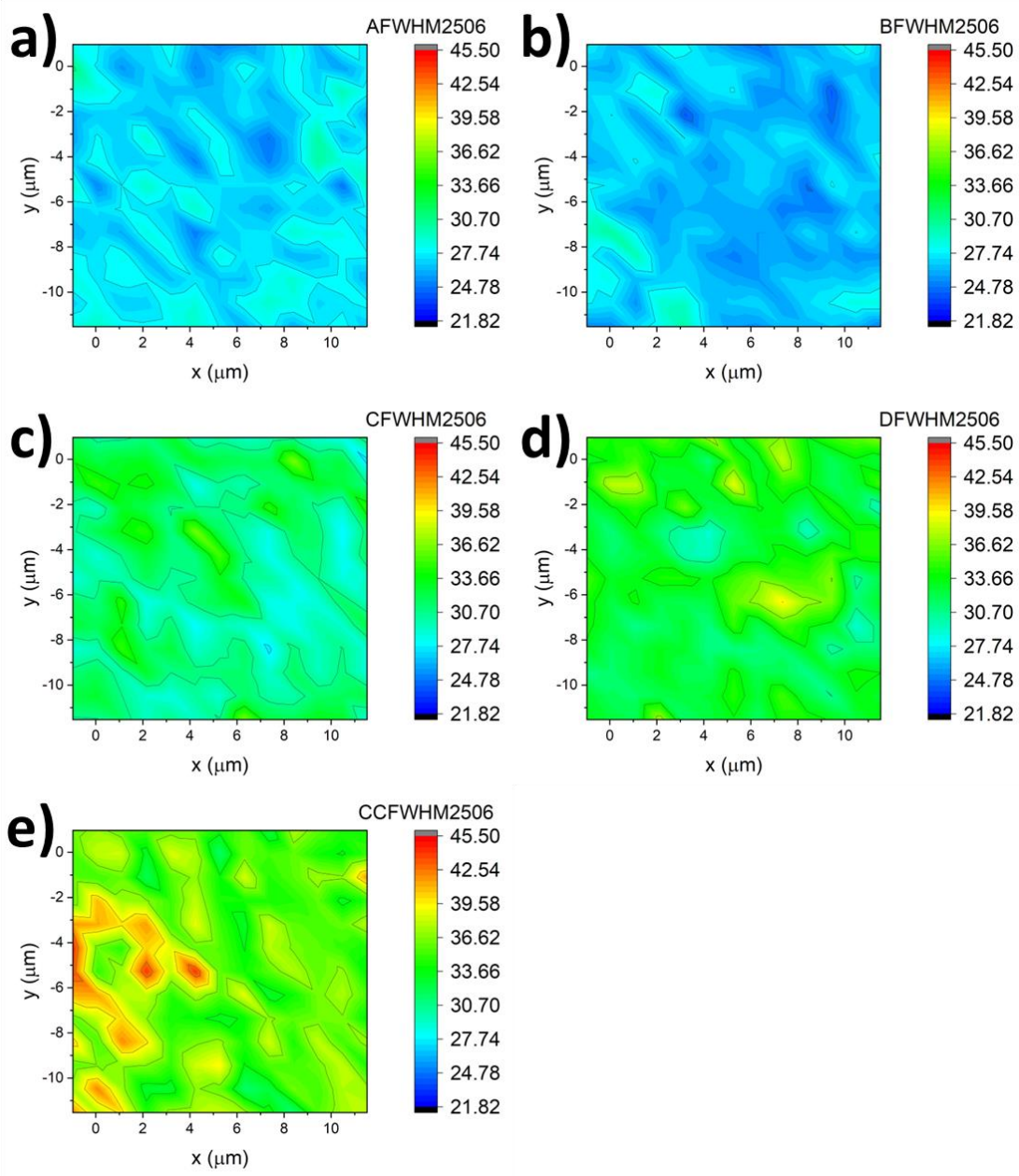

Figure 4.18 Raman maps of 2D peak FWHM for each position of batch two. Mapping areas of samples are 13 × 13 μm² with one μm step.

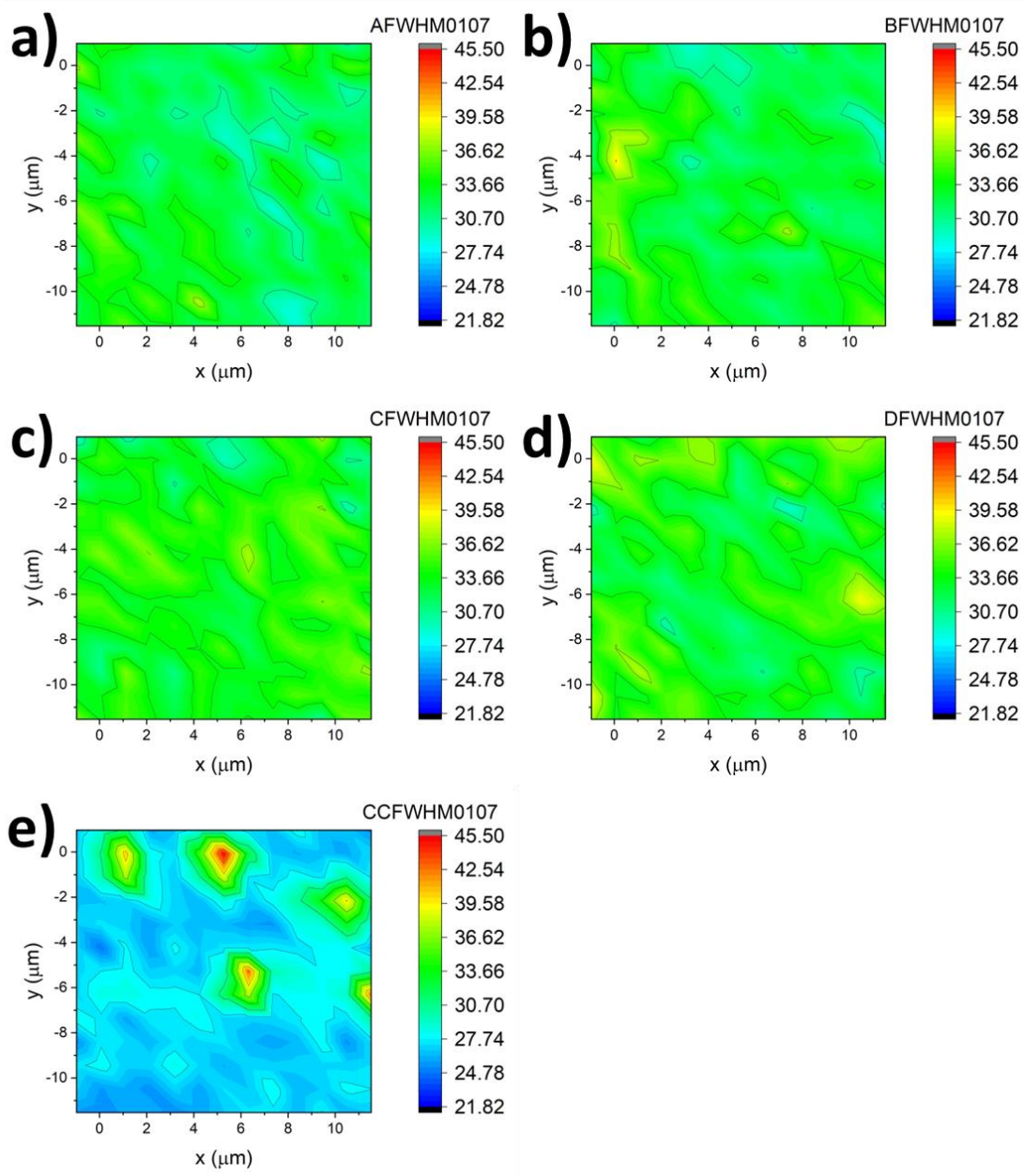

Figure 4.19 Raman maps of 2D peak FWHM for each position of batch three. Mapping areas of samples are 13 × 13 μm² with one μm step.

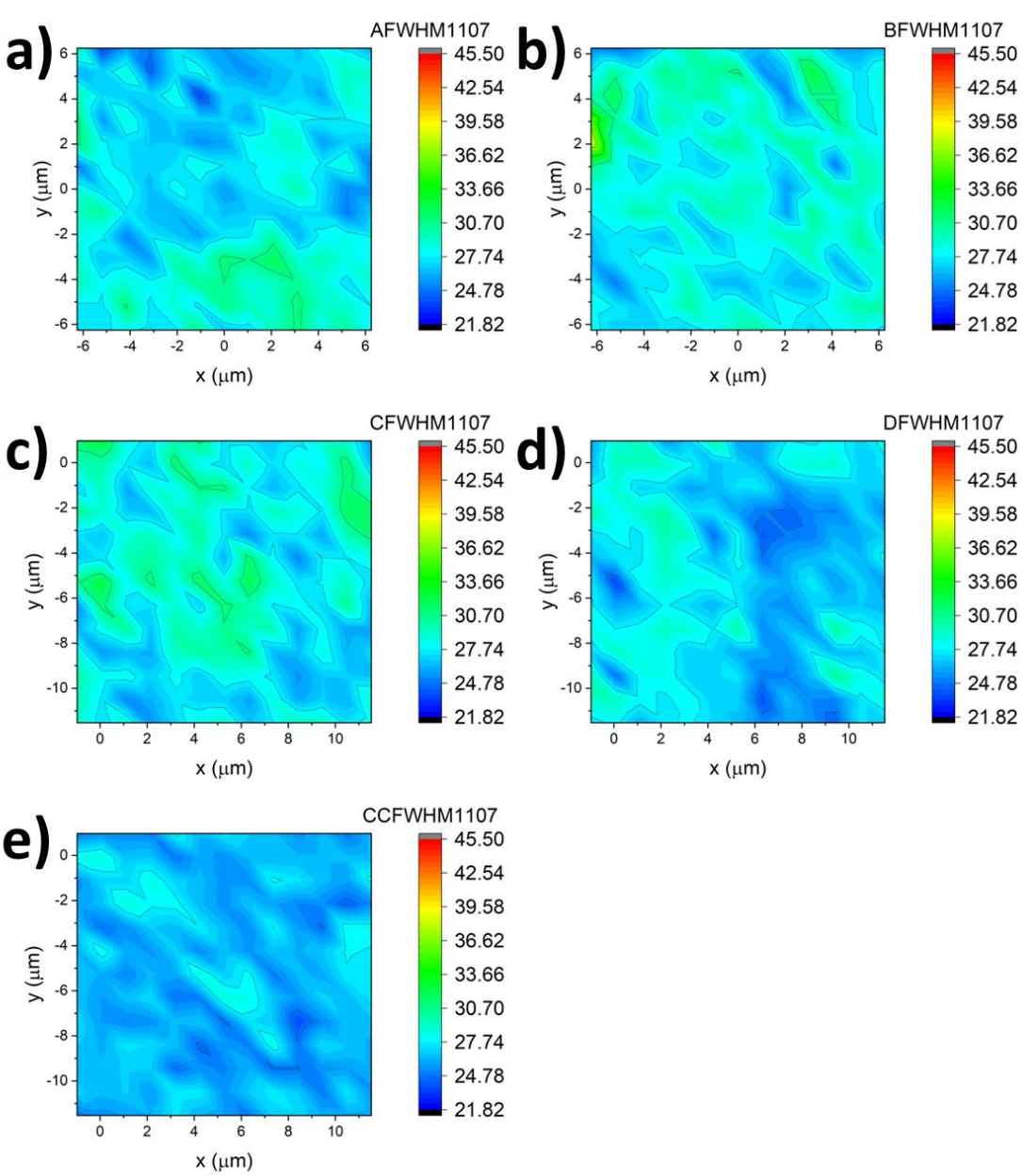

Figure 4.20 Raman maps of 2D peak FWHM for each position of batch four. Mapping areas of samples are 13 × 13 μm² with one μm step.

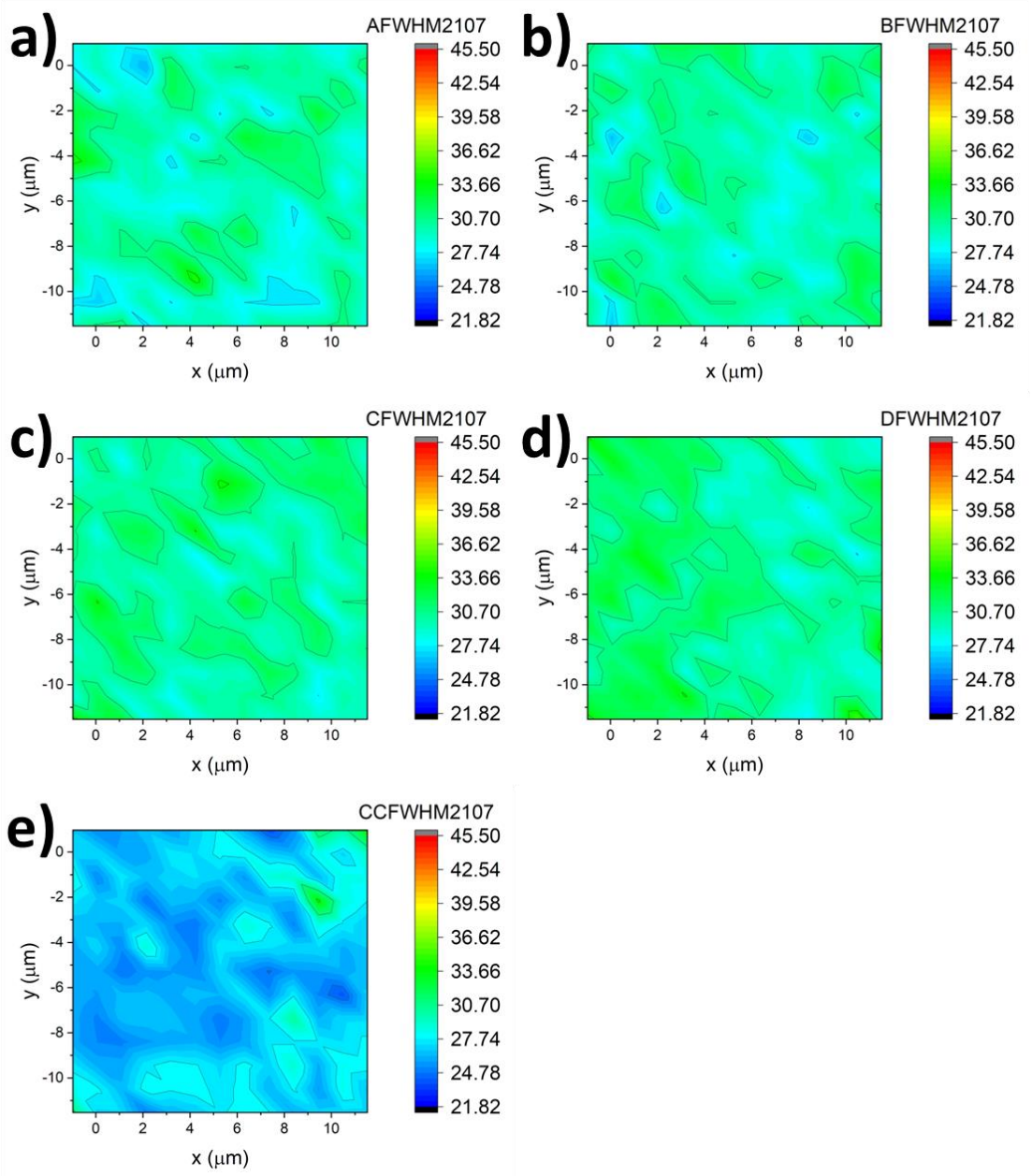

Figure 4.21 Raman maps of 2D peak FWHM for each position of batch five. Mapping areas of samples are 13 × 13 μm² with one μm step.

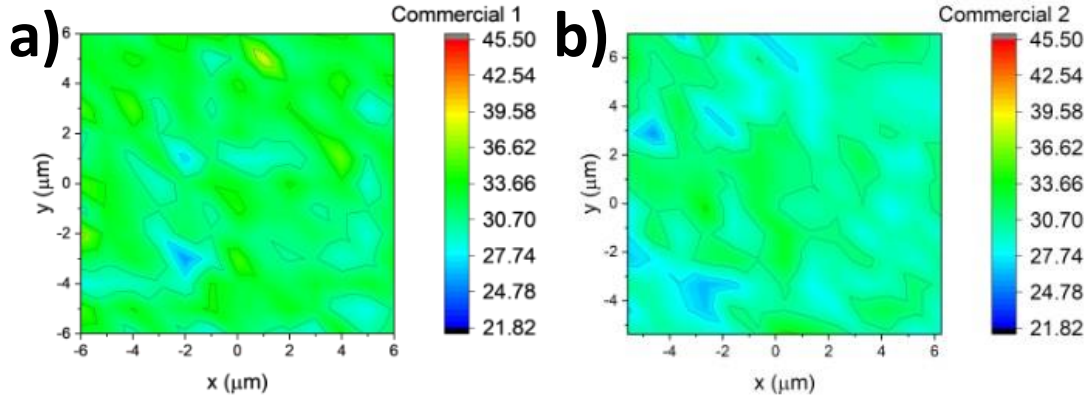

Figure 4.22 Raman maps of 2D peak FWHM from two commercial brands. Mapping areas of samples are 13 × 13 μm² with one μm step.

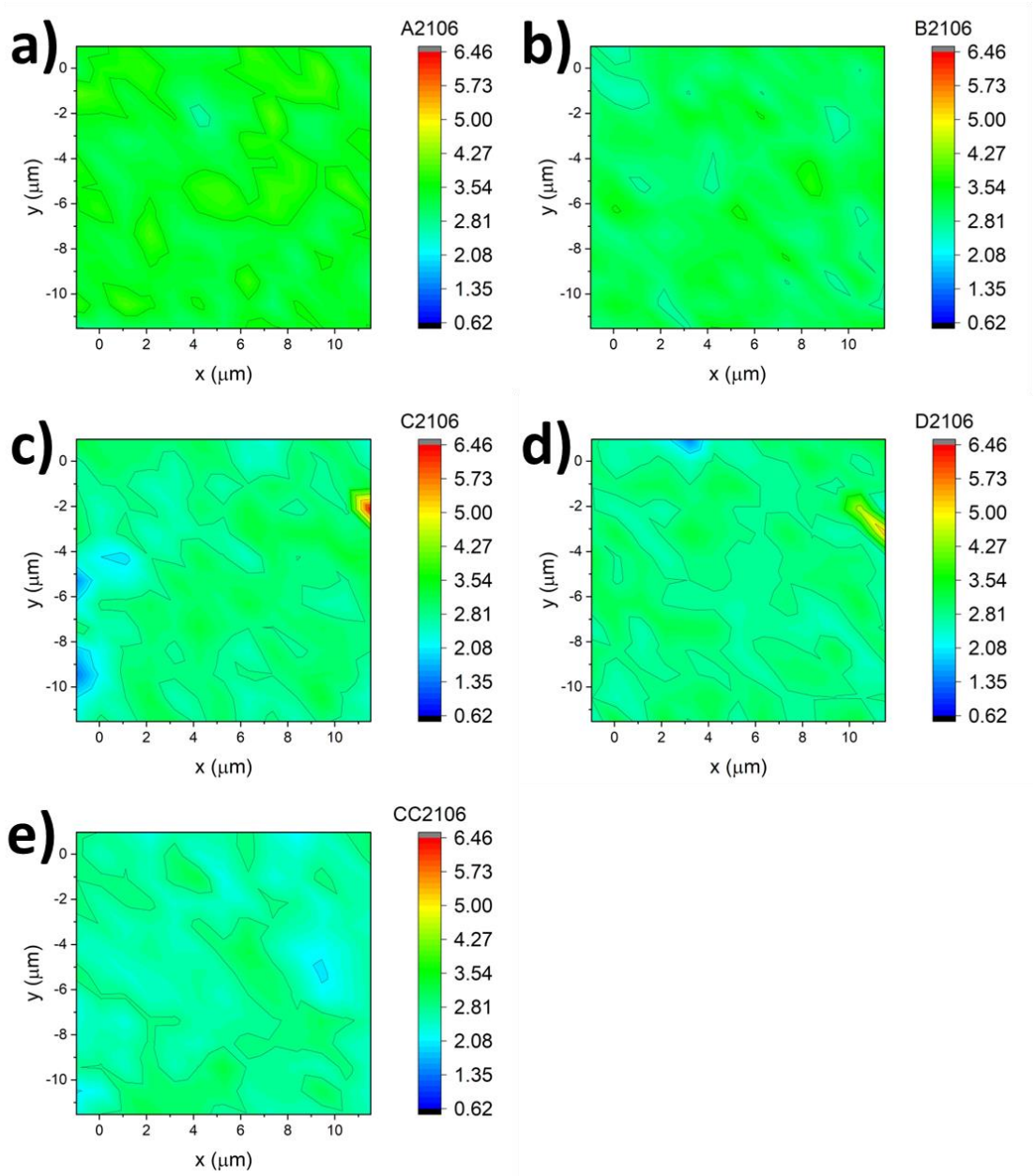

Figure 4.23 Raman maps of I_{2D}/I_G ratios for each position of batch one. Mapping areas of samples are 13 × 13 μm² with one μm step.

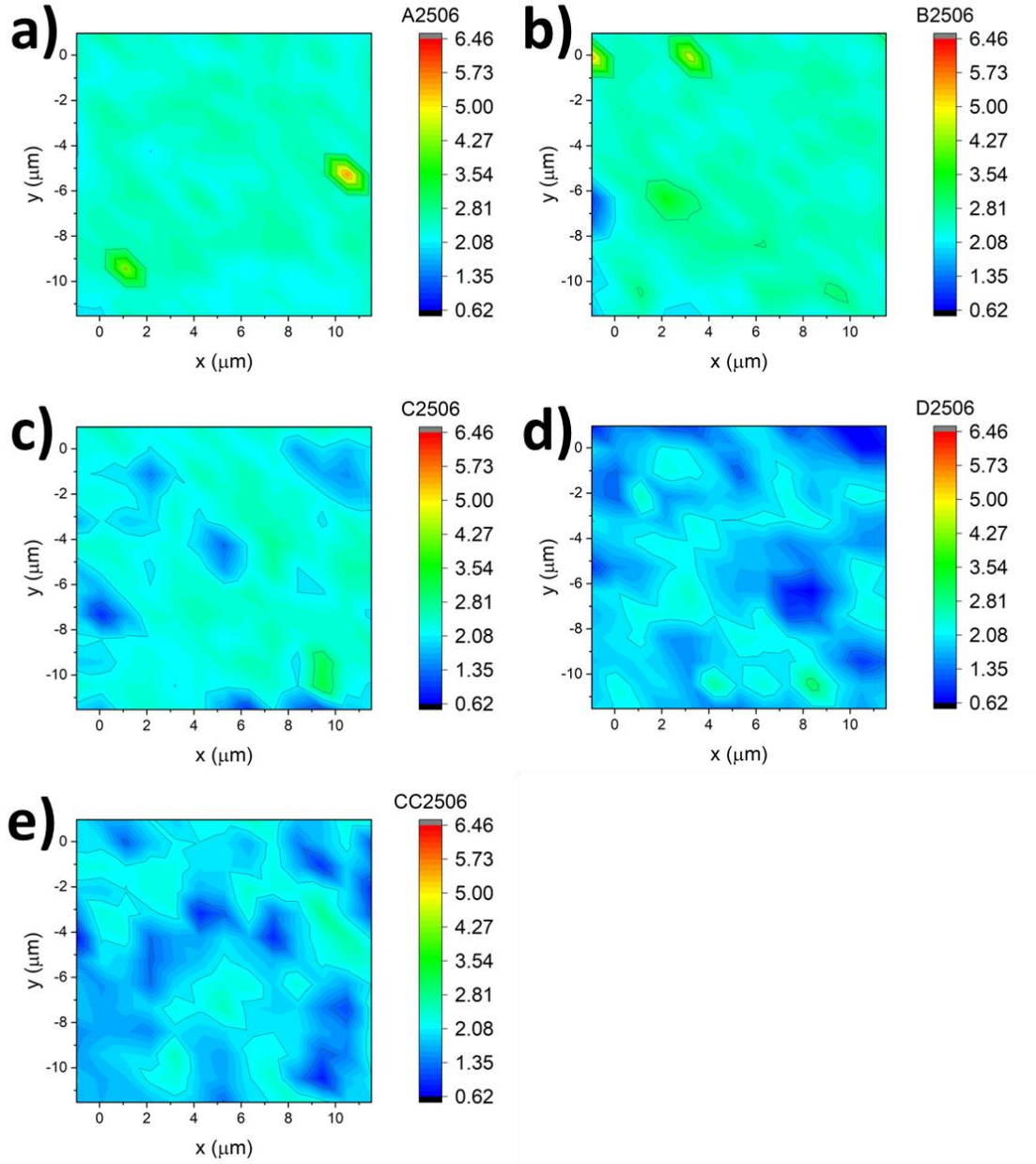

Figure 4.24 Raman maps of I_{2D}/I_G ratios for each position of batch two. Mapping areas of samples are 13 × 13 μm² with one μm step.

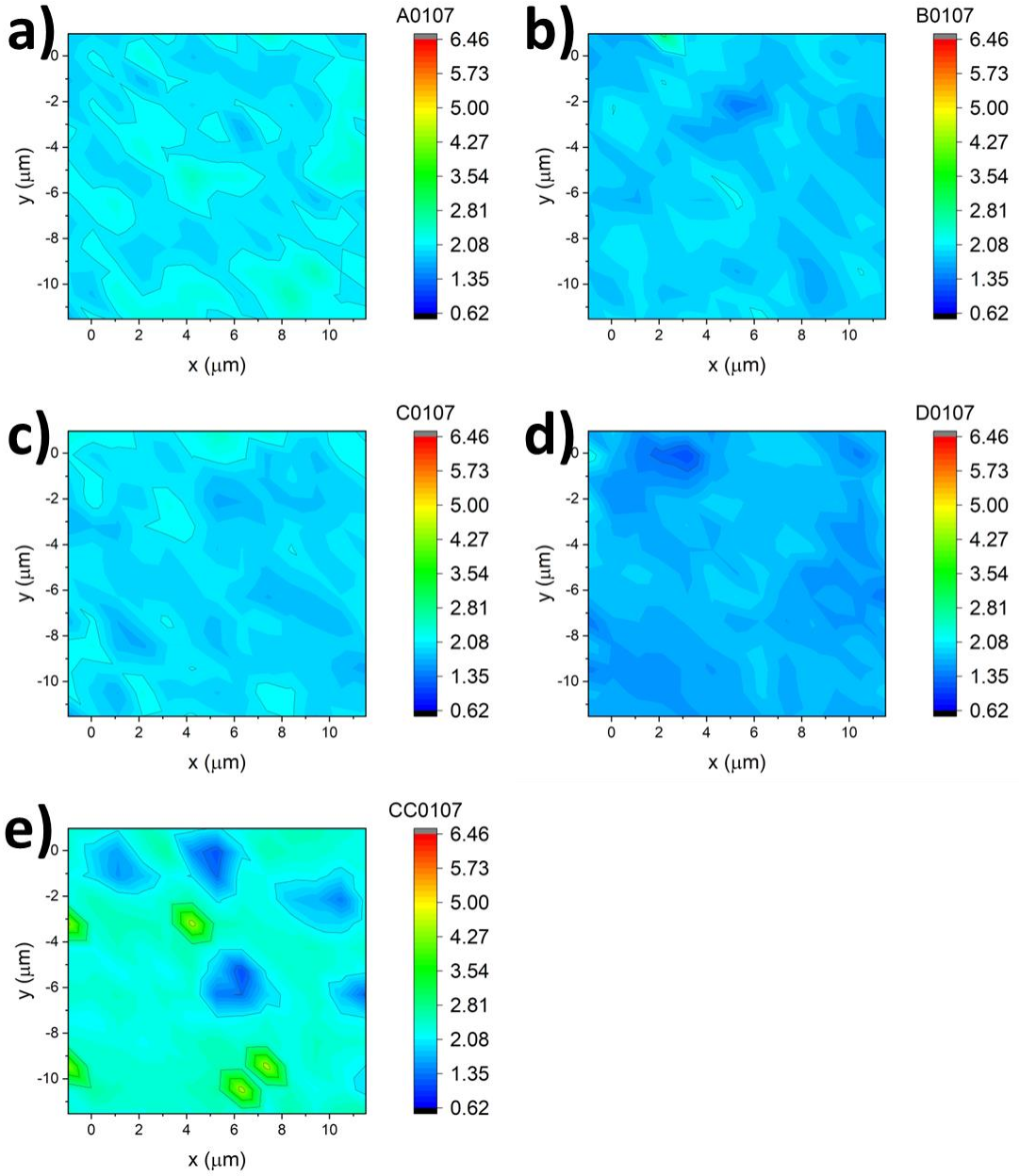

Figure 4.25 Raman maps of I_{2D}/I_G ratios for each position of batch three. Mapping areas of samples are 13 × 13 μm² with one μm step.

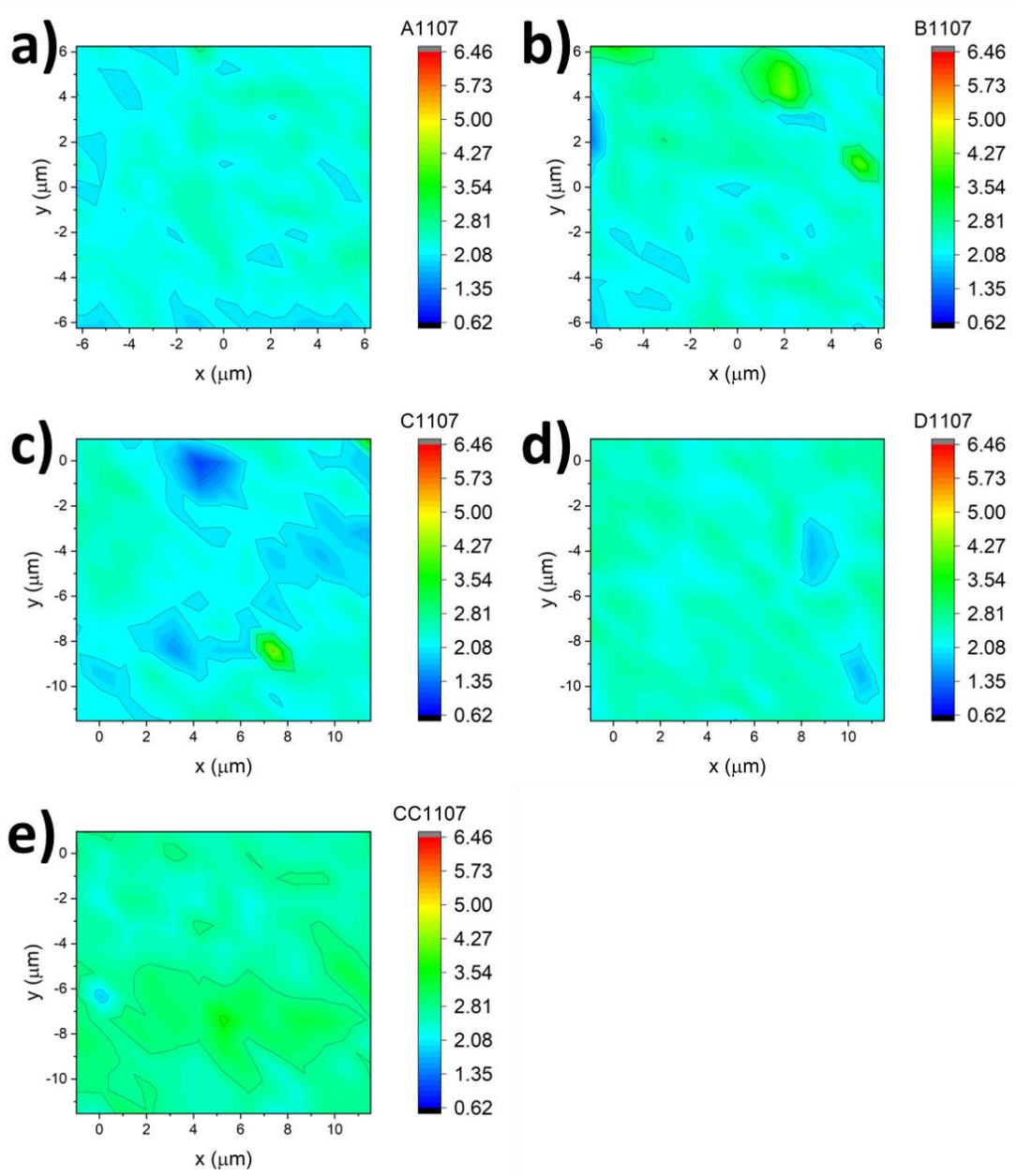

Figure 4.26 Raman maps of I_{2D}/I_G ratios for each position of batch four. Mapping areas of samples are 13 × 13 μm² with one μm step.

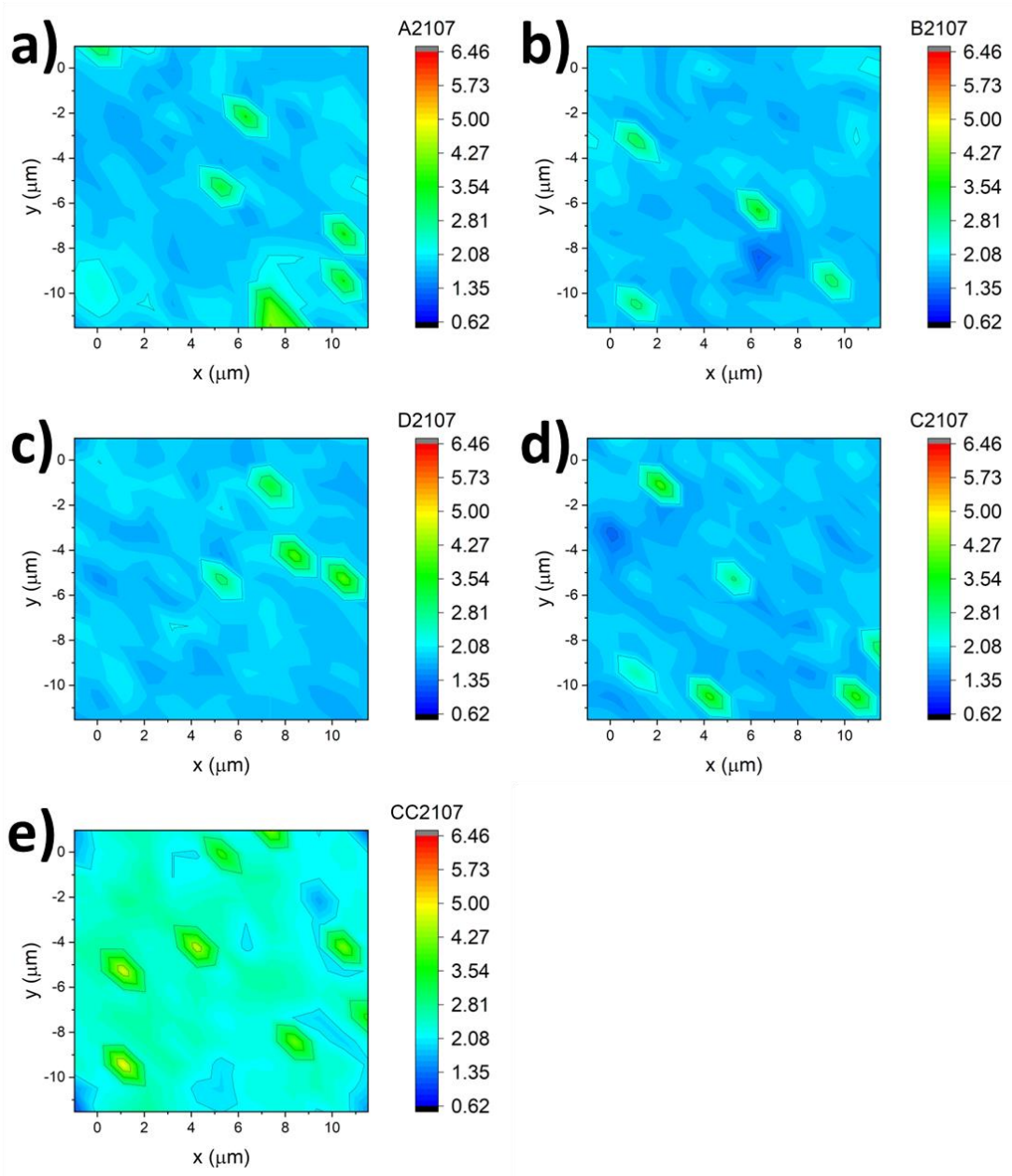

Figure 4.27 Raman maps of I_{2D}/I_G ratios for each position of batch five. Mapping areas of samples are 13 × 13 μm² with one μm step.

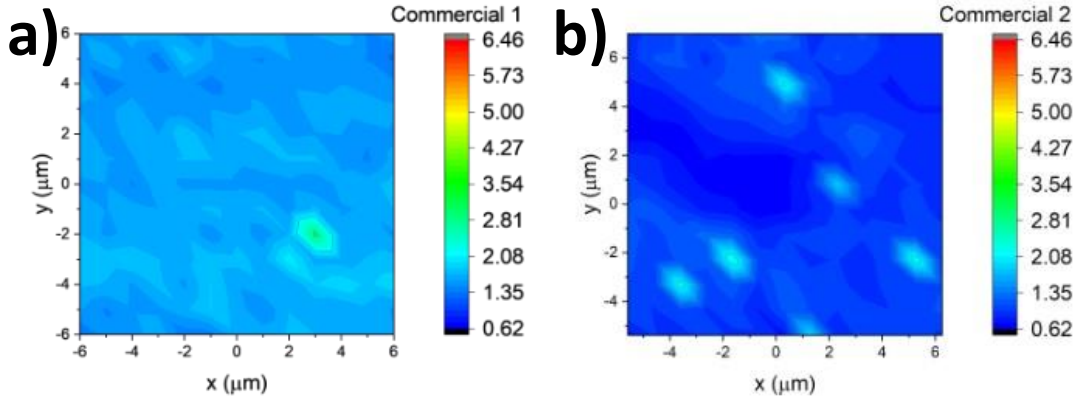

Figure 4.28 Raman maps of I_{2D}/I_G ratios for two different commercial brands. Mapping areas of samples are 13 × 13 μm² with one μm step.

The data presented in Figure 4.17 to Figure 4.28 has been summarised in box plots (Figure 4.29a and b). By establishing a threshold of 35 cm^{-1} for the FWHM of the 2D peak, it can be observed that, with the exception of sample CC250622 from batch 2, the average FWHM 2D value of all the samples falls below this threshold. The mean value of 36 cm^{-1} for the sample CC250622 slightly exceeds the predetermined threshold. Moreover, the absence of any correlation between the different positions and the assessed metrics implies the existence of alternative factors, such as random strain fluctuations and unintentional doping from ferric chloride.[187,204]

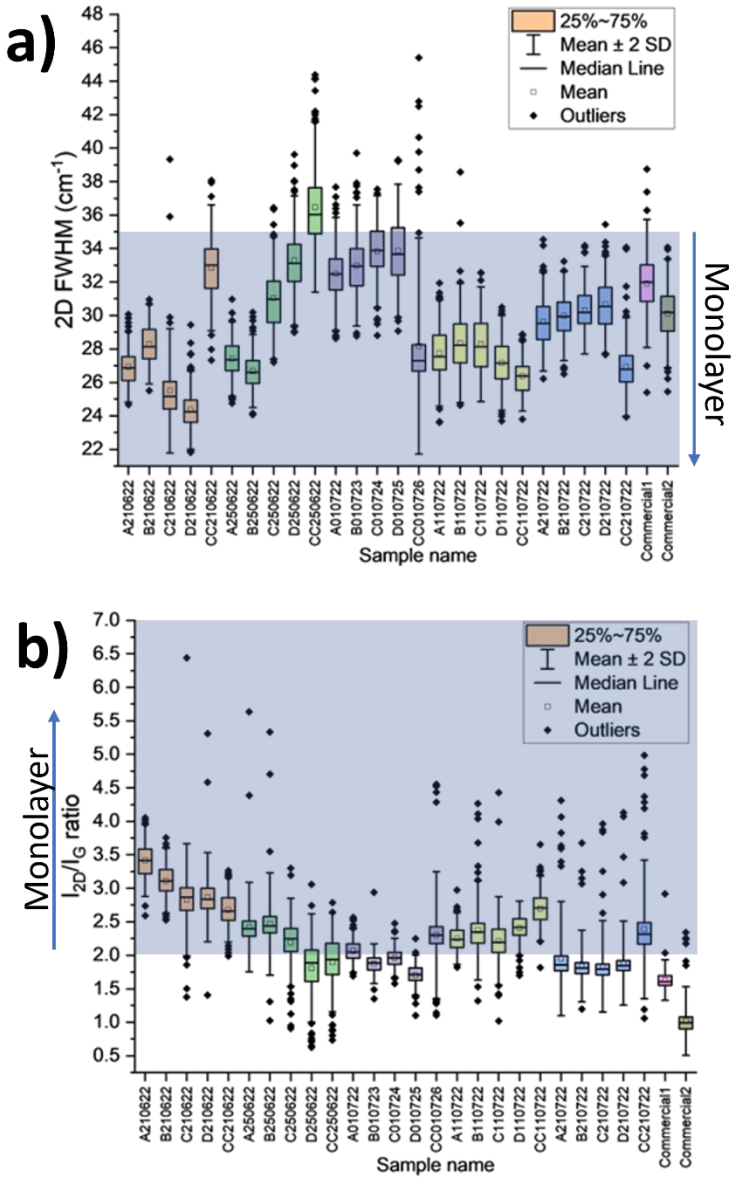

Figure 4.29 Data variations for each sample and the two commercial brands: a) 2D peak FWHM and b) I_{2D}/I_G peak ratio.

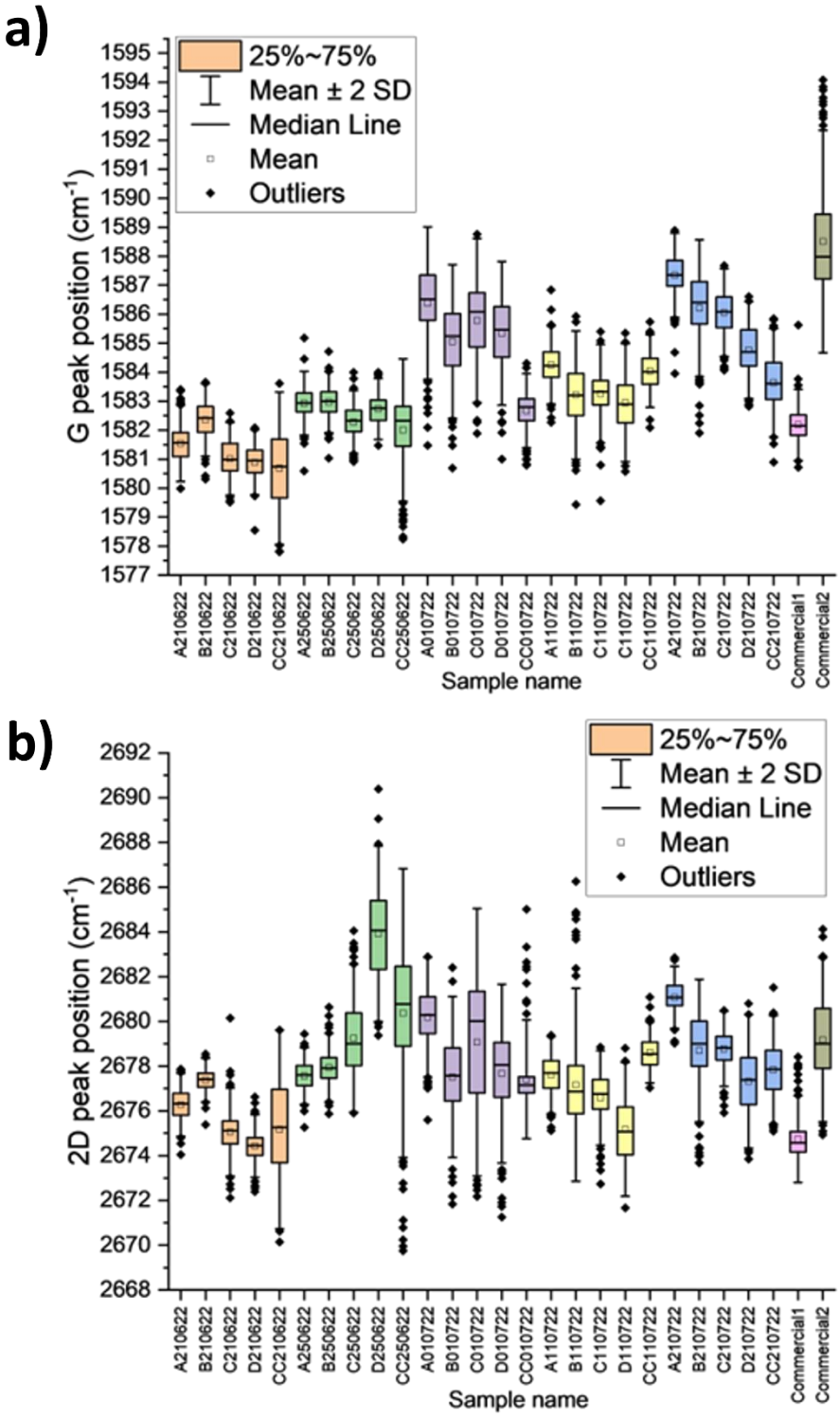

Figure 4.30 Data variations for each sample and the two commercial brands, a) G peak position and b) 2D peak position.

The relationship between doping and the I_{2D}/I_G ratio has been widely demonstrated, showing a substantial reduction in this ratio with higher levels of doping.[190,201] Also, the nanometre strain variations in the lattice of graphene can cause the G and 2D bands a shift with respect to the reference unstrained and undoped graphene.[187,205] Hence, the positions of the G and 2D bands may be influenced by strains resulting from the difference in the thermal expansion coefficients of graphene and copper during the cooling process,[206,207] as well as the high stiffness of PMMA, which restricts the stress relaxation.[208] Experimental and theoretical calculations of the Gruneisen parameter report shifts of the G and 2D bands with respect to the strain applied (%ε) as $\Delta PosG/\Delta\varepsilon$ = -57.8 cm^{-1}/% and $\Delta Pos2D/\Delta\varepsilon$ = -140 cm^{-1}/% so under biaxial strain $\frac{\Delta Pos\ 2D}{\Delta Pos\ G} \sim 2.2$.[187,188] Similar findings have been observed for the FWHM of this bands, indicating a ΔFWHM 2D/ ΔFWHM G ratio of approximately ~2.2.[209] Hence, even small strains of approximately ±0.1% can lead to a broad range of FWHM 2D values, similar to what we observed, which also applies for the commercial samples. Figure 4.30a and b show the box plots for the G and 2D peak positions, respectively; also, the FWHM for G peak is reported in Figure 4.31. In summary, this simple process can provide a large area graphene with a quality comparable to that of commercially available brands.

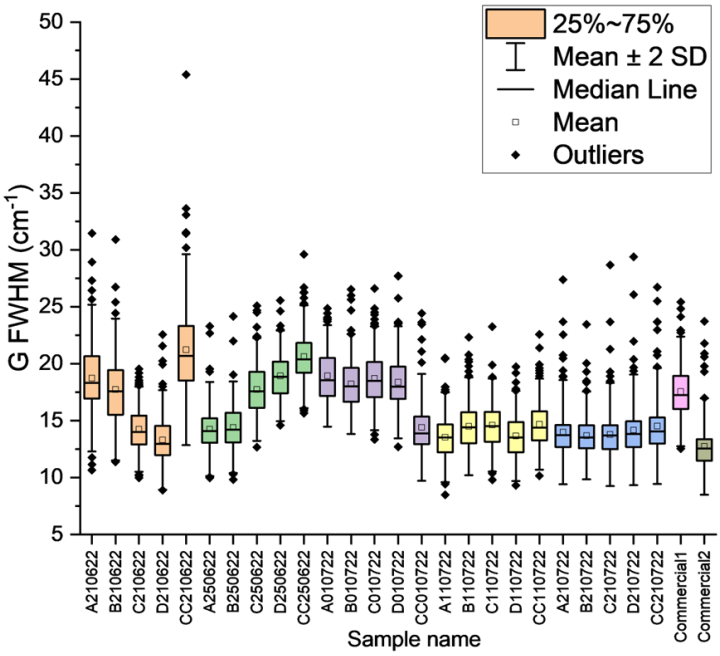

Figure 4.31 G peak FWHM for every sample from each batch and the two commercial brands analysed.

Appendix B figures B1 - B6 show all Raman spectra collected for each sample from each batch and the two commercial brands; the lowest intensities of the D peak in the average spectra indicate the high quality of graphene with negligible defects and is similar to the commercial samples. The total means considering all the data spectra from the 25 samples analysed are 29.6±3.5 cm^{-1} for the 2D FWHM, 2.3±0.5 for the I_{2D}/I_G ratio, 1583.6±2.0 cm^{-1} for the G peak position, 2677.9±2.6 cm^{-1} for the 2D peak position, and 16.0±3.4 cm^{-1} for G FWHM,. The variations between samples from our batches and the two commercial brands used for comparison are summarized in Figure 4.29, Figure 4.30, and Figure 4.31 for each parameter mentioned before. Since no pre-treatment of the metal surface was used to grow graphene, this process can produce a competitive good quality material for research in many laboratories.

4.6 Electrical measurements.

The sheet resistance from five random samples was also computed. A homemade set up for Van Der Paw measurements was used with a four-point probe, as is illustrated in Figure 4.32a,b, and c. Each corner of the sample was in contact with each electrode of the probe, so four configurations are possible by rotating the current source (100 μA) and the positions of the voltage measurements; these four configurations are shown in Figure 4.32d. The resistance was read directly from the instrument, then the average vertical and horizontal resistance was calculated according Eq. 2.8 and Eq. 2.9, respectively. Finally, the sheet resistance (R_s) was calculated by solving Eq. 4.1 using Solver complement from Excel (Generalized Reduced Gradient, GRG, nonlinear numeric method), which is an optimization algorithm used to find the maximum or minimum of a function while taking into account any constraints.[210] All these data are summarized in Table 4-2.

$$e^{-\frac{\pi R_V}{R_s}} + e^{-\frac{\pi R_H}{R_s}} = 1 \qquad \textit{Eq. 4.1}$$

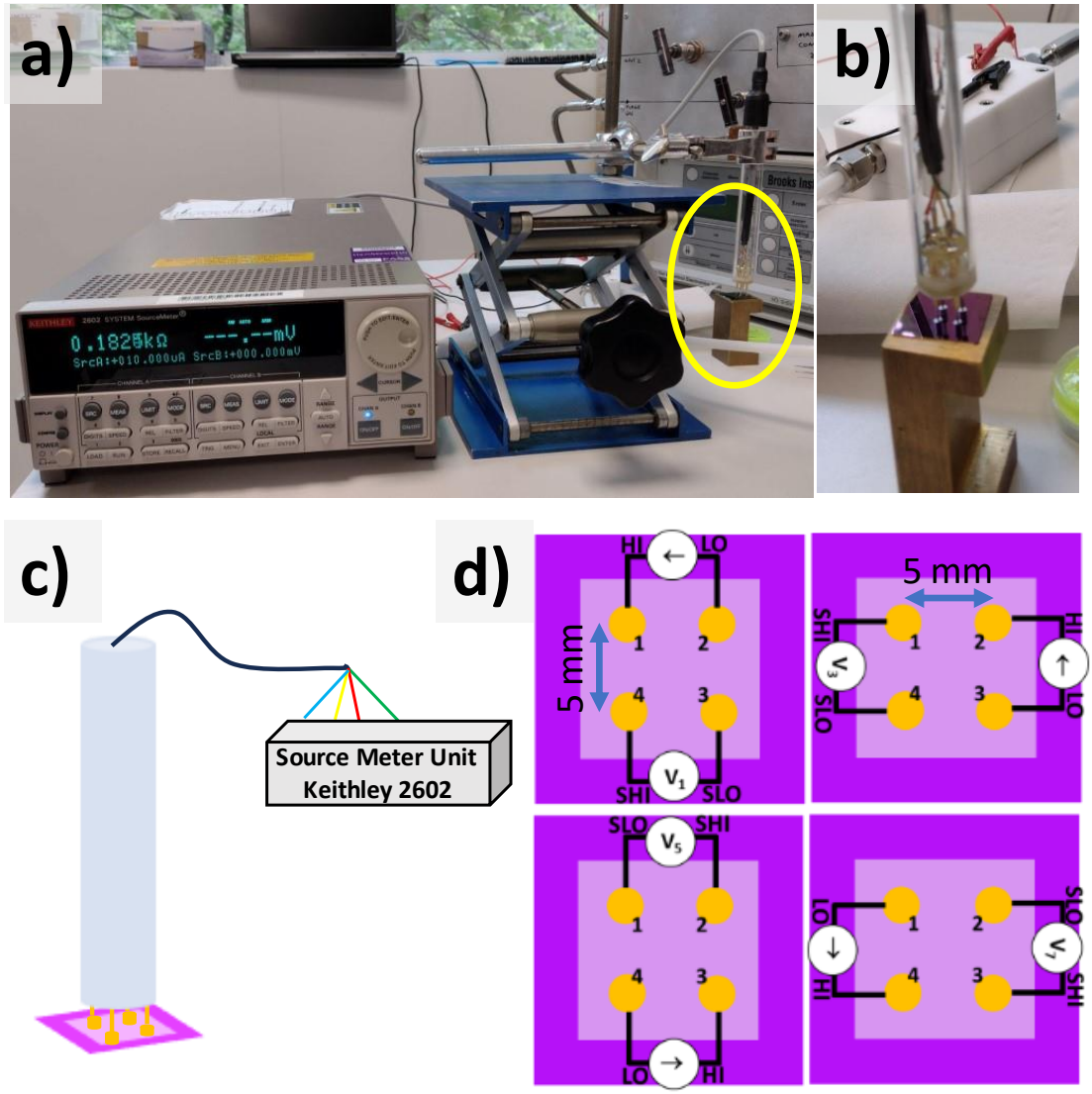

Figure 4.32 a) Homemade set up for electrical measurements, b) yellow circle zoom, c) Van der Paw probe on graphene/SiO_2/Si, and b) scheme to illustrate how the sheet resistance, in Table 4-2, was measured.

The sheet resistance is in the same range at each position with a total average sheet resistance of 1201.58±165.9 Ω/□. It is lower than 1.3×10^4 to 5.1×10^4 Ω/□ reported by Li *et al.*;[164] however is higher than the expected for grain sizes around 0.9 μm reported to be in the range of 760 Ω/□,[211] which is in the range of commercial material (from 350±40 Ω/□[212] up to 500 Ω/□[213]) so these variations could be related more to the set up used to measure it; as in the first paper they have used copper wires connected to each sample corner by silver paint and we used a more stable four-point probe but with a bigger space

between the electrodes (5 mm) when they are comparing with the configuration used in the case of the lower resistance.

Table 4-2 Sheet resistance (R_s) for each sample position.

Sample	R_1 (Ω)	R_3 (Ω)	R_5 (Ω)	R_7 (Ω)	$R_V = \frac{R_3+R_7}{2}$ (Ω)	$R_H = \frac{R_1+R_5}{2}$ (Ω)	R_s (Ω/□)
A	218	333	219	315	324.0	218.5	1213.1
B	351	232	355	233	232.5	353.0	1307.1
C	150	485	150	488	486.5	150.0	1290.4
D	233	311	234	309	310.0	233.5	1223.2
CC	269	169	270	168	168.5	269.5	974.0

Once the graphene is transferred, specific functionalisation on its surface is desirable, to tunnel its properties for specific applications. Li *et al*. reported successful direct azidation of the graphene basal plane and click chemistry of the product for different surface functions.[58] Apart from covalent functionalisation, noncovalent functionalisation is also possible; this expands the possibility of using LPCVD graphene for electrochemical, gas, and liquid sensors in chemiresistor or field effect transistor (FET) configurations.[112,214–217]

4.7 X-Ray photoelectron spectroscopy (XPS) of graphene before and after functionalisation.

Ideally, graphene growth by LPCVD was planned to be used as a gas sensor material; for this purpose, it will be tested without and with functionalization (non and covalent functionalization). Covalent functionalization was done using click chemistry on azide groups previously attached to the graphene surface by electrochemistry. XPS was used to confirm the surface chemistry of graphene. Graphene transferred onto SiO_2/Si substrates was covalently functionalized by applying +1.3 V between the graphene and the reference electrode in a sodium azide solution (NaN_3), as shown in Figure 4.33. Then click chemistry procedure as it is discussed in Section 3.6 was used to attach TU molecule. High-resolution scans were deconvoluted into asymmetric Lorentzian components (LA

lineshape) after a Shirley background correction using CASA XPS software to fit the data.[162]

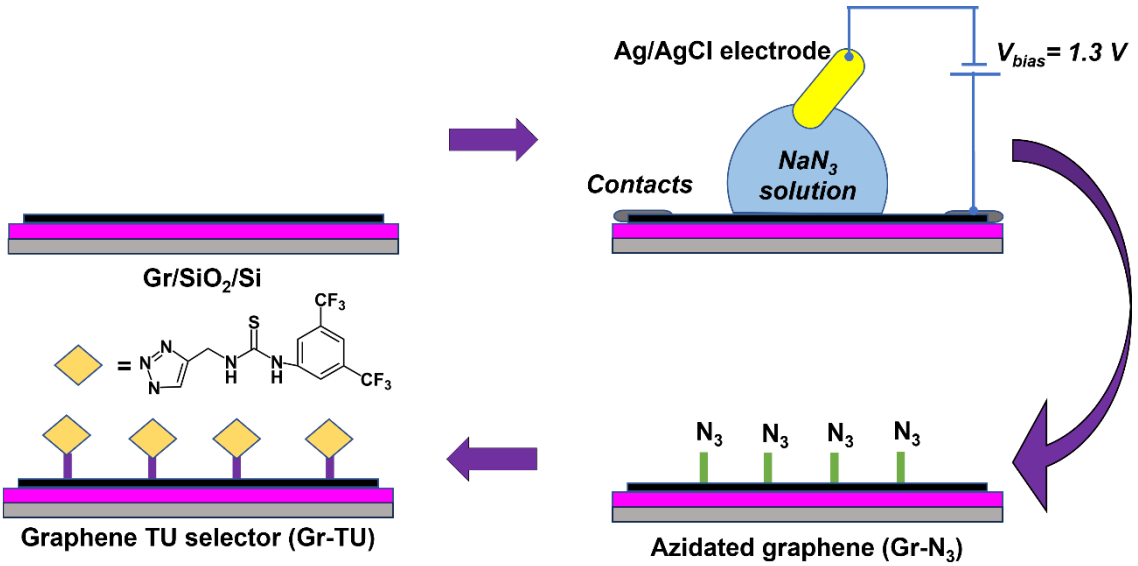

Figure 4.33 Functionalization procedure on LPCVD graphene.

Figure 4.34a shows the XPS survey mode scan for the graphene sample on SiO_2/Si, where most of the oxygen 1s (O 1s) signal is coming from the silicon dioxide (SiO_2) layer. No nitrogen signal is observed. Figure 4.34b shows the deconvoluted XPS spectra of the C 1s peak, where the presence of C sp^2 (284.41 eV), C sp^3 (284.91 eV), C-O (286.38 eV), C═O (287.67 eV), O-C═O (288.97 eV) and graphitic carbon (291.15 eV) bonds is confirmed.[58,218]

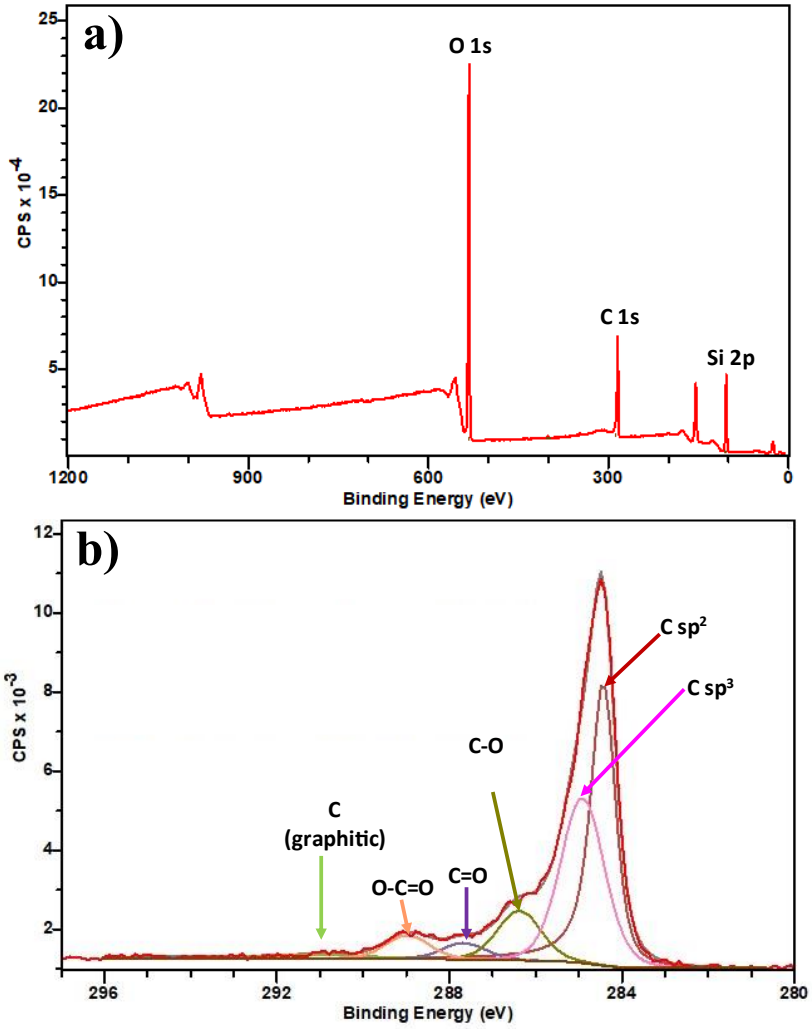

Figure 4.34 a) XPS survey mode and b) High-resolution C 1s region for bare CVD graphene onto SiO_2/Si.

Figure 4.35a, b and c illustrate survey-mode and high-resolution scans of carbon and nitrogen regions of Gr-N_3, respectively. The ~2:1 ratios of O/Si in both samples indicate that the O signal was mainly from the SiO_2 substrate. Figure 4.35b shows the deconvoluted XPS spectra of the C 1s peak, where the presence of C sp^2 (284.42 eV), C sp^3 (285.00 eV), C-O/C-N (285.98 eV), and O-C═O (288.88 eV) bonds is confirmed.[58,218] High-resolution data for N 1s was deconvoluted in three peaks: -N=N=N (400.12 eV), -N=N=N (401.53 eV) and -N=N=N (404.26 eV) for the central nitrogen in the azide group (Figure 4.35c).[219] The azide groups were successfully attached to the surface of graphene by applying a constant voltage and not considerable oxidation occurred. The next step was the "click chemistry reaction" to bond the 1-(3,5-bis(trifluoromethyl)phenyl)-3-(prop-2-yn-1-

yl)thiourea (referred to in the text as TU) selector to the surface of the graphene through the triazole ring formation.

XPS survey mode, high-resolution C 1s and N1s scans on sample G-TU are illustrated in Figure 4.36a, b, and c, respectively. The introduction of the TU selector was confirmed by the fluor signal in Figure 4.36a and the increment in the nitrogen signal. The C 1s scan in Figure 4.36b was deconvoluted in seven peaks: C sp^2 (284.43 eV), C sp^3 (284.87 eV), C-O/C-N (285.91 eV), C═O (286.93 eV), O-C═O (288.84 eV), and CF_3 (292.87 eV).[58,108,218] Figure 4.36c shows the N 1s region; the peaks at 399.03 eV and 400.32 eV correspond to N-C/N-H and -N-N=N, respectively[108] coming from the TU selector and the triazole ring formation; on the other hand peaks at 401.59 eV (-N=N=N) and 404.24 eV (-N=N=N) are from unreacted azide groups on the surface of graphene.[219]

Electrochemical covalent functionalization approach opens a new alternative to integrate functionalised graphene into electronic devices that, with subsequent click chemistry can be modified for specific applications. However, from our experience, when we tried covalent functionalisation on CVD graphene transferred onto quartz or SiO_2/Si substrates sometimes during the voltage application the film peeled off from them, this disrupts the film continuity making it less or not conductive at all. So, some improvements during the transfer graphene process need to be developed to achieve a good adhesion between graphene and substrate. Non-covalent functionalization offers a way to tackle this problem, as it did not come off during the immersion in the functionalising agent and subsequent washes. Also, the direct electrochemical functionalisation of CVD graphene on copper[220] can be an option to avoid these problems during the voltage application.

In non-covalent functionalisation, Gr/SiO_2/Si was immersed in a 0.4 mg/ml of TU solution by 1 min, it was taken out and washed with methanol and dried with nitrogen. Non-covalent functionalization on carbon nanotubes (CNTs) with a similar thiourea selector has been reported before to make a selective chemiresistor under cyclohexanone vapours exposure.[84] The discussion about the interactions of the selector with the graphene surface was discussed in Section 1.4.2. The synthesised CVD graphene will be used in Section 6.2 as a sensing material, and the devices will be tested without and non-covalent functionalisation.

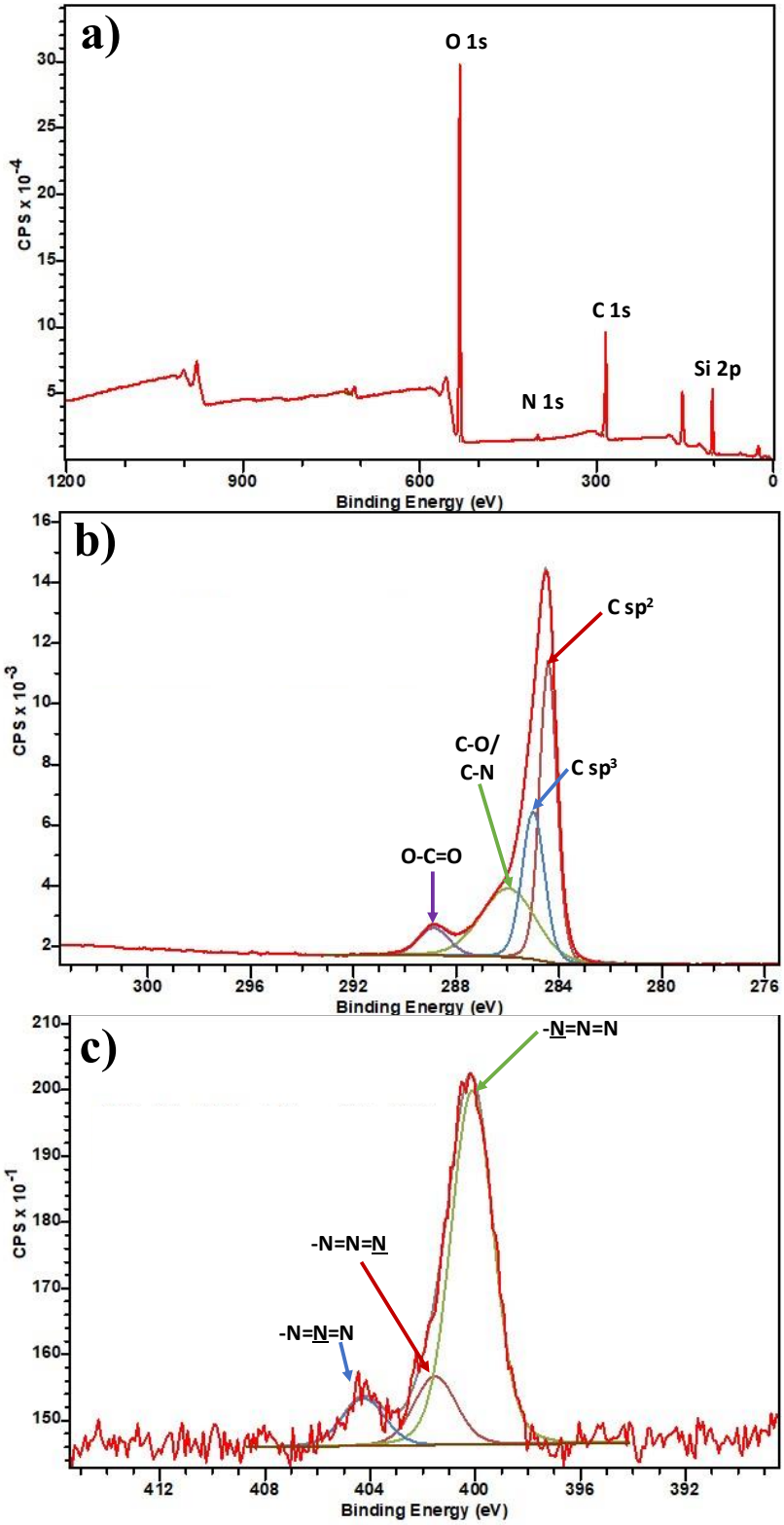

Figure 4.35 a) XPS survey mode, b) High-resolution C 1s region and c) High-resolution N 1s region for Gr-N_3.

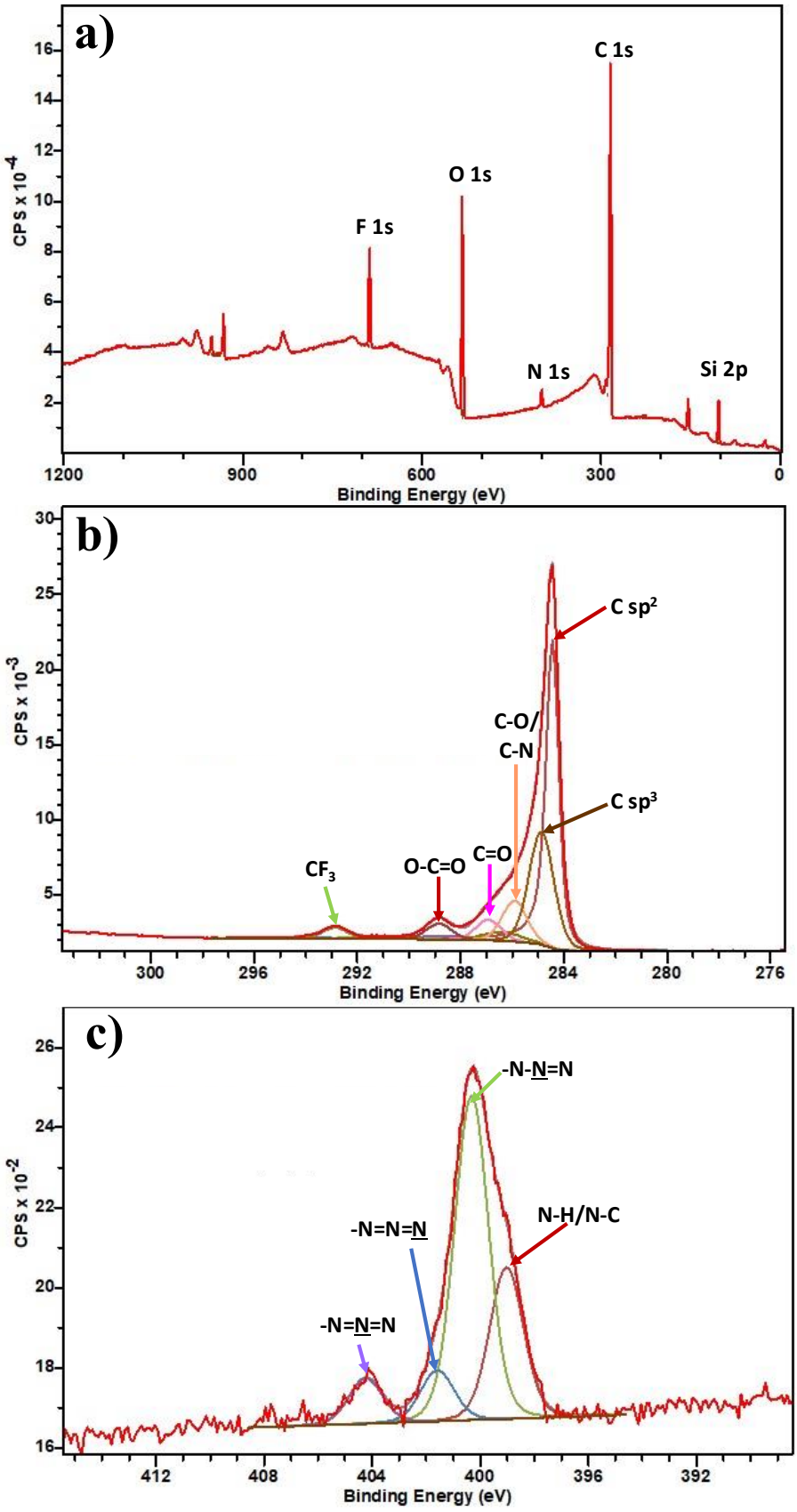

Figure 4.36 a) XPS survey mode, b) High-resolution C 1s region and c) High-resolution N 1s region for Gr-TU.

4.8 Conclusion.

Graphene films can become easily accessible to non-specialist research laboratories using simple and reproducible methodology with readily accessible low-cost equipment. This will help accelerate and encourage the development of graphene applications research. The ready reproducible production of a material comparable to commercially available graphene with minimum batch-to-batch variations is key to designing affordable and reliable devices and sensors.

Here, we designed, built, and assembled a system to grow graphene by low-pressure chemical vapour deposition (LPCVD). One of the aims of this work was to describe in detail a procedure to produce graphene films to reduce the variation between batches. By following the approach detailed in this work, it was possible to optimize the area of copper foil for growing graphene by carefully wrapping it against the quartz tube wall, this allowed the process to scale the graphene film size from 1.5×4 cm^2 to 6.5×4 cm^2.

Through SEM imaging, it was identified the presence of PMMA residues, wrinkles and few adlayers. Moreover, SEM helped to determine the average graphene grain size was 3.38 μm^2 and suggested that the graphene films was continuous. TEM imaging provided additional verification, elucidating that the films possessed self-standing characteristics, thus indicating a complete interconnection of graphene domains at the boundaries of the graphene grains. Furthermore, the characteristic diffraction pattern of the graphene demonstrated that the films were predominantly monolayer, which was also in agreement with AFM measurements.

Considering the constraints of previous methods in confirming the monolayer nature of synthesized graphene films, Raman spectroscopy proves to be a robust technique for non-destructively analysing significantly larger areas. In this field, the National Physical Laboratory (NPL, UK) has been working on developing the standards to assess the graphene quality. Here, we used the work done by the NPL as a framework to analyse the graphene and provide a statistical perspective of the quality of the synthesized films. Given that the graphene films consist of grains interconnected at the boundaries, it was deemed appropriate to conduct sampling over a significantly larger area than the average grain to obtain representative parameters of the sample. With the aim of optimizing time efficiency, the number of acquired spectra was reduced, while ensuring a balance between accuracy and acquisition time. By adopting this strategy, it was determined that utilizing a considerably smaller map (13×13 μm^2 at 1μm intervals) yielded an error of less than 1%

when compared to a significantly larger map (32 ×32 μm^2 at 1µm intervals). Furthermore, it has been shown that the D band was minimal, similar to the commercial samples, thus indicating the films have minimal defects.

According to the criteria adopted by the NPL, FWHM 2D ≤ 35 cm^{-1} is associated with monolayer graphene and most our samples from different batches meet this criterion. The variations found could be explained by minimal residual strains in the range of ±0.1%, explaining the broad range of FWHM 2D values, like those also observed in commercially available samples. Moreover, from all our samples from different batches I_{2D}/I_G ratio > 1.5 which are higher than those of commercial samples. These findings can be interpreted as indicating that the samples have a low level of doping, possibly resulting from unintentional doping from residual ferric chloride etchant. Overall, we can consider that the procedure we are reporting can produce graphene films over a large area of copper with an acceptable homogeneity according to criteria set by the NPL.

Graphene functionalization is desirable in electronics devices (like gas sensing) and biosensing. As an example of further use of the films transferred on the SiO_2/Si substrate, we electrochemically functionalized the graphene surface with azide groups. We further exploit the azide-alkyne click chemistry to attach a thiourea derivative selector. This demonstrates that the synthesized films can be potentially used to make electrodes with different surface chemistries.

5 Simultaneous electrochemical exfoliation and functionalisation of graphene.

In recent years, electrochemical exfoliation of graphite has emerged as a simple method to produce graphene materials. It is an attractive strategy to produce few-layer graphene because it is simple, economical, environmentally friendly, and operates at ambient temperature and pressure conditions.[51] Most importantly, electrochemical exfoliation can easily produce a mixture of single and few-layer graphene, and the procedure is completed in a short period of time, producing gram-scale quantities of flakes with yields as high as 80%.[26,49,221] Furthermore, sheet size, carbon/oxygen (C/O) ratio, solubility and electrical conductivity can be modified by controlling process parameters, such as applied electrical potentials, currents, processing time, as well as the composition of electrolytes. It has been found that different levels of oxidation can be obtained by controlling the electrochemical potential.[53]

In contrast to other exfoliation processes, this method is not equipment intensive. A typical set-up includes a working electrode, counter electrode, electrolyte and a power supply, as in Figure 5.1a. Depending on the potential applied on graphite electrodes, there are cathodic (applying a negative bias) and anodic (using a positive bias) electrochemical exfoliation methods. These potentials can drive positive or negatively charged ions from the electrolyte into the graphitic interlayers, respectively.[31] It has been demonstrated that the structural imperfections in graphite foils facilitate the exfoliation of graphite and reduce damages caused by oxidative reactions during electrochemical exfoliation.[222]

As discussed, in typical setups a graphite electrode can be exfoliated in the presence of an ionic intercalating agent. Previous research has shown that by applying an electrical potential, some molecules can generate radicals which can react with the graphitic basal plane.[58] This suggests the possibility of a simultaneous exfoliation and functionalisation of graphene. From the many functional groups that can be introduced to the graphene, azide groups on the surface of the graphene open the possibility of bonding an alkyne-terminated molecule using the copper(I)-catalysed alkyne–azide cycloaddition (CuAAC) click chemistry.[223] The versatility of this functional group have found applications in the development of sensors for copper detection,[224] biosensing,[225] ultrafiltration technology,[226] among others. More specifically, in the development of sensors, it is desired to preserve the electrical conductivity of graphene. This poses a challenge as in all of these

procedures, graphene oxide is used as a precursor for covalent[104,105,224–229] or a non-covalent functionalisation,[230] and further reduction can lead to the conversion of azide groups to amino groups.[231] Therefore, it is attractive to find new ways to introduce azide groups to the graphitic surface while keeping the conjugated lattice. In a previous work by Ustavytska *et al*.[56] graphene was exfoliated for 20 hours using in a 1M sodium azide solution in absence of any other intercalating agent. This investigation demonstrated that nitrogen was introduced in some way to the graphitic lattice but did not show what functional groups were introduced. More recent research by Li *et al*. demonstrated that simultaneous electrochemical exfoliation in a sodium sulphate (Na_2SO_4)/sodium azide (NaN_3) solution can introduce azide groups to graphene flakes, however this process was limited to the exfoliation of a single flake of graphite.[58,94]

Motivated by this, we explored the bulk exfoliation of graphite foil in a solution of Na_2SO_4 /NaN_3 to produce graphene flakes with azide groups on its surface. Moreover, we will demonstrate the flakes preserve their electrical conductivity, even after functionalization with an alkyne terminated molecule through CuAAC click chemistry. As a proof of concept we will introduce 1-(3,5-bis(trifluoromethyl)phenyl)-3-(prop-2-yn-1-yl) thiourea molecule for the selective detection of cyclohexanone. Although a similar molecule was proved to work using carbon nanotubes, here for the first time we will use azidated graphene, which makes the process simpler than that reported before.[108,232]

5.1 Anodic electrochemical exfoliation set-up.

A 1.2 cm^2 graphite foil piece and platinum wire were used as working (carbon source) and counter electrodes for simultaneous electrochemical exfoliation and functionalisation. The electrochemical exfoliation of graphite was carried out by applying a positive voltage on the working electrode, which was immersed into an aqueous solution containing 0.2 M Na_2SO_4/ 0.1 M NaN_3. The azidated electrochemically exfoliated graphene (EEG-N_3) was washed by vacuum filtration, redispersed in 40 ml of water, and sonicated for 15 min in a bath sonicator. The dispersion was kept for 24 h for the precipitation of un-exfoliated graphite flakes. The top third part of the dispersion was used for further characterisation. Figure 5.1a and b show the electrochemical set-up for the production of azide functionalised graphene, and the reaction steps, respectively.

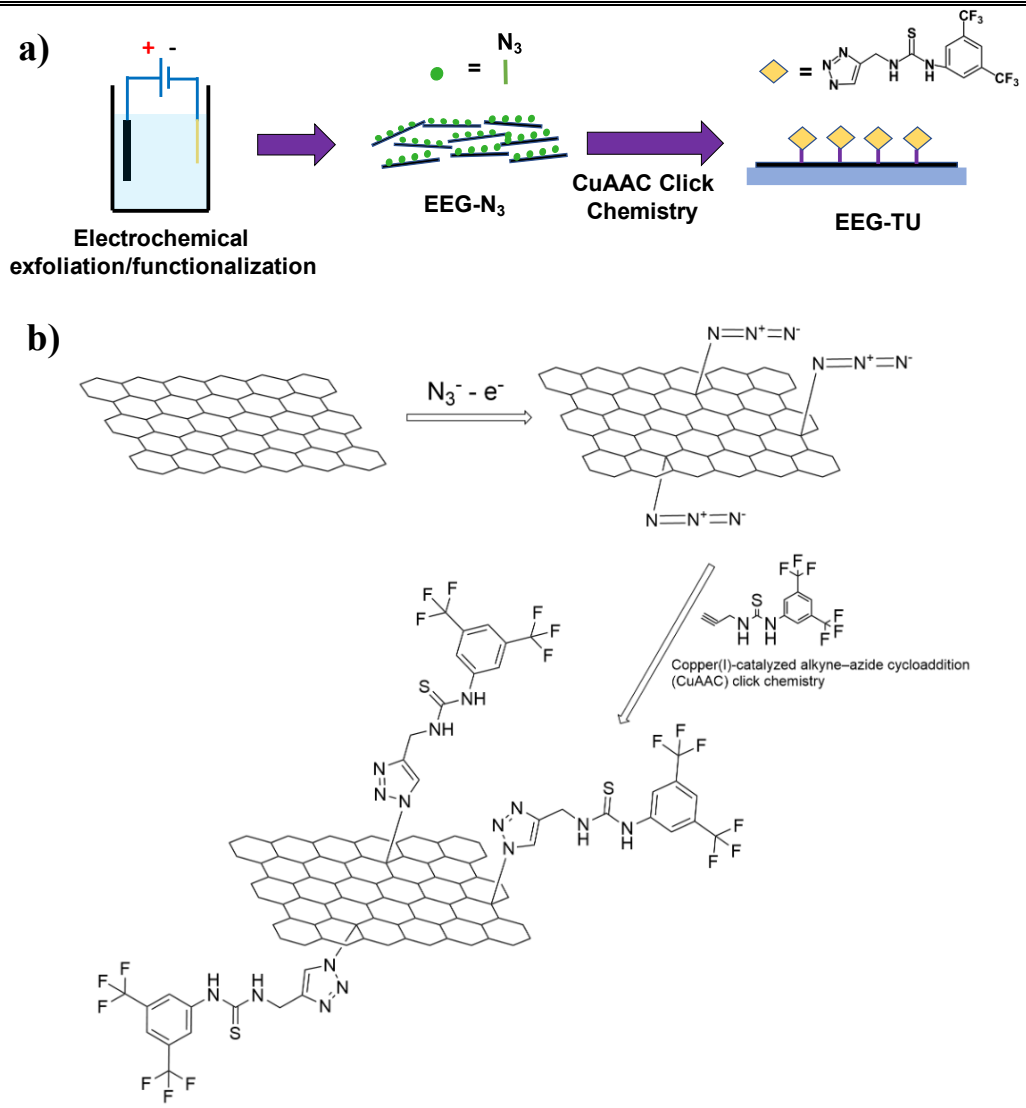

Figure 5.1 a) Experimental set-up for simultaneous electrochemical exfoliation and functionalisation of graphene flakes, b) reaction steps for the attachment of TU molecule by CuAAC click chemistry.

In Section 5.4, it was studied the effect of the voltage and the electrolyte on the exfoliation. The optimum conditions were selected according to AFM measurements, based on the lateral size and thickness of the graphene flakes. Finally, 1-(3,5-bis(trifluoromethyl)phenyl)-3-(prop-2-yn-1-yl)thiourea (referred to in the text as TU), synthesised as described in Section 3.5, was attached covalently to the graphene sheets using CuAAC click chemistry[223] (see Figure 5.1b).

5.2 X-Ray diffraction.

We used X-ray powder diffraction analysis to determine the structure of exfoliated graphene EEG sheets produced via electrochemical exfoliation of graphite foil in 0.4 M Na_2SO_4 (control experiment) and 0.2 M Na_2SO_4/ 0.1 M NaN_3 aqueous solution at 7 V. The d-spacing between layers was calculated using Bragg's law (Eq. 5.1),[233] and results are summarised in Table 5-1.

$$d = \frac{\lambda}{2 \sin \theta} \qquad \textit{Eq. 5.1}$$

where $\boldsymbol{d}$ is the interplanar spacing in a crystal lattice, $\boldsymbol{\lambda}$ is the wavelength of the source (0.15418 nm), and $\boldsymbol{\theta}$ is the diffraction angle in radians. From the Scherrer equation,[233] the crystal size ($\boldsymbol{L}$) is determined by:

$$L = \frac{K\lambda}{\beta \cos \theta} \qquad \textit{Eq. 5.2}$$

where $\boldsymbol{K}$ is the Scherrer constant (0.91), $\boldsymbol{\lambda}$ X-ray wavelength (0.15418 nm), $\boldsymbol{\beta}$ full width at half maximum (FWHM) of the peak and $\boldsymbol{\theta}$ is the Bragg angle, the angles are in radians.

Table 5-1 Interplanar spacing in crystal lattice and crystal size for graphite foil and EG samples.

Material	2θ (°)	d(002) spacing (nm)	Expanded distance (nm)	FWHM (°)	Crystal size (nm)
Graphite foil	26.86	0.332	- - - -	0.2413	34.258
EEG-N_3	26.58	0.335	0.003	0.5158	16.016
EEG	26.47	0.337	0.005	0.7163	11.529

Figure 5.2 shows the XRD patterns of our materials; the diffraction peak (002) of EEG and EEG-N_3 appears at 26.47° and 26.58 with an interlayer distance of 0.337 and 0.335 nm, respectively. In contrast, the peak of graphite foil appears at 26.86° with a d-spacing of 0.332 nm. Compared to graphite, both EEG's slightly lower 2θ angle suggests that electrochemical exfoliation increased the d-spacing due to the introduction of sulphate ions, oxygen and azide groups. They exhibited an extremely low intensity (3237 and 3388 a.u., respectively, compared to 157692 a.u. for graphite foil) and broad peak for (002)

graphite plane, denoting well exfoliation of graphite layers and reduction of the crystal size.[234,235]

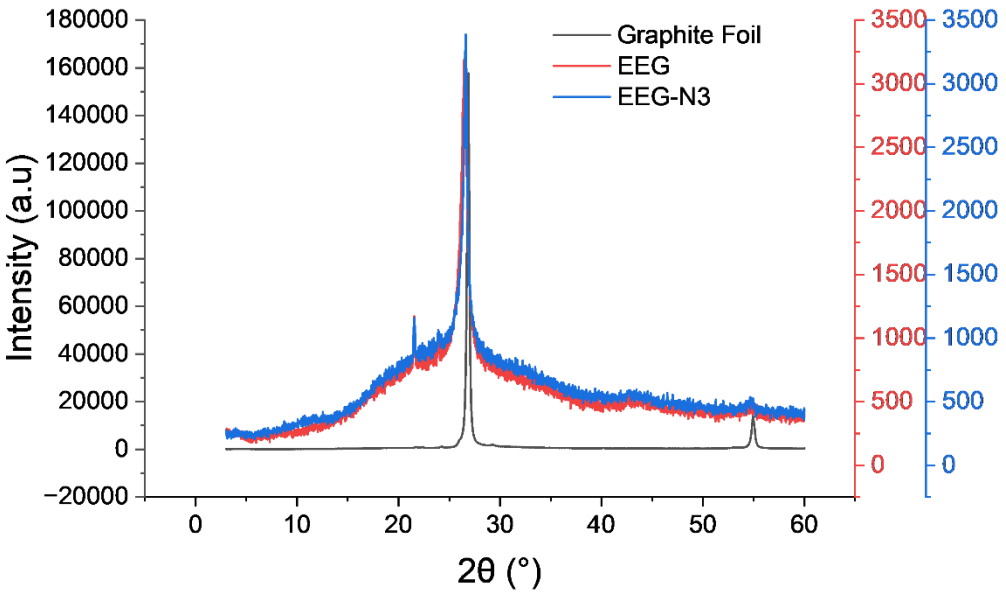

Figure 5.2 X-ray diffraction (XRD) spectra of graphite foil, EG (Na_2SO_4/NaN_3) and EG (Na_2SO_4).

5.3 Scanning electron microscopy (SEM).

Scanning electron microscopy (SEM) was used to characterise the EEG sheets. The surface and edge morphologies of the graphite foil after exfoliation at 7V in Na_2SO_4 and Na_2SO_4/NaN_3 aqueous solution are illustrated in Figure 5.3a,b and c,d, respectively.

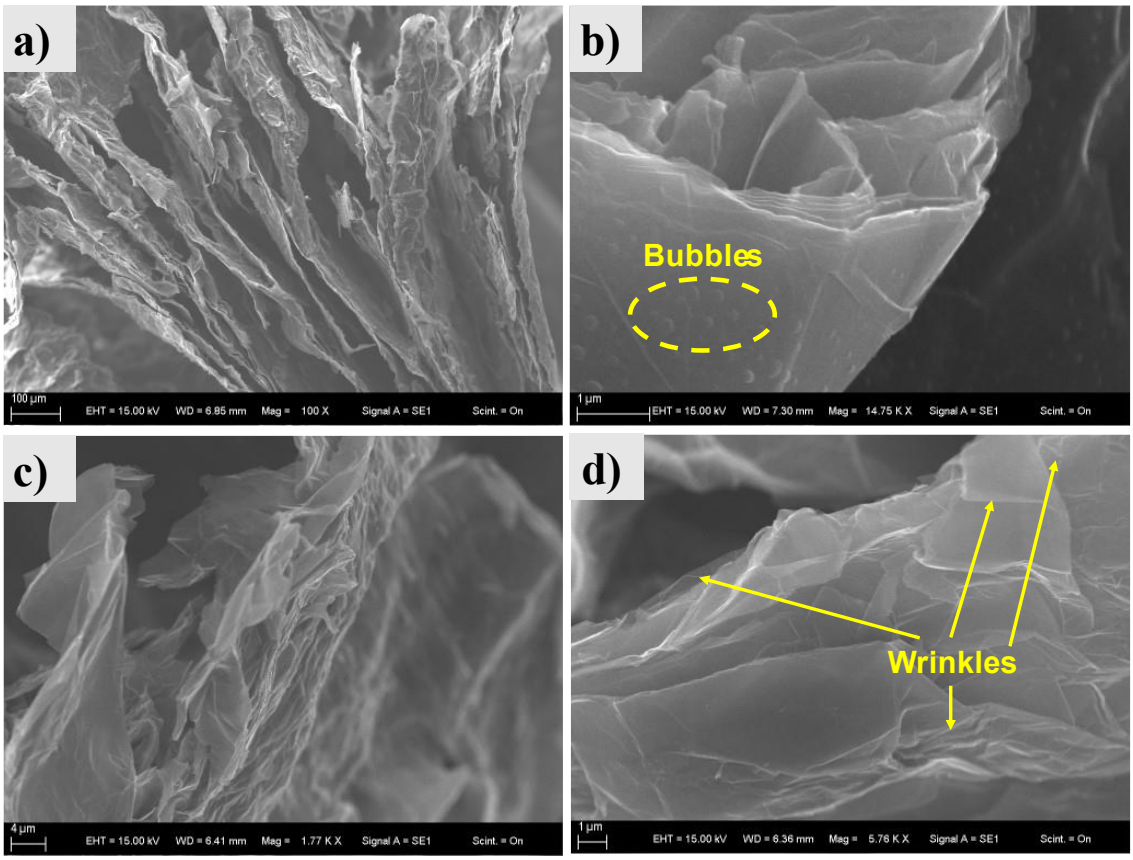

Figure 5.3 SEM images of graphite foil exfoliated in a), b) Na_2SO_4, and c), d) Na_2SO_4/NaN_3 after the electrochemical process, where the expanded graphite layer, the formation of bubbles and wrinkles are observed.

A network of wrinkles on the surface of the graphite was identified in the SEM images, which might be due to the visible gas evolution causing expansion and swelling of the graphite layers. According to Parvez *et al*., during the electrochemical process, the edge and grain boundaries of the graphite electrode open up first, which facilitates anion intercalation and results in exfoliated graphene sheets,[51] as observed in the images. The mechanism of exfoliation is discussed in Section 1.2.1.6.

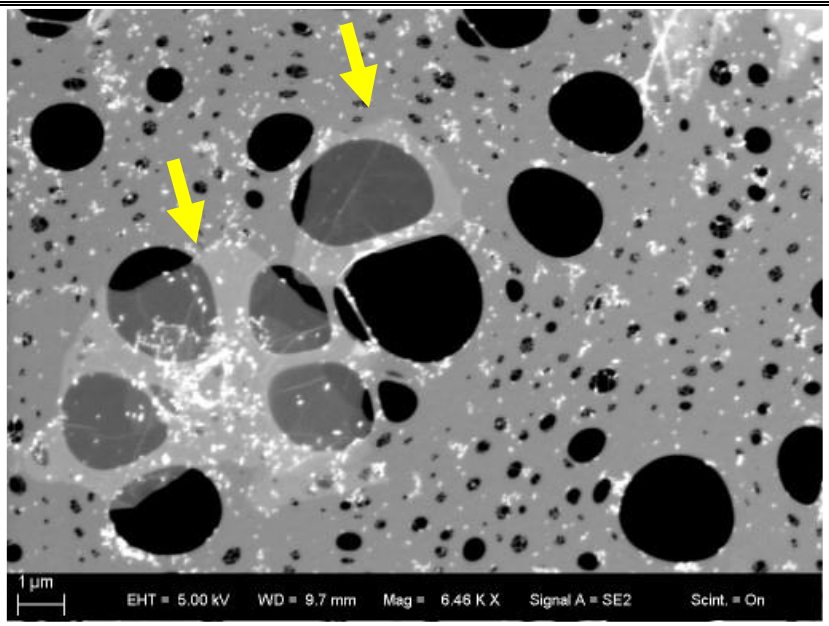

Figure 5.4 SEM image of EG flakes on holey carbon TEM grid, the yellow arrows indicate graphene sheets.

Figure 5.4 shows an SEM image of EFG-N_3 flakes (pointed out with yellow arrows) on the holey carbon TEM grid. The particles that appear as bright features are salt residues from the electrolyte. The lateral sizes of these flakes are 3 and 6 µm, respectively; in the next section the thickness and lateral size will be measured by AFM to find optimum conditions.

5.4 Effect of the voltage and electrolyte on graphene flakes thickness and lateral size.

Three different voltages (5V, 7V and 10 V) in buffer or water 0.2 M Na_2SO_4/0.1 M NaN_3 solution were applied to graphite foil for graphite exfoliation. Figure 5.5 a, b and c illustrate a typical AFM image, how the lateral size was measured and the height profile of an arbitrary flake, respectively.

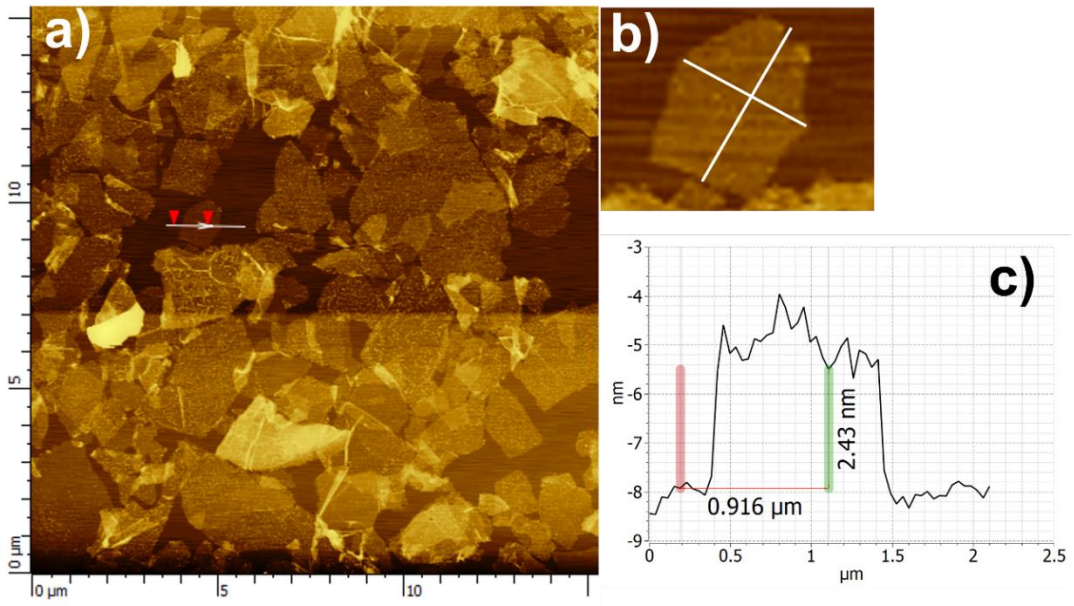

Figure 5.5 a) AFM image of flakes, b) how the flakes were measured, and c) thickness of flake in a) and b).

The length and width (perpendicular to the length) were measured for each flake using AIST software. The geometric mean was calculated using the National Physical Laboratory (NPL) protocol to obtain the lateral size.[160] Figure 5.6 and Table 5-2 summarise the average lateral size and thickness under different conditions of 80 flakes measurements for each sample. The lateral size and thickness distribution for each sample are reported in Figure 5.7 and Figure 5.8, respectively. All distribution plots follow the lognormal distribution.

Table 5-2. Average lateral size and thickness of simultaneous electrochemical exfoliation and functionalisation of graphite foil, using different voltage and electrolytes.

Voltage (V)	Electrolyte	Lateral size (µm)	Thickness (nm)
10	Water	1.71±0.18	2.18±0.18
7	Water	2.29±0.35	2.56±0.20
5	Water	1.10±0.13	2.40±0.17
10	Phosphate buffer pH 7	1.68±0.15	3.16±0.34
7	Phosphate buffer pH 7	1.47±0.12	2.86±0.21
5	Phosphate buffer pH 7	1.39±0.14	2.57±0.19

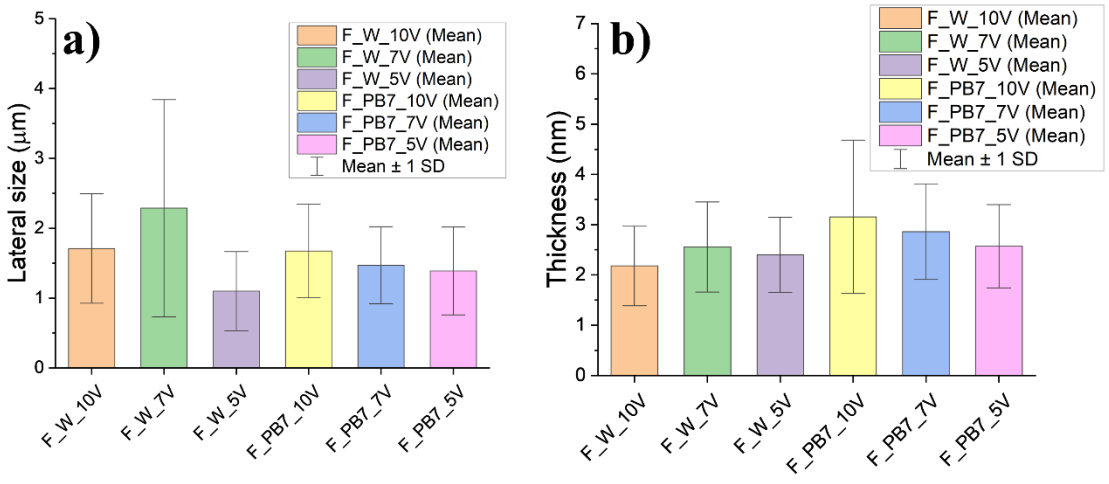

Figure 5.6 Summary of lateral size and thickness distributions of azidated EEG, where W is for samples exfoliated in water and PB7 for phosphate buffer pH 7, respectively at different voltages (5, 7 and 10 V).

Results did not show significant variations between the samples according to the thickness and lateral size, consistent with the work of Nagyte *et al.*[150] Sample exfoliated in 0.2 M Na_2SO_4/0.1 M NaN_3 aqueous solution at 7 V, analysed by XPS to confirm that azide groups were grafted to the few-layer graphene surface. The lateral size distribution of this sample revealed that over 90 % of the EEG-N_3 sheets are larger than 1 μm, and the largest flake size observed is ~9.5 μm. The thickness distribution indicates that 90 % of EEG-N_3 comprises few-layer graphene ($n \leq 10$ layers), where $3 \leq n \leq 8$ are the dominant products accounting for ~57% of the population, estimated according to Section 2.4. The sample was selected based on the previous Li *et al.* paper,[58] in which they synthesised azide-functionalised few-layer graphene by simultaneous exfoliation and functionalisation of a single graphite flake when +7 V were applied to graphite foil. In this work, graphite foil was used as a working electrode instead of one flake to increase the yield of the functionalised graphene. Then, click chemistry is used to attach the TU selector to azide groups; this sample will be referred to as EEG-TU.

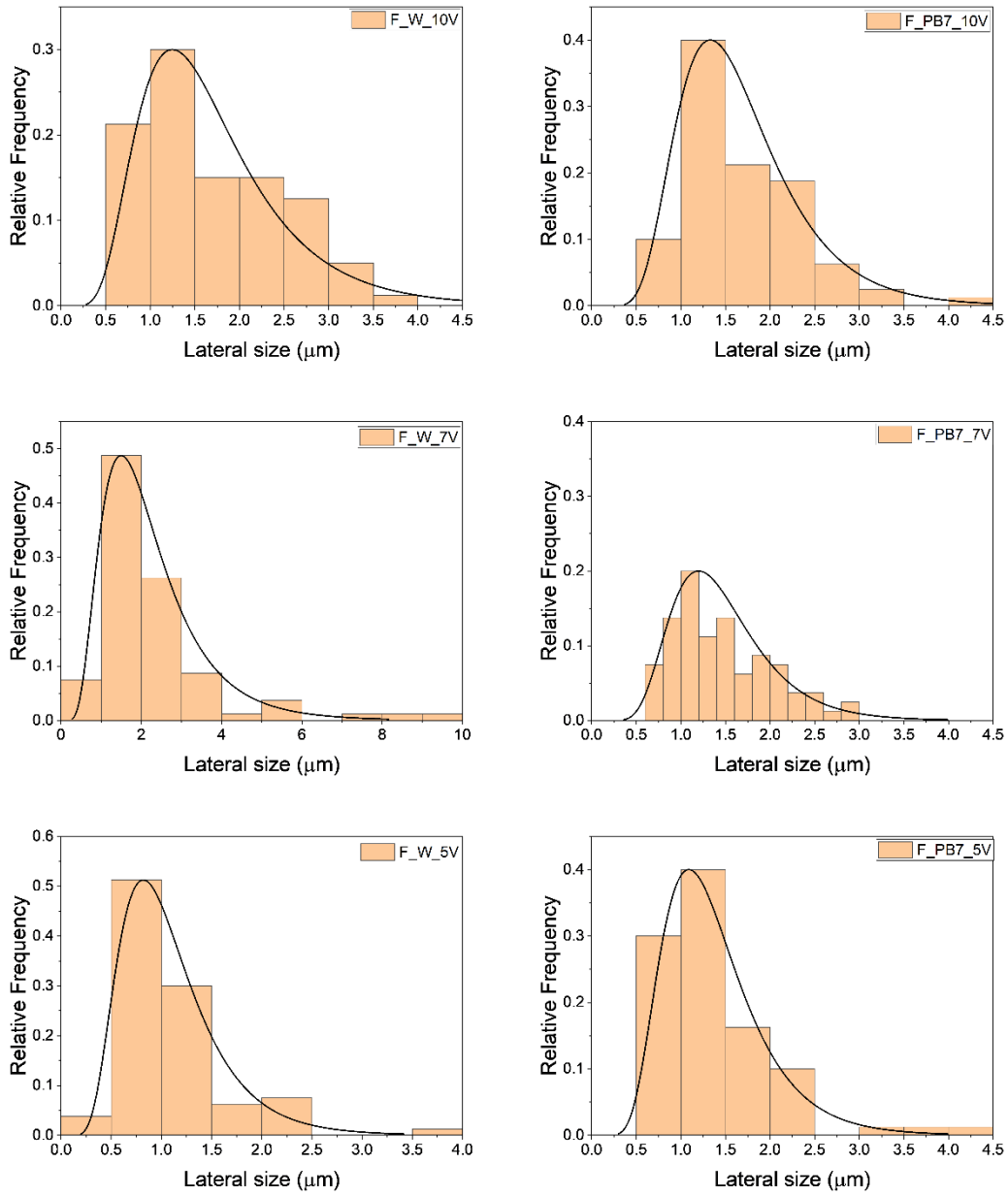

Figure 5.7 Lateral size distributions under different electrochemical exfoliation parameters; where W is for samples exfoliated in water and PB7 for phosphate buffer pH 7, respectively at different voltages (5, 7 and 10 V).

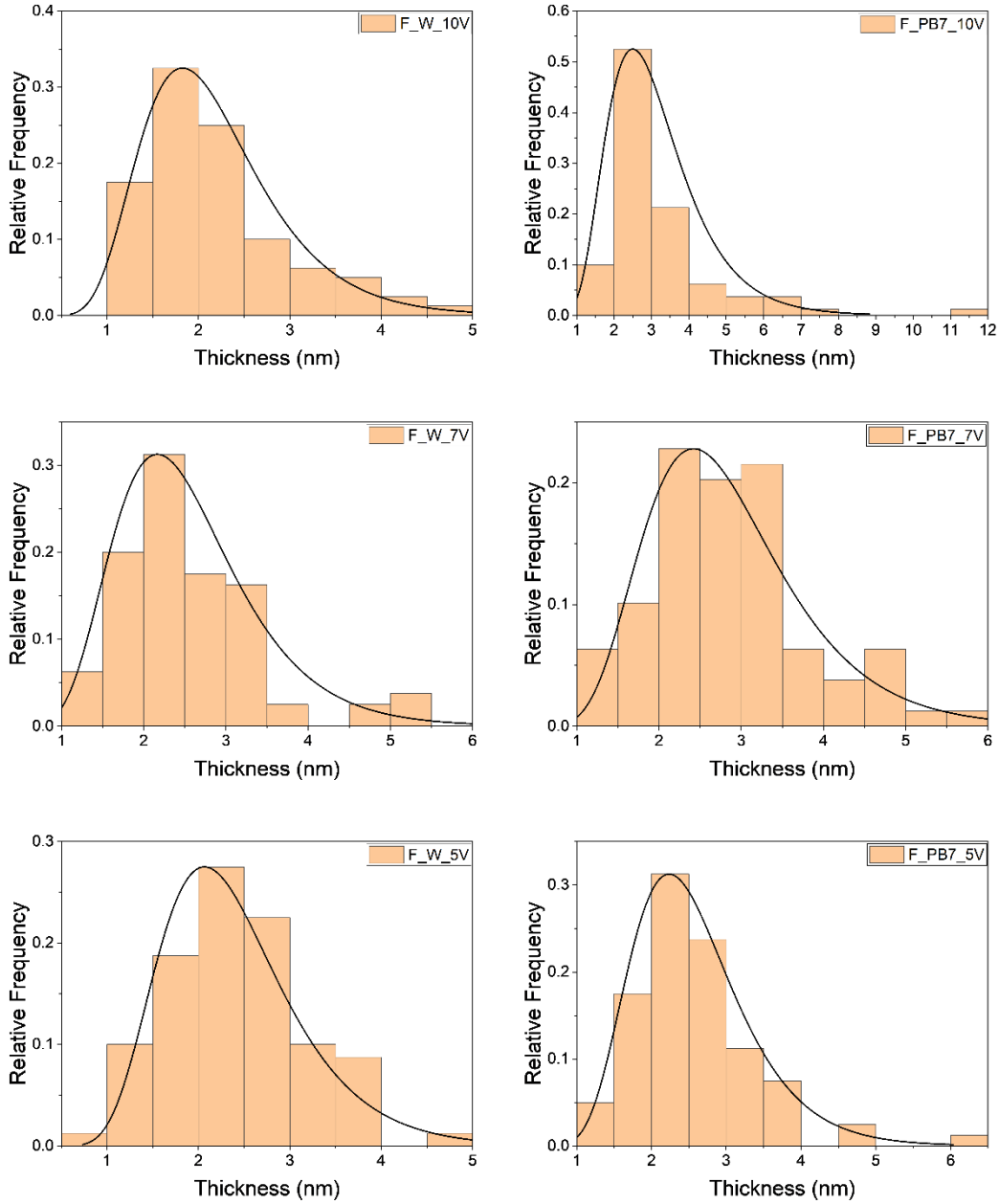

Figure 5.8 Thickness distributions under different electrochemical exfoliation parameters, where W is for samples exfoliated in water and PB7 for phosphate buffer pH 7, respectively at different voltages (5, 7 and 10 V).

5.5 Transmission electron microscopy (TEM).

Transmission electron microscopy was used to evaluate the number of graphene layers and assess the crystalline quality of the graphene films. The number of layers of graphene in three azidated graphene sheets were identified by counting the number of fringes at the edges of the flake. The fringes result from folded layers at the edges of the transferred film. In Figure 5.9a the number of layers in the EEG-N_3 flakes are 6, 7 and 11 layers, respectively. A HRTEM image of this sheet reveals the honeycomb structure of graphene with the typical interlayer distance of ~0.246 nm in Figure 5.9b.

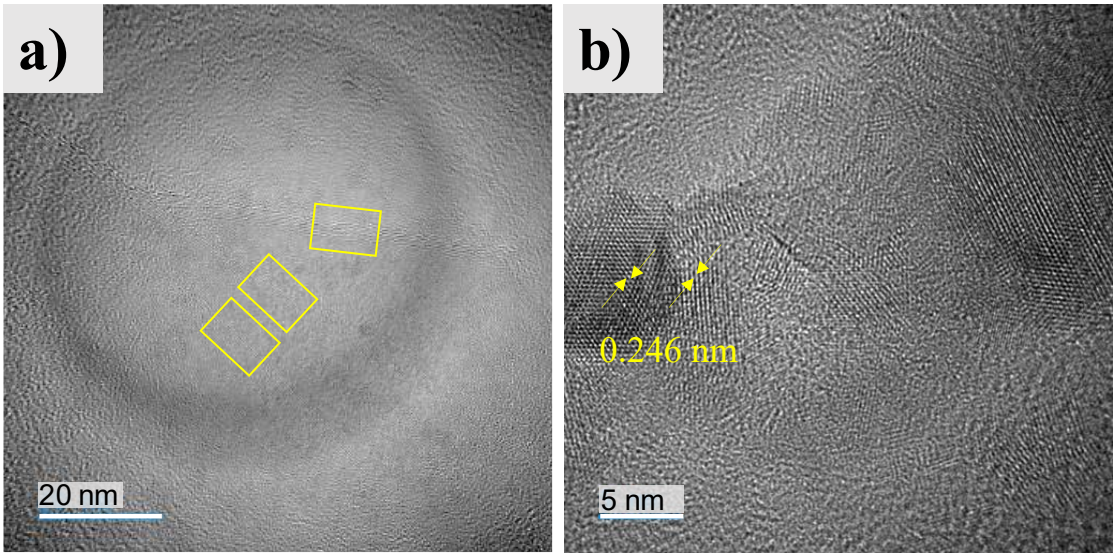

Figure 5.9 a) TEM image yellow rectangles show the edges of three stacked sheets, and b) HRTEM of EEG-N_3 flakes.

Figure 5.10 shows two suspended EG flakes (a and b), their respective selected area electron diffraction (SAED) patterns (c and d), and their intensity profiles (e and f). The SAED patterns exhibit the typical 6-fold symmetry, consistent with the hexagonal crystalline structure of graphene. The Miller–Bravais indices (*hkil*) were used to label the peaks equivalent to the graphite reflections so that the innermost hexagon and the next one correspond to indices $(0\bar{1}10)$ (2.13 Å spacing) and $(1\bar{2}10)$ (1.23 Å spacing), respectively.[130] The monolayer graphene film shows a stronger diffraction intensity for the $(0\bar{1}10)$ plane than the $(1\bar{2}10)$ plane and the opposite is also true for bilayer or trilayer graphene films.[127,236] The profile shown in Figure 5.10e corresponds to multilayer

graphene, and the one in Figure 5.10f corresponds to monolayer graphene sheet. Therefore, it is expected that our exfoliation produces a mix of monolayer and few-layer graphene.

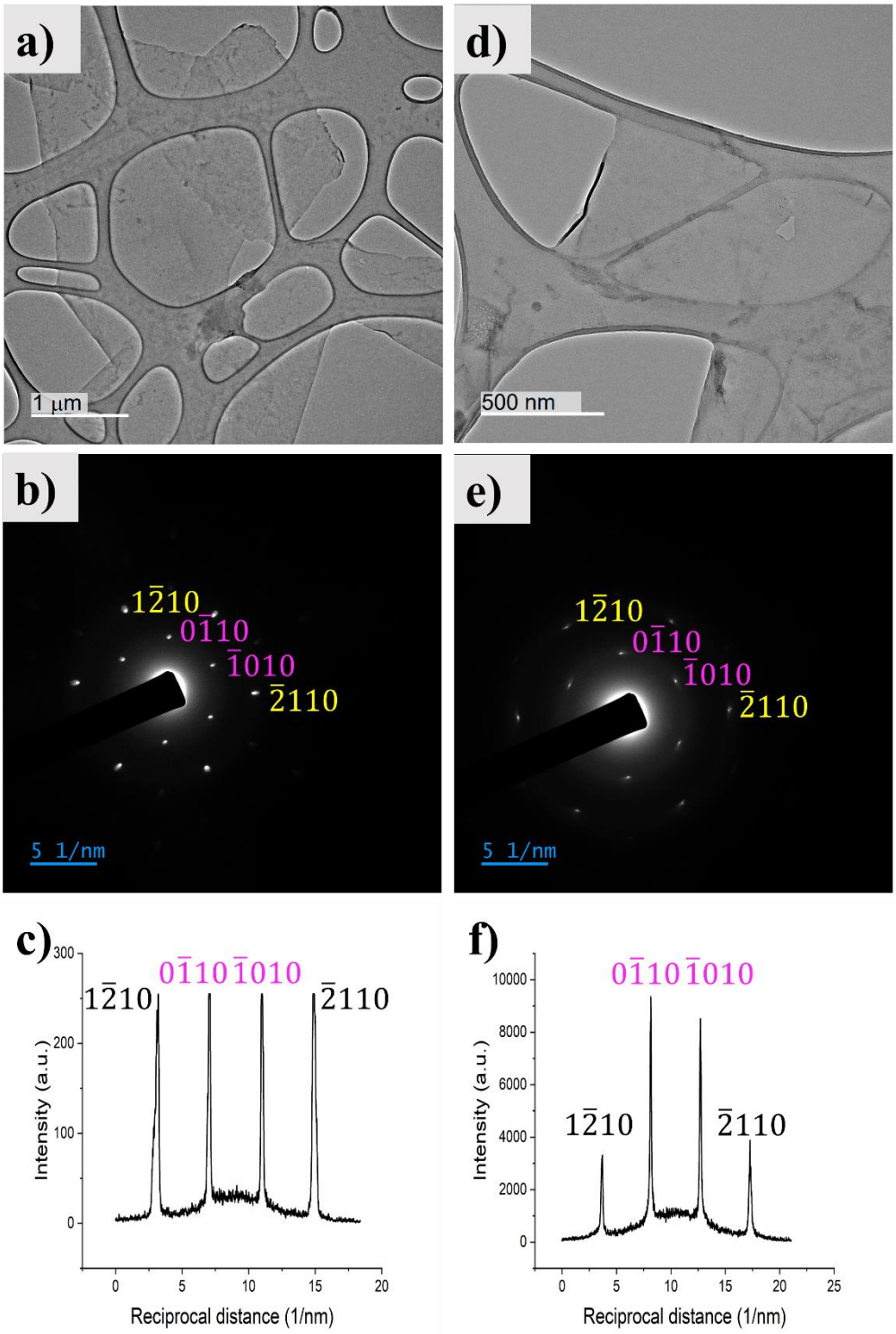

Figure 5.10 a), d) TEM image of exfoliated graphene flakes, b), e) HRTEM of EEG-N_3 sheets and c), f) SAED pattern of EEG-N_3 for bilayer and monolayer flakes, respectively.

5.6 Raman spectroscopy.

Raman spectroscopy can provide information about the thickness and structural defects of the graphene flakes.[147] Graphene exhibits three characteristic peaks; D ~1330 cm^{-1} (associated with sp^3-hybridization, which is indicative of edges and structural defects), G ~1580 cm^{-1} (related to sp^2-hybridization) and 2D ~2680 cm^{-1} (indicating the number of layers).[147] The D/G ratio roughly correlates with the density of defects and functional groups, and an additional contribution from edges due to nanosheet sizes comparable to the laser spot (~1 μm in our case) also increases this ratio.[237,238]

Figure 5.11 shows the Raman spectra of graphite foil, EEG, EEG-N_3, and EEG-TU. Table 5-3 summarises the peak position for each spectrum. Graphite foil displays 2D and G peaks at ~2710 and ~1580 cm^{-1}, respectively. However, for the exfoliated samples (EEG and EEG-N_3) a defect-related D peak appears at ~1348 cm^{-1} and the D+D' peak at ~2940 cm^{-1}. The I_D/I_G and I_{2D}/I_G ratios are 1.19 and 0.21 for EEG, 1.35 and 0.20 for EEG-N_3, and 0.96 and 0.22 for EEG-TU, respectively.

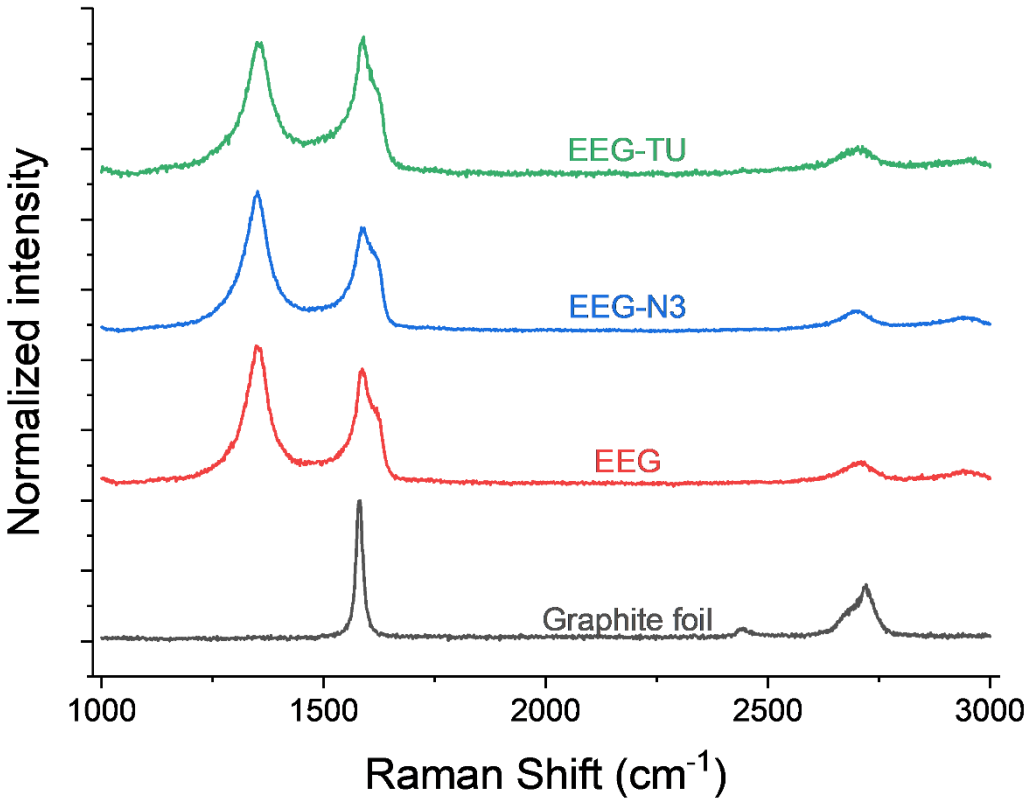

Figure 5.11 Raman spectra of graphite foil (grey), not functionalised EEG (red), EEG after azidation (blue) and EEG after click chemistry.

Table 5-3 Peak position summarised for each spectrum in Figure 5.11.

Sample	**Peak position (cm^{-1})**				**2D FWHM (cm^{-1})**
	D Peak	G Peak	2D peak	D+D' peak	
Graphite Foil	-------	1581.78	2720.59	------	----
EEG	1347.90	1586.42	2709.82	2940.73	49.87
EEG-N_3	1351.08	1591.06	2697.68	2940.73	49.33
EEG-TU	1351.08	1587.97	2701.73	2947.26	60.99

Hao *et al*. reported the dependence of the full width at half maximum (FWHM) of the 2D band on the number of graphene layers.[239] The results showed that samples EEG and EEG-N_3 can be bilayer graphene, and EEG-TU four-layer graphene in agreement with previous work.[240] Also, the symmetry of the 2D peak, their I_{2D}/I_G and its shift towards lower wavenumbers in all EEG samples compared to the graphite spectrum indicates the presence of few-layer graphene[241] as demonstrated by AFM and TEM analysis (Sections 5.4 and 5.5, respectively). The rise in D peak intensity on the EEG samples is due to the functionalisation of exfoliated graphene with azide groups and some oxygen moieties because of the intercalation with the sulphate ions using water. However, it is important to recall the D peak appearance is associated with the disruption of the symmetry of the lattice and does not tell us about the nature of the defects. Therefore, here we use XPS to determine the chemical nature of the defects introduced during exfoliation and functionalisation.

5.7 Thermogravimetric analysis (TGA).

TGA analysis provides information about the groups introduced to the graphene surface. Figure 5.12a and b show that graphite foil is thermally stable up to ~ 700 °C; EEG shows a decomposition peak at ~160 °C; and EEG-N_3 also shows a decomposition peak at ~160°C. The extra weight is attributed to the introduction of more labile groups during the electrochemical azidation reaction. Previous studies on the azidation of graphene oxide using isotopically labelled azide groups ($^{15}N^{14}N_2$) showed the thermal decomposition of these groups to be in the range of 150 - 200 °C,[104] consistent with our results. The significant weight loss in this range of temperature is related to decomposition products such as carbon monoxide (CO), nitrogen (N_2), and carbon dioxide (CO_2), as reported in

previous work.[104,242] XPS analysis was performed to confirm the identify the chemical groups attached to the surface of EEG-N_3.

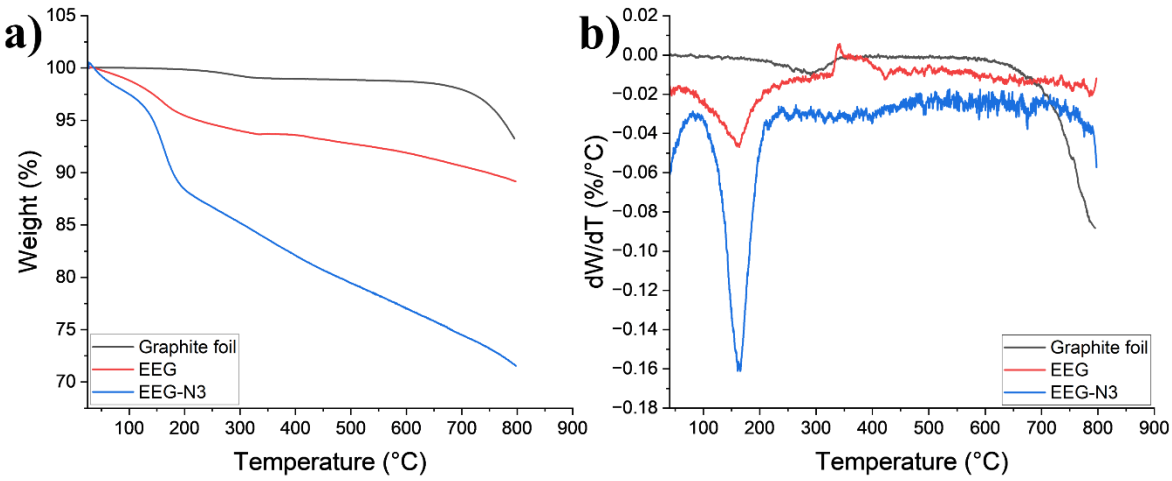

Figure 5.12 a) Comparison TGA and b) first derivative of the weight lost for graphite foil (black), electrochemically exfoliated graphene (red) and azidated electrochemical exfoliated graphene (blue).

5.8 X-Ray photoelectron spectroscopy (XPS) of graphene before and after functionalisation.

To know the chemical composition of graphene before and after functionalization steps, we used X-ray photoelectron spectroscopy (XPS). High-resolution scans were deconvoluted into asymmetric Lorentzian components (LA lineshape) after a Shirley background correction using CASA XPS software to fit the data.[162] Figure 5.13a, b and c illustrates survey-mode and high-resolution scans of carbon and nitrogen regions of EEG-N_3, respectively. The quantitative analysis shows a N/C atomic ratio of 0.011 and a C/O ratio of 2.9 after subtracting the oxygen signal from the SiO_2 substrate, which is lower than that obtained at similar conditions.[58] Figure 5.13b shows the deconvoluted XPS spectra of the C 1s peak, where the presence of C sp^2 (284.36 eV), C sp^3 (284.86 eV), C-O/C-N (286.47 eV), C═O (287.70 eV), and O═C—O (288.50 eV) bonds is confirmed.[58,218] High-resolution data showed four N 1s peaks; in organic azides, the peak at 400.17 eV corresponds to the two lateral nitrogen atoms, and the one at 403.44 eV to the central nitrogen in the azide group.[243–245] We assigned the peak at 398.97 eV to N-C[224,246] and 407.05 eV to N-O.[247,248] We conclude that the azide group has been attached to the graphene surface by simultaneous electrochemical and azide functionalisation, so the next step was the "click chemistry reaction" to bond the synthesised TU molecule to the flakes.

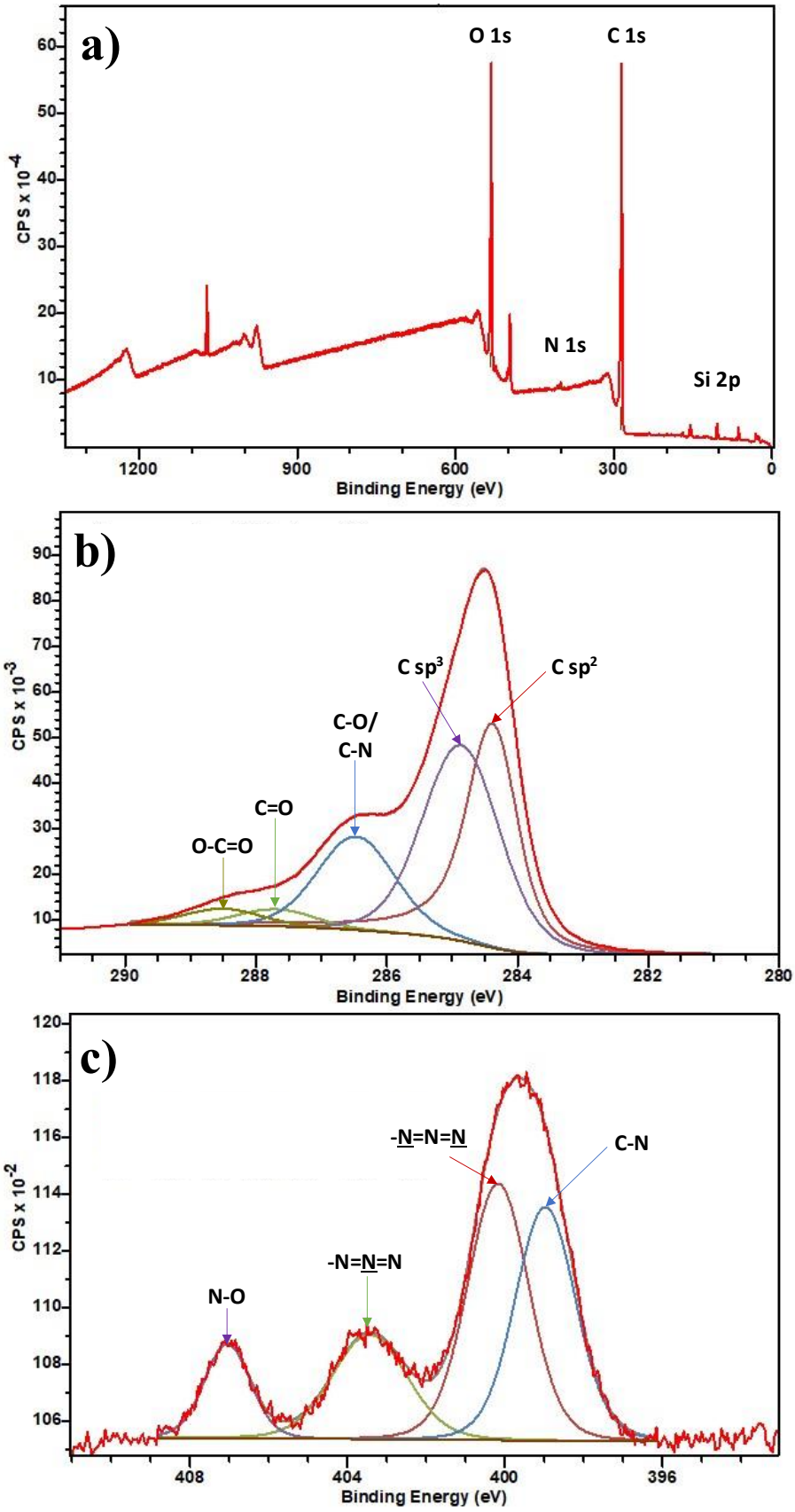

Figure 5.13 a) XPS survey mode, b) High resolution C 1s region and c) High resolution N 1s region for azidated EEG.

XPS survey mode, high-resolution C 1s and N1s scans on sample EEG-TU are illustrated in Figure 5.14a, b, and c, respectively. The quantitative analysis shows a N/C atomic ratio of 0.048 and a C/O ratio of 3.9 after subtracting the oxygen signal from the SiO_2 substrate. As expected, the increase in these ratios is due to the introduction of the thiourea derivative selector. Also, the fluor peak confirms the bonding of the selector. The C 1s scan in Figure 5.14b was deconvoluted in seven peaks: sp^2 C (284.45 eV), sp3 C (284.95 eV), C-O/C-N (286.24 eV), C═O (287.26 eV), O═C—O (288.59 eV), C graphitic (291.18 eV) and CF_3 (292.84 eV).[58,218,249] Figure 6.12c shows the N 1s region; the peaks at 398.87 eV and 400.32 eV correspond to N-C/N-H and N=N, respectively.[247,250] Assuming that the absence of the ~404 eV peak corresponding to the central nitrogen in the azide group is correlated only to product formation, we can deduce the conversion to EEG-TU.[243]

As we can see, according to the C 1s spectra, they do not show any significant difference before (EEG-N_3) and after click chemistry (EEG-TU); we can infer that the carbon structure is preserved.

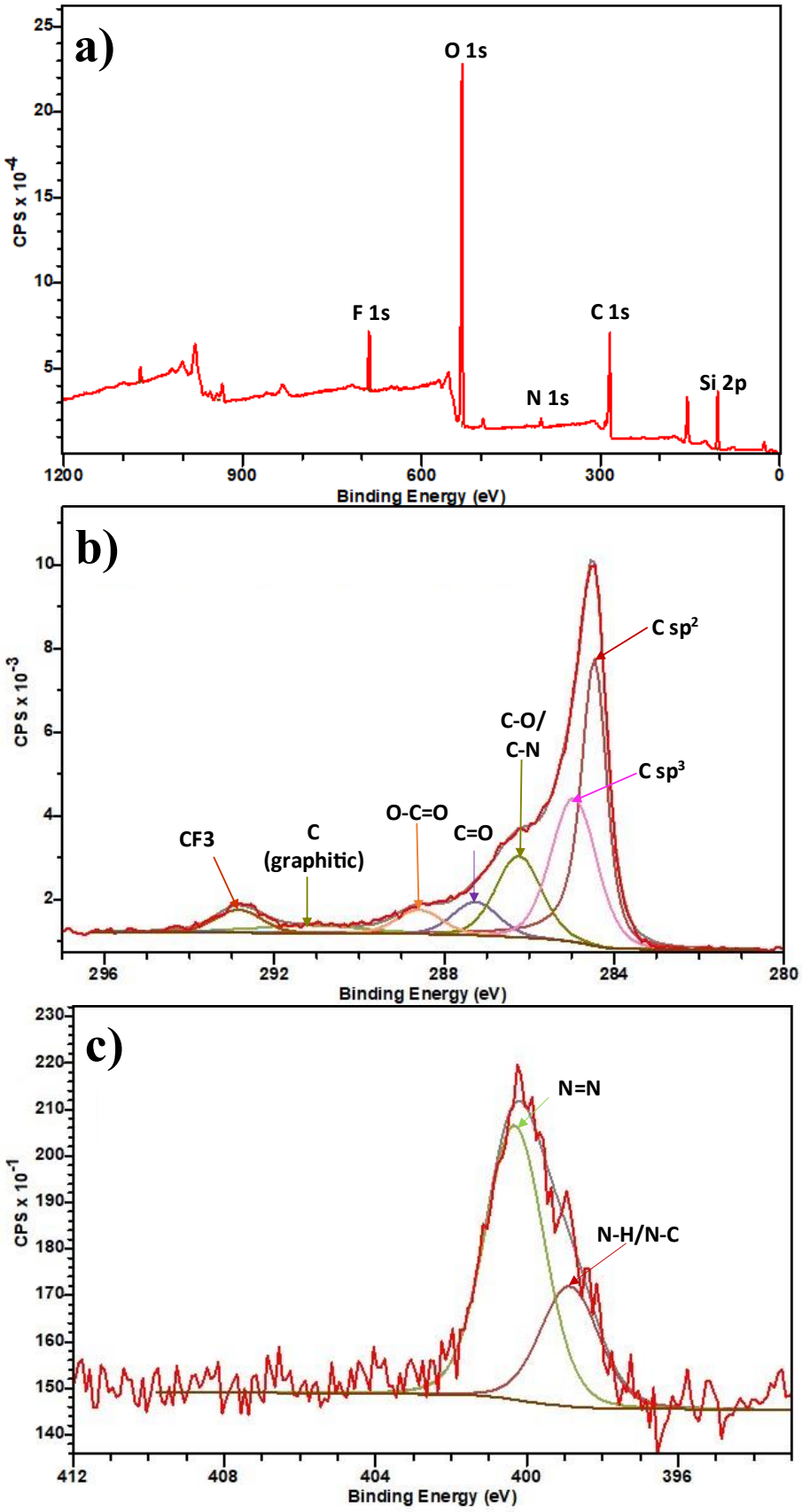

Figure 5.14a) XPS survey mode, b) High-resolution C 1s region and c) High-resolution N 1s region after click chemistry (EEG-TU).

5.9 Sheet resistance

A conductive network is a fundamental requirement in the development of graphene-based chemiresistors. Hence, the measurement of sheet resistance was conducted to track the alterations in graphene's electrical properties during the functionalization procedures. The Van der Paw method was used, as described in Section 2.8. Three different positions for each sample were measured. The average sheet resistance and standard deviation are summarised in Figure 5.15 and Table 5-4.

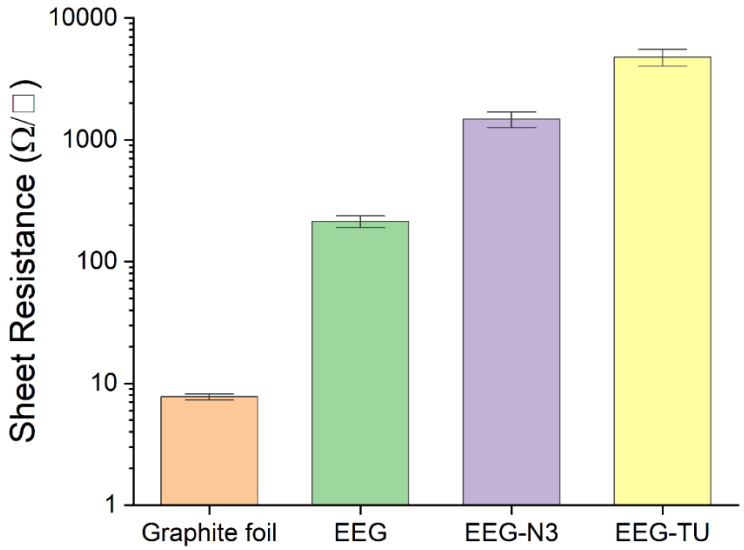

Figure 5.15 Sheet resistance after each functionalisation step.

Table 5-4 Sheet resistance mean and standard deviation after each functionalisation step.

Sample	Mean sheet resistance (Ω/□)	Standard deviation (Ω/□)
Graphite foil	7.75	0.45
EEG	214.00	22.99
EEG-N3	1475.52	216.14
EEG-TU	4770.55	756.73

As observed in Figure 5.15 covalent functionalisation causes changes to graphene's electrical properties. The disruption of the carbon lattice after introducing azide groups and the thiourea derivative selector will increase the sheet resistance compared to graphite foil

and EEG.[58,251] Even when resistivity is increased an electrical network is still preserved, making possible the development of graphene-based chemical resistors.

To demonstrate the suitability of the graphene flakes to develop a chemical resistor, EEG-N_3 flakes were deposited on a commercial interdigitated electrode (Micrux, IDE3-AU) by Langmuir-Blodgett deposition, and the measured resistance was 97 Ω. The flakes work as a bridge between the electrode gaps which is 5 μm (Figure 5.16). The flakes preserved their electrical properties even when they are functionalised, making them suitable for electrode fabrication, as it will be discussed in Section 6.3.

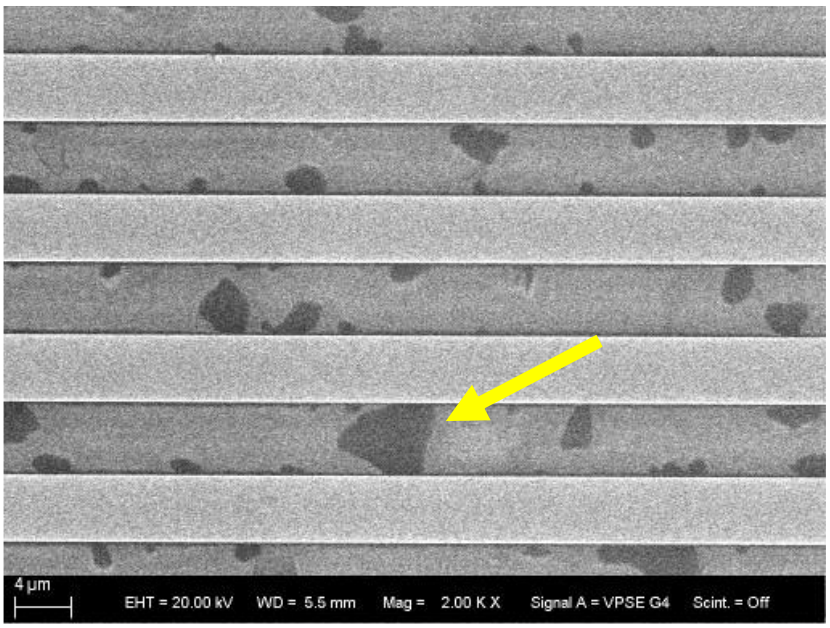

Figure 5.16 Interdigitated electrode, the yellow arrow points out a graphene sheet.

5.10 Conclusion.

The current chapter details the one-step electrochemical synthesis of bulk azidated graphene in an aqueous solution. The significance of this lies in the fact that previous research has mainly focused on utilising graphene oxide (GO) as a precursor for azidated graphene. The azidation of GO leads to the generation of a larger amount of toxic waste due to the inclusion of various steps in both synthesis and functionalization. Additionally, the required reduction step for restoring its conductive network has the risk of transforming azide groups into amino groups, decreasing the functionalisation degree through click chemistry reaction.

There is one study that reported the simultaneous exfoliation and functionalisation of a single graphite flake with azide groups. By employing commercially available graphite foil, we were able to generate significantly higher amounts of monolayer and few layer graphene in just one pot procedure, while preserving the electrical conductivity. The azidated groups were used to introduce a selector molecule through copper(I)-catalysed alkyne–azide cycloaddition, for the selective gas detection of cyclohexanone as further explained in Section 6.3.

Here, simultaneous electrochemical exfoliation and functionalisation using an anodic exfoliation process produced single-layer and few-layer graphene flakes of ~3 μm lateral size according to AFM measurements, and there is no significant difference between different voltage or if a buffer solution instead of water is used to prepare the electrolyte solution. The XRD technique confirmed the successful intercalation of the ions between the graphite layers; SEM observation showed how the layers in graphite foil were expanded and TEM observations confirmed the presence of single and few-layer graphene applying +7 V to graphite foil and using an aqueous solution of 0.2 M Na_2SO_4 and 0.1 M NaN_3.

The XPS analysis revealed that sodium azide groups are attached to the graphene surface, also supported by TGA analysis. The successful grafting of the TU derivative selector (1-(3,5-bis(trifluoromethyl)phenyl)-3-(prop-2-yn-1-yl)thiourea) to them was confirmed by the disappearance peak around 404 eV in the high-resolution nitrogen region. After each functionalisation step, there is an increase in the sheet resistance; this could be due to some disruption in the graphene lattice. However, Raman spectra did not show changes in the D peak after each functionalisation step, this signal can be related to the

laser spot size due to the small lateral dimension of the flakes more than the graphene's lattice disruption.

The successful click chemistry procedure on simultaneous electrochemical exfoliation and functionalisation of graphene flakes with azide groups on the surface opens the door to exploring more applications due to their specific functionalisation. So, this can be extended to graphene sensors for biomedical applications and gas sensors in chemiresistors or field effect transistors (FET) with higher selectivity through the analyte.

6 Graphene-based sensors for cyclohexanone detection.

A good gas sensor needs to provide high sensitivity to detect low concentrations of the target gas, rapid response, reversible operation, good selectivity towards the analyte of interest, low-manufacturing cost, stable operation over multiple cycles of usage, and low power consumption during the operation.[252] Due to their simplicity, ease of production, low cost, and capability of detecting toxic and volatile gases under different conditions, chemiresistive gas sensors are widely studied. The interaction of an analyte with graphene changes the electronic properties of graphene such as band structure, Fermi level, carrier concentration and density of states profiles. This combination results in a measurable current change. In this chapter, graphene is used as a chemiresistor sensor, where its response depends on the type of analyte. These sensing devices can exhibit an ***n***- or ***p***-type behaviour, and their response can be measured as an increase or decrease in the current when a constant voltage is applied. Of course, the behaviour is also influenced by the type of analyte gas, which can be electron-donor or electron-acceptor.[253,254]

The interactions between donor and acceptor molecules with graphene surfaces have been investigated using density functional theory (DFT); the results showed that the adsorption of these molecules does not disrupt the graphene lattice and no evidence of chemical bonding was found. The interaction between them and the graphene surface is by physisorption, revealing the fundamental role played by van der Waals forces. In addition, the carrier type and concentration of graphene can be regulated through the kind of the adsorbed molecule. According to the experimental results, defects on the surface of graphene can influence the interactions, improving the sensing response when exposed to gases.[255] Here, two different graphene production process will be used in the design of graphene-based gas sensor devices, chemical vapour deposition and electrochemical exfoliation. As it was demonstrated in Chapter 5, the synthetised graphene has low defects according to Raman spectroscopy; however, more defective few-layer graphene flakes were produced according to Chapter 5, the defects can be due to the introducing oxygen functional groups during the exfoliation process.[46]

Nowadays, there is a particular concern about explosive-based weapons; they remain the preferred tools of terrorism and are a continuing concern to society. Therefore, the need for sensors capable of detecting vapour markers in real-time is increasingly important. Cyclohexanone is a non-explosive vapour marker used to recrystallise cyclotrimethylenetrinitramine (RDX) in explosive formulations. Previous research

demonstrated that Single-walled carbon nanotubes (SWCNTs) responded more to cyclohexanone when they were functionalised (non-covalently or covalently) with thiourea derivatives.[84,108,232]

Even though both carbon nanotubes (CNTs) and graphene possess unique electrical properties suitable for sensing applications, the higher activity of graphene over CNTs could be attributed to a greater surface area per unit volume.[116] Here, both chemical vapour deposition (CVD-graphene) and electrochemical exfoliated graphene (EEG) based sensors will be tested to show their sensitivity under cyclohexanone with or without functionalization. CVD-graphene was non-covalent functionalized by dropping the 1-(3,5-bis(trifluoromethyl)phenyl)-3-(prop-2-yn-1-yl)thiourea (referred to in the text as TU) sensing molecule on it, on the other hand EEG was covalently functionalized through click chemistry between the azidated graphene and alkyne-terminated thiourea derivative molecule, these procedures of functionalization are explained in Sections 3.7 and 3.6, respectively. Sensors were exposed to vapour gases such as acetone, hexane, and ethanol to evaluate the functionalisation effect on the sensing response.[256–258]

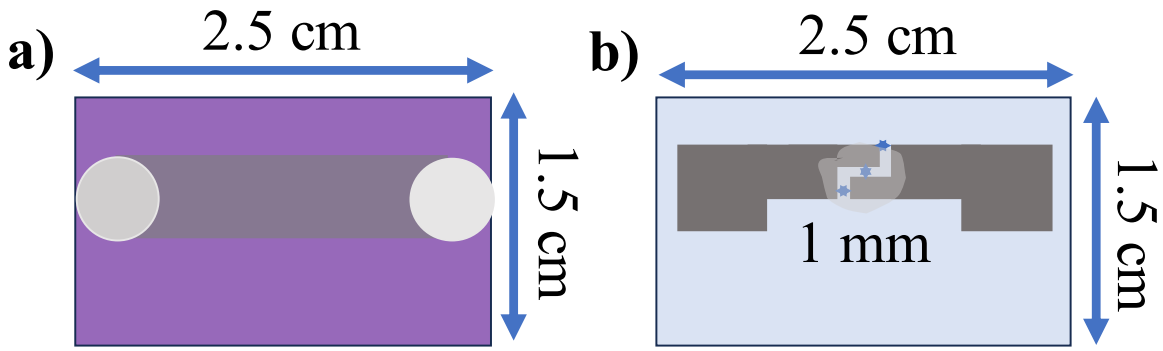

Figure 6.1 Schematic representation of a) CVD graphene-based sensors where the grey strip and light grey circles represent the CVD graphene and the silver paint, respectively. b) EEG-based sensors where the light grey stain in the middle represents the drop casted EEG flakes, and the dark grey represents the AuPd deposited electrodes that leaves 1 mm channel width.

Distinct devices were utilized to assess the electrodes, depending on whether they were fabricated from CVD graphene or flakes. Figure 6.1a illustrates an electrode based on CVD graphene which is contacted using silver paint at the ends. Figure 6.1b illustrates

gold/palladium, AuPd, electrodes deposited on a piece of glass slide using a sputter coater, followed by the addition of the solution of graphene flakes on the channel between the electrodes.

6.1 Experimental set up for testing graphene-based sensors.

A bubbler-based measurement system similar to that proposed by Kim *et al.*,[259] was used to test the sensors under different volatile organic compounds (VOCs) concentrations. This system consists of a vapor-generating bubbler, a carrier gas, and a detection chamber, as illustrated in Figure 6.2. When the gas carrier passes through the bubbler with the analyte solution, it saturates the atmosphere. To calculate the saturated vapor pressure of the analyte in the gas chamber, $\boldsymbol{P}_s$, Antoine's equation was used:[260]

$$\log_{10}(P_s) = A - \frac{B}{T + C} \qquad \textit{Eq. 6.1}$$

where ***A***, ***B***, and ***C*** are unitless constants known as Antoine's constants and ***T*** is the temperature in Kelvin or °C for $\boldsymbol{P}_s$ in bar and mm Hg, respectively. The constants for each of the VOCs tested are summarised in Table 6-1. The VOC concentration in parts per million is determined using Eq. 6.2

$$C_{ppm} = \left(\frac{P_s}{P} \times \frac{F_{VOC}}{F_{VOC} + F}\right) \times 10^6 \qquad \textit{Eq. 6.2}$$

where $\boldsymbol{P_s}$ is the saturated partial pressure in mm Hg, ***P*** is the chamber pressure (760 mm Hg), $\boldsymbol{F_{VOC}}$ is the flow in sccm of the VOC, and ***F*** is the carrier gas (Argon) flow in sccm.

Table 6-1 Antoine's parameters for each VOC (T in °C and P_s in mm Hg, except for cyclohexanone where T is in K and P_s in bar).

VOC	A	B	C	Reference
Cyclohexanone	4.10	1495.51	-63.60	261
Acetone	7.13	1219.97	230.65	262
Hexane	7.01	1246.33	232.99	
Ethanol	8.20	1642.89	230.30	

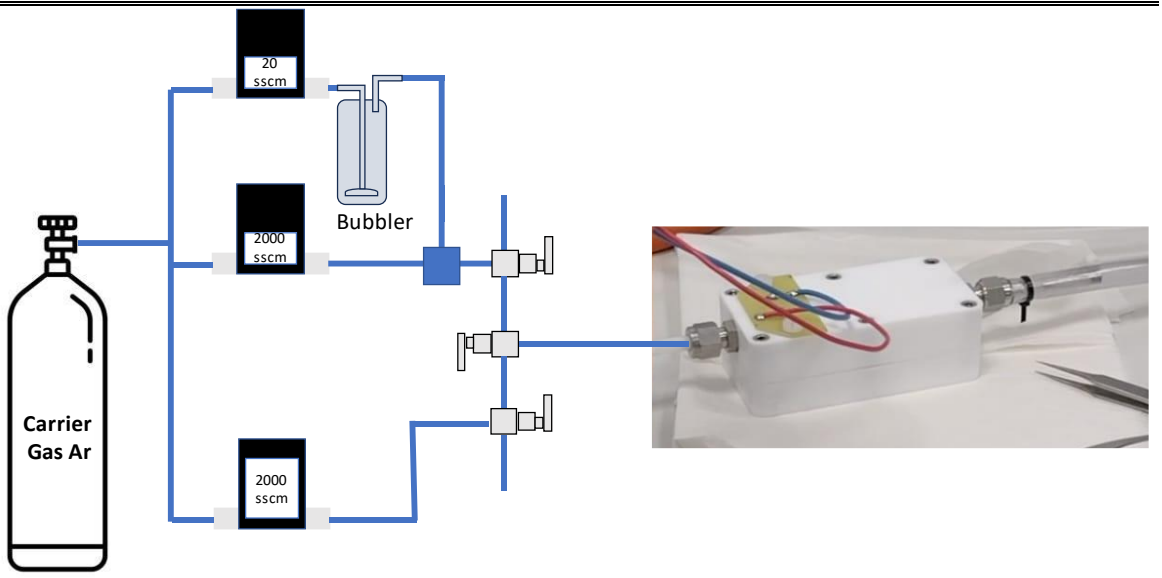

Figure 6.2 Experimental set up for gas sensing, three mass flow controllers (two for dilution and one to flushing), three three-way valves and the PTFE chamber.

The gas sensors were fabricated using CVD-graphene and EEG, as described in Section 3.7. The devices were placed in a PTFE gas testing chamber, 1 V was applied using a potentiostat (PalmSens4) and the current passing through the sensors was recorded using PSTrace 5.9 software provided by Palm Instruments®. The sensors (geometries in Figure 6.1a and b) were exposed to various VOCs three consecutive times and repeated in triplicate. In every experiment, exposure time to the analyte and flushing time with the carrier gas (Argon) were fixed to one minute.

The gas sensor performance can be expressed in terms of the following parameters: sensor response, sensitivity, selectivity, stability, limit of detection (LOD), linearity, response time, and recovery time. Sensor response is defined as the ratio of the variation in the resistance, conductance or current of the system with and without the analyte (gas molecules) in terms of the initial reference value. A large value indicates that material is a good sensor.[253] Here, the normalised response of the sensors was calculated using Eq. 6.3 for CVD-graphene-based sensors and Eq. 6.4 for EEG-based sensors.

$$\frac{\Delta G}{G_0}(\%) = \frac{I - I_0}{I_0} \times 100 \qquad \textit{Eq. 6.3}$$

$$-\frac{\Delta G}{G_0}(\%) = -\frac{I - I_0}{I_0} \times 100 \qquad \textit{Eq. 6.4}$$

where $\boldsymbol{I_0}$ is the initial current before exposure to the analyte, and $\boldsymbol{I}$ is the measured current over time. The sensitivity is determined from the slope of the calibration curve between the sensor response and gas concentration, so it is the rate of change of sensor response per unit change in gas concentration. Another important parameter is the selectivity which is the ability of a sensor material to distinguish between the analyte and other gases. As many of sensors are sensitive to many gases under similar operating conditions, the selectivity compares the signal of the sensor at the same concentration of the corresponding interfering gas.[253]

In this work, the response time was considered as the time interval over which the sensor response is 90% of the final value when it is exposed to a specific gas concentration. On the other hand, the recovery time was considered as the interval over which the sensor response reduces to 10% of its final value (after exposure to the target gas) when flushing with argon gas.[263]

Limit of detection (LOD) is the lowest concentration of the analyte which can be detected by the sensor. The theoretical LOD for cyclohexanone was calculated similarly to Li *et al*.[264] In brief, the noise for each sensor was calculated using the deviation in the response ($-\Delta G/G_0$, %) from the baseline before exposing the sensor to the analyte. Twenty-one points were taken before exposure to the cyclohexanone, and data were plotted and fitted to a 5th-order polynomial. Then, the residual sum of squares was calculated according to Eq. 6.5, where $\boldsymbol{y_i}$ is the measured data point, and $\boldsymbol{y}$ is the corresponding value from 5-th order polynomial fit. The root-mean-square noise ($\boldsymbol{rms_{noise}}$) is computed with Eq. 6.6, being $\boldsymbol{N}$, the number of data points used for curve fitting. It is considered a valid signal when the signal-to-noise ratio is equal to 3, and the LOD can be determined according to Eq. 6.7, where the slope corresponds to the linear regression fit from the calibration curve obtained at different concentrations of cyclohexanone.

$$V_{\chi^2} = (y_i - y)^2 \qquad \textit{Eq. 6.5}$$

$$rms_{noise} = \sqrt{\frac{V_{\chi^2}}{N}} \qquad \textit{Eq. 6.6}$$

$$LOD = 3\frac{rms_{noise}}{slope} \qquad \textit{Eq. 6.7}$$

6.2 CVD graphene-based sensors.

CVD graphene-based sensors were prepared using the CVD graphene synthesised and characterised according to Section 3.1, and Chapter 4, respectively. Pristine and non-covalently functionalised graphene-based sensors were compared to study the response and selectivity under cyclohexanone and other VOCs exposure. More information on preparing the sensors is given in Section 3.7. A typical normalised sensing response of each kind of CVD graphene-based sensor is shown in Figure 6.3a,b, and Figure 6.3c before and after baseline correction. The response time is approximately 45 and 10 seconds for the not functionalised and functionalised devices, respectively. The recovery time for the not functionalised sensor is 33 seconds, and for the functionalised one is 12 seconds. Under gas exposure, these sensors showed an ***n***-type behaviour, as their current increased under the gas exposure regarding the baseline.[265]

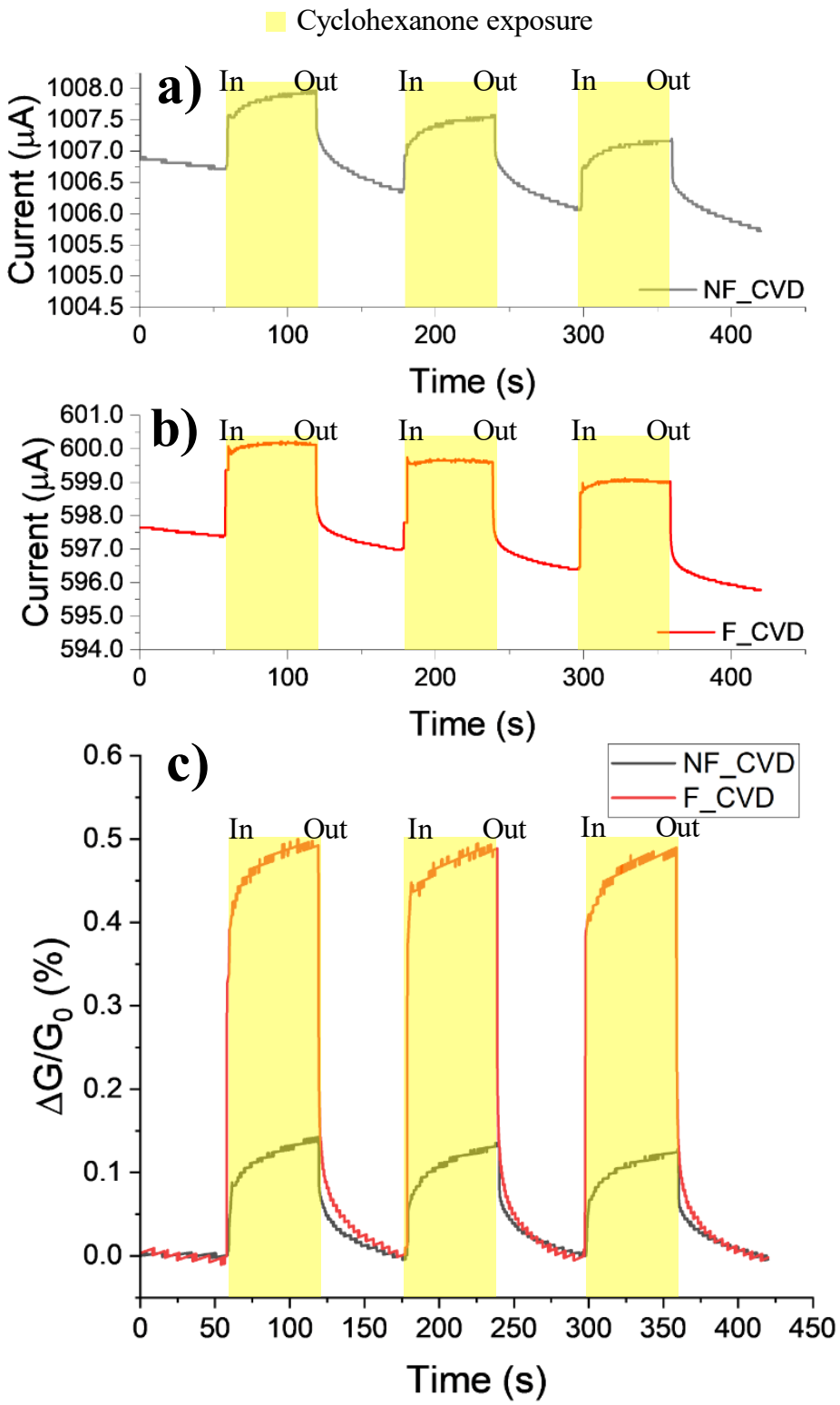

Figure 6.3 Current change in a) non and b) functionalised CVD-graphene-based sensors, c) plot of normalized conductive change and base line correction of CVD-graphene-based sensors with or without functionalisation, under 54 ppm of cyclohexanone exposure for 60 s and 60 s argon gas exposure.

The sensors were analysed in triplicate under 50 ppm of cyclohexanone vapour, and the results in Figure 6.4 show that a slight improvement is achieved when the sensing molecule with the thiourea functional group is deposited on the surface of the graphene film. The average response for devices that were not functionalised and devices that were non-covalently functionalised were 0.104% and 0.290%, respectively. The results presented herein agree with other studies that suggested more defects are needed to improve the sensing response.[266] After we had confirmed that the sensors could detect cyclohexanone vapours, they were tested under different concentrations of this gas.

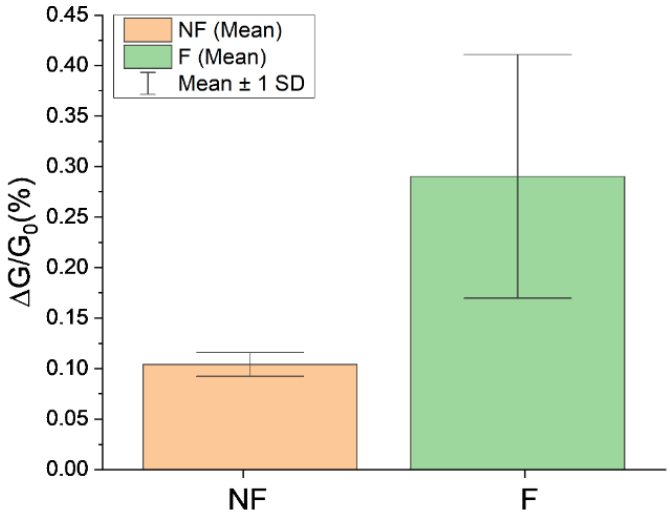

Figure 6.4 Normalised average response of non-functionalised (NF) and functionalised (F) CVD graphene-based sensors, the vertical error bars represent the standard deviation from the average based on three different devices exposed to 50 ppm cyclohexanone three times for 1 min.

The average response of monolayer graphene-based sensors exposed to different concentrations of cyclohexanone vapours, without and with selector, is summarised in Table 6-2 and plotted in Figure 6.5a and Figure 6.5b, respectively. Not functionalised and non-covalently functionalised graphene films showed a similar response, which can be attributed to the screening effect of excess of sensing molecules. Similar results were obtained when non-covalent functionalised reduced graphene oxide (rGO) based sensors were exposed to ammonia gas.[267] The considerably significant standard deviation in functionalised devices is possibly because of the non-covalent functionalisation procedure, which comprises drop-casting the selector on the surface of the graphene. However, bare

graphene is used as it comes from the transfer process; therefore, their response is more homogeneous even if they are from different batches.

Table 6-2 Mean sensor response and standard deviation of not functionalised and non-covalently functionalised CVD-graphene sensors.

Cyclohexanone vapour concentration (ppm)	Not functionalised CVD graphene		Non-covalently functionalised CVD graphene	
	Mean (%)	SD (%)	Mean (%)	SD (%)
54	0.100	0.017	0.193	0.062
131	0.206	0.018	0.262	0.038
255	0.340	0.044	0.382	0.047
368	0.426	0.044	0.478	0.072
471	0.501	0.036	0.573	0.114
583	0.592	0.041	0.654	0.138

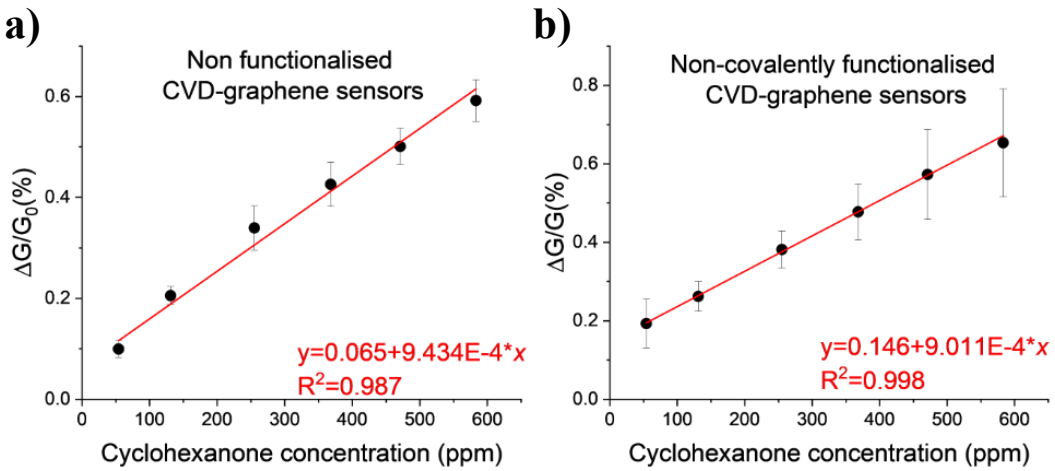

Figure 6.5 Average responses of three CVD-graphene sensors for a) non functionalised and b) functionalised devices exposed to various concentrations of cyclohexanone for 60 s and allowed to recover for 60 s.

The limit of detection for CVD-graphene-based sensors without and with functionalisation were 2.14 and 6.38 ppm, respectively. As it was suggested by Choi *et al*., free polymer residues surfaces and reduction in humidity conditions can improve the

sensor response,[268] so the control of these parameters in future studies could reveal more about the sensing mechanisms when CVD graphene-based sensors are used.

Both sensors were tested by exposing them to the various VOCs in triplicate, their responses were normalized at 50 ppm as they have different vapour pressures. The average response is summarised in Figure 6.6. The sensors exhibit high sensitivity toward 50 ppm of cyclohexanone over the other VOCs. These results confirm that even unmodified graphene has a higher affinity towards cyclohexanone detection over the rest of VOCs. Table 6-3 shows that devices with non-covalent functionalisation can increase the response by three times compared to unmodified graphene.

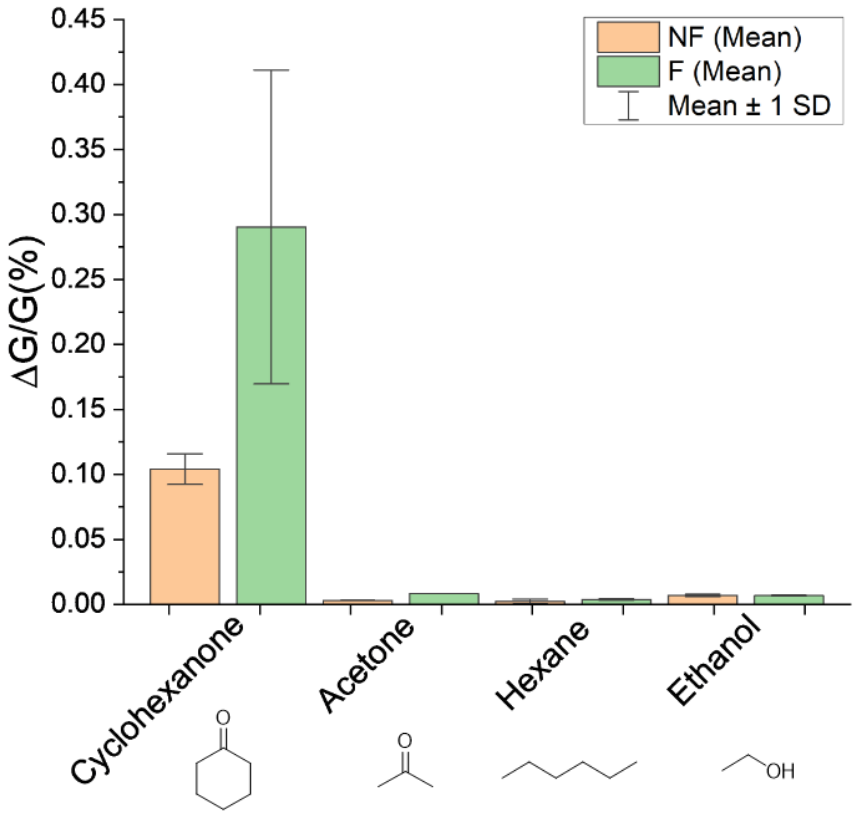

Figure 6.6 Plot of normalised average conductive change of CVD graphene-based sensors with or without functionalisation under 50 ppm of cyclohexanone vapour exposure for 1 min and 1 min recovery time.

The sensor exhibits high sensitivity and selectivity to cyclohexanone and almost not response for the other VOCs at the same concentrations even when these devices are functionalized. Yoon *et al*. discovered that the higher binding affinity to cyclohexanone is

due to the presence of strong hydrogen bonding in the TU-cyclohexanone complex. However, the response to acetone was comparatively low, despite its carbonyl group. The observed difference can be attributed to the decreased steric hindrance resulting from the cyclic nature of cyclohexanone.[108]

Table 6-3 Mean sensor response of non-functionalised and functionalised CVD graphene sensors when exposed to 50 ppm of each VOC.

Volatile organic compound	Not functionalised CVD graphene		Functionalised CVD graphene	
	Mean sensor response (%)	SD (%)	Mean sensor response (%)	SD (%)
Cyclohexanone	0.104	0.012	0.290	0.121
Acetone	0.003	1.208E-4	0.008	1.520E-5
Hexane	0.002	0.002	0.004	5.274E-4
Ethanol	0.007	9.386E-4	0.007	3.057E-4

The CVD graphene-based sensors exhibit a ***n***-type behaviour, meaning that electrons are the carriers. Electron doping in graphene causes a blue-shift of the Raman G band and a red-shift of the 2D band[269,270] when compared to previously reported Raman spectrum using a 532 nm laser excitation wavelength (G position: 1580 cm^{-1} and 2D position: 2690 cm^{-1}).[271] This is in agreement with our results from Chapter 4. Moreover, it has been demonstrated that a better adhesion of graphene to the Si/SiO_2 substrate induces a ***n***-doping effect.[272]

Considering the observed ***n***-doping behaviour of the CVD film, when an electron-donor gas molecule is adsorbed on the surface of graphene, the concentration of carriers increases, and so does the current as it was observed on our devices. Conversely, when these molecules are desorbed, the number of carriers returns to their initial value. Integrating a sensing molecule acting as a selector increases the coverage of selected molecules on the surface. However, it has been hypothesised that selectors can also change the number of carriers. The sulphur of the thiourea displays dipolar interactions with the graphene surface, increasing the resistance.[84] Then, when the cyclohexanone forms the hydrogen bonding with the hydrogens from the thiourea group (Figure 6.7), this leads to a

cancelling effect showing almost the same response as in the bare graphene. Our results agree with theoretical studies, which have shown that using high-quality graphene as a gas sensor exhibits low sensitivity, and they have determined that for better response, introducing defects is necessary.[273,274]

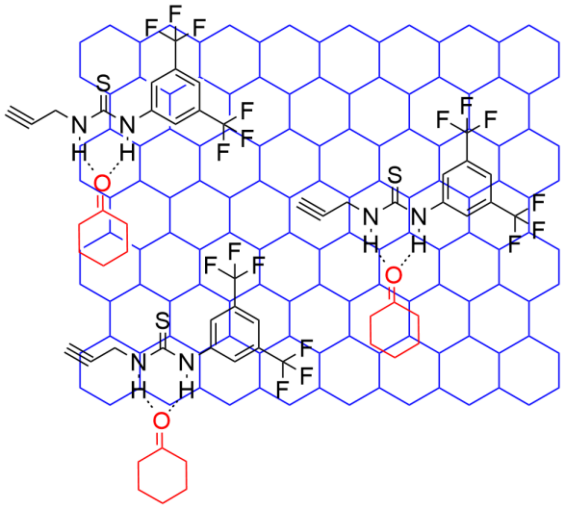

Figure 6.7 Interaction of the cyclohexanone molecule with the selector, used in non-covalent functionalisation of CVD-graphene.

6.3 Electrochemical exfoliated graphene-based sensors.

Following the idea that defects improve the sensitivity, the EEG-based sensors were investigated, as defects are introduced on the graphene lattice during electrochemical exfoliation. EEG-based sensors were prepared using the EEG synthesised and characterised according to Section 3.4 and Chapter 5. Pristine EEG and covalently functionalised sensors were studied to determine their response to cyclohexanone and other VOCs, and they were tested in triplicate. Figure 6.8a and b show the raw data, and Figure 6.8c shows the typical sensor response of non-functionalised and functionalised sensors after the baseline correction. The response time is 47 and 40 seconds, respectively. Meanwhile, the recovery time is approximately 40 seconds in both cases. The baseline drift could be attributed to the lower rates of desorption of the gas molecules from the interlayer space of adjacent graphene flakes.

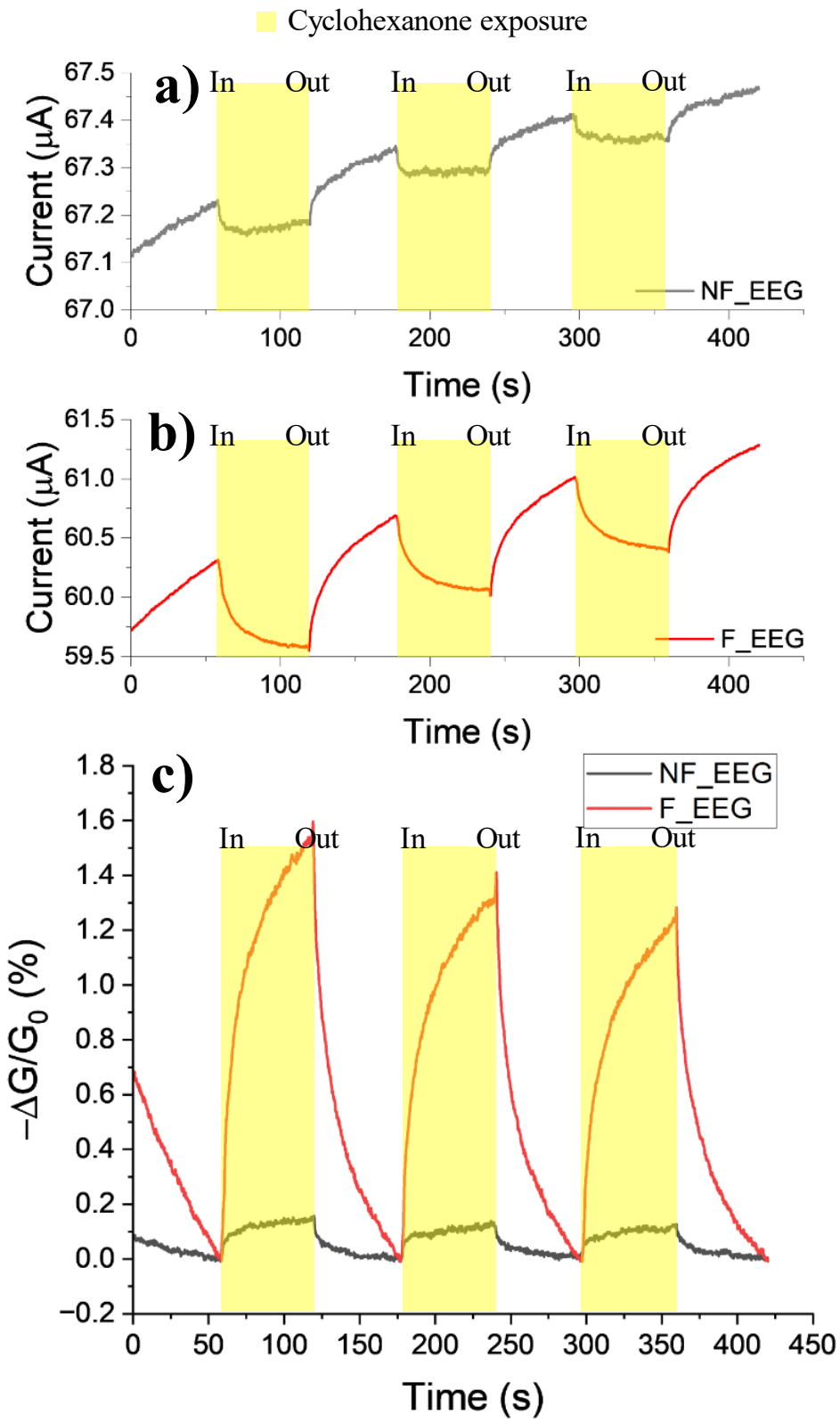

Figure 6.8 Current change in a) non and b) functionalised EEG-based sensors, c) plot of normalized conductive change and base line correction of EEG-based sensors with or without functionalisation, under 54 ppm of cyclohexanone by 60 s and 60 s argon gas exposure.

The improvement in the sensing response can be linked to the high density of defects on the graphene lattice. Yeo *et al*. have shown that the sensing responses of defective graphene increase as the number of defects increases.[266] The decrease in the response time after functionalisation reflects the effect of the sensing molecule (TU) on the attraction of the cyclohexanone analyte.[84,108] The similarity of recovery times between functionalised and non-functionalised devices can be explained due to the stronger adsorption on the defects, as it was previously reported by Zhang *et al*.[266,273]

Figure 6.9 shows the average response of three devices with and without functionalisation, measuring 0.085% and 0.715%, respectively. The response increases 7 times with respect to the non-functionalised graphene when the selector is attached by covalent functionalisation to the EEG flakes.

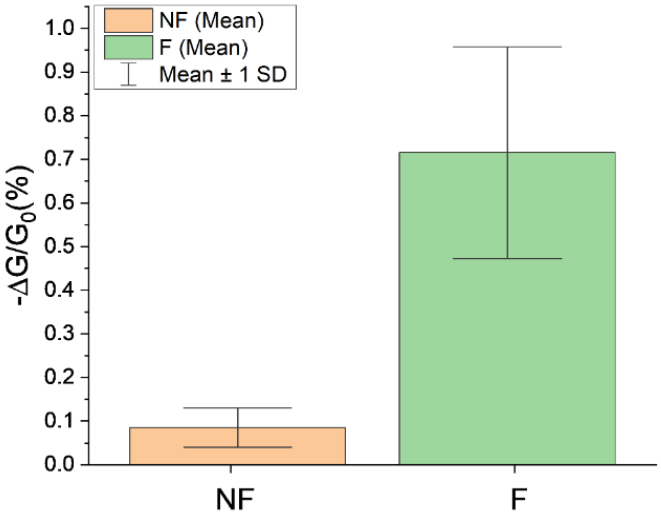

Figure 6.9 Normalise average response of not functionalised and functionalised graphene flakes. Error bars represent the standard deviation from the average based on three different devices exposed to 50 ppm cyclohexanone three times for 1 min.

The average response of EEG-based sensors exposed to different concentrations of cyclohexanone vapours, without and with the selector, is summarised in Table 6-4 and plotted in Figure 6.10a) and Figure 6.10b), respectively. The response to higher concentrations shows a marked improvement when the selector (TU) is introduced covalently, highlighting it role in improving the sensitivity. This is further supported by the estimations of the limit of detection. For EEG-based sensors with and without functionalisation, the limits of detection were 4.55 ppm and 27.24 ppm, respectively.

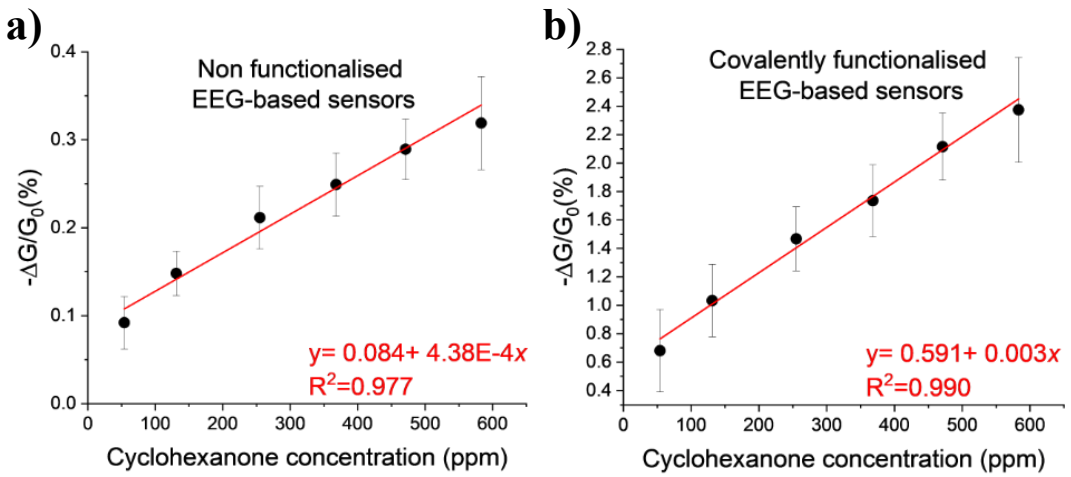

Figure 6.10 Average responses of three EEG-based sensors for a) non functionalised and b) functionalised devices exposed to various concentrations of cyclohexanone for 60 s and allowed to recover for 60 s.

Table 6-4 Sensor response of three different not functionalised graphene-flakes sensors.

Cyclohexanone vapour concentration (ppm)	Not functionalised graphene flakes		Functionalised graphene flakes	
	Mean sensor response (%)	SD (%)	Mean sensor response (%)	SD (%)
54	0.092	0.029	0.681	0.290
131	0.148	0.025	1.033	0.256
255	0.212	0.036	1.468	0.225
368	0.249	0.036	1.736	0.252
471	0.289	0.035	2.116	0.236
583	0.319	0.053	2.375	0.369

Both sensors were tested to under exposure to different VOCs and experiments were done in triplicate. Their responses were compared normalized at 50 ppm as they have different vapour pressures. The average response is summarised in Figure 6.11, highlighting the fact that including a selector molecule (TU) improves the selectivity of the molecule. Table 6-5 shows that functionalised devices can increase the response up to seven times compared to the non-functionalised devices.

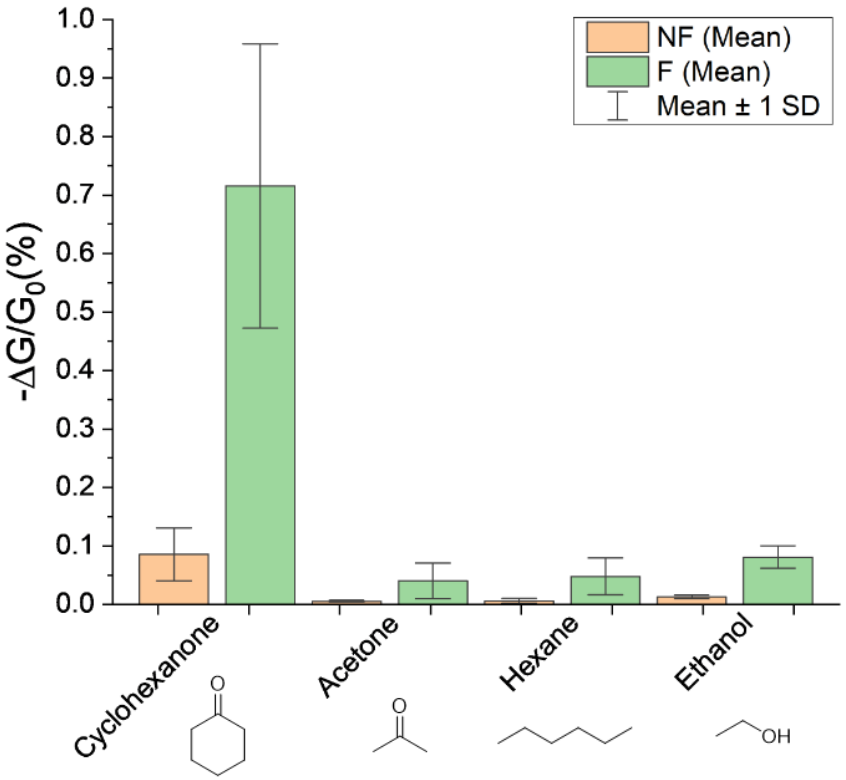

Figure 6.11 Plot of normalised average conductive change of graphene flakes sensors with or without functionalisation under 50 ppm of cyclohexanone vapour exposure for 1 min and 1 min recovery time.

Table 6-5 Mean sensor response of not functionalised and functionalised graphene flakes sensors when exposed to 50 ppm of each VOC.

Volatile organic compound	Not functionalised graphene flakes		Functionalised graphene flakes	
	Mean sensor response (%)	SD (%)	Mean sensor response (%)	SD (%)
Cyclohexanone	0.085	0.045	0.715	0.243
Acetone	0.005	0.002	0.040	0.030
Hexane	0.006	0.004	0.048	0.031
Ethanol	0.013	0.003	0.081	0.020

From all de VOCs tested, the sensor exhibits high sensitivity and selectivity to cyclohexanone at the same concentrations. The detection of cyclohexanone has been observed in sensors utilizing carbon nanotubes (CNTs).[84,108,232] However, the precise mechanism behind their preferential response to cyclohexanone over other molecules has yet to be elucidated. First, we need to consider that networks formed by graphene nanosheets are junction-limited, that is, the graphene-graphene junction resistance (R_J) is greater than the intrinsic resistance of an individual graphene flake (R_{Gr}).[275] This means that for chemical resistors, the resistivity changes observed have a major contribution from R_J. Because the surface of graphene is functionalised with a selector molecule, when the network of functionalised graphene is deposited, the selector molecule will form a bridge where current will flow, inducing a polarization effect on the sensing molecule. This is illustrated in Figure 6.12.

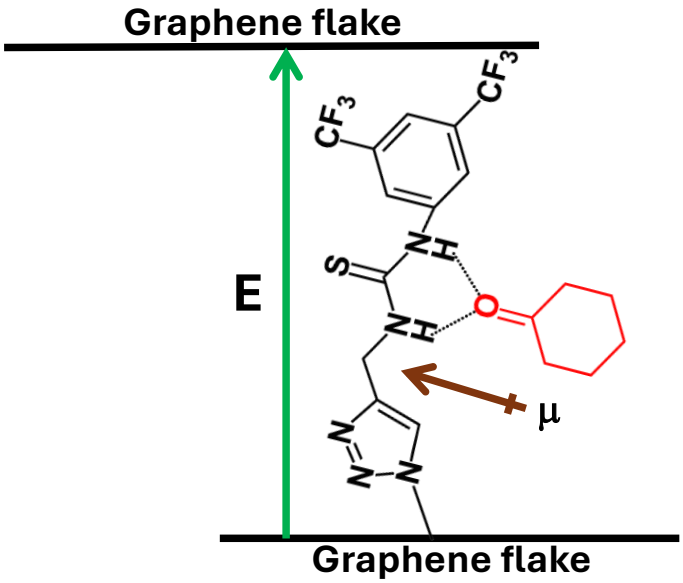

Figure 6.12 Interaction between the selector and cyclohexanone in covalent functionalised graphene flakes (EEG-TU). Where the green arrow indicates the electric field (E) and the brown arrow indicates the collective dipole moment (μ).

The examination of the polarizability of the analytes can provide insights into the selectivity towards cyclohexanone. Polarizability is the ability of a molecule to deform its electronic cloud when an electric field is applied. Experiments involving a single molecule as a junction, have showed that the resistance (***R***) increases as the polarizability of the tested molecule (***α***) increases.[276] Since the polarizability is related to the dipole moment (***μ***) and the electric field (***E***) as $\boldsymbol{\mu = \alpha E}$, a change induced by the dipole-dipole interaction between the sensing molecule and selector, should induce a change in the junction resistance. In general, for the dipole induced and a dipole interaction between the selector and the analyte we can write:[277]

$$E_{interaction} \propto \left(\mu^2_{selector}\alpha_{analyte} + \mu^2_{analyte}\alpha_{selector}\right) \qquad \textit{Eq. 6.8}$$

Although, the simplicity of the analysis we could expect a better sensitivity towards those molecules with higher dipolar moments and polarizabilities. In our specific case, it was previously demonstrated that the thiourea-based selector forms a hydrogen-bonded complex with cyclohexanone, enhancing the collective dipolar moment, changing the resistance of the graphene network.[84] We are aware that this argument must be further explored and considered carefully as the polarizabilities and dipolar moments of the

sensing molecule are not known. However, this simple argument can explain observations from this work and in other studies.[84,108] While acetone can form hydrogen bonds too, it has a very low polarizability which agrees with our results and previous ones, showing a low response. Moreover, hexane is a non-polar molecule that cannot form any hydrogen bonding, but it has a high polarizability (11.63 $Å^3$)[278] therefore showing a minimal response, comparable to that of acetone.

As the EEG-based sensors show ***p***-type behaviour, holes and not electrons are the carriers. This is in agreement with the work Ching-Yuan *et al*. which suggested that electrochemically exfoliated graphene sheets can be ***p***-doped, due to SO_4^{2-} charged impurities.[49] Then when adsorbing electron-donor gas molecules, the concentration of carriers decreases, and so does the current. On the contrary, when these molecules are desorbed, the number of carriers returns to their initial value. Ultimately, the functionalisation with a selective molecule increases the adsorbing sites that improve the selectivity of graphene.[265]

The EEG-based sensors open the possibilities for specific gas detection by functionalising them with a selective molecule, which preferentially respond to the analyte of interest. When argon instead of air is used as a carrier gas, lower sensor responses are obtained in adsorption/desorption sensing mechanisms, so the carrier change could also improve the sensing response due to the oxidative environment.[279]

Table 6-6 shows the summary of the performance parameters for the graphene-based gas sensors. It is observed a better performance by the EEG-TU which has covalently attached the TU selector.

Table 6-6 Summary of graphene-based gas sensors performance parameters under cyclohexanone exposure.

	Response at 50 ppm (%)	LOD (ppm)	Sensitivity (% / ppm)	Response time (s)	Recovery time (s)
CVD-NF	0.104	2.14	9.4×10^{-4}	45	33
CVD-F	0.290	6.38	9.0×10^{-4}	10	12
EEG-NF	0.085	27.24	4.4×10^{-4}	47	40
EEG-F	0.715	4.55	3.0×10^{-3}	40	40

6.4 Conclusion.

In this work, chemical sensors for cyclohexanone based on CVD graphene films and electrochemically exfoliated graphene flakes were prepared and studied. Since it was found that the thiourea based selector can bind to other molecules through hydrogen bonding, the devices were exposed to other preselected analytes (ethanol, acetone, and hexane) in order to assess the selectivity of the sensors towards cyclohexanone.

High-quality graphene synthetised by CVD was used to fabricate monolayer graphene-based gas sensors. Both unmodified graphene and non-covalently functionalised graphene were able to detect cyclohexanone vapour. Moreover, from the calibration curve both of them showed a similar sensitivity ($\Delta G/\Delta C$) and limit of detection. This was explained by the screening effect of the thick TU layer which prevented graphene to detect the change in the electrical current. Furthermore, the response and recovery time were lower in non-covalently CVD graphene-based sensors. Almost no response was observed towards VOCs (acetone, hexane, and ethanol). The results showed good reproducibility from devices to device when they are not functionalised, suggesting that the functionalization process needs to be standardised to reduce the variation between devices.

Electrochemically exfoliated graphene flakes can offer an advantage by increasing the surface area and the number of adsorption sites. Therefore, it is reasonable to think that the addition of a selector molecule can improve the response for cyclohexanone detection. From response and recovery times we can infer that some bonds could form with oxygen moieties, explaining the drift in the base line, because the molecules can detach quickly from the TU selector but not from the oxygen moieties present in both sensors with and without functionalisation. The devices showed a selective response for cyclohexanone when compared to other VOCs. Here we explained the better affinity of the selector molecule toward cyclohexanone in terms of the polarizability of the analytes. Although analytes such as acetone and ethanol, can form hydrogen bonding, they have much lower polarizabilities than cyclohexanone. This is in agreement with previous experimental works on CNTs reported from Swager group.[84,108]

In conclusion, sensors based on electrochemically exfoliated graphene are more sensitive than those based on CVD non-covalently functionalised. This is advantageous considering that the electrochemical exfoliation is a simpler process and more cost effective. The azide groups on the graphene flakes, open the possibility introducing

different selector molecules through click chemistry to tailor the selectivity towards other molecules.

7 Overall conclusions and future work.

The remarkable properties of graphene, including optical transparency, high electrical conductivity, mechanical strength, excellent thermal conductivity, and large surface area, have generated significant interest for its potential applications across various scientific and technological fields. Moreover, its potential for functionalisation establishes it as an ideal candidate for the creation of sensors with specialised selectivity towards molecules of interest in a multitude of research fields. The choice of graphene production methodology for such applications is dependent upon the desired attributes. In general, graphene synthesised by chemical vapor deposition (CVD) demonstrates enhanced properties in comparison to chemically exfoliated graphene, characterised by platelets containing multiple oxygen containing groups on their surface and often monolayer to a few-layer in thickness. As mentioned in Section 1.5, the primary goal of this research was to assess and compare the performance of graphene, produced by two different methodologies, in terms of its selective response to cyclohexanone compared to other volatile organic compounds. Among the methods discussed in the introduction, two approaches were selected: chemical vapour deposition that yields mainly monolayer graphene and electrochemical exfoliation that is scalable.

The first and second research objectives were achieved, and their results discussed in Chapter 4. There, a simple setup to produce graphene by low pressure chemical vapour deposition was reported in detail with the sole purpose of making it accessible for use in non-graphene specialist laboratories. Moreover, we demonstrated that using off-the-shelf copper with no pretreatment we were able to obtain graphene that was similar in quality. More specifically, we used Raman spectroscopy as an easy and non-destructive methodology to assess the quality of the graphene films synthesized. The statistical approach here is not trivial, and the graphene sector is still facing the lack of a tool to assess a batch-to-batch reproducibility and quality. Here, it was determined the minimal number of spectra required to ensure statistical accuracy when mapping and characterising the graphene films, simplifying the process of sampling a graphene film. Moreover, the guidelines from the National Physical Laboratory (UK), provided us with a framework for the identification of monolayer structure based on metrics such as de FWHM 2D and the I_{2D}/I_G ratio. From our observations variations between the positions in the reactor chamber and from one batch to another were observed, which can be explained by residual strains ($\leq$1%) and residual unintentional doping caused by the roughness of the copper substrate,

annealing and residual ferric chloride used when removing the graphene films from the copper surface. SEM, TEM and AFM were used as complementary tools for the characterisation of graphene films.

Following these results we suggest as future work the separation of the effects from doping and strain through Raman analysis. This is thoroughly explained in the work of Lee *et al*. but we will outline here the main points.[205] First, it is well established that positions of the 2D and G bands linearly shift under uniaxial or biaxial extension/compression. In a similar way, it is well known that the ratios of the positions of these bands (ΔPos2D/ ΔPosG) also have a linear dependence with the level of ***p***-doping. In light of the fact that ferric chloride has been found to induce doping in graphene films, it is rational to isolate the effects of doping and strain in order to gain a more comprehensive understanding of the variations observed in Raman measurements. We must highlight the challenge on the scarcity of data from undoped and unstrained graphene spectra, as this is the reference for any shift. This is important, as much of the research relies on correlations for the dispersion of the 2D and G bands at different excitation wavelengths to fit their results. Therefore, here it is stressed the importance of having data from free standing graphene, which can be considered as virtually charge neutral and strain free.

The results achieved from objectives 3 and 4 were discussed in Chapter 5. In that section, a one-step electrochemical synthesis of azidated graphene in an aqueous solution of sodium sulphate / sodium azide mixture was discussed. This is relevant to other reports on the production of azidated graphene that use graphene oxide as a precursor. Nevertheless, the production of GO is more time-consuming and less environmentally sustainable and often has inferior properties due to extensive oxidation. Consequently, the anodic exfoliation explored here offers a more accessible and scalable method for production of monolayer and few-layer graphene while simultaneously introducing azide groups onto the surface of graphene flakes with a reduced degree of oxidation. Our observations on the number of layer were supported by AFM and TEM/SAED pattern observation, and the identification of azide groups on the surface determined by XPS. This confirmed that the flakes had an average thickness and lateral size of 2.6 nm and 2.3 μm respectively, suggesting the formation of few-layer functionalised graphene.

The incorporation of azide groups onto the surface of graphene reported here has significant importance due to the practical implications, including tailoring the surface chemistry of graphene *via* click chemistry. Moreover, the functionalised graphene flakes

retain much of their electrical conductivity, making them suitable for the development of resistive chemical sensors. Here, we introduced a thiourea-based selector for purpose of selectively detecting cyclohexanone. XPS analysis confirmed the formation of the triazole ring from the copper catalysed alkyne-azide cycloaddition, and the grafting of thiourea-based molecule [1-(3,5-bis(trifluoromethyl)phenyl)-3-(prop-2-yn-1-yl)thiourea] on to the surface.

Since the thiourea functionalised EEG flakes can have a higher surface area and more adsorption sites than CVD films, an enhanced sensor response was predicted. Chapter 6 presented the accomplishment of research objective 5. There, it was shown that CVD based sensors showed a limit of detection of 6.32 ppm, similar to that of the EEG flakes (4.6 ppm). However, sensors based on functionalised graphene flakes are more sensitive and easier to make. Also, the devices showed a selective response for cyclohexanone when compared to other VOCs studied, including acetone, hexane, and ethanol. The implications of these findings suggest that the combination of click chemistry with a straightforward method of producing azidated graphene flakes has the potential to be utilized in the creation of diverse sensing devices, including liquid-gated field effect transistors (FET) and biological sensors.

Here, based on our results and those from the Swagger group, we proposed a simplified model based on the interaction of two dipolar molecules, through the junction formed by the sensitive molecule. In general terms, the higher the polarizabilities and dipolar moments of the sensing molecule and the analyte, the better the response of the resistive sensor and the higher response from the junction. This could explain, for example why resistive sensors are more sensitive towards cyclohexanone rather than acetone, and why nonpolar but polarizable molecules such as hexane still shows a minimal but visible response. Although simple, we consider this approach should be explored more in depth as it could provide easy design rules for other specific chemical sensors only based on these two parameters. This agrees with previous experimental results reported for carbon nanotubes from the Swager group, where the explanation on the mechanism of the selectivity and sensitivity of the selector was less discussed.[84,108] As future work the suggested sensing mechanism can be validated by tested gases able to form or not hydrogen bonding and having different polarizabilities using the same thiourea molecule from this work.

The selectivity of a sensor is always reported when the devices are exclusively exposed to the analyte one at a time, however, the sensor response under a mixture of interfering gases and the target analyte should be analysed to represent a more realistic environment. There are studies suggesting the use of dielectric spectroscopy over standard current measurements to improve the sensitivity of the devices.[280] This is an area that remains unexplored, to the best of our knowledge, for graphene based sensor at least. On the other hand, the incorporation of machine learning (ML) algorithms has demonstrated its potential to decrease the analyte exposure time during the detection and deconvolute the response upon exposure to a gas mixture.[281] We envisage the use of different functionalities to be introduce to the graphene sensors to facilitate the deconvolution of the response. Here, we highlight that azidated graphene will enable this step, as the only requirement is that the molecules have an alkyne termination.

To summarize, the key aspect of this research was to evaluate and compare the performance of chemiresistors based on graphene. These chemiresistors were synthesized using two different methods and their response to cyclohexanone and other common volatile organic compounds was examined. Each synthesis method was accompanied by a detailed procedure that showcased the properties of the synthesized material. Additionally, this provides an opportunity for other researchers to explore further applications in related fields that require tailoring the graphene chemistry.

8 References.

1 Z. Zhen and H. Zhu, in *Graphene*, Elsevier, 2018, pp. 1–12.

2 M. Sharon and M. Sharon, *Graphene: An Introduction to the Fundamentals and Industrial Applications*, John Wiley & Sons, 2015.

3 X. Wan, Y. Huang and Y. Chen, *Acc. Chem. Res.*, 2012, **45**, 598–607.

4 P. R. Wallace, *Phys. Rev.*, 1947, **71**, 622–634.

5 H. P. Boehm, R. Setton and E. Stumpp, *Carbon*, 1986, **24**, 241–245.

6 A. K. Geim and K. S. Novoselov, *Nat. Mater.*, 2007, **6**, 183–191.

7 X. Lu, M. Yu, H. Huang and R. S. Ruoff, *Nanotechnology*, 1999, **10**, 269–272.

8 K. S. Novoselov, A. K. Geim, S. V. Morozov, D. Jiang, Y. Zhang, S. V. Dubonos, I. V. Grigorieva and A. A. Firsov, *Science*, 2004, **306**, 666–669.

9 X. Li, W. Cai, J. An, S. Kim, J. Nah, D. Yang, R. Piner, A. Velamakanni, I. Jung, E. Tutuc, S. K. Banerjee, L. Colombo and R. S. Ruoff, *Science*, 2009, **324**, 1312–1314.

10 R. R. Nair, P. Blake, A. N. Grigorenko, K. S. Novoselov, T. J. Booth, T. Stauber, N. M. R. Peres and A. K. Geim, *Science*, 2008, **320**, 1308–1308.

11 S. Bae, H. Kim, Y. Lee, X. Xu, J.-S. Park, Y. Zheng, J. Balakrishnan, T. Lei, H. Ri Kim, Y. Il Song, Y.-J. Kim, K. S. Kim, B. Özyilmaz, J.-H. Ahn, B. H. Hong and S. Iijima, *Nat. Nanotechnol.*, 2010, **5**, 574–578.

12 Z. H. Ni, H. M. Wang, J. Kasim, H. M. Fan, T. Yu, Y. H. Wu, Y. P. Feng and Z. X. Shen, *Nano Lett.*, 2007, **7**, 2758–2763.

13 S. Lim, H. Park, G. Yamamoto, C. Lee and J. W. Suk, *Nanomaterials*, 2021, **11**, 2575.

14 S. De and J. N. Coleman, *ACS Nano*, 2010, **4**, 2713–2720.

15 K. I. Bolotin, K. J. Sikes, Z. Jiang, M. Klima, G. Fudenberg, J. Hone, P. Kim and H. L. Stormer, *Solid State Commun.*, 2008, **146**, 351–355.

16 J. Hass, W. A. de Heer and E. H. Conrad, *J. Phys. Condens. Matter*, 2008, **20**, 323202.

17 T. Ohta, A. Bostwick, T. Seyller, K. Horn and E. Rotenberg, *Science*, 2006, **313**, 951–954.

18 D. Metten, Université de Strasbourg, 2016.

19 L. Gao, *Graphene 2D Mater.*, 2014, **1**, 23–46.

20 C. Lee, X. Wei, J. W. Kysar and J. Hone, *Science*, 2008, **321**, 385–388.

21 C. Lee, X. Wei, Q. Li, R. Carpick, J. W. Kysar and J. Hone, *Phys. status solidi*, 2009, **246**, 2562–2567.

22 A. A. Balandin, S. Ghosh, W. Bao, I. Calizo, D. Teweldebrhan, F. Miao and C. N. Lau, *Nano Lett.*, 2008, **8**, 902–907.

23 S. Zhang, H. Wang, J. Liu and C. Bao, *Mater. Lett.*, 2020, **261**, 127098.

24 F. Schedin, A. K. Geim, S. V. Morozov, E. W. Hill, P. Blake, M. I. Katsnelson and K. S. Novoselov, *Nat. Mater.*, 2007, **6**, 652–655.

25 K. Jia, J. Zhang, Y. Zhu, L. Sun, L. Lin and Z. Liu, *Appl. Phys. Rev.*, 2021, **8**, 041306.

26 C. Backes, A. M. Abdelkader, C. Alonso, A. Andrieux-Ledier, R. Arenal, J. Azpeitia, N. Balakrishnan, L. Banszerus, J. Barjon, R. Bartali, S. Bellani, C. Berger, R. Berger, M. M. B. Ortega, C. Bernard, P. H. Beton, A. Beyer, A. Bianco, P. Bøggild, F. Bonaccorso, G. B. Barin, C. Botas, R. A. Bueno, D. Carriazo, A. Castellanos-Gomez, M. Christian, A. Ciesielski, T. Ciuk, M. T. Cole, J. Coleman, C. Coletti, L. Crema, H. Cun, D. Dasler, D. De Fazio, N. Díez, S. Drieschner, G. S. Duesberg, R. Fasel, X. Feng, A. Fina, S. Forti, C. Galiotis, G. Garberoglio, J. M. García, J. A. Garrido, M. Gibertini, A. Gölzhäuser, J. Gómez, T. Greber, F. Hauke, A. Hemmi, I. Hernandez-Rodriguez, A. Hirsch, S. A. Hodge, Y. Huttel, P. U. Jepsen, I. Jimenez, U. Kaiser, T. Kaplas, H. Kim, A. Kis, K. Papagelis, K. Kostarelos, A. Krajewska, K. Lee, C. Li, H. Lipsanen, A. Liscio, M. R. Lohe, A. Loiseau, L. Lombardi, M. Francisca López, O. Martin, C. Martín, L. Martínez, J. A. Martin-Gago, J. Ignacio Martínez, N. Marzari, Á. Mayoral, J. McManus, M. Melucci, J. Méndez, C. Merino, P. Merino, A. P. Meyer, E. Miniussi, V. Miseikis, N. Mishra, V. Morandi, C. Munuera, R. Muñoz, H. Nolan, L. Ortolani, A. K. Ott, I. Palacio, V. Palermo, J. Parthenios, I. Pasternak, A. Patane, M. Prato, H. Prevost, V. Prudkovskiy, N. Pugno, T. Rojo, A. Rossi, P. Ruffieux, P. Samorì, L. Schué, E. Setijadi, T. Seyller, G. Speranza, C. Stampfer, I. Stenger, W. Strupinski, Y. Svirko, S. Taioli, K. B. K. Teo, M. Testi, F. Tomarchio, M. Tortello, E. Treossi, A. Turchanin, E. Vazquez, E. Villaro, P. R. Whelan, Z. Xia, R. Yakimova, S. Yang, G. R. Yazdi, C. Yim, D. Yoon, X. Zhang, X. Zhuang, L. Colombo, A. C. Ferrari and M. Garcia-Hernandez, *2D Mater.*, 2020, **7**, 022001.

27 K. Edward, K. Mamun, S. Narayan, M. Assaf, D. Rohindra and U. Rathnayake,

Appl. Environ. Soil Sci., 2023, **2023**, 1–23.

28 M. Yi and Z. Shen, *J. Mater. Chem. A*, 2015, **3**, 11700–11715.

29 S. Eigler, in *Graphene Technology: From Laboratory to Fabrication*, Wiley-VCH Verlag GmbH & Co. KGaA, Weinheim, Germany, 2016, pp. 19–61.

30 S. Madhuri and S. Maheshwar, in *Graphene: An Introduction to the Fundamentals and Industrial Applications*, Wiley, 2015, pp. 167–196.

31 M. I. Kairi, S. Dayou, N. I. Kairi, S. A. Bakar, B. Vigolo and A. R. Mohamed, *J. Mater. Chem. A*, 2018, **6**, 15010–15026.

32 Q. Abbas, P. A. Shinde, M. A. Abdelkareem, A. H. Alami, M. Mirzaeian, A. Yadav and A. G. Olabi, *Materials* , 2022, **15**, 7804.

33 K. R. Paton, E. Varrla, C. Backes, R. J. Smith, U. Khan, A. O'Neill, C. Boland, M. Lotya, O. M. Istrate, P. King, T. Higgins, S. Barwich, P. May, P. Puczkarski, I. Ahmed, M. Moebius, H. Pettersson, E. Long, J. Coelho, S. E. O'Brien, E. K. McGuire, B. M. Sanchez, G. S. Duesberg, N. McEvoy, T. J. Pennycook, C. Downing, A. Crossley, V. Nicolosi and J. N. Coleman, *Nat. Mater.*, 2014, **13**, 624–630.

34 C.-H. Chuang, C.-Y. Su, K.-T. Hsu, C.-H. Chen, C.-H. Huang, C.-W. Chu and W.-R. Liu, *RSC Adv.*, 2015, **5**, 54762–54768.

35 W. S. Hummers and R. E. Offeman, *J. Am. Chem. Soc.*, 1958, **80**, 1339–1339.

36 M. S. A. Bhuyan, M. N. Uddin, M. M. Islam, F. A. Bipasha and S. S. Hossain, *Int. Nano Lett.*, 2016, **6**, 65–83.

37 N. Kumar, R. Salehiyan, V. Chauke, O. Joseph Botlhoko, K. Setshedi, M. Scriba, M. Masukume and S. Sinha Ray, *FlatChem*, 2021, **27**, 100224.

38 D. C. Marcano, D. V. Kosynkin, J. M. Berlin, A. Sinitskii, Z. Sun, A. Slesarev, L. B. Alemany, W. Lu and J. M. Tour, *ACS Nano*, 2010, **4**, 4806–4814.

39 M. F. PEREZ-PUCHETA, University of Durham, 2024.

40 E. Bourelle, B. Claude-montigny and A. Metrot, *Mol. Cryst. Liq. Cryst. Sci. Technol. Sect. A. Mol. Cryst. Liq. Cryst.*, 1998, **310**, 321–326.

41 M. Noel and R. Santhanam, *J. Power Sources*, 1998, **72**, 53–65.

42 P. Yu, S. E. Lowe, G. P. Simon and Y. L. Zhong, *Curr. Opin. Colloid Interface Sci.*, 2015, **20**, 329–338.

43 J. R. Prekodravac, D. P. Kepić, J. C. Colmenares, D. A. Giannakoudakis and S. P.

Jovanović, *J. Mater. Chem. C*, 2021, **9**, 6722–6748.

44 A. M. Abdelkader, A. J. Cooper, R. A. W. Dryfe and I. A. Kinloch, *Nanoscale*, 2015, **7**, 6944–6956.

45 H. Chen, C. Li and L. Qu, *Carbon*, 2018, **140**, 41–56.

46 A. Ambrosi, C. K. Chua, N. M. Latiff, A. H. Loo, C. H. A. Wong, A. Y. S. Eng, A. Bonanni and M. Pumera, *Chem. Soc. Rev.*, 2016, **45**, 2458–2493.

47 N. Liu, F. Luo, H. Wu, Y. Liu, C. Zhang and J. Chen, *Adv. Funct. Mater.*, 2008, **18**, 1518–1525.

48 J. Lu, J. Yang, J. Wang, A. Lim, S. Wang and K. P. Loh, *ACS Nano*, 2009, **3**, 2367–2375.

49 C.-Y. Su, A.-Y. Lu, Y. Xu, F.-R. Chen, A. N. Khlobystov and L.-J. Li, *ACS Nano*, 2011, **5**, 2332–2339.

50 K. Parvez, R. Li, S. R. Puniredd, Y. Hernandez, F. Hinkel, S. Wang, X. Feng and K. Müllen, *ACS Nano*, 2013, **7**, 3598–3606.

51 K. Parvez, Z. S. Wu, R. Li, X. Liu, R. Graf, X. Feng and K. Müllen, *J. Am. Chem. Soc.*, 2014, **136**, 6083–6091.

52 F. Beck, J. Jiang and H. Krohn, *J. Electroanal. Chem.*, 1995, **389**, 161–165.

53 F. Liu, C. Wang, X. Sui, M. A. Riaz, M. Xu, L. Wei and Y. Chen, *Carbon Energy*, 2019, **1**, 173–199.

54 V. Thirumal, A. Pandurangan, D. Jayakumar and R. Ilangovan, *J. Mater. Sci. Mater. Electron.*, 2016, **27**, 3410–3419.

55 P.-J. Yen, C.-C. Ting, Y.-C. Chiu, T.-Y. Tseng, Y.-J. Hsu, W.-W. Wu and K.-H. Wei, *J. Mater. Chem. C*, 2017, **5**, 2597–2602.

56 O. Ustavytska, Y. Kurys, V. Koshechko and V. Pokhodenko, *Nanoscale Res. Lett.*, 2017, **12**, 175.

57 Y. Yang, W. Shi, R. Zhang, C. Luan, Q. Zeng, C. Wang, S. Li, Z. Huang, H. Liao and X. Ji, *Electrochim. Acta*, 2016, **204**, 100–107.

58 W. Li, Y. Li and K. Xu, *Nano Lett.*, 2020, **20**, 534–539.

59 W. Norimatsu and M. Kusunoki, *Semicond. Sci. Technol.*, 2014, **29**, 064009.

60 X.-Y. Wang, A. Narita and K. Müllen, *Nat. Rev. Chem.*, 2017, **2**, 0100.

61 A. Roberto Ruiz Hernández, A. Gutierrez Cruz and J. Campos-Delgado, in *Graphene - A Wonder Material for Scientists and Engineers*, eds. M. Ikram, A.

Maqsood and A. Bashir, IntechOpen, 2023, p. 220.

62 M. Saeed, Y. Alshammari, S. A. Majeed and E. Al-Nasrallah, *Molecules*, 2020, **25**, 3856.

63 H. Arjmandi-Tash, N. Lebedev, P. M. G. van Deursen, J. Aarts and G. F. Schneider, *Carbon*, 2017, **118**, 438–442.

64 X. Li, W. Cai, J. An, S. Kim, J. Nah, D. Yang, R. Piner, A. Velamakanni, I. Jung, E. Tutuc, S. K. Banerjee, L. Colombo and R. S. Ruoff, *Science*, 2009, **324**, 1312–1314.

65 X. Li, Y. Zhu, W. Cai, M. Borysiak, B. Han, D. Chen, R. D. Piner, L. Colomba and R. S. Ruoff, *Nano Lett.*, 2009, **9**, 4359–4363.

66 H. Xin and W. Li, *Appl. Phys. Rev.*, 2018, **5**, 031105.

67 X. Li, L. Colombo and R. S. Ruoff, *Adv. Mater.*, 2016, **28**, 6247–6252.

68 S. Bhaviripudi, X. Jia, M. S. Dresselhaus and J. Kong, *Nano Lett.*, 2010, **10**, 4128–4133.

69 X. Chen, L. Zhang and S. Chen, *Synth. Met.*, 2015, **210**, 95–108.

70 Y. Wang, Y. Zheng, X. Xu, E. Dubuisson, Q. Bao, J. Lu and K. P. Loh, *ACS Nano*, 2011, **5**, 9927–9933.

71 C. T. Cherian, F. Giustiniano, I. Martin-Fernandez, H. Andersen, J. Balakrishnan and B. Özyilmaz, *Small*, 2015, **11**, 189–194.

72 Y.-R. Luo, *Comprehensive Handbook of Chemical Bond Energies*, CRC Press, 2007.

73 R. Muñoz and C. Gómez-Aleixandre, *Chem. Vap. Depos.*, 2013, **19**, 297–322.

74 X. Li, C. W. Magnuson, A. Venugopal, J. An, J. W. Suk, B. Han, M. Borysiak, W. Cai, A. Velamakanni, Y. Zhu, L. Fu, E. M. Vogel, E. Voelkl, L. Colombo and R. S. Ruoff, *Nano Lett.*, 2010, **10**, 4328–4334.

75 L. Sun, G. Yuan, L. Gao, J. Yang, M. Chhowalla, M. H. Gharahcheshmeh, K. K. Gleason, Y. S. Choi, B. H. Hong and Z. Liu, *Nat. Rev. Methods Prim.*, 2021, **1**, 5.

76 P. Y. Huang, C. S. Ruiz-Vargas, A. M. van der Zande, W. S. Whitney, M. P. Levendorf, J. W. Kevek, S. Garg, J. S. Alden, C. J. Hustedt, Y. Zhu, J. Park, P. L. McEuen and D. A. Muller, *Nature*, 2011, **469**, 389–392.

77 M. H. Ani, M. A. Kamarudin, A. H. Ramlan, E. Ismail, M. S. Sirat, M. A. Mohamed and M. A. Azam, *J. Mater. Sci.*, 2018, **53**, 7095–7111.

78 C.-M. Seah, S.-P. Chai and A. R. Mohamed, *Carbon*, 2014, **70**, 1–21.

79 M. Losurdo, M. M. Giangregorio, P. Capezzuto and G. Bruno, *Phys. Chem. Chem. Phys.*, 2011, **13**, 20836.

80 S. Ullah, X. Yang, H. Q. Ta, M. Hasan, A. Bachmatiuk, K. Tokarska, B. Trzebicka, L. Fu and M. H. Rummeli, *Nano Res.*, 2021, **14**, 3756–3772.

81 A. Shivayogimath, P. R. Whelan, D. M. A. Mackenzie, B. Luo, D. Huang, D. Luo, M. Wang, L. Gammelgaard, H. Shi, R. S. Ruoff, P. Bøggild and T. J. Booth, *Chem. Mater.*, 2019, **31**, 2328–2336.

82 G. Zhang, A. G. Güell, P. M. Kirkman, R. A. Lazenby, T. S. Miller and P. R. Unwin, *ACS Appl. Mater. Interfaces*, 2016, **8**, 8008–8016.

83 V. Georgakilas, M. Otyepka, A. B. Bourlinos, V. Chandra, N. Kim, K. C. Kemp, P. Hobza, R. Zboril and K. S. Kim, *Chem. Rev.*, 2012, **112**, 6156–6214.

84 K. M. Frazier and T. M. Swager, *Anal. Chem.*, 2013, **85**, 7154–7158.

85 J. Park and M. Yan, *Acc. Chem. Res.*, 2013, **46**, 181–189.

86 N. VS, R. T, S. Kempahanumakkagari, P. HR and P. BM, *Appl. Surf. Sci. Adv.*, 2023, **14**, 100386.

87 N. Alzate-Carvajal and A. Luican-Mayer, *ACS Omega*, 2020, **5**, 21320–21329.

88 I. A. Vacchi, C. Ménard-Moyon and A. Bianco, *Phys. Sci. Rev.*, 2017, **2**, 1–18.

89 Z. Xia, F. Leonardi, M. Gobbi, Y. Liu, V. Bellani, A. Liscio, A. Kovtun, R. Li, X. Feng, E. Orgiu, P. Samorì, E. Treossi and V. Palermo, *ACS Nano*, 2016, **10**, 7125–7134.

90 A. Criado, M. Melchionna, S. Marchesan and M. Prato, *Angew. Chemie Int. Ed.*, 2015, **54**, 10734–10750.

91 J. H. Jeong, S. Kang, N. Kim, R. Joshi and G.-H. Lee, *Phys. Chem. Chem. Phys.*, 2022, **24**, 10684–10711.

92 V. Sarmiento, M. T. Oropeza-Guzmán, M. Lockett, W. Chen, S. Ahn, J. Wang and O. Vazquez-Mena, *Nanotechnology*, 2019, **30**, 475703.

93 S. Eissa, G. C. Jimenez, F. Mahvash, A. Guermoune, C. Tlili, T. Szkopek, M. Zourob and M. Siaj, *Nano Res.*, 2015, **8**, 1698–1709.

94 W. Li, Y. Li and K. Xu, *Nano Lett.*, 2021, **21**, 1150–1155.

95 H. Aghamohammadi, R. Eslami-Farsani, M. Torabian and N. Amousa, *Synth. Met.*, 2020, **269**, 116549.

96 V. Georgakilas, J. N. Tiwari, K. C. Kemp, J. A. Perman, A. B. Bourlinos, K. S. Kim

and R. Zboril, *Chem. Rev.*, 2016, **116**, 5464–5519.

97 I. Shown and A. Ganguly, *J. Nanostructure Chem.*, 2016, **6**, 281–288.

98 H. Li, T. Duan, O. Sher, Y. Han, R. Papadakis, A. Grigoriev, R. Ahuja and K. Leifer, *RSC Adv.*, 2021, **11**, 35982–35987.

99 C. Mackin, V. Schroeder, A. Zurutuza, C. Su, J. Kong, T. M. Swager and T. Palacios, *ACS Appl. Mater. Interfaces*, 2018, **10**, 16169–16176.

100 R. Ramapanicker and P. Chauhan, in *Click Reactions in Organic Synthesis*, Wiley, 2016, pp. 1–24.

101 H. C. Kolb, M. G. Finn and K. B. Sharpless, *Angew. Chemie Int. Ed.*, 2001, **40**, 2004–2021.

102 C. W. Tornøe, C. Christensen and M. Meldal, *J. Org. Chem.*, 2002, **67**, 3057–3064.

103 V. V. Rostovtsev, L. G. Green, V. V. Fokin and K. B. Sharpless, *Angew. Chemie Int. Ed.*, 2002, **41**, 2596–2599.

104 S. Eigler, Y. Hu, Y. Ishii and A. Hirsch, *Nanoscale*, 2013, **5**, 12136.

105 A. Cernat, S. J. Györfi, M. B. Irimes, M. Tertiș, A. Bodoki, I. E. Pralea, M. Suciu and C. Cristea, *Electrochem. commun.*, 2019, **98**, 23–27.

106 P. Yáñez-Sedeño, A. González-Cortés, S. Campuzano and J. M. Pingarrón, *Sensors*, 2019, **19**, 2379.

107 X. Shen, Y. Liu, Y. Pang and W. Yao, *Electrochem. commun.*, 2013, **30**, 13–16.

108 B. Yoon, S.-J. Choi, T. M. Swager and G. F. Walsh, *ACS Sensors*, 2021, **6**, 3056–3062.

109 M. Sharon and M. Sharon, in *Graphene: An Introduction to the Fundamentals and Industrial Applications*, John Wiley & Sons, Ltd, 2015, pp. 145–165.

110 K. A. Madurani, S. Suprapto, N. I. Machrita, S. L. Bahar, W. Illiya and F. Kurniawan, *ECS J. Solid State Sci. Technol.*, 2020, **9**, 093013.

111 S. Trivedi, K. Lobo and H. S. S. Ramakrishna Matte, in *Fundamentals and Sensing Applications of 2D Materials*, Elsevier, 2019, pp. 25–90.

112 Y. H. Kwak, D. S. Choi, Y. N. Kim, H. Kim, D. H. Yoon, S.-S. Ahn, J.-W. Yang, W. S. Yang and S. Seo, *Biosens. Bioelectron.*, 2012, **37**, 82–87.

113 F. Yavari and N. Koratkar, *J. Phys. Chem. Lett.*, 2012, **3**, 1746–1753.

114 S. Yuan and S. Zhang, *J. Semicond.*, 2019, **40**, 111608.

115 E. Singh, M. Meyyappan and H. S. Nalwa, *ACS Appl. Mater. Interfaces*, 2017, **9**,

34544–34586.

116 S. S. Varghese, S. Lonkar, K. K. Singh, S. Swaminathan and A. Abdala, *Sensors Actuators B Chem.*, 2015, **218**, 160–183.

117 P. H. Salame, V. B. Pawade and B. A. Bhanvase, in *Nanomaterials for Green Energy*, eds. B. A. Bhanvase, V. B. Pawade, S. J. Dhoble, S. H. Sonawane and M. Ashokkumar, Elsevier, 2018, pp. 83–111.

118 D. Titus, E. James Jebaseelan Samuel and S. M. Roopan, in *Green Synthesis, Characterization and Applications of Nanoparticles*, Elsevier, 2019, pp. 303–319.

119 R. Gupta, D. K. Yadav, S. Deka and V. Ganesan, 2023, pp. 105–126.

120 H.-L. Guo, X.-F. Wang, Q.-Y. Qian, F.-B. Wang and X.-H. Xia, *ACS Nano*, 2009, **3**, 2653–2659.

121 A. Ul-Hamid, *A Beginners' Guide to Scanning Electron Microscopy*, Springer International Publishing, Cham, 2018.

122 M. Kaliva and M. Vamvakaki, in *Polymer Science and Nanotechnology*, ed. R. Narain, Elsevier, 2020, pp. 401–433.

123 A. Ul-Hamid, in *A Beginners' Guide to Scanning Electron Microscopy*, Springer International Publishing, Cham, 2018, pp. 1–14.

124 Y. Zhou, D. S. Fox, P. Maguire, R. O'Connell, R. Masters, C. Rodenburg, H. Wu, M. Dapor, Y. Chen and H. Zhang, *Sci. Rep.*, 2016, **6**, 21045.

125 H. Zhu, Z. Xu, D. Xie and Y. Fang, *Graphene: Fabrication, Characterizations, Properties and Applications*, Academic Press, 2017.

126 G. Kalita, K. Wakita and M. Umeno, *Phys. E Low-dimensional Syst. Nanostructures*, 2011, **43**, 1490–1493.

127 J. C. Meyer, A. K. Geim, M. I. Katsnelson, K. S. Novoselov, D. Obergfell, S. Roth, C. Girit and A. Zettl, *Solid State Commun.*, 2007, **143**, 101–109.

128 N. R. Wilson, P. A. Pandey, R. Beanland, R. J. Young, I. A. Kinloch, L. Gong, Z. Liu, K. Suenaga, J. P. Rourke, S. J. York and J. Sloan, *ACS Nano*, 2009, **3**, 2547–2556.

129 S. Park, H. C. Floresca, Y. Suh and M. J. Kim, *Carbon*, 2010, **48**, 797–804.

130 J. C. Meyer, A. K. Geim, M. I. Katsnelson, K. S. Novoselov, T. J. Booth and S. Roth, *Nature*, 2007, **446**, 60–63.

131 R. A. Shanks, in *Nanostructured Polymer Blends*, Elsevier, 2014, pp. 15–31.

132 W. Jung, J. Park, T. Yoon, T.-S. Kim, S. Kim and C.-S. Han, *Small*, 2014, **10**, 1704–1711.

133 C. J. Shearer, A. D. Slattery, A. J. Stapleton, J. G. Shapter and C. T. Gibson, *Nanotechnology*, 2016, **27**, 125704.

134 S. Ebnesajjad, in *Surface Treatment of Materials for Adhesion Bonding*, Elsevier, 2006, pp. 43–75.

135 E. Smith and G. Dent, in *Modern Raman Spectroscopy – A Practical Approach*, Wiley, 2004, pp. 1–21.

136 G. Gouadec and P. Colomban, *Prog. Cryst. Growth Charact. Mater.*, 2007, **53**, 1–56.

137 P. de Bettignies, in *Micro-Raman Spectroscopy*, De Gruyter, 2020, pp. 15–60.

138 M. K. Kavitha and M. Jaiswal, *Asian J. Phys.*, 2016, **25**, 809–831.

139 A. K. Ott and A. C. Ferrari, in *Encyclopedia of Condensed Matter Physics*, Elsevier, 2024, pp. 233–247.

140 A. C. Ferrari and D. M. Basko, *Nat. Nanotechnol.*, 2013, **8**, 235–246.

141 R. J. Nemanich, G. Lucovsky and S. A. Solin, *Solid State Commun.*, 1977, **23**, 117–120.

142 R. Gupta, D. K. Yadav, S. Deka and V. Ganesan, eds. R. T. Subramaniam, R. Kasi, S. Bashir and S. S. A. Kumar, Springer Nature Singapore, Singapore, 2023, pp. 105–126.

143 K. Kakaei, M. D. Esrafili and A. Ehsani, in *Graphene Surfaces Particles and Catalysts*, 2019, pp. 109–151.

144 R. Beams, L. Gustavo Cançado and L. Novotny, *J. Phys. Condens. Matter*, 2015, **27**, 083002.

145 L. G. Cançado, M. A. Pimenta, B. R. A. Neves, M. S. S. Dantas and A. Jorio, *Phys. Rev. Lett.*, 2004, **93**, 247401.

146 C. Casiraghi, A. Hartschuh, H. Qian, S. Piscanec, C. Georgi, A. Fasoli, K. S. Novoselov, D. M. Basko and A. C. Ferrari, *Nano Lett.*, 2009, **9**, 1433–1441.

147 A. C. Ferrari, J. C. Meyer, V. Scardaci, C. Casiraghi, M. Lazzeri, F. Mauri, S. Piscanec, D. Jiang, K. S. Novoselov, S. Roth and A. K. Geim, *Phys. Rev. Lett.*, 2006, **97**, 187401.

148 B. Liu, C.-M. Yang, Z. Liu and C.-S. Lai, *Nanomaterials*, 2017, **7**, 302.

149 D. Ye, S.-Q. Wu, Y. Yu, L. Liu, X.-P. Lu and Y. Wu, *Appl. Phys. Lett.*, 2014, **104**, 103105-1-103105–4.

150 V. Nagyte, D. J. Kelly, A. Felten, G. Picardi, Y. Shin, A. Alieva, R. E. Worsley, K. Parvez, S. Dehm, R. Krupke, S. J. Haigh, A. Oikonomou, A. J. Pollard and C. Casiraghi, *Nano Lett.*, 2020, **20**, 3411–3419.

151 S. Loganathan, R. B. Valapa, R. K. Mishra, G. Pugazhenthi and S. Thomas, in *Thermal and Rheological Measurement Techniques for Nanomaterials Characterization*, Elsevier, 2017, pp. 67–108.

152 M. Naebe, J. Wang, A. Amini, H. Khayyam, N. Hameed, L. H. Li, Y. Chen and B. Fox, *Sci. Rep.*, 2014, **4**, 4375.

153 F. A. Stevie and C. L. Donley, *J. Vac. Sci. Technol. A Vacuum, Surfaces, Film.*, 2020, **38**, 063204.

154 M. P. Seah and W. A. Dench, *Surf. Interface Anal.*, 1979, **1**, 2–11.

155 R. T. Haasch, in *Practical Materials Characterization*, Springer New York, New York, NY, 2014, pp. 93–132.

156 W. Zhang, L. Zhang, H. Zhang, L. Song, Q. Ye and J. Cai, *Mater. Res. Express*, 2018, **5**, 125601.

157 L. J. Van der Pauw, *Philips Tech. Rev.*, 1958, **20**, 220–224.

158 M. R. Anisur, R. K. S. Raman, P. C. Banerjee, S. Al-Saadi and A. K. Arya, *Surf. Coatings Technol.*, 2024, **487**, 130934.

159 K. S. Kim, Y. Zhao, H. Jang, S. Y. Lee, J. M. Kim, K. S. Kim, J.-H. Ahn, P. Kim, J.-Y. Choi and B. H. Hong, *Nature*, 2009, **457**, 706–710.

160 A. J. Pollard, K. R. Paton, C. A. Clifford and E. Legge, *Characterisation of the Structure of Graphene*, NPL Management Limited, 2017.

161 OriginLab Corporation, 2023.

162 N. Fairley, V. Fernandez, M. Richard-Plouet, C. Guillot-Deudon, J. Walton, E. Smith, D. Flahaut, M. Greiner, M. Biesinger, S. Tougaard, D. Morgan and J. Baltrusaitis, *Appl. Surf. Sci. Adv.*, 2021, **5**, 100112.

163 D. J. Morgan, *Surf. Sci. Spectra*, 2017, **24**, 024003.

164 X. Li, W. Cai, I. H. Jung, J. H. An, D. Yang, A. Velamakanni, R. Piner, L. Colombo and R. S. Ruoff, *ECS Trans.*, 2009, **19**, 41–52.

165 M. I. Kairi, M. Khavarian, S. A. Bakar, B. Vigolo and A. R. Mohamed, *J. Mater.*

Sci., 2018, **53**, 851–879.

166 A. Mahyuddin, A. K. Ismail, M. F. Omar and A. H. Karim, *Malaysian J. Fundam. Appl. Sci.*, 2021, **17**, 262–273.

167 A. Hussain, S. M. Mehdi, N. Abbas, M. Hussain and R. A. Naqvi, *Mater. Chem. Phys.*, 2020, **248**, 122924.

168 I. I. Kondrashov, M. G. Rybin, E. A. Obraztsova and E. D. Obraztsova, *Phys. status solidi*, 2019, **256**, 1800688.

169 J. Yang, P. Hu and G. Yu, *2D Mater.*, 2019, **6**, 042003.

170 J. Wang, Z. Ren, Y. Hou, X. Yan, P. Liu, H. Zhang, H. Zhang and J. Guo, *New Carbon Mater.*, 2020, **35**, 193–208.

171 T. Oznuluer, E. Pince, E. O. Polat, O. Balci, O. Salihoglu and C. Kocabas, *Appl. Phys. Lett.*, 2011, **98**, 183101.

172 A. Reina, X. Jia, J. Ho, D. Nezich, H. Son, V. Bulovic, M. S. Dresselhaus and J. Kong, *Nano Lett.*, 2009, **9**, 30–35.

173 H. C. Hong, J. I. Ryu and H. C. Lee, *Nanomaterials*, 2023, **13**, 2217.

174 L. Wang, R. Lai, L. Zhang, M. Zeng and L. Fu, *ACS Mater. Lett.*, 2022, **4**, 528–540.

175 T. Kobayashi, M. Bando, N. Kimura, K. Shimizu, K. Kadono, N. Umezu, K. Miyahara, S. Hayazaki, S. Nagai, Y. Mizuguchi, Y. Murakami and D. Hobara, *Appl. Phys. Lett.*, 2013, **102**, 023112.

176 E. S. Polsen, D. Q. McNerny, B. Viswanath, S. W. Pattinson and A. John Hart, *Sci. Rep.*, 2015, **5**, 10257.

177 I. Vlassiouk, M. Regmi, P. Fulvio, S. Dai, P. Datskos, G. Eres and S. Smirnov, *ACS Nano*, 2011, **5**, 6069–6076.

178 F. Qing, Y. Zhang, Y. Niu, R. Stehle, Y. Chen and X. Li, *Nanoscale*, 2020, **12**, 10890–10911.

179 C. Cai, F. Jia, A. Li, F. Huang, Z. Xu, L. Qiu, Y. Chen, G. Fei and M. Wang, *Carbon*, 2016, **98**, 457–462.

180 S. Gorantla, A. Bachmatiuk, J. Hwang, H. A. Alsalman, J. Y. Kwak, T. Seyller, J. Eckert, M. G. Spencer and M. H. Rümmeli, *Nanoscale*, 2014, **6**, 889–896.

181 F. C. Comanescu, E. Lare, A. Istrate, M. Veca, F. Nastase, R. Gavrila, A. Dinescu and M. Purica, in *2017 International Semiconductor Conference (CAS)*, IEEE, 2017, pp. 55–58.

182 B. N. Chandrashekar, B. Deng, A. S. Smitha, Y. Chen, C. Tan, H. Zhang, H. Peng and Z. Liu, *Adv. Mater.*, 2015, **27**, 5210–5216.

183 X. Zhang, C. Xu, Z. Zou, Z. Wu, S. Yin, Z. Zhang, J. Liu, Y. Xia, C.-T. Lin, P. Zhao and H. Wang, *Carbon*, 2020, **161**, 479–485.

184 W.-H. Lin, T.-H. Chen, J.-K. Chang, J.-I. Taur, Y.-Y. Lo, W.-L. Lee, C.-S. Chang, W.-B. Su and C.-I. Wu, *ACS Nano*, 2014, **8**, 1784–1791.

185 P. Nemes-Incze, Z. Osváth, K. Kamarás and L. P. Biró, *Carbon*, 2008, **46**, 1435–1442.

186 J. E. Proctor, E. Gregoryanz, K. S. Novoselov, M. Lotya, J. N. Coleman and M. P. Halsall, *Phys. Rev. B*, 2009, **80**, 073408.

187 T. M. G. Mohiuddin, A. Lombardo, R. R. Nair, A. Bonetti, G. Savini, R. Jalil, N. Bonini, D. M. Basko, C. Galiotis, N. Marzari, K. S. Novoselov, A. K. Geim and A. C. Ferrari, *Phys. Rev. B*, 2009, **79**, 205433.

188 J. Zabel, R. R. Nair, A. Ott, T. Georgiou, A. K. Geim, K. S. Novoselov and C. Casiraghi, *NANO Lett.*, 2012, **12**, 617–621.

189 F. Ding, H. X. Ji, Y. H. Chen, A. Herklotz, K. Dörr, Y. F. Mei, A. Rastelli and O. G. Schmidt, *NANO Lett.*, 2010, **10**, 3453–3458.

190 C. Casiraghi, S. Pisana, K. S. Novoselov, A. K. Geim and A. C. Ferrari, *Appl. Phys. Lett.*, 2007, **91**, 233108.

191 M. Kalbac, A. Reina-Cecco, H. Farhat, J. Kong, L. Kavan and M. S. Dresselhaus, *ACS Nano*, 2010, **4**, 6055–6063.

192 D. C. Elias, R. R. Nair, T. M. G. Mohiuddin, S. V. Morozov, P. Blake, M. P. Halsall, A. C. Ferrari, D. W. Boukhvalov, M. I. Katsnelson, A. K. Geim and K. S. Novoselov, *Science*, 2009, **323**, 610–613.

193 J. E. Johns and M. C. Hersam, *Acc. Chem. Res.*, 2013, **46**, 77–86.

194 A. C. Ferrari and J. Robertson, *Phys. Rev. B*, 2000, **61**, 14095–14107.

195 C. Thomsen and S. Reich, *Phys. Rev. Lett.*, 2000, **85**, 5214–5217.

196 F. Tuinstra and J. L. Koenig, *J. Chem. Phys.*, 1970, **53**, 1126–1130.

197 P. Turner, K. R. Paton, E. J. Legge, A. de Luna Bugallo, A. K. S. Rocha-Robledo, A.-A. Zahab, A. Centeno, A. Sacco, A. Pesquera, A. Zurutuza, A. M. Rossi, D. N. H. Tran, D. L Silva, D. Losic, F. Farivar, H. Kerdoncuff, H. Kwon, J. Pirart, J. L. E. Campos, K. M. Subhedar, L.-L. Tay, L. Ren, L. G. Cançado, M. Paillet, P. Finnie, P.

L. Yap, R. Arenal, S. R. Dhakate, S. Wood, S. Jiménez-Sandoval, T. Batten, V. Nagyte, Y. Yao, A. R. Hight Walker, E. H. Martins Ferreira, C. Casiraghi and A. J. Pollard, *2D Mater.*, 2022, **9**, 035010.

198 Y. ying Wang, Z. hua Ni, T. Yu, Z. X. Shen, H. min Wang, Y. hong Wu, W. Chen and A. T. Shen Wee, *J. Phys. Chem. C*, 2008, **112**, 10637–10640.

199 A. V Babichev, S. A. Rykov, M. Tchernycheva, A. N. Smirnov, V. Y. Davydov, Y. A. Kumzerov and V. Y. Butko, *ACS Appl. Mater. Interfaces*, 2016, **8**, 240–246.

200 R. Okuda, K. Niwano, K. Hatada, K. Kokubu, R. Suga, T. Watanabe and S. Koh, *Sci. Rep.*, 2023, **13**, 13878.

201 A. Das, B. Chakraborty, S. Piscanec, S. Pisana, A. K. Sood and A. C. Ferrari, *Phys. Rev. B*, 2009, **79**, 155417.

202 OriginLab Corporation, 2022.

203 The MathWorks Inc, 2023.

204 Z. T. Wu, W. W. Zhao, W. Y. Chen, J. Jiang, H. Y. Nan, X. T. Guo, Z. Liang, Y. M. Chen, Y. F. Chen and Z. H. Ni, *J. Raman Spectrosc.*, 2015, **46**, 21–24.

205 J. E. Lee, G. Ahn, J. Shim, Y. S. Lee and S. Ryu, *Nat. Commun.*, 2012, **3**, 1024.

206 L. Meng, Y. Su, D. Geng, G. Yu, Y. Liu, R.-F. Dou, J.-C. Nie and L. He, *Appl. Phys. Lett.*

207 R. Kato, Y. Koga, K. Matsuishi and M. Hasegawa, *Jpn. J. Appl. Phys.*, 2017, **56**, 30307.

208 J.-Y. Hong, Y. C. Shin, A. Zubair, Y. Mao, T. Palacios, M. S. Dresselhaus, S. H. Kim and J. Kong, *Adv. Mater.*, 2016, **28**, 2382–2392.

209 C. Neumann, S. Reichardt, P. Venezuela, M. Drögeler, L. Banszerus, M. Schmitz, K. Watanabe, T. Taniguchi, F. Mauri, B. Beschoten, S. V Rotkin and C. Stampfer, *Nat. Commun.*, 2015, **6**, 8429.

210 Microsoft Corporation, 2023.

211 A. Isacsson, A. W. Cummings, L. Colombo, L. Colombo, J. M. Kinaret and S. Roche, *2D Mater.*, 2016, **4**, 012002.

212 Graphenea, Monolayer Graphene on Cu, https://www.graphenea.com/collections/buy-graphene-films/products/monolayer-graphene-on-cu-4-inches?variant=276514394.

213 BGI, Polycrystalline graphene film Cu-P, https://en.bgi-c.com/product/3.html,

(accessed 22 November 2023).

214 M. Gautam and A. H. Jayatissa, *Mater. Sci. Eng. C*, 2011, **31**, 1405–1411.

215 F. Yavari, E. Castillo, H. Gullapalli, P. M. Ajayan and N. Koratkar, *Appl. Phys. Lett.*, 2012, **100**, 203120.

216 D. Dutta, A. Hazra, S. K. Hazra, J. Das, S. Bhattacharyya, C. K. Sarkar and S. Basu, *Meas. Sci. Technol.*, 2015, **26**, 115104.

217 X. Hu, Y. Zhang, X. Chen, M. He and Z. Jin, *Electroanalysis*, 2023, **35**, 26.

218 J. M. Fehr, C. G. McKenas, B. Liu and M. R. Lockett, *Appl. Surf. Sci.*, 2019, **480**, 1109–1115.

219 P. Fortgang, T. Tite, V. Barnier, N. Zehani, C. Maddi, F. Lagarde, A.-S. Loir, N. Jaffrezic-Renault, C. Donnet, F. Garrelie and C. Chaix, *ACS Appl. Mater. Interfaces*, 2016, **8**, 1424–1433.

220 M. Kim, S. H. Joo, M. Wang, S. G. Menabde, D. Luo, S. Jin, H. Kim, W. K. Seong, M. S. Jang, S. K. Kwak, S. H. Lee and R. S. Ruoff, *ACS Nano*, 2023, **17**, 18914–18923.

221 S. Yang, M. R. Lohe, K. Müllen and X. Feng, *Adv. Mater.*, 2016, **28**, 6213–6221.

222 J. M. Munuera, J. I. Paredes, S. Villar-Rodil, M. Ayán-Varela, A. Pagán, S. D. Aznar-Cervantes, J. L. Cenis, A. Martínez-Alonso and J. M. D. Tascón, *Carbon*, 2015, **94**, 729–739.

223 M. Meldal and C. W. Tornøe, *Chem. Rev.*, 2008, **108**, 2952–3015.

224 Q. Tu, L. Zhao, X. Han, D.-E. Wang, M.-S. Yuan, C. Tian and J. Wang, *RSC Adv.*, 2016, **6**, 95628–95632.

225 T. Wei, T. Dong, H. Xing, Y. Liu and Z. Dai, *Anal. Chem.*, 2017, **89**, 12237–12243.

226 Z. Xu, X. Ye, P. Hu, M. Yin, B. Lv, G. Zhang, Q. Meng and C. Gao, *Sep. Purif. Technol.*, 2022, **283**, 120162.

227 Z. Wang, Z. Ge, X. Zheng, N. Chen, C. Peng, C. Fan and Q. Huang, *Nanoscale*, 2012, **4**, 394–399.

228 Z. Yan, L. Yang, J.-M. Han and H. Li, *Nanotechnology*, 2021, **32**, 385704.

229 K.-C. Mei, N. Rubio, P. M. Costa, H. Kafa, V. Abbate, F. Festy, S. S. Bansal, R. C. Hider and K. T. Al-Jamal, *Chem. Commun.*, 2015, **51**, 14981–14984.

230 I. Kaminska, M. R. Das, Y. Coffinier, J. Niedziolka-Jonsson, J. Sobczak, P. Woisel, J. Lyskawa, M. Opallo, R. Boukherroub and S. Szunerits, *ACS Appl. Mater. \&*

INTERFACES, 2012, **4**, 1016–1020.

231 R. Salvio, S. Krabbenborg, W. J. M. Naber, A. H. Velders, D. N. Reinhoudt and W. G. Van Der Wiel, *Chem. - A Eur. J.*, 2009, **15**, 8235–8240.

232 J. M. Schnorr, D. van der Zwaag, J. J. Walish, Y. Weizmann and T. M. Swager, *Adv. Funct. Mater.*, 2013, **23**, 5285–5291.

233 Y. Waseda, E. Matsubara and K. Shinoda, *X-Ray Diffraction Crystallography*, Springer Berlin Heidelberg, Berlin, Heidelberg, 2011.

234 O. Zabihi, M. Ahmadi, Q. Li, S. M. Fakhrhoseini, Z. Komeily Nia, M. Arjmand, K. Parvez and M. Naebe, *FlatChem*, 2019, **18**, 100132.

235 A.-S. Al-Sherbini, M. Bakr, I. Ghoneim and M. Saad, *J. Adv. Res.*, 2017, **8**, 209–215.

236 J. Wang, K. K. Manga, Q. Bao and K. P. Loh, *J. Am. Chem. Soc.*, 2011, **133**, 8888–8891.

237 D. Yang, A. Velamakanni, G. Bozoklu, S. Park, M. Stoller, R. D. Piner, S. Stankovich, I. Jung, D. A. Field, C. A. Ventrice and R. S. Ruoff, *Carbon*, 2009, **47**, 145–152.

238 D. Parviz, F. Irin, S. A. Shah, S. Das, C. B. Sweeney and M. J. Green, *Adv. Mater.*, 2016, **28**, 8796–8818.

239 Y. Hao, Y. Wang, L. Wang, Z. Ni, Z. Wang, R. Wang, C. K. Koo, Z. Shen and J. T. L. Thong, *Small*, 2010, **6**, 195–200.

240 A. Grabowska, J. Kowalczyk, R. Tomala, M. Ptak, M. Małecka, A. Wędzyńska, M. Stefanski, W. Stręk and P. Głuchowski, *Materials* , 2023, **16**, 2188.

241 V. T. Nguyen, H. D. Le, V. C. Nguyen, T. T. T. Ngo, D. Q. Le, X. N. Nguyen and N. M. Phan, *Adv. Nat. Sci. Nanosci. Nanotechnol.*, 2013, **4**, 35012.

242 C. Halbig, P. Rietsch and S. Eigler, *Molecules*, 2015, **20**, 21050–21057.

243 J. P. Collman, N. K. Devaraj, T. P. A. Eberspacher and C. E. D. Chidsey, *Langmuir*, 2006, **22**, 2457–2464.

244 A. Devadoss and C. E. D. Chidsey, *J. Am. Chem. Soc.*, 2007, **129**, 5370–5371.

245 A. C. Gouget-Laemmel, J. Yang, M. A. Lodhi, A. Siriwardena, D. Aureau, R. Boukherroub, J.-N. Chazalviel, F. Ozanam and S. Szunerits, *J. Phys. Chem. C*, 2013, **117**, 368–375.

246 A. Saad, M. Abderrabba and M. M. Chehimi, *Surf. Interface Anal.*, 2017, **49**, 340–

344.

247 M. Ayiania, M. Smith, A. J. R. Hensley, L. Scudiero, J.-S. McEwen and M. Garcia-Perez, *Carbon*, 2020, **162**, 528–544.

248 I. Matanovic, K. Artyushkova, M. B. Strand, M. J. Dzara, S. Pylypenko and P. Atanassov, *J. Phys. Chem. C*, 2016, **120**, 29225–29232.

249 H. Hantsche, *Adv. Mater.*, 1993, **5**, 778–778.

250 A. E. Daugaard, S. Hvilsted, T. S. Hansen and N. B. Larsen, *Macromolecules*, 2008, **41**, 4321–4327.

251 T. S. Sreeprasad and V. Berry, *Small*, 2013, **9**, 341–350.

252 T. Pandhi, A. Chandnani, H. Subbaraman and D. Estrada, *Sensors*, 2020, **20**, 5642.

253 T. Sabu, J. Nirav and T. Vijay K, *Functional Nanomaterials*, Springer Singapore, Singapore, 2020.

254 L. Kaur, *J. Indian Chem. Soc.*, 2023, **100**, 101019.

255 G. Capote Mastrapa and F. L. Freire, *J. Sensors*, 2019, **2019**, 1–7.

256 S. Yong-Jiao, W. Shi-Zhen, Z. Wen-Lei, W. Wen-Da, Z. Wen-Dong and H. Jie, *Acta Phys. Sin.*, 2022, **71**, 100701.

257 T. L. H. Doan, J.-Y. Kim, J.-H. Lee, L. H. T. Nguyen, Y. T. Dang, K.-B. T. Bui, A. T. T. Pham, A. Mirzaei, T. B. Phan and S. S. Kim, *Sensors Actuators B Chem.*, 2021, **348**, 130684.

258 X.-Z. Song, Y.-L. Meng, Z. Tan, L. Qiao, T. Huang and X.-F. Wang, *Inorg. Chem.*, 2017, **56**, 13646–13650.

259 Y. S. Kim, S.-C. Ha, H. Yang and Y. T. Kim, *Sensors Actuators B Chem.*, 2007, **122**, 211–218.

260 J. A. Dean, *Lange's handbook of chemistry*, 1999.

261 E. F. Meyer and R. D. Hotz, *J. Chem. Eng. Data*, 1973, **18**, 359–362.

262 D. GmbH, Saturated Vapor Pressure Calculation by Antoine Equation, http://ddbonline.ddbst.com/AntoineCalculation/AntoineCalculationCGI.exe.

263 S. S. Sidhu, Z. Redouane, B. S. Preetkanwal and Y. Morteza, *Materials Horizons : From Nature to Nanomaterials Futuristic Composites*, 2018.

264 J. Li, Y. Lu, Q. Ye, M. Cinke, J. Han and M. Meyyappan, *Nano Lett.*, 2003, **3**, 929–933.

265 X. Tang, M. Debliquy, D. Lahem, Y. Yan and J.-P. Raskin, *Sensors*, 2021, **21**, 1443.

266 S. Yeo, C. Y. Lee, D.-S. Kim, Y. S. Hwang, J. K. Park, M.-H. Jung, W.-J. Cho, J. S. Lee and C. Kim, *Thin Solid Films*, 2019, **677**, 73–76.

267 M. S. Polyakov, T. V. Basova, M. Göksel, A. Şenocak, E. Demirbaş, M. Durmuş, B. Kadem and A. Hassan, *Synth. Met.*, 2017, **227**, 78–86.

268 J. H. Choi, J. Lee, M. Byeon, T. E. Hong, H. Park and C. Y. Lee, *ACS Appl. Nano Mater.*, 2020, **3**, 2257–2265.

269 C. Deng, W. Lin, G. Agnus, D. Dragoe, D. Pierucci, A. Ouerghi, S. Eimer, I. Barisic, D. Ravelosona, C. Chappert and W. Zhao, *J. Phys. Chem. C*, 2014, **118**, 13890–13897.

270 H. E. Romero, N. Shen, P. Joshi, H. R. Gutierrez, S. A. Tadigadapa, J. O. Sofo and P. C. Eklund, *ACS Nano*, 2008, **2**, 2037–2044.

271 I. Childres, L. Jauregui, W. Park, H. Caoa and Y. . Chena, in *New Developments in Photon and Materials Research*, 2013, pp. 403–418.

272 B. Zhuang, S. Li, S. Li and J. Yin, *Carbon*, 2021, **173**, 609–636.

273 Y.-H. Zhang, Y.-B. Chen, K.-G. Zhou, C.-H. Liu, J. Zeng, H.-L. Zhang and Y. Peng, *Nanotechnology*, 2009, **20**, 185504.

274 Y. You, J. Deng, X. Tan, N. Gorjizadeh, M. Yoshimura, S. C. Smith, V. Sahajwalla and R. K. Joshi, *Phys. Chem. Chem. Phys.*, 2017, **19**, 6051–6056.

275 C. Gabbett, A. G. Kelly, E. Coleman, L. Doolan, T. Carey, K. Synnatschke, S. Liu, A. Dawson, D. O'Suilleabhain, J. Munuera, E. Caffrey, J. B. Boland, Z. Sofer, G. Ghosh, S. Kinge, L. D. A. Siebbeles, N. Yadav, J. K. Vij, M. A. Aslam, A. Matkovic and J. N. Coleman, *Nat. Commun.*, 2024, **15**, 4517.

276 S. K. S. Mazinani, R. V. Meidanshahi, J. L. Palma, P. Tarakeshwar, T. Hansen, M. A. Ratner and V. Mujica, *J. Phys. Chem. C*, 2016, **120**, 26054–26060.

277 J. N. Israelachvili, in *Intermolecular and Surface Forces*, Elsevier, 2011, pp. 91–106.

278 National Institute of Standards and Technology, Experimental Polarizabilites, https://cccbdb.nist.gov/pollistx.asp.

279 J. Mäklin, T. Mustonen, K. Kordás, S. Saukko, G. Tóth and J. Vähäkangas, *Phys. status solidi*, 2007, **244**, 4298–4302.

280 R. A. Potyrailo, S. Go, D. Sexton, X. Li, N. Alkadi, A. Kolmakov, B. Amm, R. St-Pierre, B. Scherer, M. Nayeri, G. Wu, C. Collazo-Davila, D. Forman, C. Calvert, C.

Mack and P. McConnell, *Nat. Electron.*, 2020, **3**, 280–289.

281 N. S. S. Capman, X. V. Zhen, J. T. Nelson, V. R. S. K. Chaganti, R. C. Finc, M. J. Lyden, T. L. Williams, M. Freking, G. J. Sherwood, P. Bühlmann, C. J. Hogan and S. J. Koester, *ACS Nano*, 2022, **16**, 19567–19583.

Appendix A

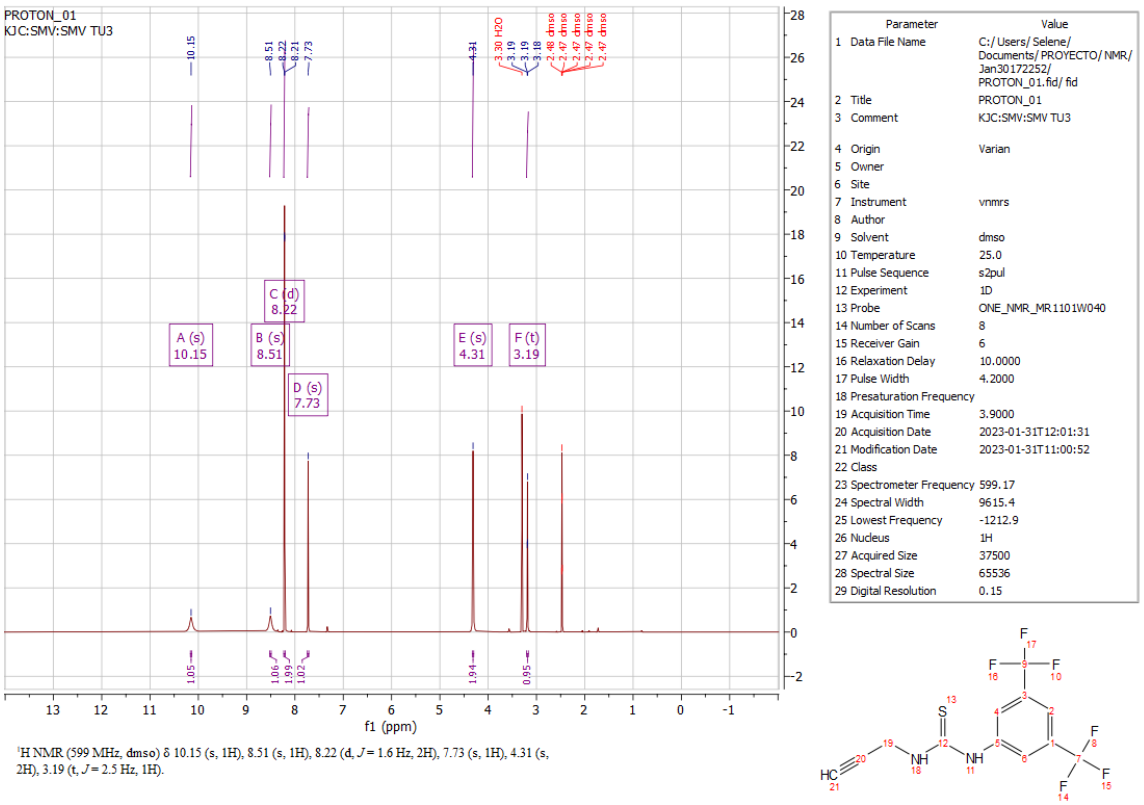

^{1}H NMR (599 MHz, dmso) δ 10.15 (s, 1H), 8.51 (s, 1H), 8.22 (d, J = 1.6 Hz, 2H), 7.73 (s, 1H), 4.31 (s, 2H), 3.19 (t, J = 2.5 Hz, 1H).

A1 ^{1}H NMR Spectrum of TU.

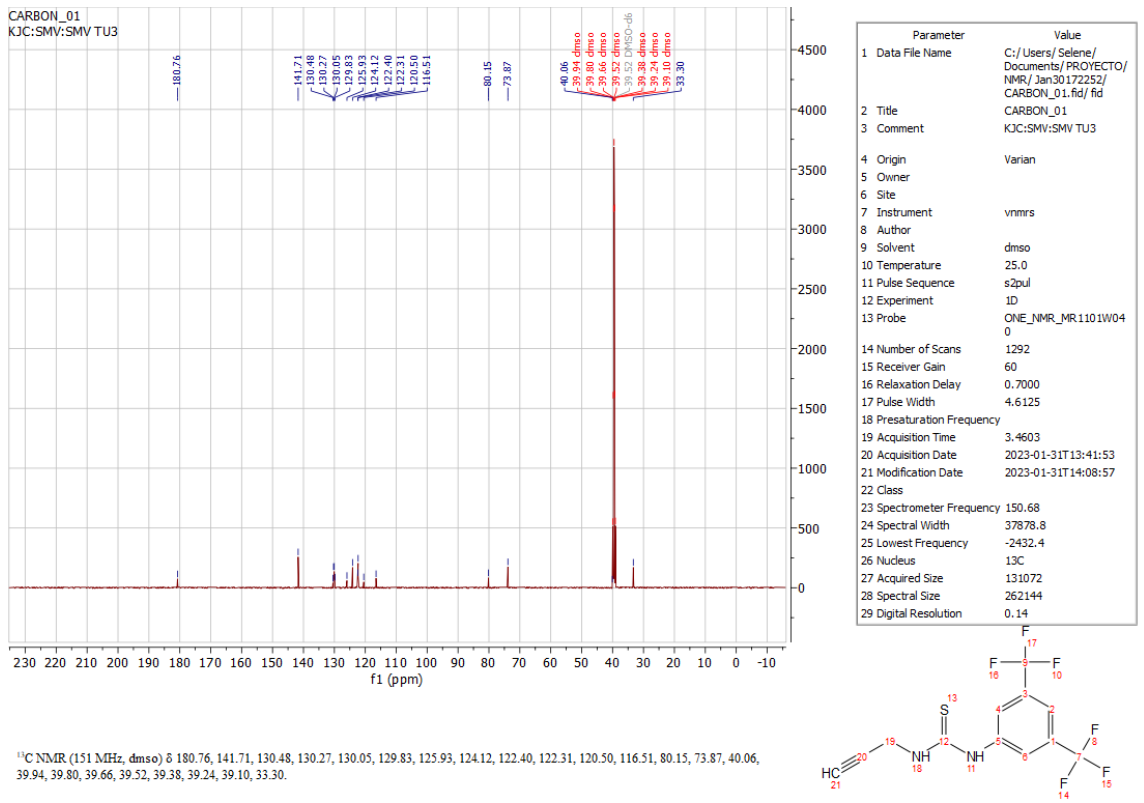

^{13}C NMR (151 MHz, dmso) δ 180.76, 141.71, 130.48, 130.27, 130.05, 129.83, 125.93, 124.12, 122.40, 122.31, 120.50, 116.51, 80.15, 73.87, 40.06, 39.94, 39.80, 39.66, 39.52, 39.38, 39.24, 39.10, 33.30.

A2 ^{13}C NMR Spectrum of TU.

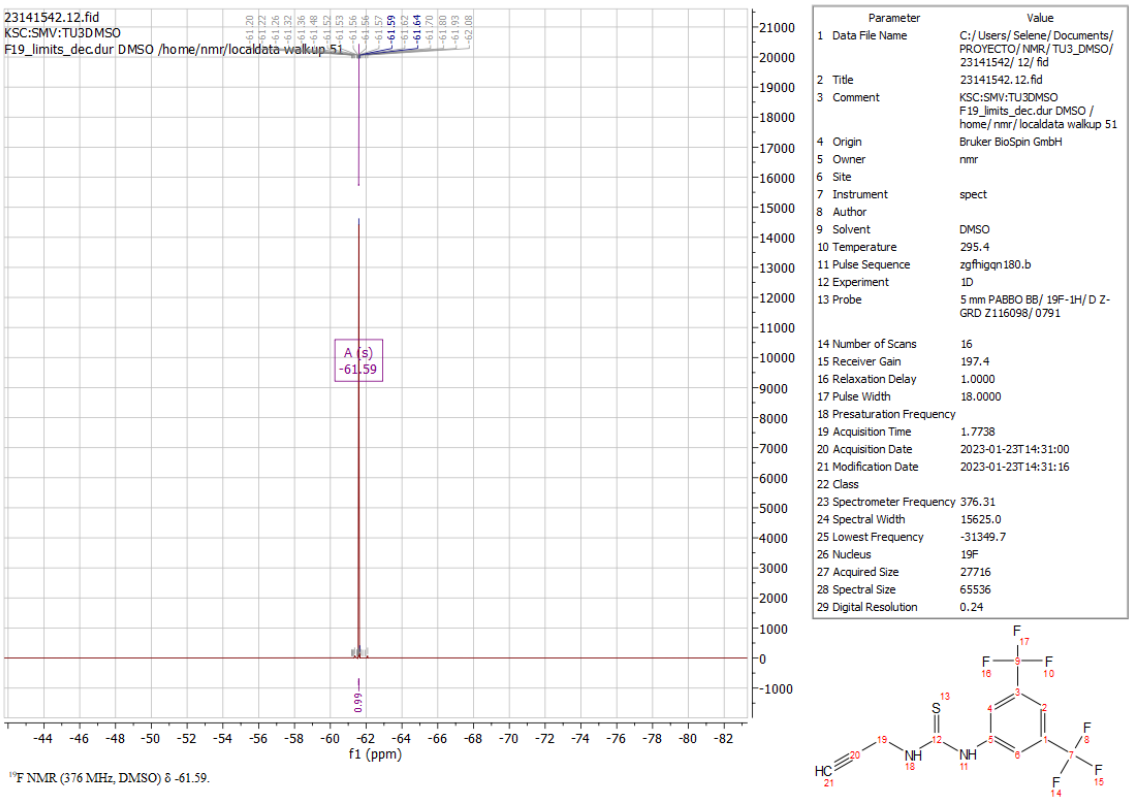

A3 ^{19}F NMR Spectrum of TU.

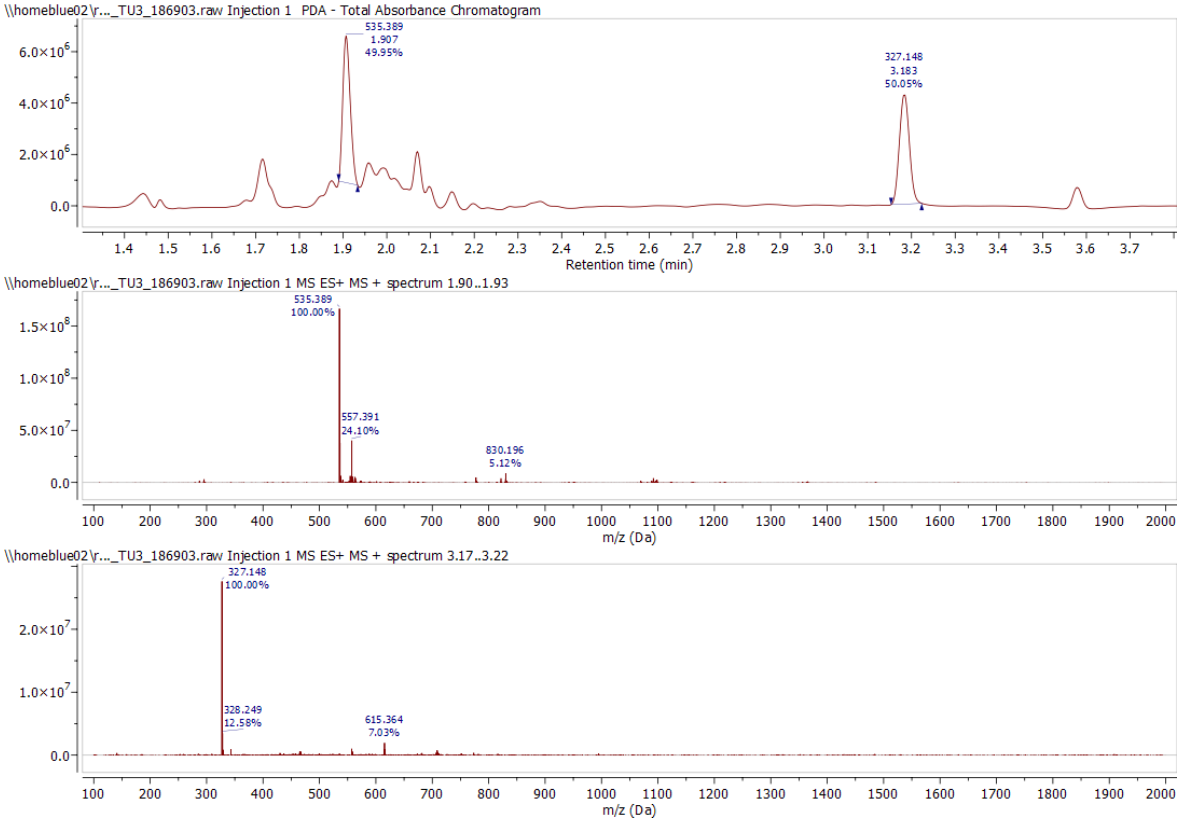

A4 Mass spectroscopy results.

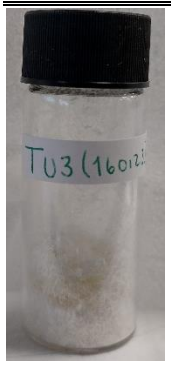

Table A1 Elemental analysis results.

Measured			Expected			Difference		
% C	% H	% N	% C	% H	% N	% C	% H	% N
44.09	2.41	8.55	44.18	2.47	8.58	-0.09	-0.06	-0.03

Appendix B

MATLAB code:

```
clear
clc
%Calling the file that contains the matrix
load('ratio.mat')
A=matrixformatS2; %Calling the matrix
T=table;
for sizei=1:32
    for i=1:100
idx = randi(size(A,1)-sizei+1);
idy = randi(size(A,1)-sizei+1);
   selected = A(idx:idx+sizei-1,idy:idy+sizei-1);
   selected;
m1=mean(selected,"all");
x_t= table(idx,idy,sizei,m1);
T = [T; x_t];
    end
end
T
writetable(T,'ratio1.txt','Delimiter',' ')
```

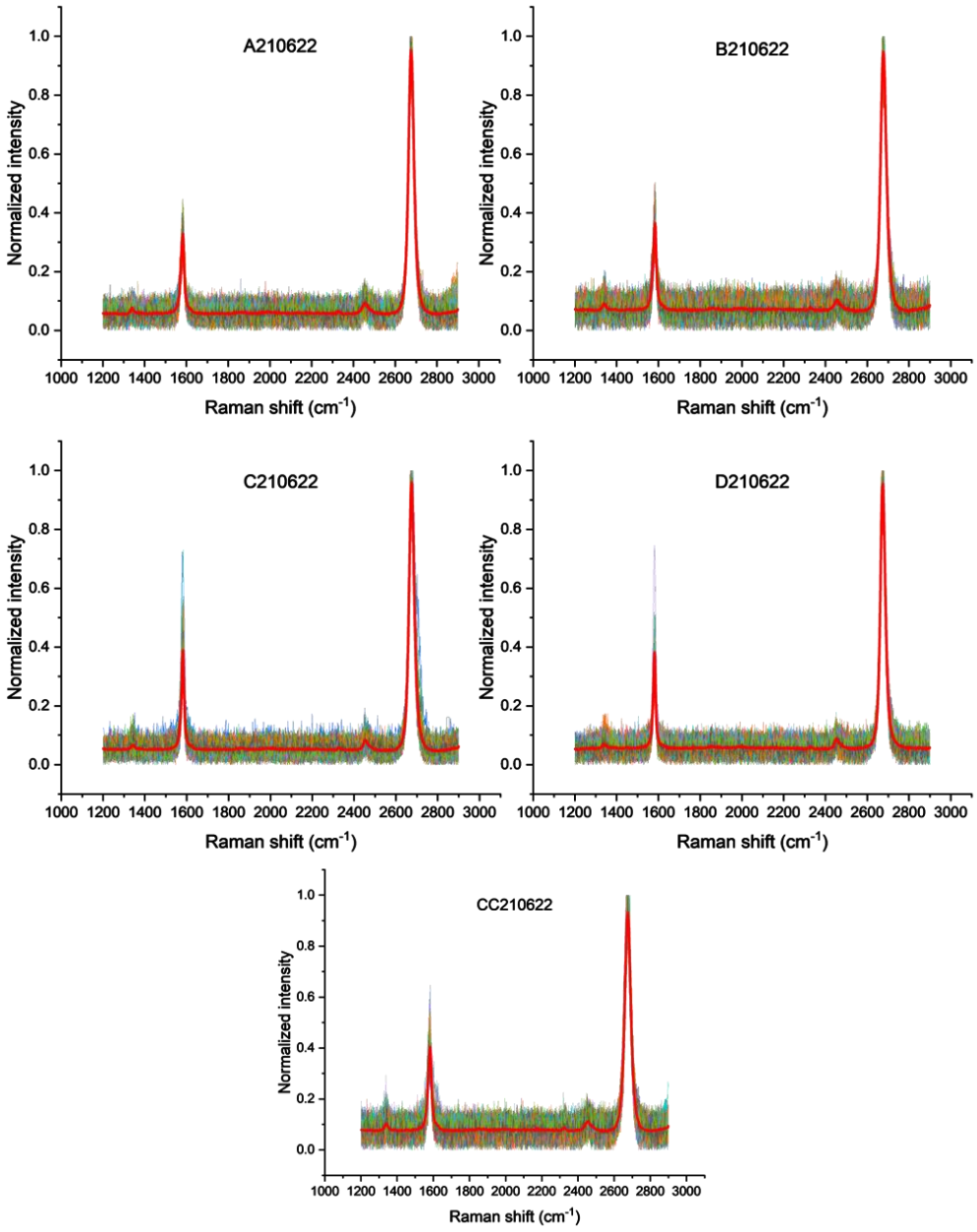

B1 All spectra measured for each position of batch 1, after cosmic ray contribution removal, baseline correction and normalisation. The red spectrum is the averaged spectra.

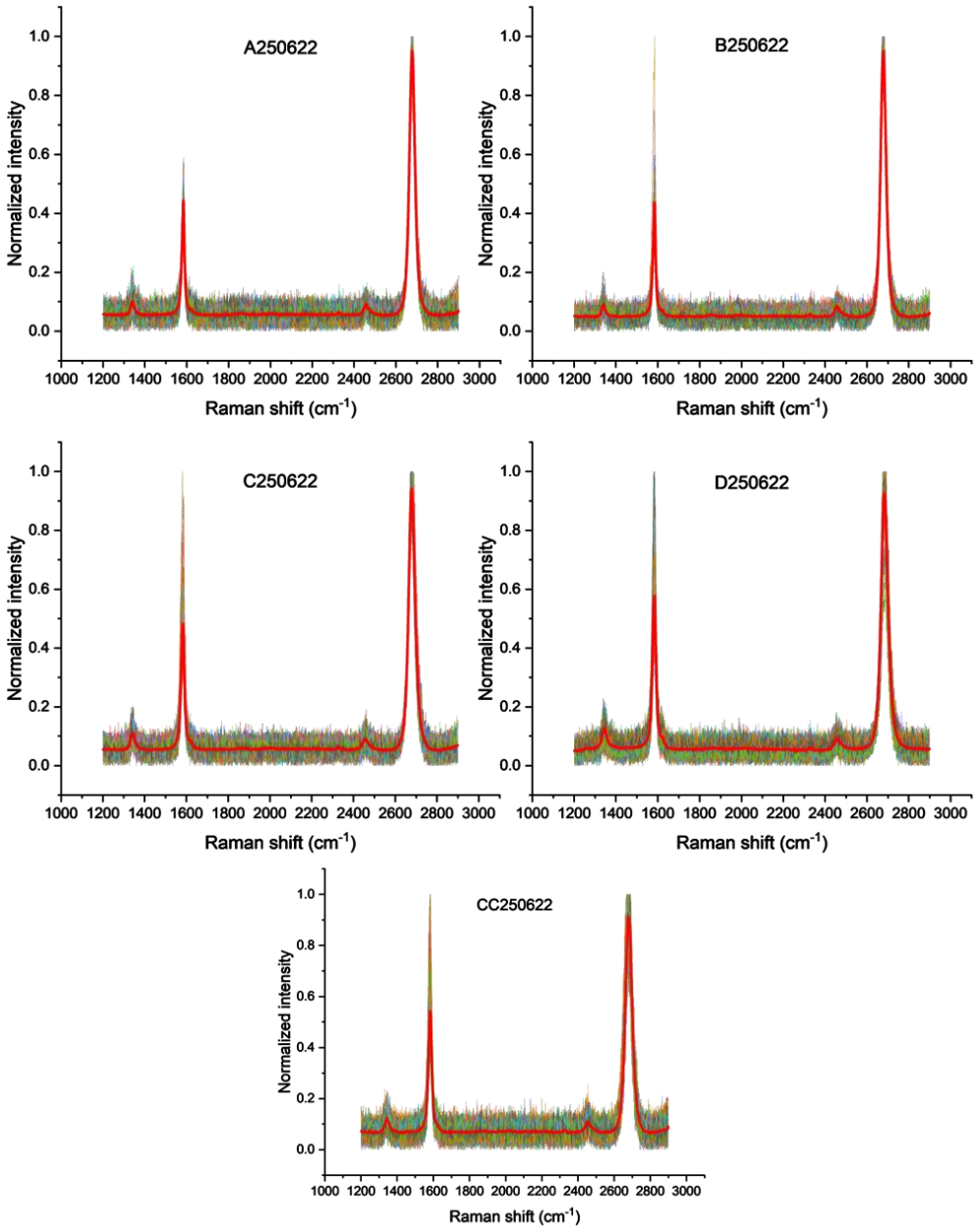

B2 All spectra measured for each position of batch 2, after cosmic ray contribution removal, baseline correction and normalisation. The red spectrum is the averaged spectra.

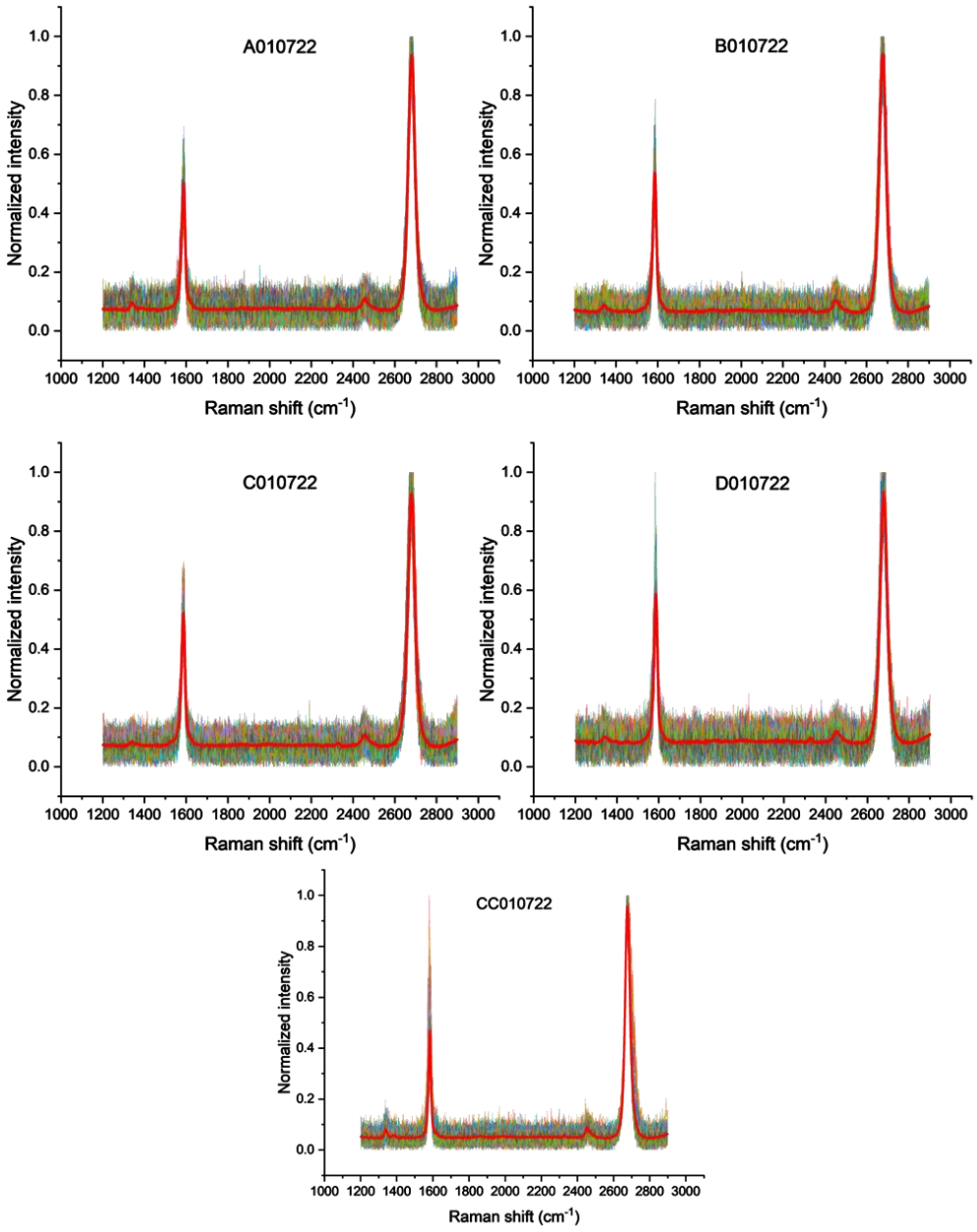

B3 All spectra measured for each position of batch 3, after cosmic ray contribution removal, baseline correction and normalisation. The red spectrum is the averaged spectra.

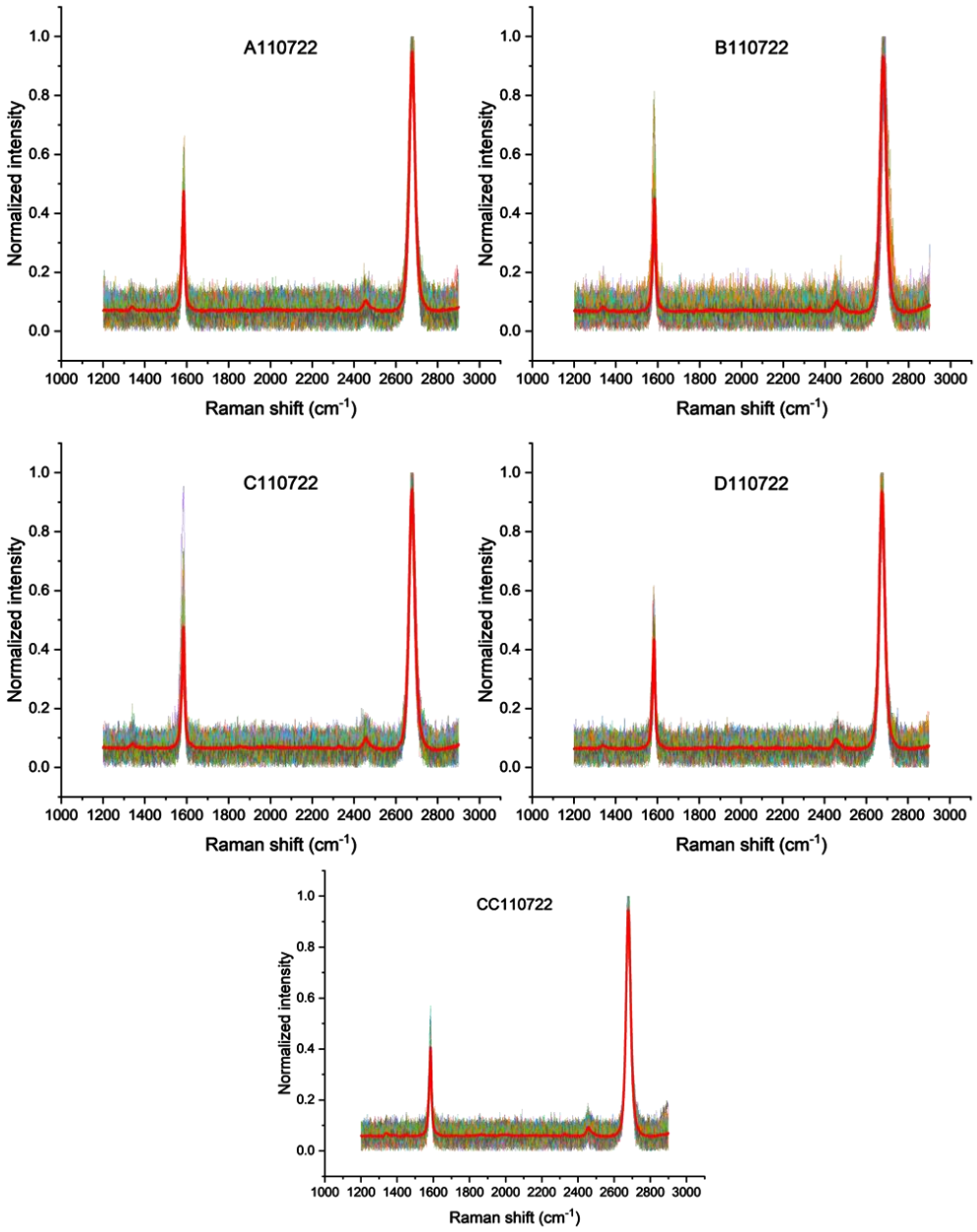

B4 All spectra measured for each position of batch 4, after cosmic ray contribution removal, baseline correction and normalisation. The red spectrum is the averaged spectra.

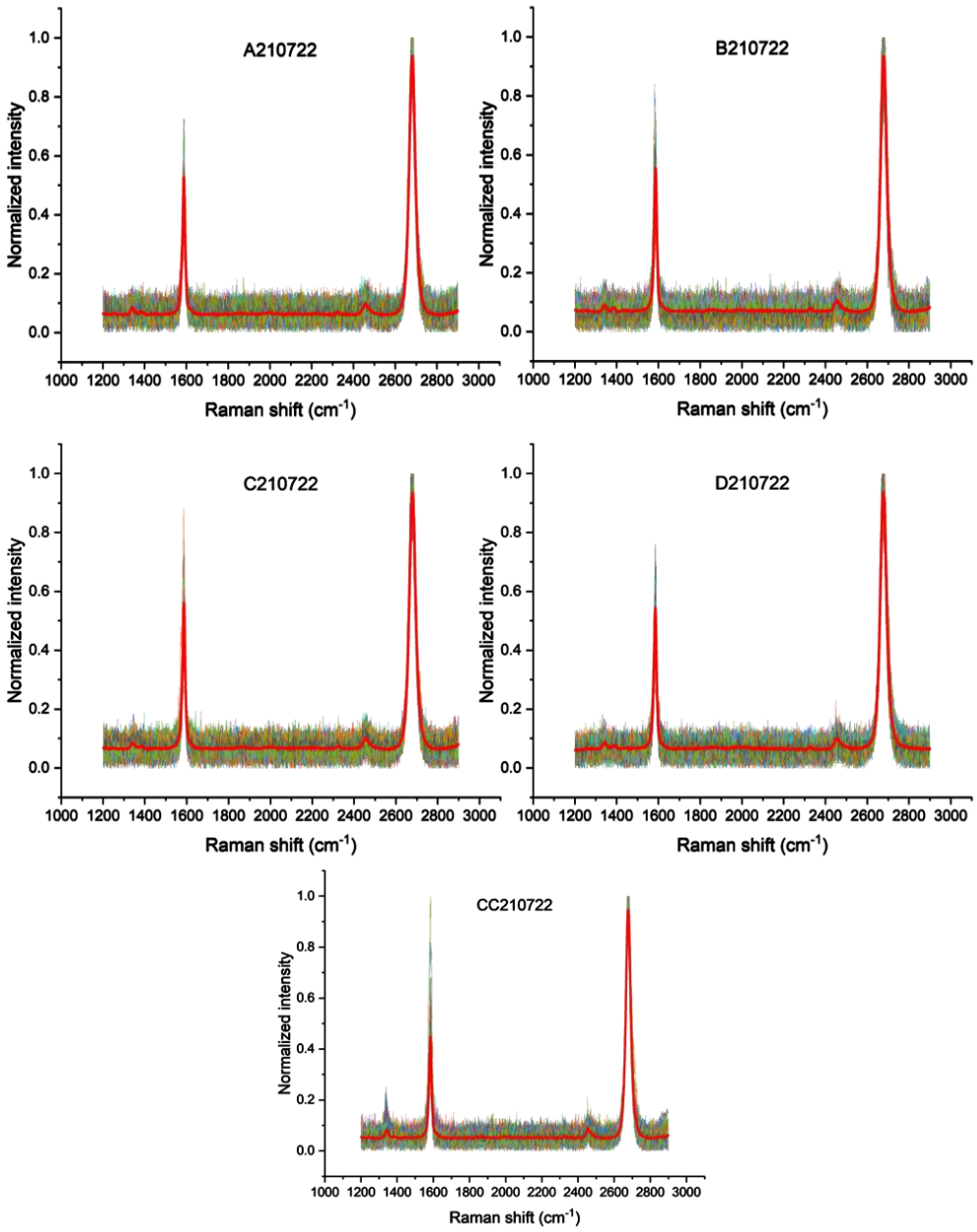

B5 All spectra measured for each position of batch 1, after cosmic ray contribution removal, baseline correction and normalisation. The red spectrum is the averaged spectra.

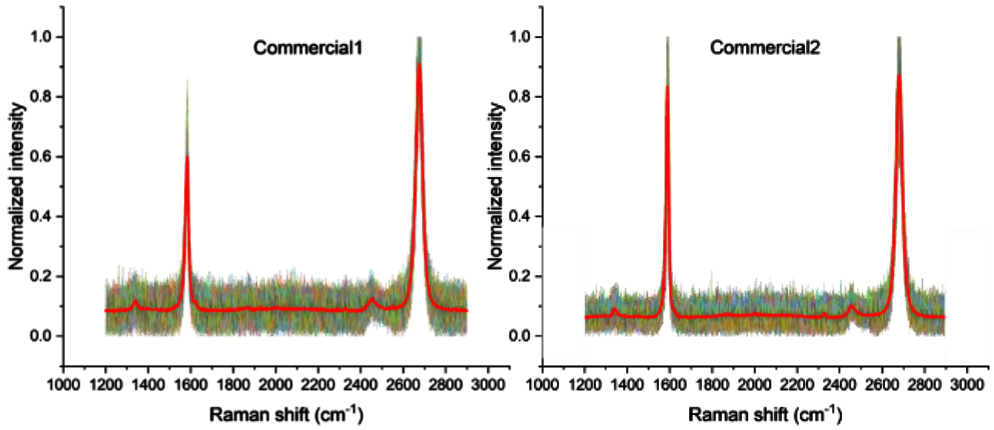

B6 All spectra measured for the commercial brands, after cosmic ray contribution removal, baseline correction and normalisation. The red spectrum is the averaged spectra.

Table B1 Mean and standard deviations from the background (1800-2200 cm^{-1}) of every map and the average spectrum

Batch	From mappings		From the average spectra		D peak intensity from the averaged spectra
	Mean	Standard deviation	Mean	Standard deviation	
A210622	0.06	0.02	0.06	0.00	0.08
B210622	0.07	0.02	0.07	0.00	0.09
C210622	0.05	0.02	0.05	0.00	0.07
D210622	0.06	0.02	0.06	0.00	0.07
CC210622	0.08	0.03	0.08	0.00	0.10
A010722	0.08	0.03	0.08	0.00	0.10
B010722	0.08	0.03	0.08	0.00	0.09
C010722	0.07	0.03	0.07	0.00	0.09
D010722	0.09	0.03	0.09	0.00	0.10
CC010722	0.05	0.02	0.05	0.00	0.08
A110722	0.07	0.02	0.05	0.00	0.08
B110722	0.07	0.03	0.07	0.00	0.08
C110722	0.07	0.02	0.07	0.00	0.08
D110722	0.07	0.02	0.07	0.00	0.08
CC110722	0.06	0.02	0.06	0.00	0.07
A210722	0.07	0.02	0.07	0.00	0.09
B210722	0.07	0.02	0.07	0.00	0.09
C210722	0.07	0.02	0.07	0.00	0.08
D210722	0.07	0.02	0.07	0.00	0.09
CC210722	0.05	0.02	0.05	0.00	0.08
A250622	0.06	0.02	0.06	0.00	0.10
B250622	0.05	0.02	0.05	0.00	0.09
C250622	0.06	0.02	0.06	0.00	0.11
D250622	0.06	0.02	0.06	0.00	0.13
CC250622	0.07	0.02	0.07	0.00	0.12
Commercial 1	0.09	0.03	0.09	0.00	0.12
Commercial 2	0.07	0.02	0.07	0.00	0.09